

Rafael da Cruz Ribeiro Berti

Interaction of turbulent structures with ethanol sprays in mixture  
formation processes in a constant-flow chamber

São Paulo

2018



Rafael da Cruz Ribeiro Berti

Interaction of turbulent structures with ethanol sprays in mixture  
formation processes in a constant-flow chamber

Thesis submitted to the Escola  
Politécnica of University de São Paulo for  
the fulfilment of requirements for the  
degree of Doctor of Science

São Paulo

2018



Rafael da Cruz Ribeiro Berti

Interaction of turbulent structures with ethanol sprays in mixture  
formation processes in a constant-flow chamber

Thesis submitted to the Escola  
Politécnica of University de São Paulo for  
the fulfilment of requirements for the  
degree of Doctor of Science

Area of Concentration:  
Mechanical Engineering of Energy and  
Fluids

Advisor:  
Prof. Dr. Guenther Carlos Krieger Filho

São Paulo

2018

Este exemplar foi revisado e corrigido em relação à versão original, sob responsabilidade única do autor e com a anuência de seu orientador.

São Paulo, \_\_\_\_\_ de \_\_\_\_\_ de \_\_\_\_\_

Assinatura do autor: \_\_\_\_\_

Assinatura do orientador: \_\_\_\_\_

#### Catálogo-na-publicação

Berti, Rafael

Interaction of the turbulent structures with ethanol sprays in mixture formation processes in a constant-flow chamber / R. Berti -- versão corr. -- São Paulo, 2018.

264 p.

Tese (Doutorado) - Escola Politécnica da Universidade de São Paulo. Departamento de Engenharia Mecânica.

1.Etanol 2.Turbulência 3.Mecânica dos Fluidos 4.Injeção (Engenharia) 5.Motores de Combustão Interna I.Universidade de São Paulo. Escola Politécnica. Departamento de Engenharia Mecânica II.t.

## ACKNOWLEDGEMENTS

Throughout the years of this research, the expected and also unexpected challenges could only be overcome with the help of many important people. Their support will always be appreciated.

For my lab colleagues and friends, I would like to thank you for all the support and assistance during the development of the experimental results. My special thanks to Andre, Helio, Robinson, Vitor for the uncountable days, nights and weekends devoted to building, machining and measuring. I am also grateful to Clayton Zabeu for sharing and teaching much of my knowledge on the vast field of engines. Without them, I would not have gone far.

I also would like to express my gratitude to the workshop staff at Escola Politécnica da USP. Thank you Adilson and Carlos for all the support and teaching that started during my undergraduate studies and continued until today. The acquired knowledge I will carry to my career.

For my advisor prof. Krieger, I would like to thank you for your confidence on my work and for all the required and never denied assistance. His effort on transforming our laboratory on a leading-edge most certainly worth it.

To my second home, the Escola Politécnica, I would like to thank you for providing all tools and knowledge that I have. I also should thank the Fundação de Amparo à Pesquisa do Estado de São Paulo (FAPESP) for the financial support.

To my friends, Andre, Caroline, Pedro, Raphael and Romulo. I thank you all for understanding the absence during many parts of my work. Regardless of the moment, you were always ready to talk and help. I owe you more than these pages can explain.

To my parents, sister and family, I am forever grateful for all kind of supports and encouragements not only during this phase but throughout my life. Thank you for all the years of love and companionship. This work would not be possible without them.

To my beloved Carolina, my partner on life. I should thank you for being a source of support and for being part of the important moments. Thank you for your interest in my work, not mentioning all the help in my experiments!

This work is dedicated to you all.



## ACKNOWLEDGEMENTS

The authors acknowledge the financial support of the Fundação de Amparo à Pesquisa do Estado de São Paulo (FAPESP) grant 2013/25733-0.



A cada enxadada, uma minhoca.

(autor desconhecido)



## RESUMO

O estudo da formação e evolução dos sprays é essencial para o desenvolvimento de modelos físicos mais detalhados e novas estratégias de injeção para motores de combustão interna de injeção direta. No presente trabalho, os *sprays* de um injetor multi-furos são avaliados em um esforço para caracterizar os efeitos do desenvolvimento do spray em fluxo de ar constante. Estas interações são estudadas em termos de características de turbulência do ar, do fluxo mássico de ar e da pressão de injeção de combustível. *Sprays* de etanol são injetados em uma câmara de fluxo constante. O objetivo do aparato é isolar o experimento de propriedades do escoamento intrínsecas ao funcionamento de motores de combustão interna, tais como instabilidades e geometrias móveis. Os fatores que afetam as interações de ar-*spray* foram avaliados com os campos de velocidade do ar obtidos na presença de *spray*. A técnica de velocimetria por imagem de partículas de duas fases foi aprimorada para permitir a medição nas condições experimentais. Em todas as condições, a interação é baseada em um diferencial de pressão formado entre as regiões interna e externa do spray. Os resultados indicam um mecanismo diferente quando comparado com condições quiescentes. O vortex formado na fronteira do spray é observado apenas nos estágios iniciais de injeção. No entanto, o transiente de fim de injeção ainda está presente para essas condições. O mecanismo de interação acelera as distribuições de velocidade em direção à fronteira do jato. Os experimentos indicam que o aumento do fluxo de massa de ar modifica a velocidade de penetração do ar, mas sem alterar as características do mecanismo de interação. Distribuições de intensidade turbulenta são calculadas para o fluxo de ar durante o evento de injeção. As distribuições indicam que os sprays atenuam a intensidade turbulenta em todas as condições, consistente com as observações dos campos de velocidade. Para avaliar os efeitos da turbulência do ar, conjuntos de placas perfuradas intercambiáveis são utilizadas para limitar as escalas integrais de turbulência. As análises do espectrograma indicam que a turbulência é reduzida não apenas nas escalas integrais, mas também em todas as escalas de frequência medidas. Estas escalas integrais de turbulência do fluxo de ar de entrada têm pouca influência no desenvolvimento do spray. No campo de turbulência, os níveis de potência ao final da injeção foram semelhantes, independentemente das escalas integrais de turbulência de entrada.



## ABSTRACT

The study in formation and evolution of sprays is essential for developing more detailed physical models and new injection strategies for direct injection internal combustion engines. In the present work, the sprays from a multi-hole injector are evaluated in an effort to characterize the effects of the spray development in a constant surrounding air flow. These interactions are studied in terms of the air turbulence characteristics, the inlet air mass flow and the fuel injection pressure. Ethanol sprays are injected in a constant-flow chamber. The apparatus purpose is to isolate the experiment from the fluid flow properties intrinsic to engine operations, such as instabilities and moving walls. The factors that affects the air-spray interactions were assessed with the air velocity fields in the presence of the ethanol spray. The two-phase particle image velocimetry technique was enhanced to allow measuring in the required experimental conditions. In all conditions, the interaction is based in a pressure gradient formed between the inner and outer regions of the spray. The results indicates a different mechanism when compared to quiescent conditions. The recirculation vortex at the spray border is present only in the initial injection stages. However, the end of injection transient, an instability initiated with the injector needle closing, is still present for these conditions. The interaction mechanism accelerates the velocity distributions towards the spray main boundary. The experiments indicate that the increase of the air mass flow modifies the air penetration velocity but without altering the interaction mechanism characteristics. Higher injection pressures suggests a lower degree of air interaction at the initial instants of the spray development. Turbulent intensity distributions are calculated for the air flow during the injection event. The distributions indicate that the sprays attenuate the turbulent intensity in all conditions, consistent with the observations of the velocity fields. To assess the effects of air turbulence, sets of interchangeable perforated plates are used to limit the integral scales of turbulence. The spectrogram analyses indicate turbulence is reduced not only in the integral scales, but also in all the measured frequency scales. The inlet turbulence integral scales of the air flow have little influence in the spray development. In the turbulence field, the power levels at the end of injection were similar regardless of the inlet turbulence integral scales.



## LIST OF FIGURES

Figure 2.1 - Schematic drawing of operation modes in direct injection engines. Adapted from [1].	23
Figure 2.2 - Injection strategies for direct injection spark ignition engines. Adapted from [1].	24
Figure 2.3 - Types of injector for direct-injection SI engines. Adapted from [1].	26
Figure 2.4 - Effects of ambient pressure on the sprays generated by the three injector types shown. Adapted from [1].	27
Figure 2.5 - Induction of the swirl movement on pressure-swirl injectors. Adapted from [1].	27
Figure 2.6 - Ohnersorge number for liquid jet break-up regimes. Adapted from [1].	29
Figure 2.7 - Primary liquid jet break-up regimes. Adapted from [1].	30
Figure 2.8 - Droplet break-up mechanisms according to Wierzba [7]. Adapted from [1].	31
Figure 2.9 - Typical spray development for a multi-hole injector. Adapted from [1].	32
Figure 2.10 - Primary break-up mechanisms for spray generated by multi-hole injector. The spray disintegration starts with the flow leaving the injector hole. Adapted from [1].	33
Figure 2.11 - Description of hollow-cone spray formation. Figure a indicates the primary and secondary break-ups. Figure b shows the development of the pre-spray and secondary flow at the tip of the spray. Adapted from [1].	35
Figure 3.1 - Identification of the interaction zones between spray and ambient air. Extracted from [9].	38
Figure 3.2 - Zone qualification of diesel spray development according to [10]. Adapted from [10].	39
Figure 3.3 - Ambient air velocity fields obtained by [4]. The presence of the penetration wave and recirculating structure at two different instants is observed.	43
Figure 3.4 - Flow bench for analysis of the interaction of air flow and port fuel injection spray. Adapted from [14].	44

Figure 3.5 - Localization of the regions used by Begg et al [14] for evaluating the droplet secondary break-up regime.....	45
Figure 3.6 - Integral model for calculating the air penetration rate in a non-evaporative spray. Adapted from [13].....	47
Figure 3.7 - Velocity rms values for spray and surrounding air obtained by PDA measurements in [8]. Extracted from [8].....	48
Figure 3.8 - Air velocities evolution during the injection event. Extracted from [8].....	49
Figure 3.9 - Total air mass absorbed by the diesel spray during injection - effects of injection pressure. Adapted from [8].....	50
Figure 3.10 Spray formation model for hollow-cone injectors. Adapted from [3]. ....	51
Figure 3.11 - Air velocity field surrounding the spray of an outward opening injector. The velocities were obtained with the two-phase PIV technique. Extracted from [16].....	53
Figure 3.12 - Funnel flow phenomenon during EOI. The mechanism is also related to EOI transient. Extracted from [16]. ....	54
Figure 3.13 - Temporal evolution of the spray inside a DISI optical accessible engine. The spray evaluation presents similar aspects to those found in other works. Extracted from [17].....	57
Figure 3.14 - Effects of multiple injections on mixture formation inside a DISI optical engine. Extracted from [17]. ....	58
Figure 3.15 - Spray characteristic position as defined in [17]. ....	58
Figure 3.16 - Example of light scattering image from the spray and gas phase. The presence of both phases in the image makes it hinder to apply the standard statistical correlation algorithms. Extracted from [4]. ....	60
Figure 3.17 - Cross-correlation field of an interrogation window containing tracer particles and spray droplets. Adapted from [3].....	61
Figure 3.18 - Velocity vectors obtained for the gas phase and spray. Separation methods by intensity and by the two peaks on cross-correlation maps. Adapted from [3].....	62
Figure 3.19 - Schematic drawing of the simplified phase separation technique by particle fluorescence. Adapted from [19].....	63
Figure 3.20 - Common equipment arrangements of the two-phase PIV.....	64
Figure 3.21 -Time diagram for calculating the statistical correlations of velocity in the case of a single laser equipment. Adapted from [9] .....	64

Figure 3.22 – Survey of works using the two-phase PIV technique to analyze the interaction between air and fuel. The works are arranged according to the time interval between the image pairs and the velocity magnitude of their respective phases. Adapted from [9].	65
Figure 5.1 The Isothermal Spray Chamber. The figure to the left is a section view of the chamber showing the main components. The figure to the right is a photograph of the apparatus showing the proportion between the air preparation section and the optical accessible section.	69
Figure 5.2 - Schematics of the three possible sets of perforated plates to be used in IESC.	70
Figure 5.3 - Concept of IESC bench design. Flow uniformization is performed with the passage of air through the set of perforated plates. The injector is disposed on the central axis of the chamber. Optical access is possible from all the four sides.	71
Figure 5.4 - The Delphi multi hole central GDI injector used during experiments with IESC.	73
Figure 5.5 - Plumes center cross section for a distance of 50 mm from the injector tip.	74
Figure 5.6 - Example of actuation current for the multi-hole injector. Adapted from [26].	74
Figure 5.7 - Schematics of the injector control system.	75
Figure 5.8 - Working principle diagram of the fuel system second stage. Adapted from [28].	77
Figure 5.9- Schematics of the electronic fuel pressure control system.	77
Figure 5.10 - Schematics of the air supply for operation of IESC.	79
Figure 5.11 - Operation of the equipment during the experiments with IESC.	80
Figure 5.12 – An example of the equipment layout for the application of the PIV technique.	81
Figure 5.13 - Light scattering according to Mie theory for particles of oil in air with diameters of 1 $\mu m$ (superior) and 10 $\mu m$ (inferior image). Adapted from [32].	83
Figure 5.14 - Scattering cross-section as a function of normalized particle diameter. Adapted from [37].	84

Figure 5.15 – Schematics of the working principles for Laskin generators. Adapted from [32].	87
Figure 5.16 - Detail of the tracer particles inlet on IESC. The injection is performed at the center line of the main air flow pipes close to the optical access section.	89
Figure 5.17 - Example of the event diagram for the laser system between two consecutive acquisition pairs.	90
Figure 5.18 - Lenses set for the generation of the laser light sheet. Adapted from [32].	92
Figure 5.19 - Graphic illustration of the cross-correlation operation between two images. Adapted from [32]	95
Figure 5.20 - Example of pre-processing for background subtraction. Figure to the left is the acquired image. On the right is the resulting image after background subtraction	96
Figure 5.21 - Example of the pre-process operation for balancing the pixel intensity fields. Figure to the left is the image after background subtraction. Figure to the right is the result of the image balancing operation.	97
Figure 5.22 - Neighborhood of 5x5 vectors used in the universal outlier detection algorithm. The central vector is the vector under analysis. The gray vectors correspond to the neighbors of the central vector. [34].	101
Figure 5.23 - Mask filter application to the region where the valve was present. The upper image shows the position of the valve in the image. In the middle figure, the region where the valve was located after pre-processing is highlighted. This region must be removed from the correlation calculations. The application of this mask (bottom image) defines the region where the wall treatment will be used.	101
Figure 5.24 - The use of the wall function in the adaptive PIV method [40]. The upper figure represents the area designated as the wall (in blue) and its correlation field. In the lower figure, the wall function is used. The symmetrical arrangement of the wall results in the field of correlations as shown in the lower right figure.	102
Figure 5.25 – Emission and absorption spectra of rhodamine B dissolved in ethanol. The green vertical line indicates the incident laser wavelength. The	

orange line represents the cut-off wavelength of the longpass filter used on the cameras. Adapted from [42].	104
Figure 5.26 - Illustration of the filters assembly section view. The use of a set of filters was required due to the high levels of energy scattered from the spray during illumination.	105
Figure 5.27 - Sequence of steps performed to enhance the velocity calculation for air field with adaptive PIV algorithm. The presence of spray in the fluorescence images is removed by subtraction of the synchronized Mie-scattering camera.	106
Figure 5.28 - An example of the image enhancement procedure to remove remaining spray plume signals from the fluorescence images. The resultant images were used to perform the adaptive PIV algorithm.	107
Figure 5.29 - Tailor-made transparent target used to ensure the same field-of-view and resolution of the synchronized cameras.	108
Figure 5.30 - Example of image calibration for spatial coordinates and magnification corrections between cameras.	109
Figure 5.31 - Mass flow balance model for an incompressible stationary flow.	110
Figure 5.32 - The model to describe the five-point central-difference formulation for the first derivative.	111
Figure 5.33 - The standard uncertainty for the inlet air mass flow rate as a function of the temperature and the volumetric flow rate.	115
Figure 5.34 - The electrical response of the piezo-resistive sensor as a function of the static pressure. The vertical axis is the voltage between the terminals of the sensor in volts. The horizontal axis is the measured pressure in bars.	116
Figure 6.1 - Experimental arrangement for acquisition of images during the stationary flow analysis	121
Figure 6.2 – The F.O.V. used for the stationary TR-PIV analyses in the IESC symmetric middle plane. The colormap illustrates the size of the F.O.V.	122
Figure 6.3 – Error estimation of the mean normalized by the number of pixels.	124
Figure 6.4 - Mean velocity fields over the measurement plane for $x$ and $y$ coordinates	124

Figure 6.5 - Reynolds stress components $\langle uxux \rangle$ (a) and $\langle uyuy \rangle$ (b) obtained for the stationary conditions on the measurement plane. ....	125
Figure 6.6 - Reynolds stress component $uxuy$ (a) and turbulent kinetic energy $k$ (b) obtained for the stationary conditions in the measurement plane. ....	126
Figure 6.7 – The autocorrelation function estimation for three different points. The function characteristics are related to local differences in the flow field. ....	127
Figure 6.8 – The integral of the autocorrelation estimation as a function of the integral limits. The behavior is related to the non-consistency of the estimator ....	128
Figure 6.9 – The power spectrum density estimation for a particular point in measurement space. Comparison between the Periodogram and the Welch's method. ....	129
Figure 6.10 - An example of the power spectrum estimation for a point inside the measured region (continuous line) following the -5/3 inertial sub-range rule (dashed line). ....	130
Figure 6.11 - Illustration of the procedure to calculate the space-dependent Integral time scales $\tau$ . A sequence of the velocity fields is acquired over time interval $t$ . For every location, a PSD is calculated. The integral time scale is then determined. ....	130
Figure 6.12 - Integral time scales $\tau$ in the $x$ coordinate (a) and $y$ coordinate (b) obtained with the values of the PSD for every measurement point. ...	131
Figure 6.13 - The Integral length scales for the $x$ and $y$ coordinates. ....	132
Figure 6.14 - The mean velocity fields of the stationary conditions for the three sets of perforated plates. ....	133
Figure 6.15 – The Reynolds stress tensor component $uxux$ comparison between the different sets of perforated plates. ....	134
Figure 6.16 – The Reynolds stress tensor component $uyuy$ - comparison between the different sets of perforated plates. ....	135
Figure 6.17 – The Reynolds stress tensor component $uxuy$ - comparison between the different sets of perforated plates. ....	136

Figure 6.18 – The turbulence intensity distributions for the three perforated plates set. The color range was adjusted to highlight the effects of the perforated plates on the region out of the recirculation zone.....	137
Figure 6.19- The integral length scales distributions $L_y$ obtained with the velocity in the $y$ direction for the three perforated plates set.....	138
Figure 6.20- The integral length scales distributions $L_x$ obtained with the velocity in the $x$ direction for the three perforated plates set.....	139
Figure 6.21 - Power spectra density estimation for a point inside the measurement plane – point 1. The distributions are consistent estimations obtained with the Welch method.....	141
Figure 6.22 - Power spectra density estimation for a point inside the measurement plane – point 2. The distributions are consistent estimations obtained with the Welch method.....	141
Figure 6.23 - Power spectra density estimation for a point inside the measurement plane – point 3. The distributions are consistent estimations obtained with the Welch method.....	142
Figure 6.24 - Experimental arrangement used for the 3D velocity estimation. The arrangement is the same of the WSS stationary analysis. ....	144
Figure 6.25 - The F.O.V. comprising the acquisition of the consecutive planes used in the estimation of the third velocity component. The dimensions are in millimeters.....	145
Figure 6.26 – The mean velocity field of the flow around the injector cartridge.....	146
Figure 6.27 – The volumetric representation of the velocity magnitude of the flow around the injector cartridge.....	147
Figure 6.28 – The horizontal velocity components of the air flow in the measured volume. Figure a. – the $U_z$ component and figure b. the $U_x$ component. ....	147
Figure 6.29 – The experimental arrangement for the two-phase PIV measurements. ....	152
Figure 6.30 – The F.O.V. in IESC for spray-air interaction analyses.....	152
Figure 6.31 - The timing box representing the sequence of events during the two-phase PIV experiments .....	153

Figure 6.32 – The velocity magnitude evolution for a particular point in the sample space. A proper choosing of time window is necessary to evaluate the spray ensemble-average temporal evolution.....	154
Figure 6.33- The ensemble-average velocity and variance as a function of the number of samples. The values are calculated in two point inside the velocity fields. The points are represented in the streamline illustrations. ....	157
Figure 6.34 – The global development of the air flow velocity during spray event in Case PP4-01.....	159
Figure 6.35 - - Global development of the air flow velocity during spray event for Case PP4-02.....	161
Figure 6.36 - Global development of the air flow velocity during spray event for Case PP4-03 .....	163
Figure 6.37 – The global development of the velocity distributions during spray event for Case PP2-01.....	165
Figure 6.38 – The global development of the velocity distributions during the spray event for Case PP2-02.....	166
Figure 6.39 – The global development of the velocity distributions during the spray event for Case PP2-03.....	167
Figure 6.40 - Global development of the air flow velocity during spray event for Case PP6-01 .....	170
Figure 6.41 - Global development of the air flow velocity during spray event for Case PP6-02 .....	171
Figure 6.42 - Global development of the air flow velocity during spray event for Case PP6-03 .....	172
Figure 6.43 - Comparison of the case conditions: PP4-01 and PP2-01. The effects of the perforated plates set. Timestamp: 0.25 <i>ms</i> after SOI. ....	175
Figure 6.44 - Comparison of the case conditions: PP4-01 and PP2-01. The effects of the perforated plates set. Timestamp: 0.375 <i>ms</i> after SOI.....	176
Figure 6.45 - Comparison of the case conditions: PP4-01 and PP2-01. The effects of the perforated plates set. Timestamp: 2.625 <i>ms</i> after SOI.....	177
Figure 6.46 - Comparison of the case conditions: PP4-01 and PP2-01. The effects of the perforated plates set. Timestamp: 3.125 <i>ms</i> after SOI.....	178

Figure 6.47 - Turbulent intensity calculated with $y$ direction component. The comparison between cases conditions PP4-01 and PP2-01. 0.250 $ms$ before SOI.....	179
Figure 6.48 - Turbulent intensity calculated with $y$ direction component. The comparison between cases conditions PP4-01 and PP2-01. 0.250 $ms$ after SOI.....	180
Figure 6.49 - Turbulent intensity calculated with $y$ direction component. The comparison between cases conditions PP4-01 and PP2-01. 0.375 $ms$ after SOI.....	181
Figure 6.50 - Turbulent intensity calculated with $y$ direction component. The comparison between cases conditions PP4-01 and PP2-01. 2.625 $ms$ after SOI.....	182
Figure 6.51 - Turbulent intensity calculated with $y$ direction component. The comparison between cases conditions PP4-01 and PP2-01. Two different timestamps are show: 3.125 $ms$ after SOI and 3.375 $ms$ after SOI.....	184
Figure 6.52 - Turbulent intensity calculated with $x$ direction component. The comparison between cases conditions PP4-01 and PP2-01.....	186
Figure 6.53 – The comparison of the case conditions: PP4-03 and PP2-03. The effects of the perforated plates set. Timestamps: 0.125 $ms$ and 0.375 $ms$ after SOI.....	187
Figure 6.54 – The comparison of the case conditions: PP4-03 and PP2-03. The effects of the perforated plates set. Timestamps: 2.625 $ms$ and 3.125 $ms$ after SOI.....	188
Figure 6.55 - Turbulent intensity calculated with $y$ direction component. The comparison between cases conditions PP4-03 and PP2-03.....	191
Figure 6.56 - Turbulent intensity calculated with $y$ direction component. The comparison between cases conditions PP4-02 and PP2-02.....	192
<i>Figure 6.57 - The ensemble-average velocity fields and turbulent intensity calculated with <math>y</math> direction component for case condition PP6-01.....</i>	<i>193</i>
Figure 6.58 – The comparison of the case conditions: PP4-01 and PP4-02. The effects of the injection pressure. Timestamp: 0.250 $ms$ after SOI.....	194

Figure 6.59 – The comparison of the case conditions: PP4-01 and PP4-02. The effects of the injection pressure. Timestamp: 0.500 <i>ms</i> after SOI.....	195
Figure 6.60 – The comparison of the case conditions: PP4-01 and PP4-02. The effects of the injection pressure. Timestamp: 2.625 <i>ms</i> after SOI.....	196
Figure 6.61 – The comparison of the case conditions: PP4-01 and PP4-02. The effects of the injection pressure. Timestamp: 3.125 <i>ms</i> after SOI.....	197
Figure 6.62 – The turbulent intensity distributions calculated with <i>y</i> direction component. The comparison between cases conditions PP4-01 and PP4-02. 0.125 <i>ms</i> before SOI.....	198
Figure 6.63 – The turbulent intensity distributions calculated with <i>y</i> direction component. The comparison between cases conditions PP4-01 and PP4-02. 0.250 <i>ms</i> after SOI.....	199
Figure 6.64 – The turbulent intensity distributions calculated with <i>y</i> direction component. The comparison between cases conditions PP4-01 and PP4-02. Two different instant are shown: 0.750 <i>ms</i> and 2.625 <i>ms</i> after SOI.....	200
Figure 6.65 – The turbulent intensity distributions calculated with <i>y</i> direction component. The comparison between cases conditions PP4-01 and PP4-02. 3.250 <i>ms</i> after SOI.....	201
Figure 6.66 – The turbulent intensity calculated with <i>y</i> direction component. The comparison between cases conditions PP2-01 and PP2-02.....	204
Figure 6.67 – The turbulent intensity calculated with <i>y</i> direction component. The comparison between cases conditions PP6-01 and PP6-02.....	205
Figure 6.68 – The temporal evolution of space-average velocity near the injector tip (right figures) for case PP4-01. The space-averaging is performed considering the 8 points highlighted by the black dots (left figures). ..	207
Figure 6.69 – The comparison between two space-average velocities in the region near injector tip. The red points indicate the ones used in the previous analysis (region A). The blue dots represent a second evaluated region B.....	209
Figure 6.70 – The time history of the space-average velocity - the effects of the injection pressure. ....	210

Figure 6.71 – The temporal evolution of velocity near the spray boundary (left figures) in the case PP4-01. The velocity magnitude over the highlighted line is shown in figures to the right. ....	212
Figure 6.72 – The effects of injection pressure in temporal evolution of the velocity near spray boundary (left figures) in the case PP4-02. The velocity magnitude over the highlighted line is shown in figures to the right. ..	214
Figure 6.73 – The comparison of the case conditions: PP4-01 and PP4-03. The effects of the inlet air mass flow. Timestamp: 0.125 ms after SOI. ....	215
Figure 6.74 – The comparison of the case conditions: PP4-01 and PP4-03. The effects of the inlet air mass flow. Timestamp: 0.250 <i>ms</i> after SOI. ....	216
Figure 6.75 – The comparison of the case conditions: PP4-01 and PP4-03. The effects of the inlet air mass flow. Timestamp: 2.625 <i>ms</i> after SOI. ....	217
Figure 6.76 – The comparison of the case conditions: PP4-01 and PP4-03. The effects of the inlet air mass flow. Timestamp:3.250 <i>ms</i> after SOI. ....	218
Figure 6.77 – The comparison of the case conditions: PP2-01 and PP2-03. The effects of the inlet air mass flow. ....	219
Figure 6.78 – The turbulent intensity distributions calculated with <i>y</i> direction component. The comparison between cases conditions PP4-01 and PP4-03. 0.125 <i>ms</i> before SOI. ....	220
Figure 6.79 – The turbulent intensity distributions calculated with <i>y</i> direction component. The comparison between cases conditions PP4-01 and PP4-03. 0.250 <i>ms</i> after SOI. ....	221
Figure 6.80 – The turbulent intensity distributions calculated with <i>y</i> direction component. The comparison between cases conditions PP4-01 and PP4-03. 0.750 <i>ms</i> after SOI. ....	222
Figure 6.81 – The turbulent intensity distributions calculated with <i>y</i> direction component. The comparison between cases conditions PP4-01 and PP4-03. 1.625 <i>ms</i> after SOI. ....	223
Figure 6.82 – The turbulent intensity distributions calculated with <i>y</i> direction component. The comparison between cases conditions PP4-01 and PP4-03. 2.875 <i>ms</i> after SOI. ....	224

Figure 6.83 – The turbulent intensity distributions calculated with $y$ direction component. The comparison between cases conditions PP4-01 and PP4-03. 3.250 $ms$ before SOI.....	225
Figure 6.84 – The turbulent intensity calculated with $y$ direction component. The comparison between cases conditions PP2-01 and PP2-03.....	227
Figure 6.85 – The time history of the space-average velocity - the effects of the inlet air mass flow. ....	228
Figure 6.86 – The effects of the inlet air mass flow in temporal evolution of the velocity near the spray boundary (left figures) in the case PP4-03. The velocity magnitude over the highlighted line is shown on figures to the right. ....	230
Figure 6.87 – The spectrogram estimation in a point inside the external flow. The spectrogram estimation is obtained with the STFT method.....	232
Figure 6.88 – The spectrogram evolution of point inside in the air flow during the injection event. The Case PP4-01. The red vertical lines indicate the SOI and EOI.....	233
Figure 6.89 - The spectrogram analysis in a point inside the air flow field. The effects of the perforated plates set. Cases PP2-01 and PP4-01.....	235
Figure 6.90 - The spectrogram analysis in a point inside the air flow field. The effects of the perforated plates set. Cases PP2-03 and PP4-03.....	236
Figure 6.91 – The spectrogram analysis in a point inside the air flow field. The effects of the injection pressure. Cases PP4-01 and PP4-02. ....	238
Figure 6.92– The spectrogram analysis in a point inside the air flow field. The effects of the inlet air mass flow. Cases PP4-01 and PP4-03.....	239

## LIST OF TABLES

Table 5.1 – Minimum particle diameter according to the flow characteristic frequency and $\eta = 0.99$ . Adapted from [37]. .....	85
Table 5.2 - Maximum particle diameter for propylene carbonate in air according to criterion developed in [37]. .....	86
Table 6.1 - The conditions of the cases in the spray-air interaction analyses .....	151

CA: Crank angle.

CMOS: Complementary metal oxide sensor.

DFT: Discrete Fourier Transform.

DI: Direct injection.

DISI: Direct-injection spark-ignition.

EOI: End of injection.

F.O.V.: Field of view.

FFT: Fast Fourier transform.

GUM: Guide to the Expression of Uncertainty in Measurement.

IA: Interrogation Area.

ICE: Internal Combustion Engine.

IESC: Isothermal ethanol spray chamber.

Nd: YLF: Neodymium; Yttrium and Lithium Fluoride.

OD: Optical density.

PDA: Phase-doppler anemometry.

PIV: Particle image velocimetry.

SMD: Sauter mean diameter.

SNR: Signal to noise ratio.

SOI: Start of injection.

STFT: Short-time Fourier Transform.

TR-PIV: Time-resolved particle image velocimetry.

WSS: Wide-sense stationary.

## TABLE OF CONTENTS

1	Text structure.....	19
2	Introduction.....	21
2.1	Direct injection on spark ignition engines.....	22
2.1.1	Operation modes in direct injection.....	22
2.1.2	Injector types for direct injection SI engines.....	25
2.2	Spray and mixture formation fundamentals.....	28
2.2.1	Liquid jets break-up regime.....	29
2.2.2	Liquid droplets break-up regimes.....	31
2.2.3	Spray structure – multi-hole injectors.....	32
2.2.4	Spray structure – hollow-cone injectors.....	34
3	Literature review.....	37
4	Objectives of the study.....	67
5	Experimental procedures.....	69
5.1	The Isothermal Ethanol Spray Chamber (IESC).....	69
5.1.1	The importance of studies in continuous flow chamber.....	72
5.2	Injector.....	73
5.3	Injection control system.....	75
5.4	High-pressure fuel system.....	76
5.5	Air supply system.....	78
5.6	The operation of experiments.....	79
5.7	Techniques for spray and air flow analysis.....	80
5.7.1	Standard particle image velocimetry (PIV).....	81
5.7.2	Two-phase particle image velocimetry (Two-phase PIV).....	103
5.7.3	Velocity estimation by multiple planes acquisition.....	110
5.8	Uncertainty analyses.....	113
5.8.1	Air mass flow rate.....	114

5.8.2	Injection pressure .....	116
5.8.3	PIV measurements .....	117
6	Results.....	119
6.1	Stationary flow analyses.....	120
6.1.1	Setup and TR-PIV configuration .....	120
6.1.2	Integral scales and statistical treatment of turbulence .....	123
6.1.3	Effects of perforated plates sets .....	132
6.1.1	Velocity estimation by multiple planes acquisition .....	144
6.2	Sprays-air interaction analyses .....	149
6.2.1	Acquirement of spray events .....	151
6.2.2	Statistical description of the spray event.....	154
6.2.3	Global development of the air flow velocity fields .....	158
6.2.4	Effects of the perforated plates set .....	174
6.2.5	Effects of the injection pressure.....	194
6.2.6	Effects of the inlet air mass flow .....	215
6.2.7	Spectrogram analyses .....	231
7	Conclusions and future works.....	241
7.1	Two-phase PIV technique .....	243
7.2	Air-spray interaction analyses .....	244
8	References .....	i

## **1 Text structure**

This work is divided in 7 chapters. The initial chapters are devoted to the problem statement and the importance of the study In spray-air interactions between spray and ambient gas. The chapters 2 and 3 present the fundamentals related to spray development, droplet formation and also to the literature review of the most important works related to the objectives of this work. In the chapter 5 all the instrumentation and apparatus used in the experiments with IESC chamber are detailed. The particularities of each subsystem and the special necessary conditions are addressed in this section. The section 6 comprises the results and conclusions obtained with the stationary and the air-spray interaction analysis in the IESC experiments. Finally, chapter 7 discuss the next steps and suggestions of future works that should investigate important aspects in the air-spray interactions field.



## 2 Introduction

Over the past decades, regulations on pollutants emission of internal combustion engines (ICE) led to the development of new technologies. Increasingly challenging limits encourage innovations for both engines and after treatment systems. The fulfillment of these requirements in an internal combustion engine depends mainly on the mixture formation and on combustion processes. The use of high-pressure injection systems currently provides fast and more precise controls of the mixture formation processes, allowing considerable gains in terms of fuel consumption and emission levels. Thus, the optimization of fuel injection systems and mixture formation has become increasingly important [1] [2].

In this sense, the improvement of flexible direct injection (DI) systems, for both gasoline and diesel, plays an essential role. For diesel engines, direct injection technology is the most commonly strategy used in small and medium-sized engines [1]. However, for gasoline engines the use of such systems has only recently occurred. At even lower scales, this technology is used for injection of other fuels such as biofuels.

The large-scale use of the benefits of direct injection systems depends heavily on the understanding of the injection processes, spray development and the flammable mixture formation. The mechanisms responsible for spray droplets breakup, their interaction with the air motion within the cylinder, as well as the spray structure are important parameters for designing the new systems. Even currently, there is a lack of experimental data for these mechanisms [3] [4] [1] inside and outside an ICE, mainly due to the difficulty of measuring the spray properties, even with advanced laser diagnostic techniques. Consequently, the lack of experimental results forces the numerical models to their limits. Since there are no models capable of describing all these dynamics properly, numerical simulations provide results associated with a high level of uncertainty. Yet often these are the only tools available [1].

Therefore, studies to investigate mixture formation processes are essential for the advancement of direct injection technologies. Regarding the use of alternative fuels to gasoline, fewer aspects are known. For the case of ethanol, differences in physical properties such as viscosity and vapor pressure may modify the

development of the spray and its interaction with the air flow. In Brazil, where most small passenger cars are equipped with flex-fuel engines, it is necessary to understand the performance of the injectors operating with both gasoline and ethanol.

In this section, the advantages of using direct injection in spark ignition engines are presented. The application of this type of injection system are briefly discussed, showing the main advantages and disadvantages. The main types of injectors for direct injection are described below. Finally, the spray structures of these injectors are discussed in light of the theory of break up regime of liquid jets and drops. These characteristics form the theoretical basis of mixture formation and air-spray interaction processes.

## **2.1 Direct injection on spark ignition engines**

According to Baumgarten [1], among techniques such as cylinder deactivation, variable valve timing, direct gasoline injection is the technology with the highest individual potential for reducing fuel consumption and consequently  $CO_2$  emissions. Compared with a similar port-fuel injection engine, it is estimated that the reduction in fuel consumption at partial load can reach 15 to 25% [1]. Another advantage of direct injection systems is the more precise control of the amount of fuel injected in the engine cycle [5]. Since there is no fuel puddles formation inside the intake port, a common condition in port-fuel injections, the amount of fuel injected into the cylinder depends only on the injector characteristics. However, one of the main advantages of direct injection systems may be the cooling of the flammable in-cylinder mixture prior to combustion – the charge cooling effect. Evaporative cooling, which is caused by the injection of liquid fuel into the chamber, reduces the temperature of the mixture inside the cylinder, allowing increasing the volumetric efficiency by up to 10% [1]. In addition, the reduction of mixture temperature reduces the possibility of abnormal combustion during the compression and combustion phase, which allows increasing the compression ratio by 1 to 1.5 units.

### **2.1.1 Operation modes in direct injection**

Due to the greater flexibility and control of the injection event, two main modes of operation were developed, as can be seen in Figure 2.1. In homogeneous charge

mode, the injection occurs during the intake stroke. In this case, the fuel must interact with the in-cylinder air flow, providing a homogeneous and stoichiometric mixture to be compressed and subsequently burned. In the concept of stratified charge, the injection occurs during the compression stroke. The objective of this strategy is to ensure a flammable mixture in the region close to the spark plug and a lean mixture in the rest of the chamber.

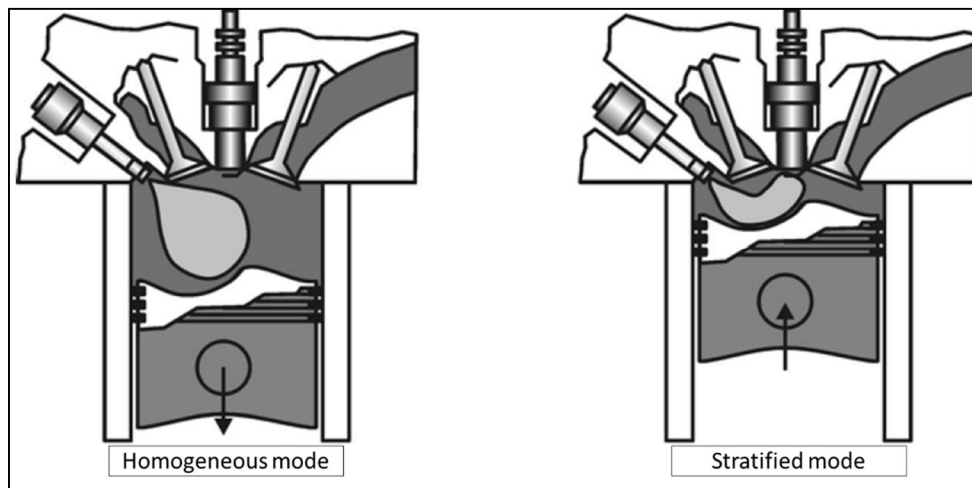


Figure 2.1 - Schematic drawing of operation modes in direct injection engines. Adapted from [1].

During the development of the first generation of direct injection, engine operation concentrated on the stratified mode. This type of mixture formation strategy, by operating with globally lean mixtures, could reduce fuel consumption [1] [5]. Since fuel is injected only at the end of the compression stroke, it could reduce the risks of abnormal combustion. Thus, a higher compression ratio could be achieved. However, the use of stratified charge resulted in higher levels of unburned hydrocarbon emissions and higher fuel consumption. This occurs because regions with very lean mixtures did not burn, even with a flame propagation from the stoichiometric region. In many cases the fuel sprays have not completely evaporated, forming flames in fuel puddles that wet the chamber walls and piston, which in turn increased emission levels [5]. The task of ensuring a specific fuel distribution for all the ranges of engine operation proved to be very challenging. Another disadvantage of the stratified charge mode is the excess oxygen ( $O_2$ ) in the exhaust gases. The amount of  $O_2$  inhibits the use of the robust three-way catalytic converter for after treatment of the exhaust gases. More expensive and sophisticated equipment is needed for after-treatment methods.

For the operation of the 1st generation of direct injection engines, three strategies were developed to improve the mixing process of the fuel and flow: the mixture guided by the walls of the chamber and piston, the one guided by the air flow and that guided by the spray. Figure 2.2 shows the concept.

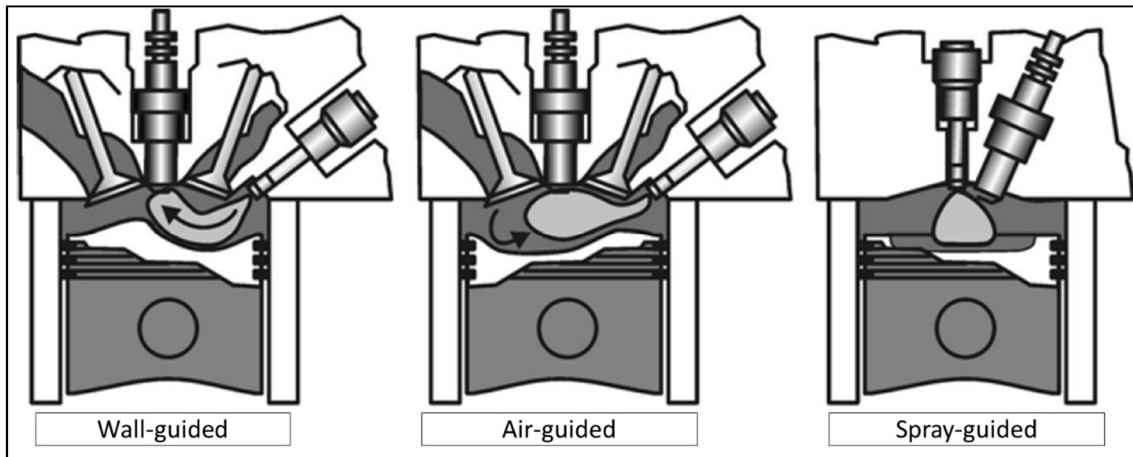


Figure 2.2 - Injection strategies for direct injection spark ignition engines. Adapted from [1].

In the wall-guided strategy, special designs for piston heads are used. The geometry is intended to transport fuel spray to the region near the spark plug, which is placed at a central position. However, since much of the fuel impinges the piston head and cannot evaporate prior to ignition, this strategy suffers from high levels of unburned hydrocarbons and  $CO$  [1]. The advantage of the strategy is robustness, ensuring ignition at virtually all the points of operation.

In the air-guided strategy, a stable flow generation maintains the spray compacted and transports it to a region close to the spark plug. Fuel mixing enhancement by the air flow is essential close to the spark plug region and during the ignition time. Ensuring these requirements for all the points of operation is impossible. In general, a large scale motion, such as swirl and tumble flows, promotes the mixture formation between air and fuel.

The spray-guided strategy is geometrically simpler when compared to the others, but more complex in terms of applicability. The formation of the flammable mixture is guaranteed by the close positioning of the spark plug and injector. The air flow and the geometry of the chamber are of secondary importance. In this case there is no contact of the fuel with the piston head. The great difficulty of the technique lies in the robustness and reproducibility of the spray for different

pressures and velocities within the chamber. The arrangement between injector and spark plug should also be carefully studied.

An important advantage of the spray-guided strategy is the ability to operate in both stratified and homogeneous charge modes. Since there are no extreme specific requirements for the internal geometry and air flow, the use of both modes of operation can increase engine performance in both partial and full loads, especially in conditions whereby the stratified mode encounters unstable regimes.

In order to obtain reliable operations and using the advantages of direct injection systems, the homogeneous load mode appears to be more attractive than the modes in stratified load, mainly due to the increase in efficiency due to evaporative cooling of the mixture and the reduced emission levels. Stoichiometric mixtures allow using the three-way catalyst, which is already a well stated technology for port fuel injection engines. Another important factor is that during intake, the pressure inside the cylinder is relatively low. Lower pressure values allow greater spray reproducibility in different conditions, increasing the robustness of the engine operation.

### **2.1.2 Injector types for direct injection SI engines**

Injection valves for direct injection engines must be able to provide the optimum amount of fuel at specific instants and with good reproducibility. The injection period should ensure sufficient time for the spray development and fuel mixture formation. Moreover, the ambient pressure in the combustion chamber may vary from sub atmospheric to compression ranges. Thus, injectors must be capable of delivering sprays with the desired quality regardless of the ambient pressure. Since the time available for injection is very small, these injectors work at higher injection pressures, increasing the rate of penetration and decreasing droplet size. When compared to port fuel injection, in which pressures are in the range of 1 to 4 bar, direct injection of gasoline presents pressures 50 times as high. However, these pressures are much lower than those used in compression ignition diesel engines. In these engines, the injection pressure can reach pressures from 2000 to 3000 *bar*. One of the disadvantages of gasoline under high injection pressures is that, unlike diesel sprays, gasoline has no lubricating

properties at high pressures. Fuel pump wear is one of the factors limiting the injection pressure [1].

Figure 2.3 shows the three configurations most commonly used in direct injection spark ignition engines. The first type of injector is multi-hole nozzle. The actuation and spray formation of each individual outlet is similar to the operation of the diesel injectors. These nozzles produce sprays with greater penetration lengths and relatively large droplets as compared to diesel sprays [1]. The spray as a whole is heterogeneous - very rich regions of fuel are separated from each other by very poor regions. The advantage of using this type of injector is that the spray structure and its properties such as cone angle do not change with increasing ambient pressure. The multi-hole injectors operate reasonably for stratified charge mode multiple injection events. Another important feature of multi-hole injectors is that the spray structure can be easily modified with the quantity and arrangement of the holes in the nozzle.

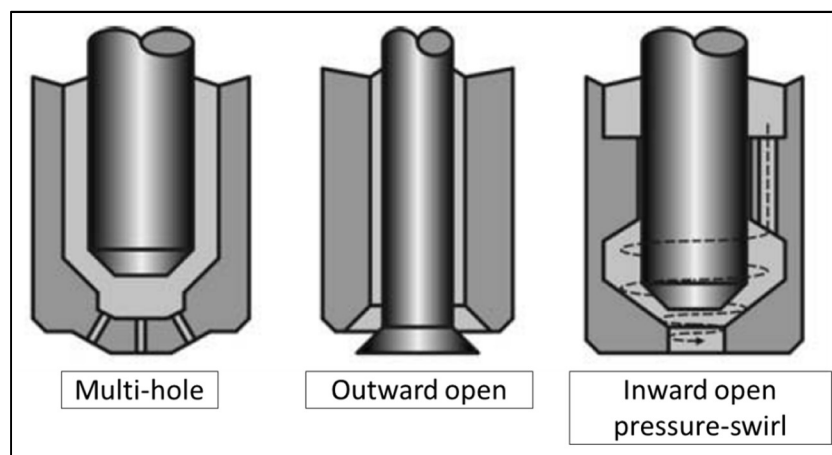


Figure 2.3 - Types of injector for direct-injection SI engines. Adapted from [1].

The other two types of injectors generate a spray structure different from the multi-hole injector. In both the injection valve opening induces the formation of a single spray having the shape of a hollow cone. For this reason, these injectors are also known as hollow-cone type injectors. The advantage of hollow-cone sprays is the greater area-volume ratio, which ensures good atomization at lower penetration lengths.

In the case of pressure-swirl injectors, the fuel passes through holes disposed tangentially (see Figure 2.5). These passages induce the swirl movement in the fuel flow exiting the nozzle. This in turn forms a spray internal region filled by air.

The fuel is released into the environment around this central region, generating the characteristic hollow cone. Figure 2.4 shows sprays formed with the three different configurations previously described. The pressure increase is observed to have an effect on hollow-cone sprays, collapsing the spray structure with pressure increase above a critical value.

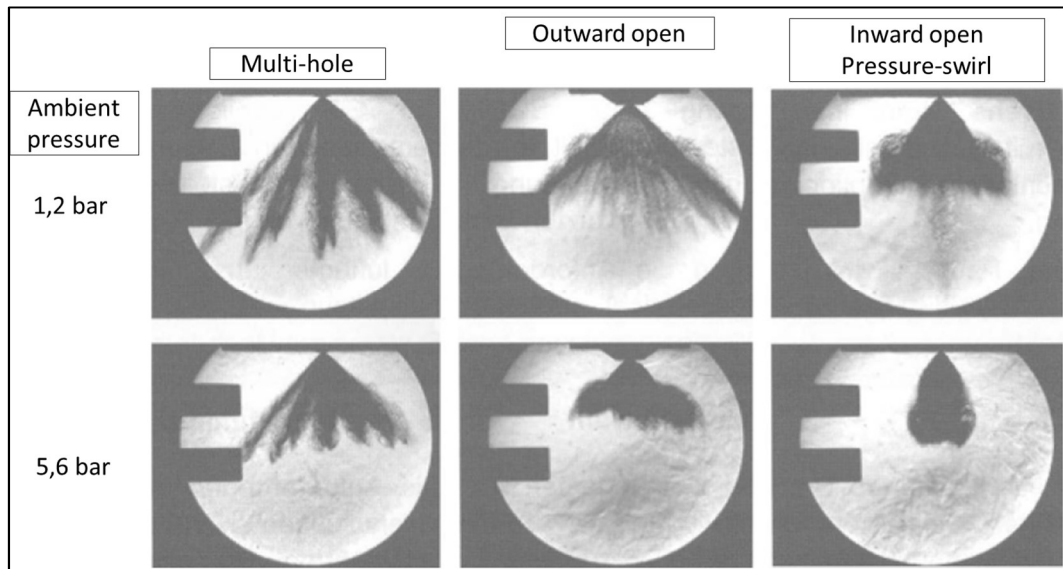


Figure 2.4 - Effects of ambient pressure on the sprays generated by the three injector types shown. Adapted from [1].

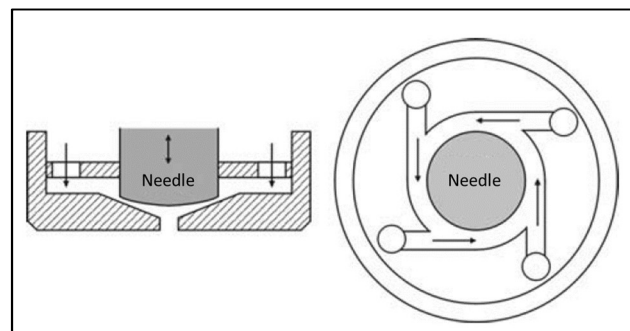


Figure 2.5 - Induction of the swirl movement on pressure-swirl injectors. Adapted from [1].

## 2.2 Spray and mixture formation fundamentals

During the spray development in a gaseous medium, two main mechanisms are responsible for the disintegration and subsequent liquid flow break up: the liquid jet break-up regime and the liquid droplet break-up regime. The first mechanism, called the primary break-up regime, is responsible for the disintegration of the liquid jet emanating from the injector nozzle. The liquid droplet break-up mechanism, the secondary regime, describes the break-up phenomena of ligaments and droplets resulting from the primary regime. The two mechanisms occur simultaneously in different regions of the spray and depend on the properties of the liquid and ambient gas. The interaction of the ambient gas flow with the jet of the spray is indirectly incorporated to the mechanisms by means of non-dimensional relationships from the velocity difference between phases.

The effects of the liquid properties and the velocity difference between ambient gas and liquid jet are usually characterized by the Reynolds number ( $Re_l$ ) and the Weber number ( $We_l$ ) [1] [6] which represent the relation of the inertia forces and the liquid surface tension. The Reynolds number is expressed as:

$$Re_l = \frac{uD\rho_l}{\mu_l} \quad 2.1$$

In which  $u$  is the relative velocity between the liquid and the gas,  $D$  is the outlet diameter of the injector nozzle,  $\rho_l$  and  $\mu_l$  are the liquid density and dynamic viscosity.

The Weber number is given by:

$$We_l = \frac{\rho_l u^2 D}{\sigma_l} \quad 2.2$$

Where  $\sigma_l$  is the liquid surface tension.

A quantitative description of the jet break-up processes is given by the Ohnesorge number – the relation between the Reynolds number  $Re_l$  and the Weber number of the liquid phase  $We_l$ . The Ohnesorge number includes all the relevant properties of the fluid and is defined as:

$$Oh = \frac{\sqrt{We_l}}{Re_l} = \frac{\mu_l}{\sqrt{\sigma_l \rho_l D}} \quad 2.3$$

### 2.2.1 Liquid jets break-up regime

From the relationships between  $Oh$  and  $Re_l$ , it is possible to define four types of break-up mechanisms in the primary regime for a spray generated by a straight and circular nozzle. These are usually characterized by the break-up length - distance between the nozzle to the point where the first droplets formation occurs [1] [6]. Figure 2.6 shows the Ohnersorge diagram in which the four types of regime are presented: the Rayleigh Regime, the first and second wind-induced regimes and the atomization regime. The increase of  $Oh$  and  $Re_l$  leads to faster and more intense break-ups. However, the atomization is also influenced by the density of the ambient gas. Therefore, a complete description of the break-up regimes should include properties of the gaseous phase. In some cases including the ratio between the liquid and gas phase densities is proposed. However, to date, no relation has been able to include all these properties in a single variable [6].

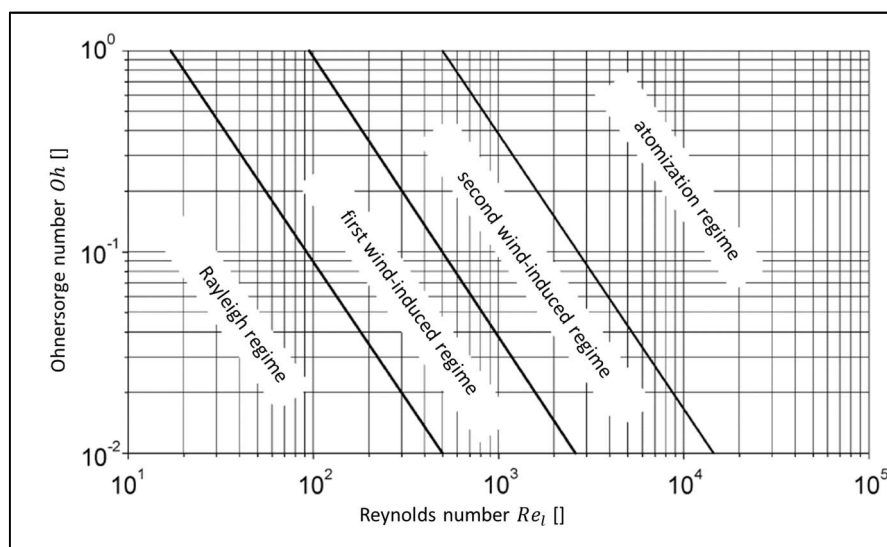


Figure 2.6 - Ohnersorge number for liquid jet break-up regimes. Adapted from [1].

Figure 2.7 shows a schematic drawing of jets primary break-ups for these types of regimes. The Rayleigh regime occurs at very low speeds. The jet break-up occurs due to the growth of axisymmetric instabilities of the jet volume as a whole, initiated by the inertia forces of the liquid and jet surface tension. The liquid detaches itself from the jet in a drip-like manner. The droplets are larger than the diameter  $D$  of the nozzle. With the increase of the jet velocity, the jet break-up occurs in the first wind-induced regime. The break-up length decreases and the

droplet size is now close to the nozzle diameter. The forces acting on the Rayleigh regime are amplified by the aerodynamic forces. The influence of the ambient gas is described with the Weber number of the gas phase  $We_g$ .

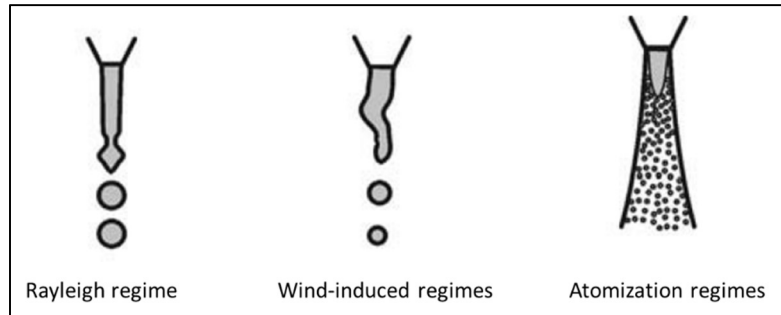


Figure 2.7 - Primary liquid jet break-up regimes. Adapted from [1].

In the second wind-induced regime, the flow inside the nozzle becomes turbulent. The jet break-up mechanism now depends on the growth of small surface waves at the jet boundary. These waves are generated by jet turbulence and are amplified by aerodynamic forces. The droplets are now smaller than the nozzle diameter and the break-up length decreases with increasing Reynolds number  $Re_l$ . As the smaller droplets are stripped from the jet surface, the disintegration process occurs from the surface to the jet center. Two different break-up lengths are defined. The intact surface length, which describes the beginning of the jet surface break-up, and the break-up length itself.

The atomization regime begins when the intact surface length tends to zero. A conical spray develops from the nozzle and the divergence starts at the nozzle outlet. The droplets are much smaller than the nozzle diameter. A detailed description of the break-up mechanism is more complex than in any other regime, mainly because the disintegration process strongly depends on the flow conditions within the nozzle, which are often unknown [1].

## 2.2.2 Liquid droplets break-up regimes

The droplets formed from the jet core break-up are subjected to the aerodynamic drag induced by the velocity difference in the ambient gas. This drag causes instabilities on the surface of the droplet itself. There is balance between aerodynamic forces, which try to disintegrate the droplet and the surface tension, which keeps the droplets as spheres. The smaller the radius of droplet curvature, the greater the surface tension force. Subsequent droplet breaks will only occur if the velocity difference increases. This mechanism is described by the Weber number  $We_g$  of the gas phase - the relation between aerodynamic forces to surface tension:

$$We_g = \frac{\rho_g u^2 d}{\sigma_l} \quad 2.4$$

Where  $\rho_g$  is the gas density and  $d$  is the droplet diameter prior to break-up.

According to Wierzba [7], the different droplet break-up regimes are identified as shown in Figure 3.8. For small values of  $e_g$  ( $< 12$ ), droplet deformation does not cause its disintegration.

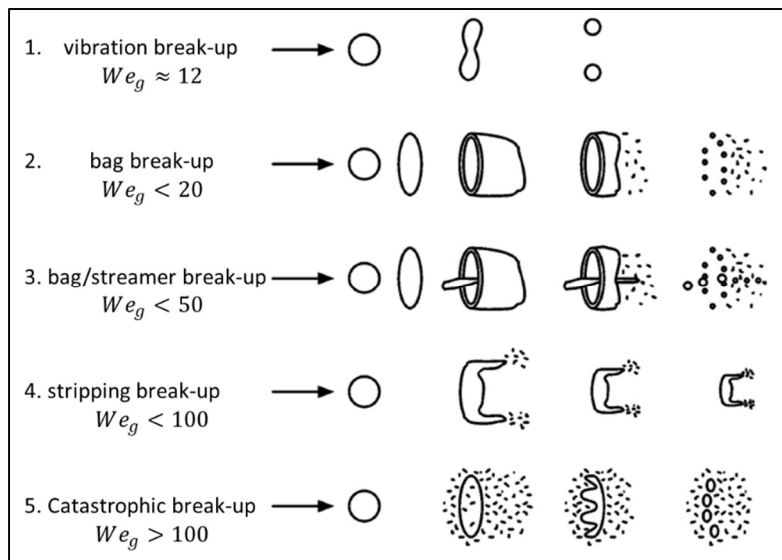


Figure 2.8 - Droplet break-up mechanisms according to Wierzba [7]. Adapted from [1].

The values of  $We_g$  that indicates the transition between the break-up modes are also shown in Figure 2.8. Note that these values are not consistent between the different results in the literature [1].

For applications in internal combustion engines, every break-up mechanisms may occur during spray development. However, most disintegrations occur near the injection nozzle, in which the Weber number is high. Along the spray length, the Weber number decreases significantly due to evaporation, previous break-ups and decrease in relative velocity.

### 2.2.3 Spray structure – multi-hole injectors

Figure 2.9 shows a schematic drawing of the spray development formed from the nozzle of a multi-hole injector. The fuel injection begins with the needle movement, allowing the fuel to pass through the injection holes. Immediately after the spray ejection through the hole, the liquid jet break-up is present. This initial disintegration is defined as the primary break-up. Flow cavitation and turbulence inside the injection holes are the mechanisms responsible for the liquid break-up in large ligaments and droplets that forms the denser region of the spray. These structures now interact with each other by collision and coalescence. Due to the relative velocity of the droplets and ambient gas, disintegration occurs mainly by the action of aerodynamic forces, forming droplets of smaller sizes and accelerating the evaporation process. In this region, the secondary break-up occurs.

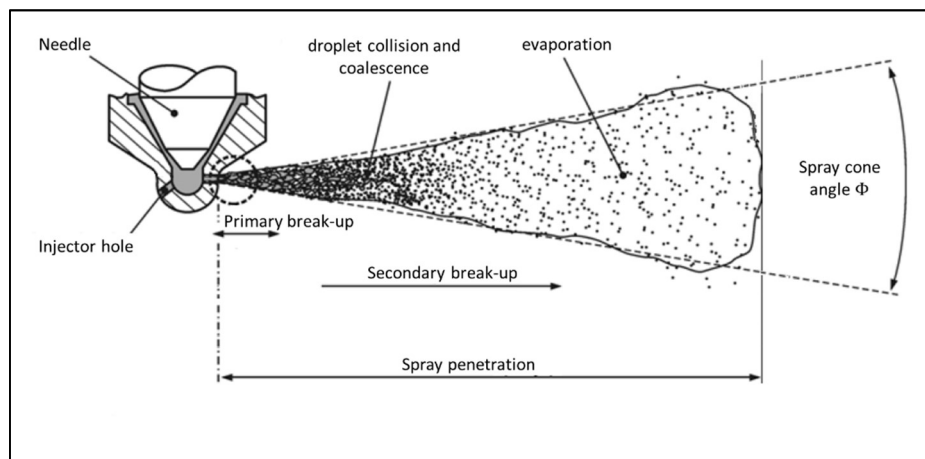


Figure 2.9 - Typical spray development for a multi-hole injector. Adapted from [1].

Aerodynamic forces also decelerate droplets that are disintegrating. Droplets at the spray tip are more decelerated than those on the wake are due to aerodynamic drag. With the spread of the spray, the droplets at the border are continuously replaced with the ones behind, causing the spray penetration to increase. The droplets that now have low kinetic energy are released to the external region of the spray. The frontier becomes increasingly diluted with the air penetration. At this instant, the factors that influence subsequent spray break-up and droplet evaporation are the environmental conditions, such as density and temperature of the ambient gas and their velocity distributions.

As previously stated, the disintegration of the spray begins immediately after the exit from the injection hole. Two break-up mechanisms are the most accepted to explain this rapid disintegration: Turbulence-induced break-up and cavitation-induced break-up. Figure 3.10 shows the flow inside an injection hole where the turbulence and cavitation break-up mechanisms are present.

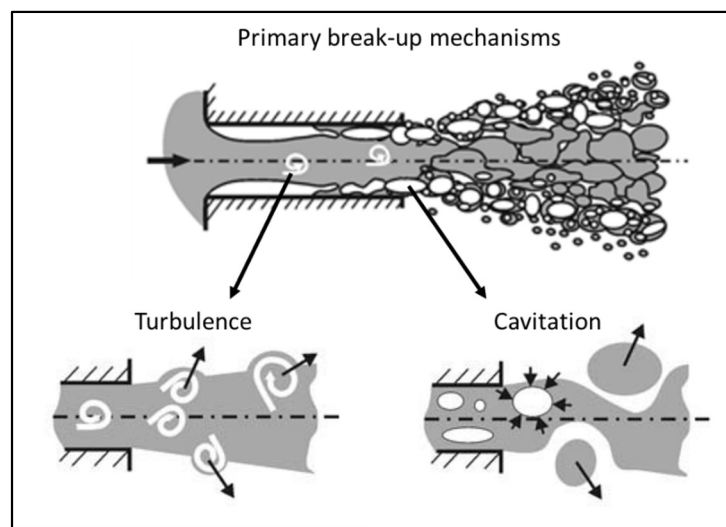


Figure 2.10 - Primary break-up mechanisms for spray generated by multi-hole injector. The spray disintegration starts with the flow leaving the injector hole. Adapted from [1].

The turbulence disintegration mechanism depends on the fluctuation of the radial velocity component within the jet. If this magnitude is intense enough, vortices are able to overcome surface tension, releasing structures to form larger ligaments and droplets [1].

In the cavitation break-up mechanism, the high axial flow velocity, associated with the radial gradient of axial velocity due to the area reduction in the injection hole, decreases the static pressure inside the injection hole to values lower than the fuel vapor pressure at that temperature. This pressure reduction induces fuel evaporation, forming bubbles of fuel vapors. When associated with turbulence, these vapor bubbles can detach and travel with the flow, developing a two-phase flow. The intensity and spatial distribution of cavitation depend on the pressure and geometric characteristics of the injection hole [1] [6]. Due to its geometric dependence, the cavitation mechanism is studied as a way of controlling the spray break-up process. For further information on mathematical models and characteristics of the cavitation phenomenon in injectors, the reader is referred to the works by Baumgarten [1] and Van Romunde [6].

#### **2.2.4 Spray structure – hollow-cone injectors**

Hollow-cone injectors are generally used in low ambient pressure situations. The main advantage of this type of injector against the multi-hole injector is the higher atomization efficiency. When compared to the multi-hole injector, the hollow-cone injector produces smaller droplets, better air mixing and less penetration, which leads to its better efficiency [1]. These injectors are widely used in the first generation of gasoline direct-injection spark-ignition (DISI) engines, usually operating in stratified charge mode. The tendency of the replacement with multi-hole injectors occurs due to the behavior of the hollow-cone injector with the ambient pressure increase. Depending on a critical pressure value, the jet is not disintegrated and therefore no spray is effectively formed. This type of behavior is called spray collapse. Since engines usually require good spray reproducibility, even at high pressures, spray collapse increases the difficulty in using hollow-cone injectors. However, for conditions operating in homogeneous load, these injectors seem to be more promising than multi-holes, which justifies the interest in hollow-cone injectors.

Figure 2.11-a shows the primary and secondary break-up regions during the development of the hollow-cone spray. Unlike multi-hole sprays, the primary break does not occur entirely within the injection hole. The main break-up

mechanisms are turbulence and aerodynamic forces. The mechanism induced by turbulence already initiate inside the injection hole. Disturbances initiated at the liquid surface are amplified with interaction of the aerodynamic forces and become unstable. At this instant, the liquid jet begin to disintegrate into ligaments and larger droplets. In the spray development, the secondary break-up is dominated by the mechanism induced by the aerodynamic forces, as previously described.

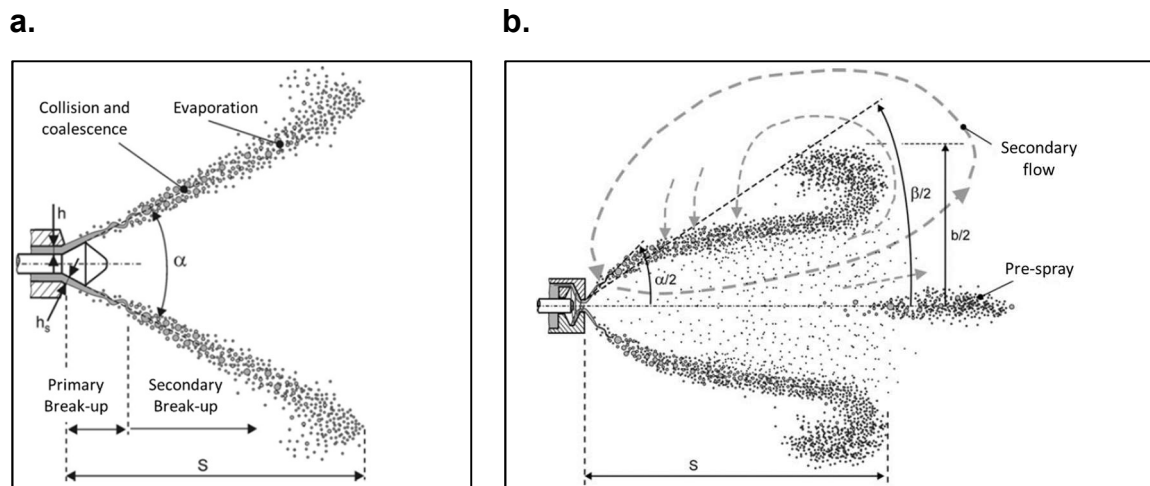


Figure 2.11 - Description of hollow-cone spray formation. Figure a indicates the primary and secondary break-ups. Figure b shows the development of the pre-spray and secondary flow at the tip of the spray. Adapted from [1].

Figure 2.11-b shows the development of the spray generated by a pressure-swirl injector. A unique feature of this spray is the formation of a group of droplets that do not participate in the cone and are thrown axially. This group of droplets are formed at the beginning of the needle lift. At the initial instants, the fuel does not have sufficient tangential velocity to generate the swirl movement and thus is transported along the symmetry axis of the injector. This small group of larger droplets is called the pre-spray.

As the tangential velocity increases, the liquid acquires the swirl movement and initiates the formation of a hollow structure at the tip of the injection valve. The air inside the cone is accelerated by the linear momentum transfer with the droplets. This acceleration induces a low pressure region within the spray, reducing the spray cone angle. The process reaches the equilibrium and the cone angle remains constant as the penetration increases. The pressure reduction inside the spray also induces the formation of a secondary flow in the outside which generally has lower intensity when compared to the main flow.



### 3 Literature review

As seen previously, the fuel mixture formation of in direct injection spark ignition engines is a critical process. [8] The combustion efficiency, as well as the pollutant emission levels, depends on the quality of the air-fuel mixture. In the case of these types of engines, the mixture is influenced mainly by the spray characteristics and its interaction with the ambient gas [9] [3] [4]. Turbulent structures formed in the shear layers and jet boundaries intensify contact between air and fuel droplets, allowing the interaction to occur at microscopic levels [2].

Therefore, the study into the formation and evolution of these structures in the spray is essential for developing more detailed physical models and new injection strategies. In this chapter, recent works related to the interaction between spray and ambient gas are discussed. Emphasis is given to studies that used experimental techniques similar to those of this research. The discussions are based on the models and the phenomenological characteristics of the spray evolution presented in these studies. Finally, different approaches of the two-phase PIV technique are presented and their applicability on air-spray flows are discussed based on the advantages of each methodology.

The air-fuel interaction of a direct injection spray is studied in Zhang et al [9] by analyzing the momentum transfer between the phases and the penetration of the ambient gas into the spray. Fuel injection is investigated in a constant volume chamber with quiescent air. Based on the angle of the velocity vectors, the authors divide the spray development into 3 zones, as can be seen in Figure 3.1.

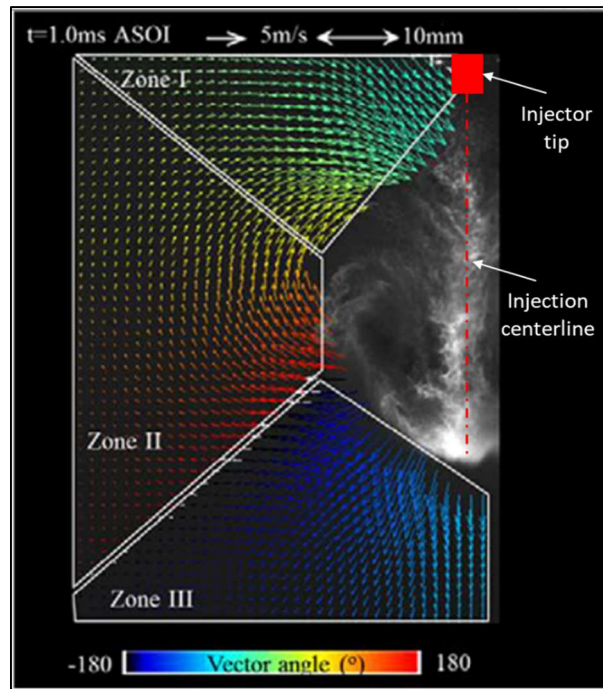


Figure 3.1 - Identification of the interaction zones between spray and ambient air. Extracted from [9].

In zone I, the ambient gas is dragged by the spray boundary near the nozzle. Zone III corresponds to the spray, region where the mixture between spray droplets and air takes place. It is also the region in which the flow is pushed out of the spray. Zone II is an intermediate region. Due to the pressure decrease in zone I, as a result of the ambient gas flow drawn into the spray, the air flow in zone II is directed towards zone I.

During injection, the kinetic energy of the ambient gas increases rapidly, mainly by the momentum transfer of the spray and by the expansion of the interface zone of the two phases. According to the authors, by analyzing the evolution of the total kinetic energy in each zone of the measurement plane, it is possible to evaluate the momentum transfer between the two phases. Note that this transfer during the spray development is a feedback mechanism due to the formation of a recirculating structure at the tip of the spray. This structure is defined as the recirculating vortex: The momentum transfer between the spray tip and the ambient gas induces the creation of the recirculating structure. The propagation of this vortex through the rest of the spray cone increases the interaction between the phases. This interaction is reflected in the increase of the interface region with the spray, which in turn contributes to increasing the kinetic energy of the ambient gas. The process is amplified until the end of the injection. The air kinetic energy

continues to increase even after the injector valve closing. This increase occurs since the recirculating vortex still propagates at the interface between spray and air. After the end of the injection, the ambient gas of zone I, by continuity, is forced to the region where the spray was, also contributing to increasing the momentum transfer.

The same type of zone qualification is made by Zhu et al [10] studying a diesel spray formation. As can be seen in Figure 3.2, the authors divide the diesel spray into three zones, as by Zhang et al [9]. In Zhu et al [10], the interaction between surrounding air and fuel is based on a method for calculating the air momentum flux on the external surface of the spray. This approach requires certain simplifications - the spray is considered axisymmetric and the spray droplets must have the same air velocity at the interface region. As for Zhang et al [9], the ambient gas velocity and momentum transfer between phases increases with the spray time evolution. For Zhu et al [10], the maximum value for air momentum may occur at the end of the injection or shortly thereafter. This observation is in accordance with the statements in Zhang et al [9] - the ambient gas near the injector nozzle is induced to the region where the spray was propagated due to the injection valve closure. The recirculating structure continues to propagate through the spray interface even at the end of the injection. The increase in injection pressure has an influence on the interaction between spray and ambient air, increasing the momentum transfer, especially in the region near the nozzle.

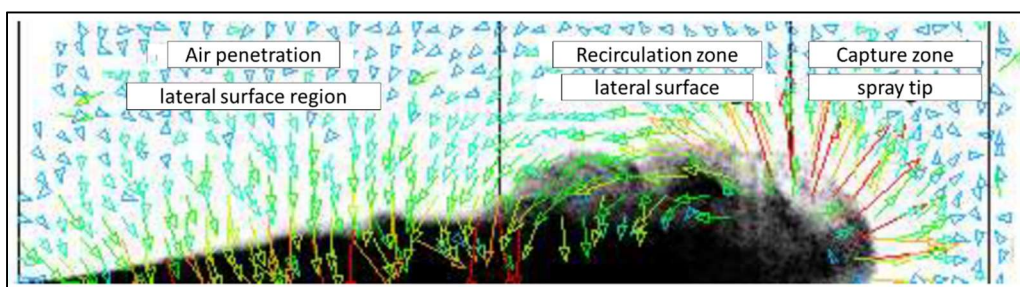


Figure 3.2 - Zone qualification of diesel spray development according to [10]. Adapted from [10].

Zhu et al [10] also discuss the air mass flow that penetrates the tip of the spray. According to the authors, this flow corresponds to 70 to 90% of the total penetration flow. With the development of spray, the importance of penetration on the lateral surface increases. These findings indicate a temporal evolution similar to that in Zhang et al [9]. In the first instants of the injection, a momentum

transfer occurs and is responsible for the recirculating vortex formation. At this stage, most air penetration into the spray occurs at the tip of the spray, where the recirculating structure is being formed. With time evolution and vortex propagation, the lateral interface zone and the air penetration increase. At this moment, the importance of air tip penetration decreases with the increasing lateral penetration at the recirculation region and at the lateral penetration region (Zone I of Zhang et al [9]).

Although Zhang et al [9] evaluated the behavior of a gasoline spray and Zhu et al [10] a diesel spray, the evolution of both is very similar. This suggests that the mixture formation mechanism for the two cases is essentially the same, changing only the characteristics related to the physical properties of the fuel and the boundary conditions for injection, such as the momentum transfer magnitude, the size of the interface zones, velocity magnitudes, etc.

The study by Yeom [10] on the development of a diesel spray in a constant volume chamber also indicates the formation of the recirculating vortex at the spray tip. Note that, in the work, the size of the recirculating structure corresponds to 30% of the total spray length, regardless of the injection pressure. Although the author does not directly discuss the cause of this finding; a possible consequence is that the momentum transfer should increase in the recirculation region and in the region of air penetration near the nozzle (Zones I and II of Zhang et al [9]). As the size of the recirculating structure has not changed with increasing injection pressure, the fuel momentum, which is higher at higher pressures, should be transferred to the ambient gas on the side surface of the spray. An evidence of this hypothesis is in Zhu et al [10] - the increase in pressure directly affects the penetration of air near the nozzle region.

A common characteristic of the sprays studied by Zhu et al [10], Zhang et al [9] and Yeom [11] is the behavior during and after the end of the injection. In all cases, the air penetration increases with the injector valve closing. In this line, the work by Moon et al [12] evaluates the interaction between air and diesel spray during the injector valve closing. The study on mixing properties after the end of the injection is very important for the new strategies of injection of diesel engines. In these new engines, the fuel ignition occurs after the end of the injection. The

objective of the strategy is to reduce the emission levels of  $NO_x$  and particulate matter by reducing the maximum temperature reached in combustion. However, one of the problems is the increase in hydrocarbon emissions. This increase suggested to be linked to the mixture formation characteristics after the end of the injection.

Moon et al [12] analyze two different injectors in a constant volume pressurized chamber. Nitrogen is used as the quiescent ambient gas and pressure is maintained at 1.6 MPa. Both injectors have a single injection orifice. One with 0.135 mm in diameter and the other with 0.096 mm, resulting in half the cross-sectional area of the first. The injectors are compared with a fixed injection duration, thus varying the amount of fuel injected into the chamber. For each injector, two types of injection are studied, one of a long period and another of a short period. The objective is to simulate a quasi-permanent injection and a total transient regime. The ambient gas penetration is analyzed in terms of gas velocity and air mass flow penetration into the spray. For more details of the calculation of the air mass flow, the reader is referred to [12] [13].

An important result of this work, which agrees to the previous studies, is that, regardless of the diameter of the injector orifice, the air mass flow rate of  $N_2$  and velocity increased during and after the injector valve closing. The phenomenon occurs to compensate for the decrease in fuel flow during the same period. However, the rate of increase in the  $N_2$  mass flow is higher for the injector with larger diameter, possibly due to the higher rate of fuel flow decrease. This phenomenon of increased air flow, which starts at the beginning of the spray, generates an instability that is transported through the spray. The ambient gas is forced into the spray with the passage of this instability, called the penetration wave. The valve opening period has no effect on the generation of the penetration wave. In the case of transient injection, the maximum value of the penetration rate is lower than in the *quasi-permanent* injection. However, the rate of flow increase is the same for both types of injection, since the valve closure event is the same for both cases.

Note that the interaction of the ambient gas with the spray does not occur only during the injection event. Much of the interaction between the two phases occurs with the propagation of the penetration wave across the spray length. For Moon et al [12], the propagation velocity of this instability depends mainly on the fuel mass flow rate during injection and the rate of decrease of the fuel flow during valve closing.

In all the works described above, fuel injections are studied in chambers with quiescent ambient gas. No observation is made in the case of chambers with constant ambient gas flow. The interaction of the fuel with an air flow can significantly alter the formation properties of the recirculating structure and ambient gas penetration. Depending on the magnitude and distribution of the gas flow velocity fields, the propagation velocity of the recirculating structure at the edge of the spray decreases, preventing smaller droplets from being transported from the spray tip. Moreover, there is no evidence that this recirculation structure is also present in constant ambient gas flow conditions. The propagation of the penetration wave is also compromised, since the air flow present around the nozzle compensates for the decrease of the pressure induced by the end of the injection event. None of these questions are raised by the authors. For direct injection engines operating under a homogeneous load regime, in which the injection occurs during the admission stroke, the influence of the air flow is very important in mixture formation and development of the spray.

In Dankers et al [4], an injector for direct gasoline injection is also studied in a high-pressure chamber. Unlike the other works, this chamber has a continuous low magnitude axial flow that has the function of scavenging the injection residues from chamber. In this apparatus, it is possible to vary the chamber pressure from 0.2 to 42 *bar*. The internal ambient air can be heated up to 400 °C. Figure 3.3 shows two instantaneous velocity fields extracted from Dankers et al [4].

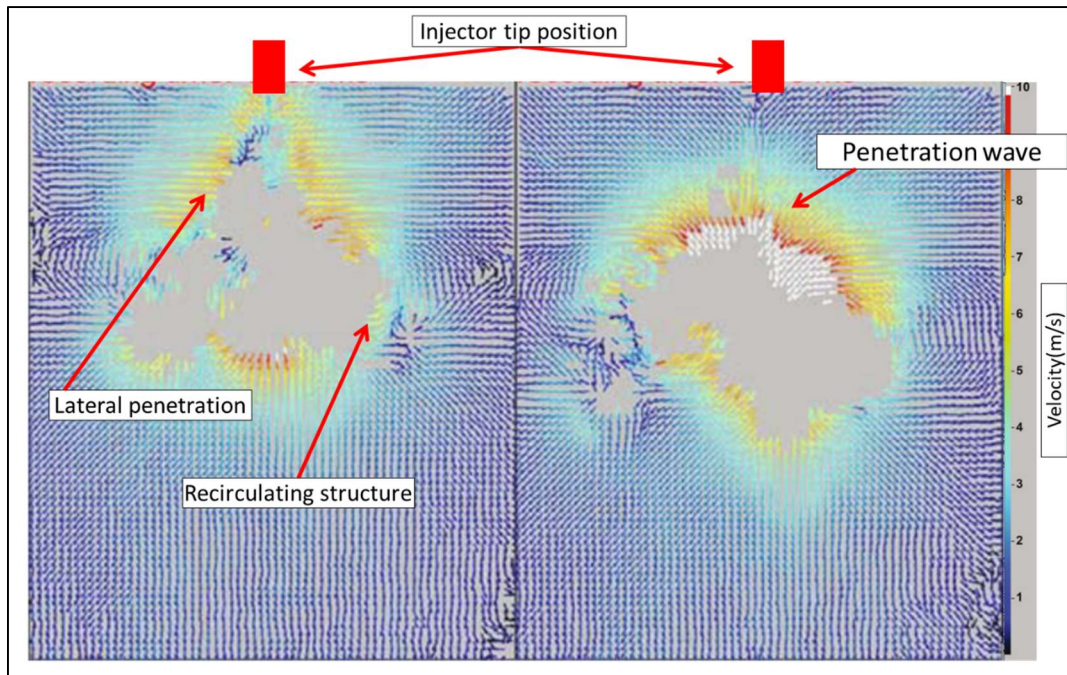


Figure 3.3 - Ambient air velocity fields obtained by [4]. The presence of the penetration wave and recirculating structure at two different instants is observed.

The results of this work are very similar to the previous studies – the distinction of three zones during spray propagation, the formation of the recirculating structure at the spray boundary and the air penetration at the end of the injection. However, the spatial resolution of the velocity fields allows analyzing the penetration wave and recirculating vortex with detail. From Figure 3.3 and from other results of their work, it is possible to identify the momentum transfer between the phases, especially during instability formation associated with the penetration wave. The air flow momentum is also verified not to be enough to alter the spray development mechanism, mainly by the absence of lateral components to interact directly with the spray. In conclusion, the authors indicate that there is no influence of the air flow. However, since the technique used by the authors does not have sufficient temporal resolution, it was not possible to obtain sufficient data from the same injection event, which hinders the analysis of the interaction.

In order to evaluate the effect of the air flow in the droplet distributions and in mixture formation, Begg et al [14] study the interaction between fuel spray and air in a flow bench for port-fuel injection. This bench was developed with an engine head of a gasoline BMW engine. An optical access chamber is placed below a cylinder head. There is no piston and a constant air flow is supplied to the workbench. The intake port also allows visualizing the injector and the spray. Intake valves lift is manually adjusted and the exhaust valves are kept closed. Figure 3.4 shows the flow bench used in Begg et al [14].

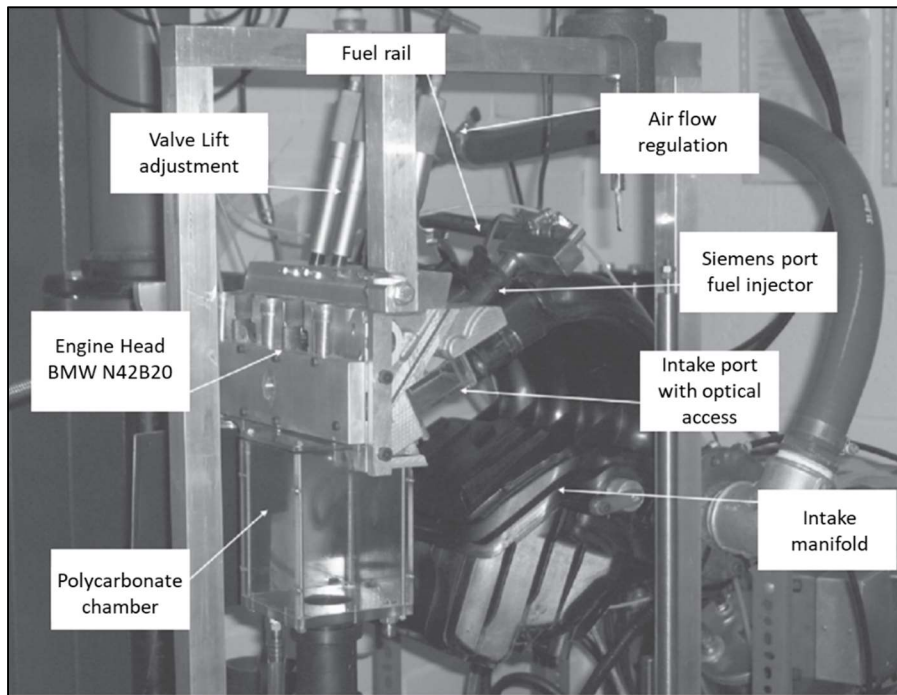


Figure 3.4 - Flow bench for analysis of the interaction of air flow and port fuel injection spray. Adapted from [14].

The results of air flow analysis inside the chamber without the presence of spray indicate a flow pattern strongly dependent on the intake valves lift. Three different types of regimes are identified for the flow around the valves. For maximum lift, a free jet forms at the valve outlet. For intermediate lifts, between 3 to 9 mm, the region delimited by the back of the valve and seat generates a contraction in the streamlines, generating the *vena contracta* phenomenon. For lifts of less than 3 mm, the boundary layer does not separate from the valve surface, generating discharge coefficients close to 1. The flow behavior around the valve affects the distribution of droplets entering the chamber, since the injection in this case is performed inside the intake port. The relative velocity between air and fuel

droplets, which changes significantly depending on the regime within the valve restriction, is an important parameter in the droplet formation and break-up regimes. Begg et al [14] evaluated the droplets behavior during the passage through the restriction with the Weber number ( $We$ ) of the gas phase, which is the ratio of the inertia forces to the surface tension of the droplet. Figure 3.5 shows the sections where the droplet break-up and formation regimes were studied.

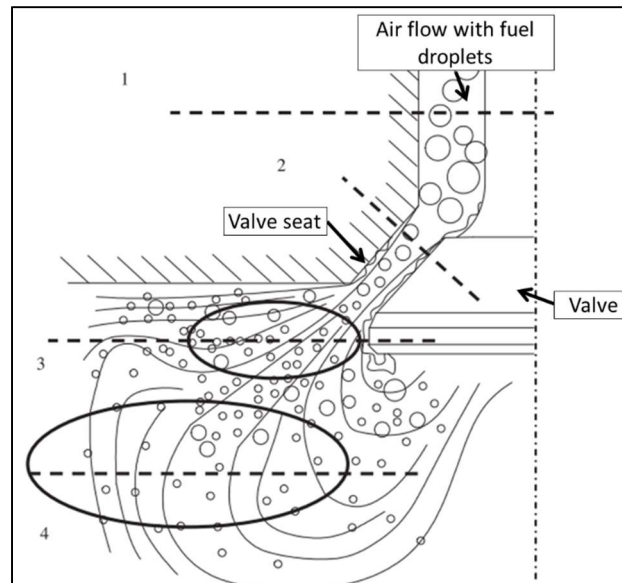


Figure 3.5 - Localization of the regions used by Begg et al [14] for evaluating the droplet secondary break-up regime.

In the first section, the fuel droplet velocities are comparable to the air flow velocities. Therefore, the relative velocity and  $We$  are very small. In section 2, the behavior of the droplets changes completely. When the position of the intake valve induces the formation of a flow contraction, the droplets are subjected to a strong acceleration ( $We > 50$ ), resulting in a catastrophic break-up. Droplets collide with the valve walls and seat forming a liquid film. Eventually droplets are stripped from this film in the boundary layer separation region.

Section 3 comprises the region of the air jet flow exiting the restriction. The particles in the jet stream experience high levels of turbulence due to the instabilities generated at the valve edge. The Weber number remains high and the secondary break-up mode is the bag type (section 2.2.2). When leaving the jet region, the droplets undergo a strong deceleration, which contributes to collision and coalescence. This region presents a bi-modal distribution of droplet

diameters, representing the smaller droplets that can directly cross the region and the larger droplets, which detach from the liquid film or collide and coalesce when decelerated. In section 4, in turn,  $We$  is not high enough to induce subsequent droplet break-ups.

The methodology and results in Begg et al [14] partly resemble the objective of this project. Although Begg et al [14] focused on indirect injection, the determination of droplet break-up modes can help to explain the air-fuel interaction in direct injection sprays. Moreover, the turbulence present in the flow, which is not directly counted in the Weber number, plays a significant role. Our interest here lies in correlating the droplets interaction phenomena with aspects of turbulent flow in terms of the size of both temporal and spatial scales.

Another way of analyzing the spray development is presented in Prosperi et al [13]. In this study, besides the direct analysis of the velocity fields, the authors compare their results with an integral model for air penetration in a non-evaporative spray cone [15]. With the theory of the model, the authors define the air penetration in the lateral zone as the transfer zone to the spray. This region is divided into two sections: the near region and the far region. In the near region, the fuel jet is so dense that the cumulative mass flow rate of air penetration is proportional to  $Z^{3/2}$ , where  $Z$  is the axial position in the spray (see Figure 3.6). Over the far region the dependence becomes linear. Figure 3.6 shows a schematic drawing of the cumulative air penetration mass flow rate and the axial position  $Z$ . An interesting result of the analysis is that, with increasing ambient pressure, the spray has higher interaction with the surrounding medium, decreasing the penetration length and cone angle. If the ambient pressure increases by a ratio of 15, the cumulative air mass flow increases by 12 times.

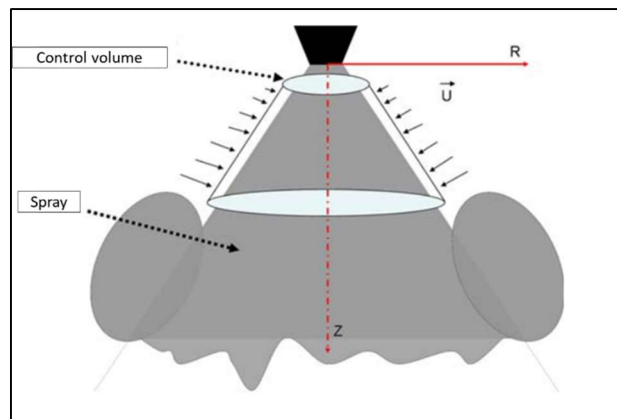


Figure 3.6 - Integral model for calculating the air penetration rate in a non-evaporative spray. Adapted from [13].

In Prosperi et al [13], a hollow-cone injector is studied in a constant-volume high-pressure chamber. The chamber internal pressure can reach 12 *bar*. As seen in section 2.2.4, hollow-cone injectors generate cone-shaped sprays. This configuration, different from multi-hole injectors, can modify the mixture formation mechanism since the droplets are now injected with a significant tangential velocity component. However, both injectors seem to possess certain common characteristics. The air velocity fields obtained by Prosperi et al [13] indicate the presence of the recirculating structure that is transported along the surface of the spray, as seen in the case of multi-hole injectors in quiescent environments.

One of the studies discussing air turbulence during injection event is Staudt et al [8]. A diesel spray is studied in a constant-volume chamber with controlled air pressure and temperature. The chamber maintains a constant low velocity flow to scavenge fuel and to inject tracer particles for the air ( $TiO_2$ ). Measurements of the diameter and velocity distributions for the fuel droplets are performed with the phase-Doppler anemometry (PDA). The air velocity distributions are also measured with the PDA technique. The surrounding air velocity field is acquired by 2D particle image velocimetry (PIV). No fluorescent seeding is used to separate the two phases. Figure 3.7 shows the velocity rms values along the radial distance for the diesel spray and surrounding gas at 25 *mm* from the injector tip. The profiles represent the time instant 1 *ms* after the start of injection (SOI). The rms operation is performed on the ensemble-average PDA data. According to the study, there is no significant difference in velocity fluctuation with the injection pressure variation from 80 to 100 *MPa*. For the condition of 135 *MPa*

of injection pressure, larger air velocity fluctuations can be found near the spray boundary. In the case of spray velocity, the rms values increase at lower pressures.

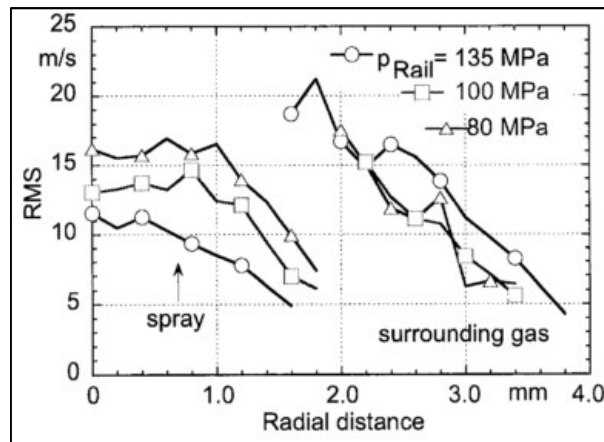


Figure 3.7 - Velocity rms values for spray and surrounding air obtained by PDA measurements in [8].  
Extracted from [8].

Although the authors quantify a turbulence parameter in terms of velocity fluctuations for instant 1 *ms* after SOI, no discussions are made on the temporal evolution of these properties. No data from the surrounding air flow before and after the injection is described. Thus, the evaluation of turbulence modification is restricted to the timestamp assumed as quasi-steady conditions and no further aspects are explored.

Figure 3.8 shows the image sequence of the air velocity fields. The vector fields are ensemble-averaged over 15 injection events. The evaluation of the spray development characteristics is similar to that of previous cases – the development of the recirculation structure that generates a feedback mechanism at the near injector tip region. This region is accelerated towards the spray boundary during the injection. Unfortunately, there is no analysis of the study providing information on the end of injection phenomenon.

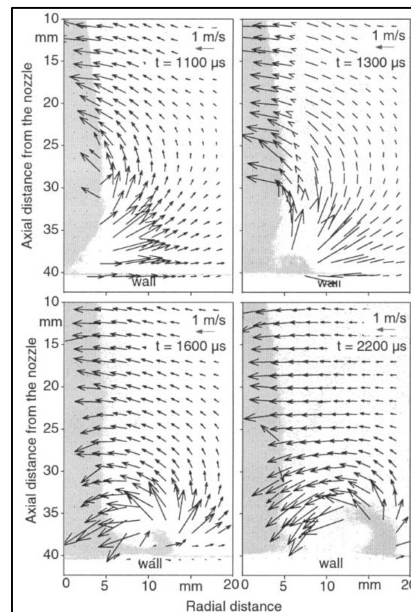


Figure 3.8 - Air velocities evolution during the injection event. Extracted from [8]

With the 2D PIV data, the relation between air entrainment on the spray and injection pressure is evaluated. Using a procedure similar to that in [13], the total air mass absorbed by the spray is calculated. The integral of the velocity over the spray surface is performed considering an axisymmetric condition. Figure 3.9 shows the results over time evolution. The figure allows noting that with higher injection pressures, the absorption process is intensified. However, the total absorbed air mass is roughly the same for all the cases. To maintain the same amount of injected fuel, the case with higher pressure should decrease the injection period. Therefore, the absorption process occurs at a shorter time interval.

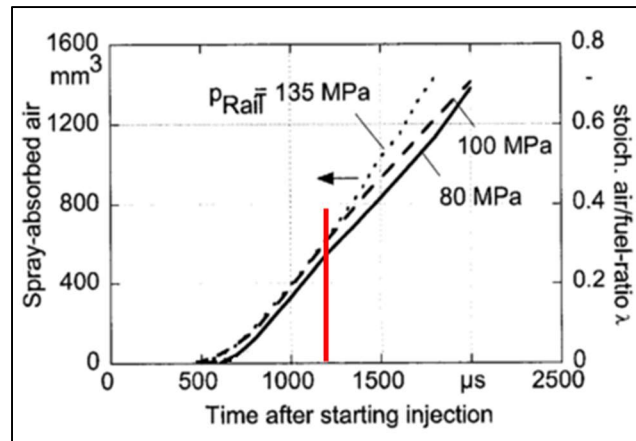


Figure 3.9 - Total air mass absorbed by the diesel spray during injection - effects of injection pressure. Adapted from [8].

One characteristic not mentioned in the discussions of the study is the behavior of cumulative absorbed air mass. During the initial stages and until about 1250  $\mu\text{s}$  after SOI, the three curves have the same roughly linear tendency. After this phase, the three curves show distinct tendencies. There is not enough data to confirm, but this aspect suggests a stabilization period of the recirculation structure over the spray. After the respective period, the air entrainment may be controlled by the vortex strength that induces the velocity feedback mechanism near the injector tip region. This could explain the relation between the air entrainment with injection pressure for this experiment.

In order to study the spray formation mechanism of a gasoline hollow-cone injector, Rottenkolber et al [3] analyzed the evolution of sprays in a constant-volume pressurized chamber. Nitrogen  $N_2$  is used as ambient gas with pressures up to 50 *bar*. From observing the gas phase velocity fields and spray, the authors propose a model for the velocity distribution around the spray that identifies two types of structures. These are formed during jet propagation, as can be seen in Figure 3.10

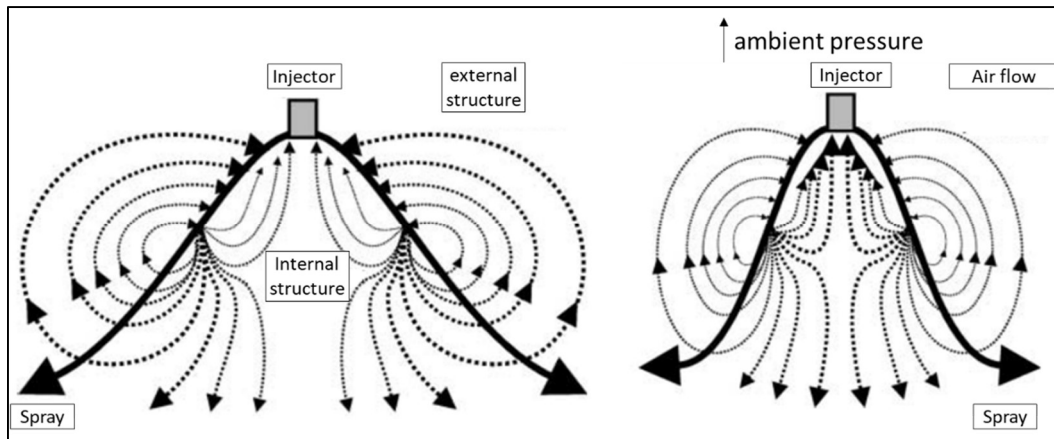


Figure 3.10 Spray formation model for hollow-cone injectors. Adapted from [3].

In this model, the authors do not distinguish the air penetration zone and the recirculation zone as in the analysis of multi-hole injector sprays. For the hollow cone injector, the external recirculating structure is observed to be so large that there is no difference between the penetration zone due to the recirculating vortex and the continuity-equilibrium penetration zone.

The spray internal structure has an interesting velocity distribution. The upper portion directs the droplets and the nitrogen towards the injector nozzle. This induction of movement is caused by the decrease in internal pressure due to the propagation of the spray cone. The lower portion is influenced by the external recirculating structure and by the propagation of the spray in the axial direction. The presence of two distinct regions in the inner structure generates an intersection in which the motion cannot be well defined.

A common feature of hollow cone injectors is the collapse of the spray with increasing ambient pressure. The higher the ambient pressure, the lower the spray cone angle is and the lower the penetration of air into the spray is. For a given value of pressure, the injector is not able to form the droplets cone. At this point, the collapse of the spray occurs. According to Rottenkolber et al [3], the phenomenon responsible for the decrease of the spray cone is the increase of the internal structure intensity. Higher pressures lead to lower air mass penetration rates. This creates a zone of low pressure inside the spray, which intensifies the internal structure. This condition, in turn, pushes the droplets towards the symmetry axis of the cone. An important implication of spray collapse concerns the operation of engines with stratified charge strategy. For the

injections during the compression stroke, where the ambient pressure is high, the atomization of fuel is not sufficient to ensure the mixture formation in a short time interval.

Another type of fuel injector used in the first generations of gasoline SIDI engines is the outward opening injector. As described in section 2.1.2, these types of injector produce sprays with hollow interiors similar to the hollow-cone injectors. However, since the spray is produced by the passage of the fuel through an annular gap and not by centrifugal force, these injectors are less sensitive to the effects of pressure. This type of injector was analyzed in Sauter et al [16]. The sprays were studied in a constant volume chamber with the two-phase PIV technique. The effects of ambient pressure and injection period on the surrounding air flow were investigated. The study also evaluated the effects of multiple injections. Due to the low acquisition rate of the PIV system, the spray evolution was analyzed by mean values performed separately for each timestamp. The average is performed with 30 events.

Figure 3.11 shows a velocity field calculated for time instant  $500 \mu s$  after SOI. The injection pressure was  $200 \text{ bar}$  and ambient pressure  $6.2 \text{ bar}$ . Note the similarities of the hollow-cone and outward open injectors in the development of the surrounding airflow. In [16], the same recirculation structure that occurs for hollow-cone injectors is observed. With the spray evolution, the recirculation structure is formed during the initial spray and is transported along the spray boundary. However, for the case of the studied outward open injector, the effects of pressures are less pronounced than those for hollow-cone injectors. According to the results, ambient pressure variations from 5 to 7 *bar* and injection pressures from 100 to 200 *bar* have little effect on the cone angle, on the position and on the trajectory of the recirculation vortex.

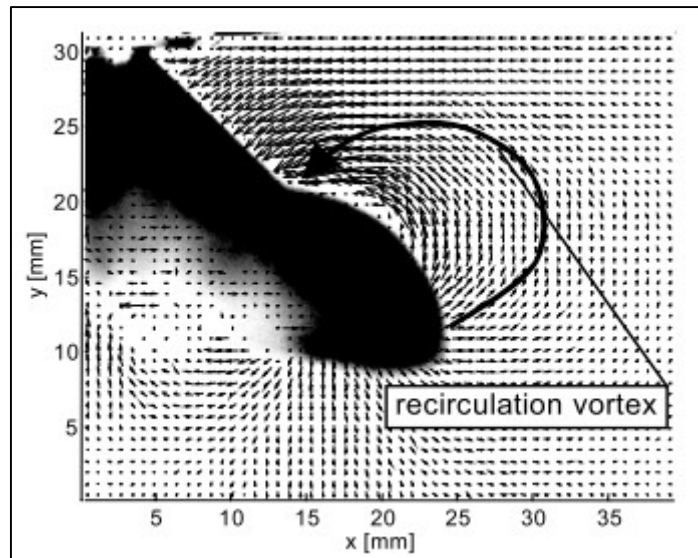


Figure 3.11 - Air velocity field surrounding the spray of an outward opening injector. The velocities were obtained with the two-phase PIV technique. Extracted from [16].

Investigations on the injection duration in [16] reported effects on the transport of the recirculation structure. With an increase in injection duration from  $400 \mu s$  to  $800 \mu s$ , the strength of the recirculation structure increases. This strength is evaluated by the defined vortex number. Due to the increased fuel impulse, the surrounding air flow reaches higher velocities and the vortex structure trajectory changes direction accordingly.

Note the phenomenon reported by the authors in [16] occurring at the end of injection. In this study, the acceleration during the end of injection not only accelerates the surrounding air outside the spray but also the air inside the hollow cone. The velocity increase in the inner region is named funnel flow. By comparing the analysis of [10] [9] [11], this phenomenon is observed to be related to the end of injection transient (EOI transient). The acceleration of the inner region for the outward open injector suggests that a similar behavior should be expected for the sprays of hollow-cone injectors.

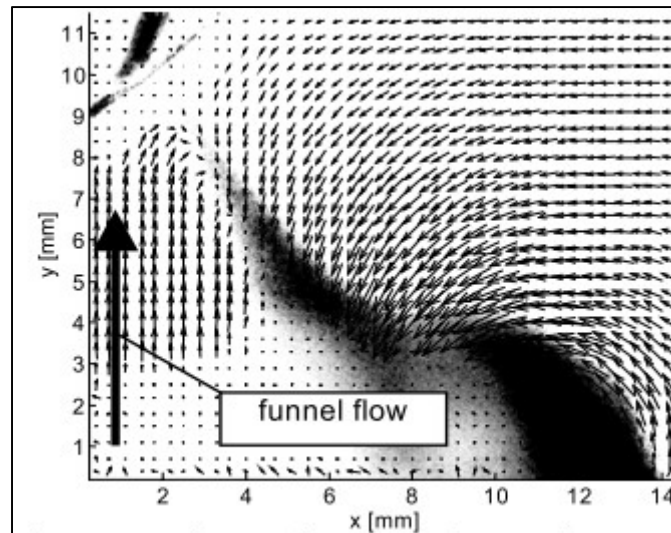


Figure 3.12 - Funnel flow phenomenon during EOI. The mechanism is also related to EOI transient.  
Extracted from [16].

The use of different types of fuel in the previous works had no influence in the discussions on the mechanism of spray formation. In the case of injectors with a similar operating principle, such as gasoline multi-hole injectors and piezoelectric diesel injectors or the hollow-cone and outward open injectors, spray formation always contains recirculation and penetration zones. For all injectors, the needle valve closing generates instabilities that influence the spray behavior. These instabilities propagate along the spray length, intensifying the mixture between air and fuel. Even when fuel surrogates are used, which do not evaporate under test conditions [13], the mechanisms of interaction between air and fuel at large scales are essentially the same. However, characteristics such as penetration, cone angle and droplet diameter are intrinsically linked to the properties of the fluid. Moreover, the droplet break-up regime is also a function of these properties, such as viscosity and density.

In this context, in Aleiferis et al [5] is a comparative study between the characteristics of gasoline sprays and E85 (85% ethanol, 15% gasoline). Sprays of a multi-hole injector are studied in a constant-volume chamber and in an optical access engine. Initially, the sprays are characterized in the constant-volume chamber where the temperature is varied from 20 – 120 °C and the total pressure from 0.5 – 1 bar absolute. Information, such as spray angle, jet penetration and droplet diameters distribution, is obtained. The same injector is then used in an optical access engine operating in cold conditions (coolant water at 20°C) and hot

(coolant water at 90°C) and at two loads, 0.5 *bar* and 1 *bar* respectively. The authors also evaluate combustion characteristics during the operation of the optical access engine.

In the constant volume chamber analysis, the authors report that E85 droplet sizes are always larger, regardless of the pressure and temperature conditions tested. When analyzing the Weber number of the gas phase for the two fuels, for E85, the secondary regime of droplet break-up is noticed to be different from gasoline, predicting larger droplets. The surface tension of ethanol at 20 ° C seems to be the explanation for the differences.

By analyzing the primary fuel atomization regime, the Ohnesorge number ( $Oh$ ) for ethanol is verified to be more than the double of values for the main components of gasoline under standard conditions of temperature and pressure. This aspect shows the importance of the viscosity of the fuel in the atomization process. An interesting result is that at low temperatures such as 7°C, the estimated primary break-up regime for ethanol is the second wind-induced regime rather than the expected atomization regime. This difference in atomization and droplet break-up efficiency has implications for the use of ethanol as a fuel for engines, especially during cold starts conditions.

In the experiments with the optical access engine, the authors state that the trends in the droplets size distribution obtained in the constant volume chamber remain for the engine conditions studied. However, the atomization and droplet break up processes are more efficient due to air-fuel interactions. This higher interaction suggests that the secondary droplet break-up regime are probably different from those found in the constant volume chamber.

Temperature affects the properties of ethanol. According to the authors, at temperatures close to 20°C, viscosity for example, has roughly twice the values of the main components of gasoline. As discussed earlier, this difference has an effect on the primary and secondary atomization regimes and may explain the lower break-up efficiency of the ethanol droplets. For temperatures between 80 – 100°C, the viscosity of ethanol becomes only 40% greater than that of gasoline components. In this case, the spray formation for the two fuels has similar developments. This is evident when evaluating the combustion performance

inside the optical access engine. For low temperatures, the cylinder peak pressure is lower and the mass fraction burned is slightly lower for E85. At higher temperatures, the combustion efficiency of gasoline and E85 is very similar.

Most works shown evaluated the air-spray interaction in controlled experiments such as constant volume chambers, with the exception of Aleiferis et al [5] that also presents results on an optical accessible engine. One of the reasons for such discrepancy is that these apparatus provide boundary conditions that are less subjected to instabilities. Nevertheless, experiments closer to real engine conditions are needed to evaluate additional related aspects. For example, in Stiehl et al [17], the effects of multiple injections on mixture formation and flow stabilization are analyzed in a DISI optical accessible engine operating in stratified mode. The air flow and spray development are studied by means of time-resolved PIV (TR-PIV) and Mie-scattering. A statistical description of the air velocity fields is achieved in crank-angle (CA) resolution. The ensemble-average velocity fields are obtained by 136 subsequent events. Only the events during injection phase close to the top dead center are evaluated. Figure 3.13 shows a time sequence of the spray evolution during the end of the compression stroke. Figure 3.13a shows that the recirculation vortex is also present in these conditions. However, by observing the velocity magnitudes at the near tip region, the feedback mechanism appears to have a less prominent effect. This vortex structure has an important role at the end of injection. According to the authors, after the needle closing, droplets trapped in the toroidal vortex do not penetrate further into the cylinder. This vortex is convected by the global tumble flow toward the right side of the images in Figure 3.13.

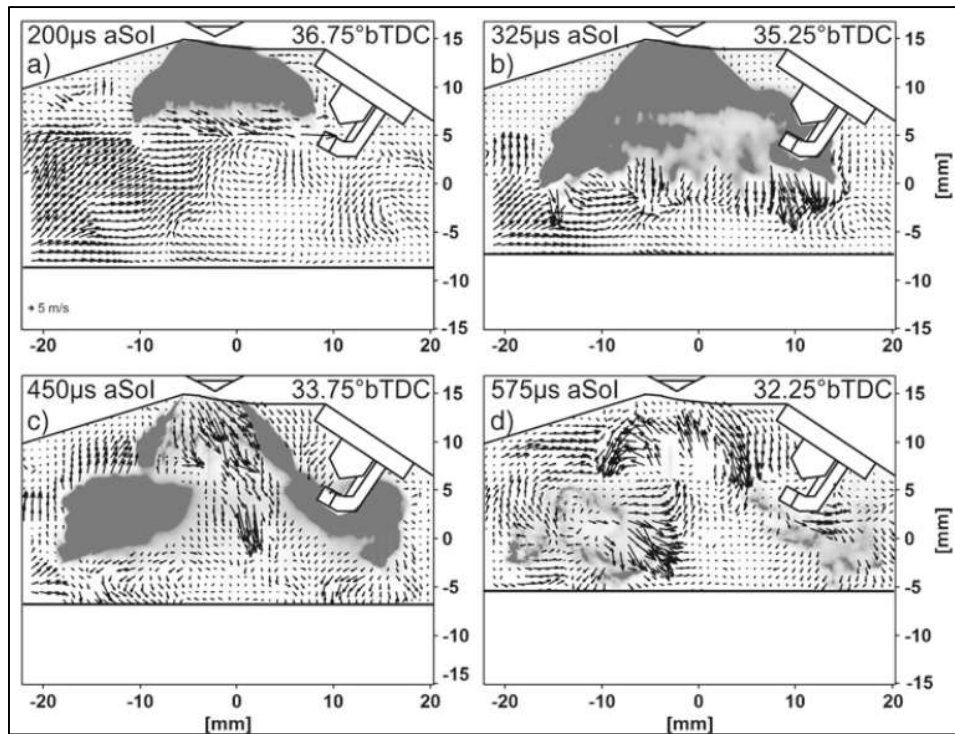


Figure 3.13 - Temporal evolution of the spray inside a DISI optical accessible engine. The spray evaluation presents similar aspects to those found in other works. Extracted from [17].

Note that the authors highlight a presence of EOI transient also in these engine-like conditions. The authors indicate that the characteristics described are similar to the “funnel flow” stated in [16]. During the analysis of multiple injections, the effects of this phenomenon are significant. Figure 3.14 shows the velocity fields inside the engine cylinder at the time interval between multiple injections. The conditions of the velocity fields for the second injection are heavily dependent on the first injection. During the first injector operation, the spray destroys the expected global tumble flow. This large structure is interrupted by vortical structures generated by the interaction of air and spray. Due to the spray high momentum, the air velocity fields are redirected towards the spray boundary. Additionally, as stated by the authors, the “funnel flow” caused by EOI transient is also responsible for these modifications. The sudden acceleration near the injector tip induces upward in the inner region of the former spray – the region between structures II and III in image a.

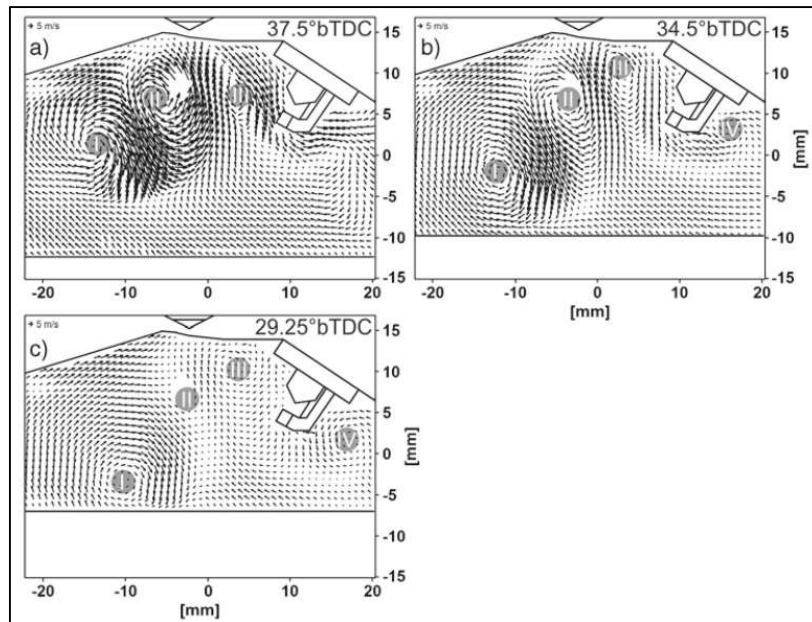


Figure 3.14 - Effects of multiple injections on mixture formation inside a DISI optical engine. Extracted from [17].

Note that the conditions established for the second injection are instable due to cycle-to-cycle variations caused by spray-air interactions. The authors quantify these variations by evaluating a characteristic position of the spray plume inside the cylinder – the Spray Height. The definition is shown in Figure 3.15. By evaluating conditional averages related to the defined spray height of the first injection events, the authors point out that the velocity fields after the first injection and the second injection correlate with the spray plumes positions. These positions also affect the EOI transient, which, in turn, modifies the air velocity fields.

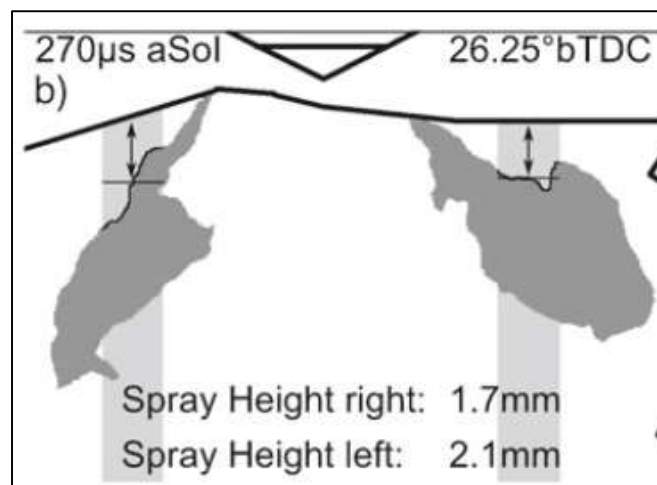


Figure 3.15 - Spray characteristic position as defined in [17].

These results demonstrate that not only the parameters related to spray but also the air field properties are important in the spray-air interaction. Depending on the conditions prior to injection, these interactions are constantly changed. The pressure effects and the velocity distributions also show to affect the air penetration. The impacts of the air properties, such as velocity distribution and mainly turbulence properties, are still not well understood, regardless of the ambient gas boundary conditions of the spray event.

From the point of view of turbulence, few works investigate the effects on the spray development. To date, it is not clear which the effects of space-dependent turbulence properties are on the air-spray interactions and there is a need for further investigation.

Concerning the experimental methodology, a trend of using the PIV technique to analyze the air-fuel interaction can be observed. This interaction is quantified in terms of air penetration in the spray and velocity magnitudes inside the recirculation and lateral penetration regions. These parameters are calculated through the analysis of the gas phase ([9] [10] [11] [12] [4] [13] [3] [18]). Some authors study the spray air interaction with an indirect approach, as is the case of Begg et al [14] - evaluating the air flow without the presence of spray with the PIV technique and the air flow with spray with the Mie-scattering technique. In most cases, the laser equipment has a low repetition rate, of the order of 10 Hz, resulting in velocity fields with no temporal correlation. The low acquisition rate can hinder the analysis of the spray time evolution, which may justify the trend of using quantities such as the penetration mass flow rate. In Zhang et al [9], for example, the use of a laser with a higher repetition rate up to 9 kHz allows the authors to discuss the temporal evolution of the total kinetic energy of the flow and its relation with the spray momentum. As in Zhang et al [9], high repetition rate equipment was chosen for analyzing air-fuel interaction in our project.

The PIV technique, described in section 5.7.1, depends on recording particle images usually illuminated by a laser light source. The velocity is estimated using statistical correlation methods. However, when the phenomenon of interest is a flow with more than one distinct phase, the light scattered from both phases is essentially the same from the camera sensors point of view. The application of a

standard statistical correlation method to an image similar to Figure 3.16 results in a velocity field that does not correctly represent the phenomenon studied. The algorithm is not able to differentiate the light scattering from the spray and ambient air. If any artifice is used, the algorithm will correlate the air tracer particles motion with the movement of the spray droplets.

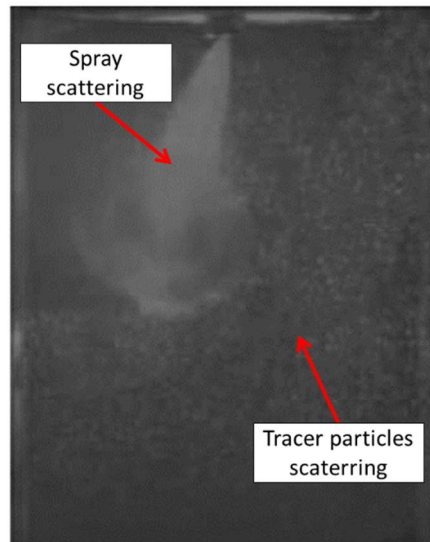


*Figure 3.16 - Example of light scattering image from the spray and gas phase. The presence of both phases in the image makes it hinder to apply the standard statistical correlation algorithms. Extracted from [4].*

To overcome the problem of phase separation, some separation methods were proposed. The first method is the spray differentiation by the intensity value of the pixels recorded in the image. When a set of particles or droplets are illuminated by a coherent light beam, the resulting light scattering is multidirectional. If we consider the light incidence in a spray of a DI injector, where the particles are small and the spray is very dense, the light scattering will be much more pronounced than that of the air flow tracer particles. The technique takes advantage of this characteristic to distinguish the spray by analyzing the contribution of each phase to the grayscale values of the image as a whole or of a region of interest. The procedure proposed by Rottenkolber et al [3] is defined as follows: From the determination of the grayscale histogram of the image, a limit value is determined. The image is then subdivided into two sets, one with values above the limit and another with values below it. These values are normalized based on a predetermined background value. However, the technique lies heavily on the correct limit value determination. The relationship

between the particle tracer distributions and spray droplets is associated with the choice of the limit value.

Another distinction method is the technique of peak separation [3]. When tracer particles and spray droplets are present in the same interrogation window, depending on the velocity difference between the two phases, the cross-correlation field may contain two distinct peaks - one for the velocity of each phase. Figure 3.17 shows the presence of two peaks in the correlation field of an area at the spray boundary.

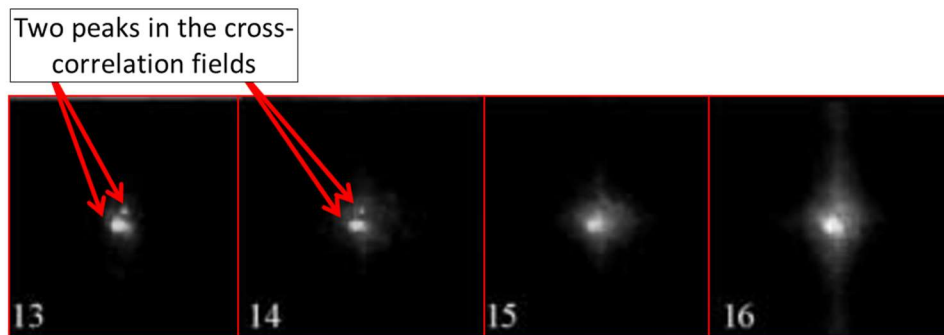


Figure 3.17 - Cross-correlation field of an interrogation window containing tracer particles and spray droplets. Adapted from [3]

The appearance of two peaks in the cross-correlation field depends on the velocity difference between the two phases. The higher the velocity difference, the better the peaks resolution is. An interesting example is shown by Rottenkolber et al [3] and is reproduced in Figure 3.17. In regions where velocities are very different, such as in images 13 and 14, it is possible to recognize the two peaks. In images 15 and 16, where the velocity difference has decreased, the peaks are not resolved and it is impossible to distinguish them. For more details on the correlation algorithm for the PIV technique, the reader is referred to section 5.7.1.4.

Figure 3.18 shows the velocity fields obtained with the two discussed separation techniques. It is evident that the techniques present hinders for the sprays studied by Rottenkolber et al [3], since the velocity distributions are different.

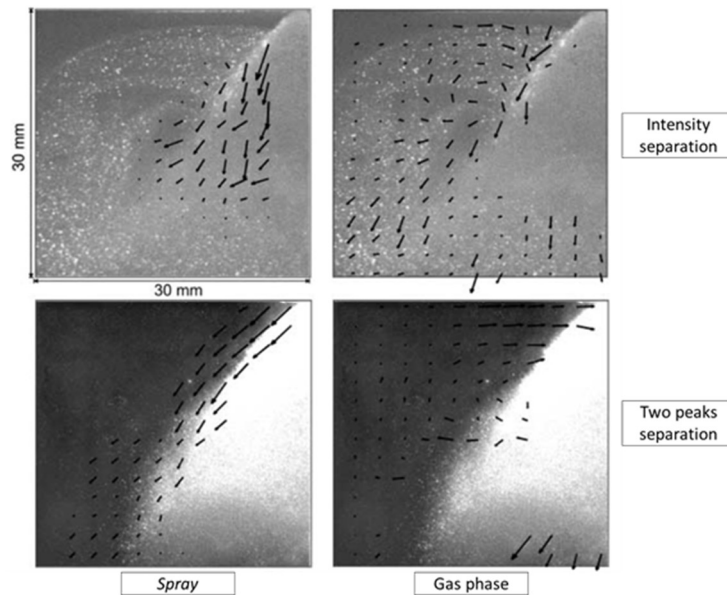


Figure 3.18 - Velocity vectors obtained for the gas phase and spray. Separation methods by intensity and by the two peaks on cross-correlation maps. Adapted from [3].

In Yeom [11], for example, uses the separation method derived from the two peaks technique. In this case, the distinction is made in the velocity vectors themselves. For velocities lower than  $8\text{ m/s}$ , the vectors are excluded from the gas phase. An obvious implication is that the information about the interaction near the spray border is lost.

Since the separation methods presented so far are strongly dependent on the spray conditions, new techniques based on particle fluorescence have been developed. One of the pioneering works of this type of approach is discussed in Towers et al [19]. The simplified method proposed in it is the preferred approach in recent studies, mainly due to the reduced amount of equipment required and its simplicity ([9] [10] [12] [13] [3] [18] [4] [20]).

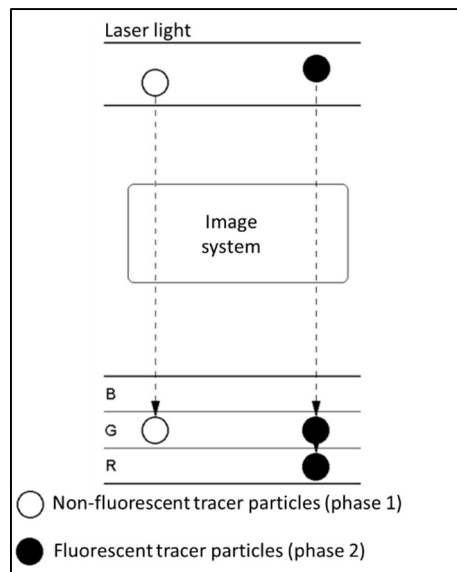


Figure 3.19 - Schematic drawing of the simplified phase separation technique by particle fluorescence. Adapted from [19]

Figure 3.19 illustrates the phase discrimination principle with particle fluorescence. Laser light excites two types of particles, fluorescent and non-fluorescent. The particle that does not fluoresce will only scatter the incident light, represent by band G in the figure. However, the fluorescent particle will absorb part of the incident light and emit a portion of the energy at another wavelength, represented by the R region in the drawing. The application of this principle to the PIV technique is therefore relatively simple. The image capture system shall be able to differentiate the received wavelengths. The use of interference filters in these systems satisfactorily fulfills the function. The PIV techniques that use this type of separation are called two-phase PIV, two-color PIV or fluorescent PIV. The application of two-phase PIVs can undergo numerous variations, depending on the purpose or amount of equipment available. Figure 3.20 shows the most common experimental arrangements. Figure 3.20a shows the use of two cameras and a laser system. In this case, each camera records one of the flow phases depending on the optical filter used. When only one phase is of interest, one only camera is strictly necessary. This approach is the most widely used in the presented works ( [10] [12] [4] [13] [3] [18]). The acquirement of the two phases is also possible with a single camera, as shown in Figure 3.20b. In this case, an image doubler divides the camera sensors into two distinct regions ( [9]). Figure 3.20c shows the presence of two cameras and two lasers of different wavelengths. In this case, the fluorescent properties of the two particles are used.

Each laser excites a particle and each camera acquires the respective phase. ([20] [18])

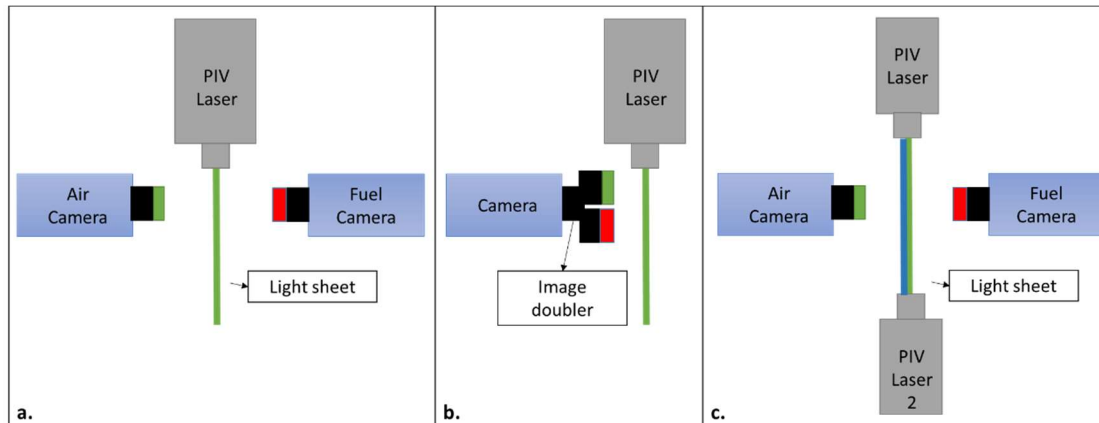


Figure 3.20 - Common equipment arrangements of the two-phase PIV

The advantage of using two Lasers systems is regards the temporal resolution of the two phases. Since spray velocities are generally much higher than air velocities, the time interval between images required for calculating statistical correlations is different for each phase. The use of a single Laser device only allows using a time interval for the two phases, which can affect the velocity estimations. ([20] [9]).

The problem of the different temporal resolution of the phases when using a single Laser system can be relatively solved. If the time interval for the gas phase is a multiple of the time interval for the spray, then the pairs of images can be assembled from multiple acquisitions. Figure 3.21 shows the time diagram of the strategy. The quality of this solution will depend on the velocities ratio, since it is a compromise between the time interval for the spray and for the ambient gas.

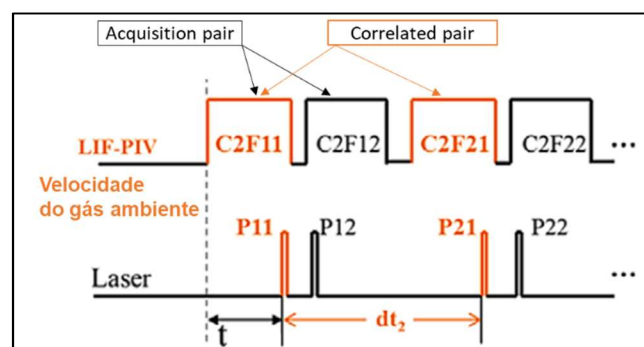


Figure 3.21 -Time diagram for calculating the statistical correlations of velocity in the case of a single laser equipment. Adapted from [9]

Figure 3.22, adapted from Zhang et al [9], provides a survey of the works with two-phase PIV as a function of the velocity magnitudes and time interval between consecutive images. Note the velocity magnitudes determined for the ambient gas. With the exception of Peterson and Sick [21] and Omrane et al [22], performed on optical access engines, the other studies obtained relatively low magnitudes for the ambient gas. The use of constant volume chambers and quiescent ambient gas is the reason for the low velocities in most other jobs. Few studies of spray-air interaction in conditions with constant ambient gas flow can be found, even with the importance of the phenomenon for applications in direct injection engines. In none of the mentioned studies was the two-phase PIV technique used for this specific case.

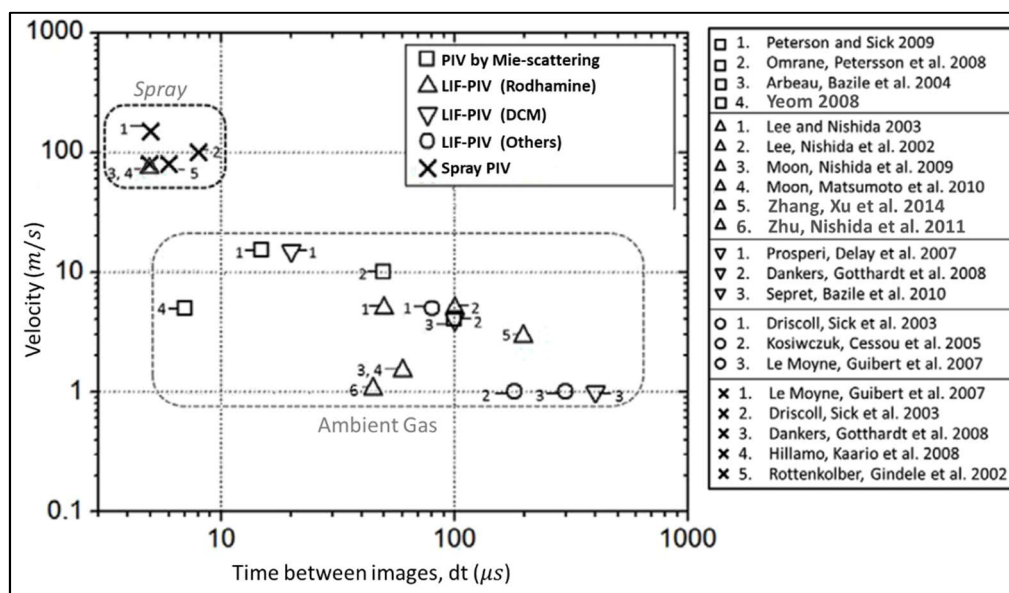


Figure 3.22 – Survey of works using the two-phase PIV technique to analyze the interaction between air and fuel. The works are arranged according to the time interval between the image pairs and the velocity magnitude of their respective phases. Adapted from [9].

Another important observation is the number of studies that analyze the ambient gas flow, but does not calculate the velocity field for the spray. This is due to the difficulty of applying the PIV technique to direct injection sprays. Since these dense sprays produce small droplets and droplet clusters, light scattering prevents the identification of individual particles. This characteristic increases the difficulty to apply the cross-correlation algorithms, since it may cause peak deformation in the cross-correlation fields. However, in some cases it is possible to estimate the velocity of entire regions rather than a discrete group of particles. In these cases, vectors representing velocity are a spatial mean of a certain

region. Some examples of this type of calculation are Rottenkolber et al [3] and Driscoll et al [18]. It is worth emphasizing that the use of hollow cone injectors facilitates the estimations of the correlations, since the spray is less dense than the one generated by a multi-hole injector. Multidirectional scattering effects are also less predominant. The spatial resolution of the velocity vectors obtained in the works using the hollow cone injector ([4] [3]) is higher than that in the studies with multi-hole injectors. ([20] [18])

Finally, it is possible to conclude that the study on the spray-air interactions has an essential role in mixture formation. In internal combustion engines, the formation of the mixture is directly linked to the formation of pollutants and to efficiency. The characterization of mixture processes is important for both spark ignition and compression ignition engines. With the advancement in direct injection spark ignition engines, the study on gasoline and diesel sprays have found similarities. The macroscopic mechanisms of air-fuel interaction are similar for the two fuels, apart from characteristics such as penetration length and cone angle. There are few studies on ethanol sprays and other biofuels and their interaction with the ambient gas. In most studies, the interaction is characterized by the study on gas phase flow. Information is extracted as mass inflow, recirculation structures. There is a lack of studies investigating the evolution of the spray in terms of interaction with the air and formation of mixture with equipment of higher temporal resolution. Regarding the use of the PIV technique, separation of the phases by means of particle fluorescence seems to be the most accepted and used technique. In the past, most studies were performed using low repetition rate PIV techniques. Constant volume pressurized chambers are the most commonly used experimental apparatus for investigations of spray evolution. Studies on the interaction between spray and air flow are rare and to date few studies with two-phase PIV technique have been used for analysis.

## 4 Objectives of the study

The objective of this work is to characterize the evolution of direct-injection ethanol sprays in constant air flow conditions. The time-resolved air velocity fields and in the presence of the ethanol sprays are obtained using the two-phase PIV technique. The experimental results evaluate the influence of the air turbulence properties in the spray development and in the air-spray interactions. Additionally, other factors such as the injection pressure and the air mass flow rate are also studied.

To contribute significantly to understand of the mechanisms behind the interaction of spray and surrounding air, this study aims to following objectives:

- To enhance and evaluate the use of the two-phase PIV in the study of ethanol sprays from multi-hole injectors.
- To provide a comprehensive data base of time evolution of the velocity fields during the injection events in conditions of constant air flow.
- To evaluate the spray development in a multi-hole injector using ethanol as the injected fuel.
- To investigate which are the effects of the spray evolution in the surrounding air flow.
- To investigate if the air turbulence properties contribute significantly to the air-spray interaction mechanism and to the spray development.
- To compare the differences between the interaction in quiescent and in constant-flow environments in engine-like similar conditions. Moreover, to investigate if the instabilities identified for quiescent conditions are also present in constant flows experiments.
- To investigate if the air mass flow rate and the injection fuel pressure can significantly modify the air-spray interactions mechanisms.



## 5 Experimental procedures

In this chapter, the experimental apparatus and measurement techniques are described. Each experiment subsystem is detailed emphasizing important aspects for the proper use of the measurement techniques. The important features of the PIV technique are presented and discussed, both in terms of equipment configurations and aspects of the velocity calculation algorithms.

### 5.1 The Isothermal Ethanol Spray Chamber (IESC)

To evaluate the flow field and its turbulent properties, experiments were conducted in a continuous-flow spray chamber - the Isothermal Ethanol Spray Chamber (IESC). This apparatus was specifically designed for studying spray-air interactions. Figure 5.1 shows a section view of the IESC. The whole design, project and manufacturing processes were performed by the author.

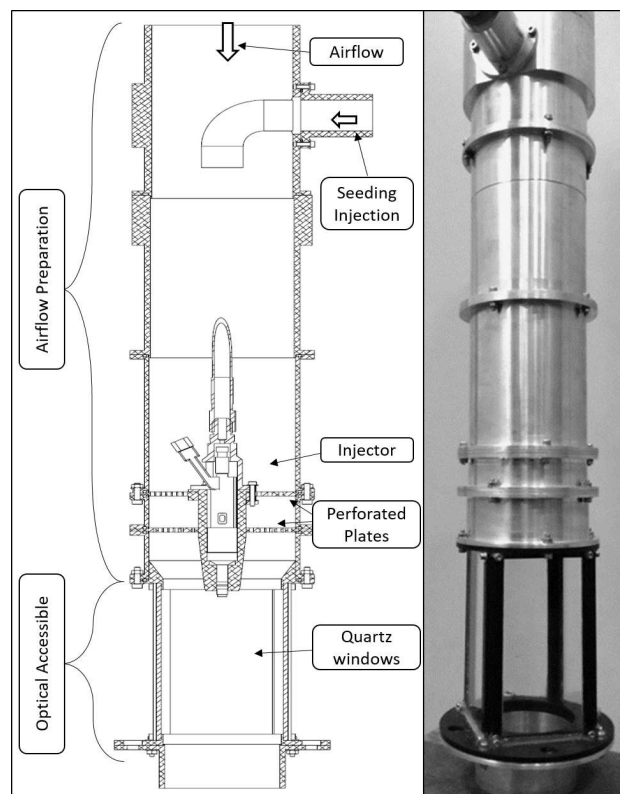


*Figure 5.1 The Isothermal Spray Chamber. The figure to the left is a section view of the chamber showing the main components. The figure to the right is a photograph of the apparatus showing the proportion between the air preparation section and the optical accessible section.*

The chamber is divided into two main sections: the airflow preparation and the optical accessible section. In the first section of 500 mm in length and 100 mm in diameter, air is injected from the upper entrance. Tracers for the optical techniques can be injected by the side entrance at the centerline of IESC. The seeding injection occurs at a proper distance to ensure good mixing with incoming air. A set of two perforated plates were installed near the end of the airflow preparation section. Each perforated plate is composed of cylindrical holes disposed radially, thus providing a more controllable turbulence in terms of temporal and length scales. Three different types of perforated plates set can be used during the experiments. The design of the perforated plates comprises three different hole diameters: 2, 4 and 6 mm. In all the sets, the holes are organized to maintain an approximate equal solidity [23]. The parameter is used to scale the degree of turbulence with respect to the different inlet geometries in wind tunnels [24] [25]. Figure 5.2 shows the schematics of the holes disposal in the three different perforated plates sets.

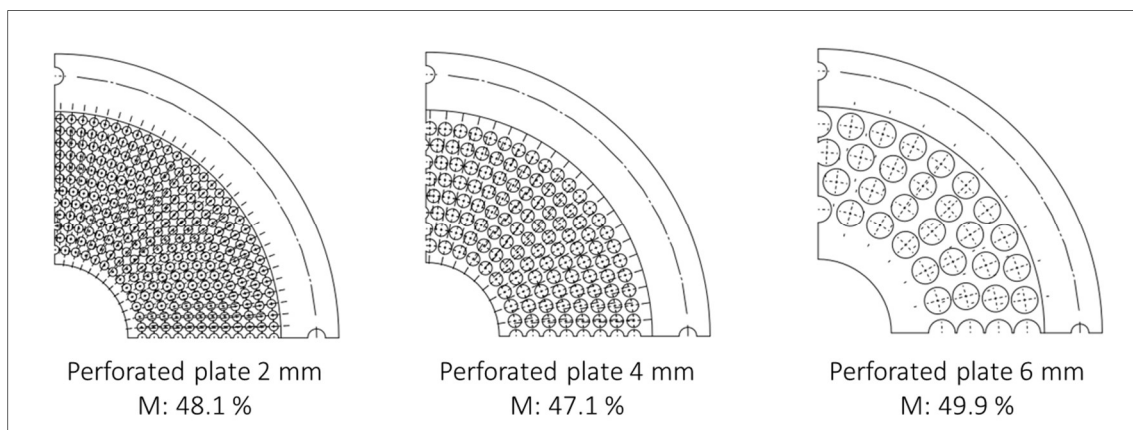


*Figure 5.2 - Schematics of the three possible sets of perforated plates to be used in IESC.*

The perforated plates sets also limit the turbulence integral length scales in the flow. The IESC-W design allows a practical changing of the plates set. It is in the interest of this project to characterize the interaction of the spray with the air flow according to different lengths scales.

At the centerline of the airflow preparation section, an automotive multi-hole GDI Delphi Injector is placed inside a cartridge coupled with the set of perforated plates. Anhydrous ethanol is supplied to the injector by the upper connection of the cartridge. The optical accessible section is composed of four quartz windows of  $85 \times 136 \text{ mm}^2$  and  $3.14 \text{ mm}$  thick in a square arrangement to reduce light distortions. The aluminum parts of the section received an anodized finishing and a black coat to reduce light scattering. The size of the windows allows full visualization of the spray and its interaction with the incoming controlled airflow. Figure 5.3 shows the injector cartridge mounting on the perforated plates set.

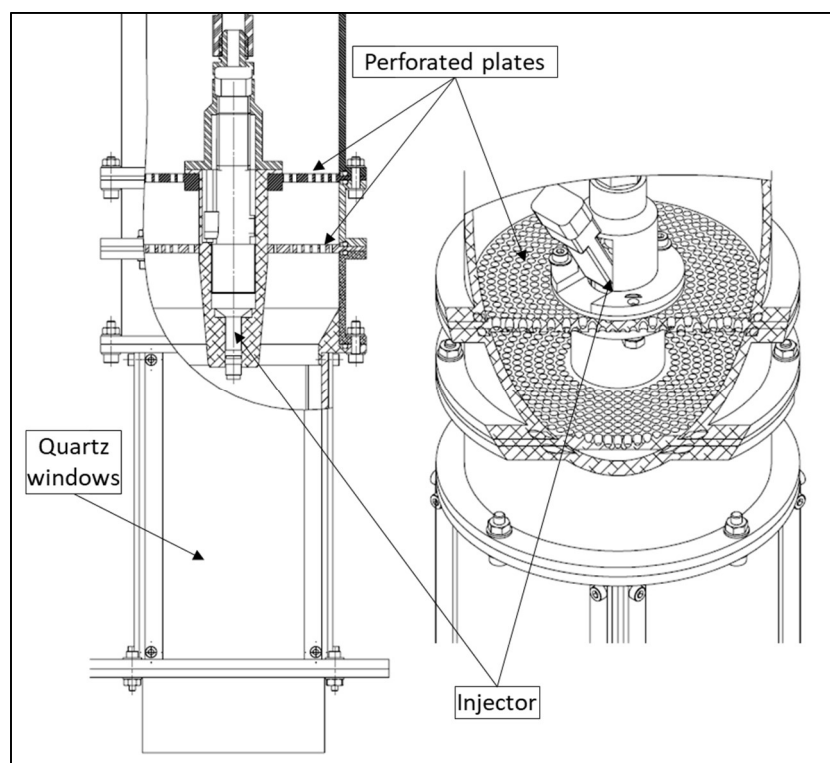


*Figure 5.3 - Concept of IESC bench design. Flow uniformization is performed with the passage of air through the set of perforated plates. The injector is disposed on the central axis of the chamber. Optical access is possible from all the four sides.*

### **5.1.1 The importance of studies in continuous flow chamber**

Most modern commercial DISI engines operate in homogeneous charge mode for the majority of the conditions. In this strategy, the main injection event occurs during the intake stroke. During this phase, the spray encounters the air flow entering the cylinder and the ambient pressure is relatively low. The effects of the air flow and spray interaction, especially in terms of turbulence are still not well understood. Thus, experiments to address the issue are needed.

As previously explained, the IESC apparatus was designed to evaluate the effects of continuous flow properties on air-spray interactions. The advantage of these types of apparatus is to provide more controllable boundary conditions in terms of air flow characteristics, turbulence and fuel injection. When compared to engine operations, these experiments are less sensitive to instabilities and cycle-to-cycle variations. Although there are many aspects of the real engine not present in IESC, rather than obtaining parameters of engine operation, the objective of the study is to further understand the air-spray interaction mechanisms. Spray injections in a real engine present both interaction mechanisms that occurs in quiescent and continuous-flow environments. Therefore, consistent results in modelled environments provide the additional tools required to integrate the more complex processes that occur in the engine conditions.

## 5.2 Injector

The injector selected for experiments with the IESC bench consists of a high-pressure multi-hole injector for direct injection engines. This injector, from manufacturer Delphi Powertrain Systems, is a multi-hole injector with five openings arranged radially in relation to the axis of the injector. The injector, as well as a macro representation of the produced fuel cone, are shown in the figure below.

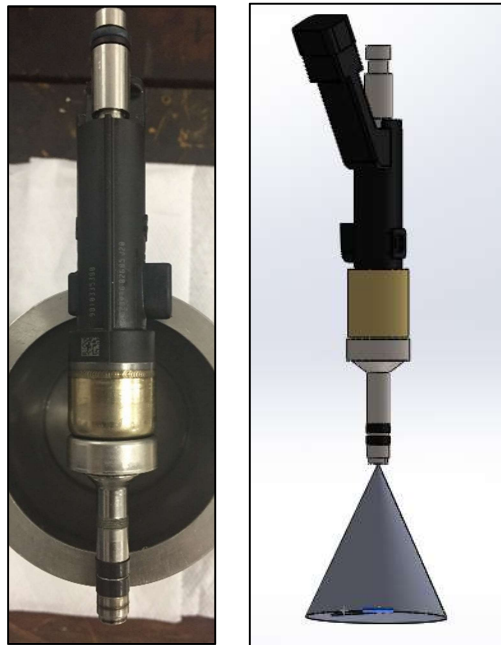


Figure 5.4 - The Delphi multi hole central GDI injector used during experiments with IESC.

The positions of the plumes have a distinct pattern to accommodate the features of the engine design using the injector. Figure 5.5 illustrates the position of the center plumes in the cross-section 50 mm distant from the injector tip. The figure shows that the injector does not have a symmetric positioning of the plumes. Plumes 1 and 5 are closer to the tip center line – represented by the Z dot. According to the nominal conditions provided by the manufacturer, the injector is capable of 7.63 mg/pulse of dynamic fuel flow for n-heptane operating at 100 bar of injection pressure. The characteristic droplet Sauter mean diameter (SMD) for the same conditions is 12  $\mu\text{m}$ .

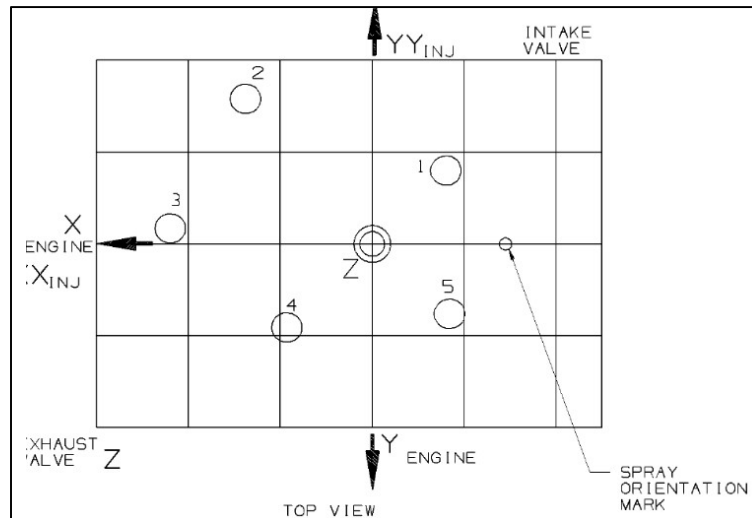


Figure 5.5 - Plumes center cross section for a distance of 50 mm from the injector tip.

The operation principle is based on the actuation of a solenoid valve which in turn moves the needle that will release the fuel flow to the openings. To ensure a quick response from the injector, the coil is actuated with a high voltage peak ( $\sim 70V$ ) and then a certain level of tension is maintained to hold the needle in the raised position (pick-and-hold strategy). Figure 5.9 shows the current plot equivalent to the actuation strategy of the injector opening. The time interval for holding  $I_{Maint\ eff}$  depends on the duration of the injection period.

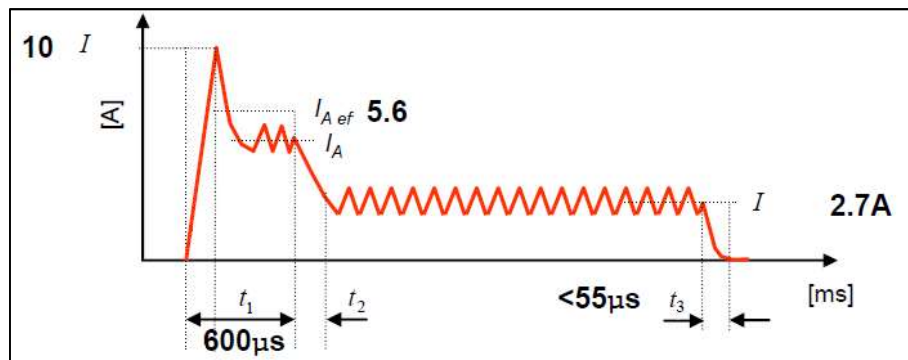


Figure 5.6 - Example of actuation current for the multi-hole injector. Adapted from [26].

### 5.3 Injection control system

The control of the injection event in direct injection engines is an important requirement that directly affects their performance. The duration and synchronism of the event must be accurately determined, since the formation of the air-fuel mixture depends on these parameters. For this reason, the injector actuator has a dedicated electronic unit. This equipment is responsible for controlling the injector according to its actuation curve, guaranteeing reliability and precision. This unit is also synchronized with the other experiment controllers described in this chapter.

The injector controller used in the work is the direct injection module NI 9751 from the manufacturer National Instruments. This module is capable of controlling 3 solenoid type injectors, which is the case of the used injector, or 2 piezo-electric injectors. The module amplifies voltages up to 120 V and supports peak currents up to 40 A [27]. The NI 9751 configuration is achieved with an interface created in the LabView software. Figure 5.7 shows the schematic design of the injection system control operation. The actuation curve is specified directly in terms of 8 phases, describing as first reaction, the peak and a phase in which the voltage is maintained. Communication between the LabView interface and the NI 9751 module is carried out by the NI 9075 chassis which, among other functions, physically links the modules to all the controls. The NI 9751 module connects to the multi hole injector with a separate power supply from the chassis (24 V). A signal is sent to the system to synchronize the injection event with the equipment of the PIV technique.

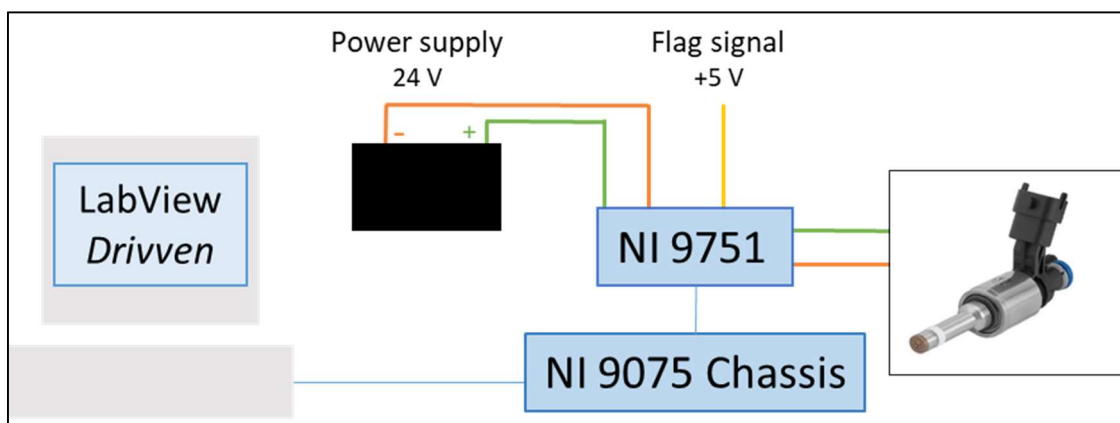


Figure 5.7 - Schematics of the injector control system.

## 5.4 High-pressure fuel system

To supply fuel at the injection pressures for direct injection, a system has been designed and manufactured. Fuel pressurization occurs in two stages. The first is responsible for elevating the fuel pressure to 2 bar of relative pressure. This work is performed by a common electric automotive fuel pump in a by-pass circuit. The second stage should increase the pressure from 2 bar to the desired one, which can be varied from 80 to 120 bar. A piston fuel pump used in gasoline DI engines provides the pressure increase. Figure 5.8 shows the operating diagram of the high pressure pump as well as the operation of the first stage. The fuel enters the low pressure pump. The pressure in the downstream line is regulated by the valve that limits the fuel return flow to the reservoir. This pressure is measured by the manometer indicated in the figure. The operation of the second stage is based on the actuation of the debit control valve according to the reading of the pressure sensor at the pump outlet. The pressure raising piston is driven by a cam mounted internally to the pump. The pump, in turn, is connected to the valve control shaft in the case of a motor and in this design connected to a three-phase electric motor. The angular velocity of this electric motor is kept constant for simplicity. When the flow control valve is not activated, the fuel can go back through the line to the first stage. By the actuation of the debit control valve, the flow can no longer return to the first stage and the fuel is pressurized towards the fuel rail. The actuation is carried out by an electronic control mechanism that observes the pressure in the sensor downstream of the pump. The pressure relief valve is the pump overpressure safety mechanism.

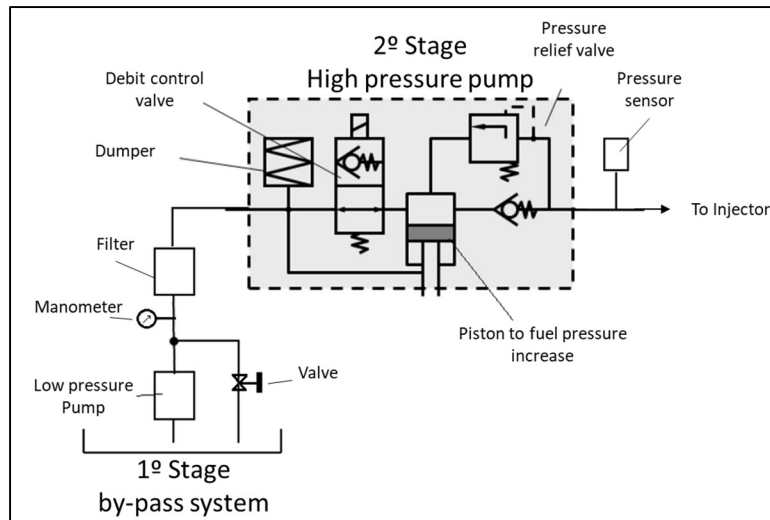


Figure 5.8 - Working principle diagram of the fuel system second stage. Adapted from [28]

The electronic control of the fuel system was developed in LabView software. This interface is responsible for modifying the fuel control law, the reference pressure and safety logics. Figure 5.9 shows the operation of this control. As previously described, the control is performed by the actuation of the debit control solenoid valve and by observing the pressure on the sensor at the high pressure circuit. As the pressure rises in the line, the actuation in the pump is reduced and the rotation of the electric motor is kept fixed. The solenoid valve piloting is achieved with the high frequency digital output module for valve control NI 9478, manufacturer National Instruments [29]. The pressure sensor reading, a piezo resistive sensor, is performed with the NI 9201 analog input module from the same manufacturer [30]. The configuration and communication of the modules are accomplished with the LabView interface and is guaranteed by the NI 9075 chassis, which integrates this control with the injection control system.

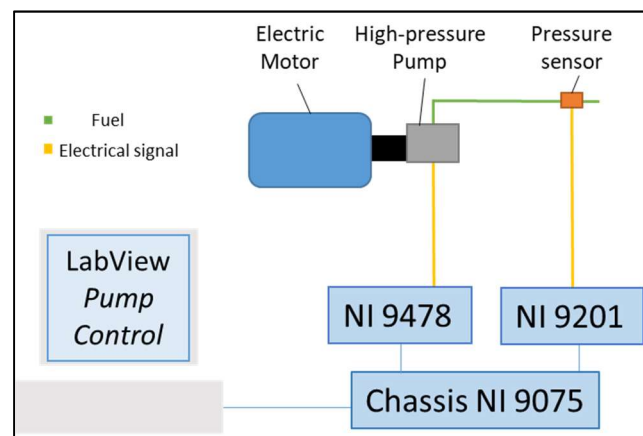


Figure 5.9- Schematics of the electronic fuel pressure control system.

## 5.5 Air supply system

In the analysis of the interaction between air and ethanol spray, the air mass flow is measured and supplied to the IESC apparatus by the air supply system. Figure 5.10 illustrates the equipment set of the air system. The supply is composed of the blower, the air flow meter, pressure transducer, thermocouple, Laskin generator and filter. The air flow generated by the blower is directed to the entrance of IESC by a supply line. After the passage into the chamber, the flow passes through the filter box and is released into the environment. The equipment for generating the air flow is a rotary lobe blower model DB 236 C, manufactured by Kaeser Compressors. The air flow is adjusted by controlling the rotation of the electric motor of the blower with a frequency inverter, model CFW08 manufactured by WEG. At the supply line are installed the pressure transducer, the thermocouple, the air flow meter and the Laskin generator. A pressure transducer is placed to measure the pressure drop across the pipeline. The sensor, model MBS-33 from manufacturer Danfoss, has an absolute measurement range of 0 to 4 *bar* and communicates with the control interface with the NI 9201 analog input module from National Instruments [30].

The air flow meter is a turbine type model SMRIX G400, from Instromet. The instrument is capable of measuring volumetric air flow rates from 32 to 650  $m^3/h$ . The air flow meter output is computed by the NI 9401 digital input and output module [31], National Instruments. This module is also coupled to the NI 9075 chassis. The thermocouple of type T with grounded tip, Inconel sheath, 200 *mm* in length and 1.5 *mm* in diameter, is installed at the centerline of the supply pipe upstream the air flow meter. The thermocouple output is transmitted to the NI 9201 analog input module by a temperature Amp-op transmitter that converts the thermocouple voltage signal to a current signal – model S201E, manufacturer Contemp. The equipment called the Laskin generator accounts for the aerosol production of air tracer particles for PIV measurements. Its principle of operation and other specifications are described in section 5.7.1.1.

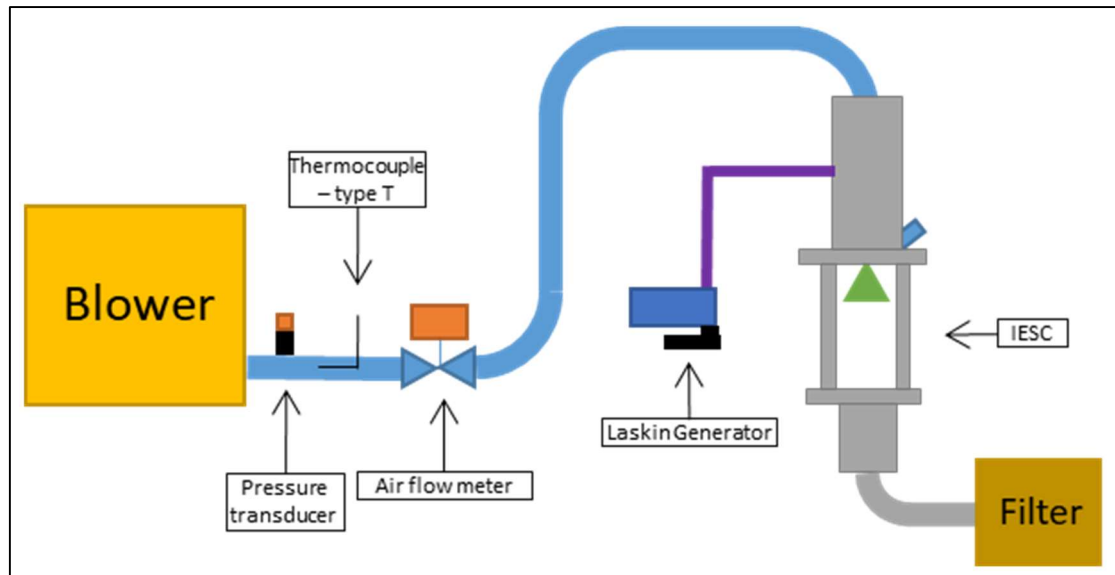


Figure 5.10 - Schematics of the air supply for operation of IESC.

## 5.6 The operation of experiments

All the subsystems described previously constitute the experimental apparatus used to obtain the results with IESC. During the experiments, the subsystems operate simultaneously and in conjunction with the PIV laser system. Figure 5.11 shows the schematic drawing of the experimental apparatus. The air supply system maintains the constant air mass flow in the IESC chamber by the rotation control of the blower and the air mass flow measurement by the SMRIX G400 flow meter. The system pressure drop across the system is recorded on the pressure transducer installed downstream of the blower. The desired injection pressure is imposed on the National Controller (set of NI modules and the NI 9075 chassis) with interface developed in LabView. The control acts on the second stage of the fuel system to ensure the reference pressure. Injection control is also performed by the National Controller, which operates according to the operation current curve of the multi hole injector. The event of injection is synchronized with the laser system for the PIV technique and only occurs with the Laser Controller command. This system is also responsible for synchronizing all the equipment used in the PIV technique.

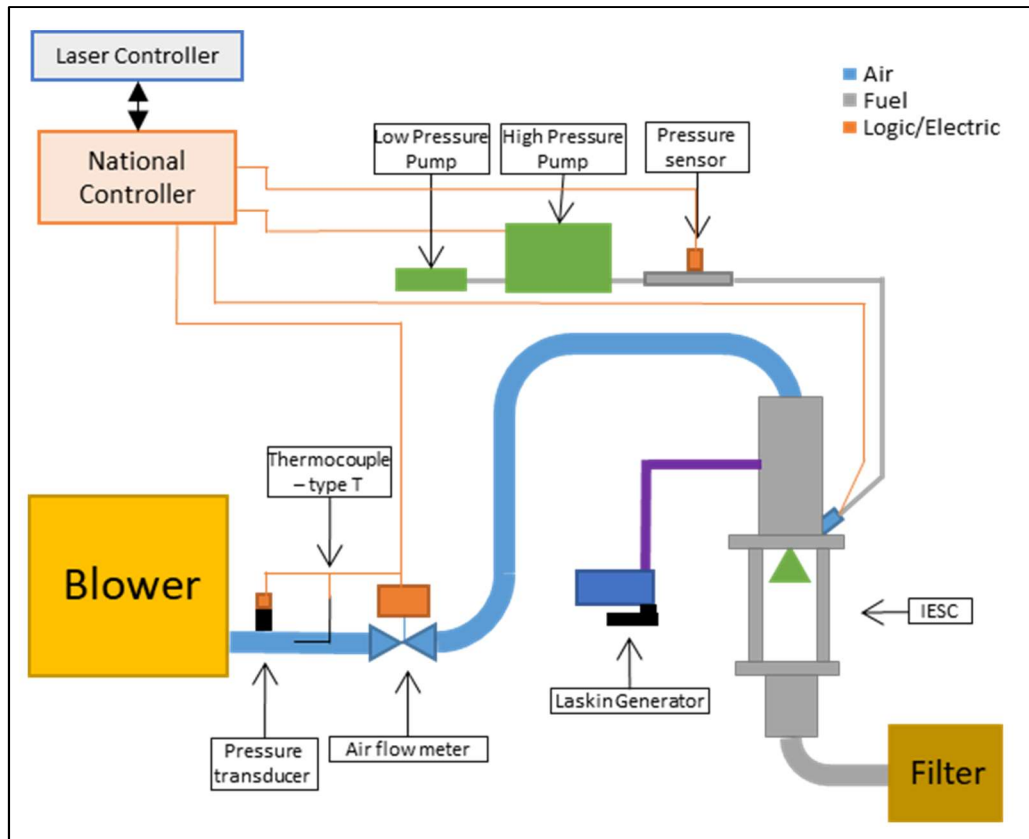


Figure 5.11 - Operation of the equipment during the experiments with IESC.

## 5.7 Techniques for spray and air flow analysis

In order to achieve the objectives of this work, ethanol sprays injected on continuous air streams are measured and characterized mainly by an optical technique for investigating the phenomenon and mechanisms of interaction between the spray and turbulent structures present in the air flow. Most analysis are based on spray images and air flow with tracer particles and subsequent processing to obtain velocity fields by means of the two-phase PIV technique.

This section is dedicated to discussing the use of the standard particle image velocimetry and the two-phase PIV techniques. Important aspects and algorithms that control both techniques are presented. The choice of parameters and configurations highlighted in this section are used as a standard to calculate all velocity fields. When needed, particularities of certain PIV estimations are addressed separately.

### 5.7.1 Standard particle image velocimetry (PIV)

In this section, the fundamentals of the particle image velocimetry technique and the application of this technique to obtain airflow velocity fields in the IESC chamber are briefly described. The important characteristics of the equipment and image processing are described for proper use of the technique. For further details on the theory and details of the equipment, the reader is referred to the literature ( [32] [33] [34]).

Figure 5.12 shows an example of layout of the equipment that can be used for applying the PIV technique to a continuous flow chamber. For determining the velocity field, particles must be inserted into the flow and illuminated by a light source, typically pulsed laser light. The light scattered by these particles is recorded by a camera with a small known time interval between the images. These are subdivided into small regions, the so-called interrogation windows, and analyzed by spatial correlation algorithms to identify shifts of small groups of particles, where each group is contained in an interrogation window. The displacements and the time interval between frames results in the velocity components representing the mean velocity of the group of particles in that time interval.

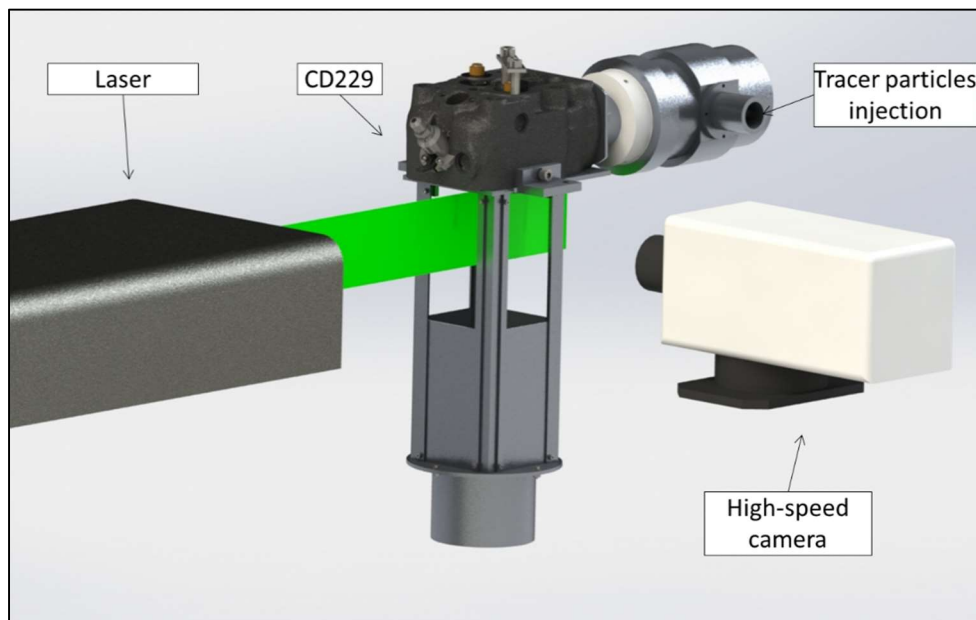


Figure 5.12 – An example of the equipment layout for the application of the PIV technique

### **5.7.1.1 Tracer particles**

The first subsystem to be analyzed is the injection of tracer particles. Their characteristics and the way they are injected into the flow are important parameters of the technique, since the velocities are calculated based on the displacement of the tracer particles and not of the air flow. The selection of these particles is a compromise between the ability to represent the flow into which they are inserted and the light scattering properties.

In general, light scattering by a small particle is a function of particle size, shape, orientation and the ratio of the refractive index of the medium to the particle itself. The scattering also depends on the polarization of the light and orientation of the point of observation [32].

If the particle is spherical and with diameter  $d_p$  greater than wavelength  $\lambda$  of incident light, then the Mie theory is applicable [32]. Figure 5.13 shows the scattered light intensity as a function of the Mie theory for 1  $\mu m$  and 10  $\mu m$  diameter air oil particles. For both particles, the directions with the highest scattered intensity are observed to be 0° and 180°. However, due to limitations to the field of view, the particles are recorded at 90° to the incident light. Note that there is an increase in the image intensity of individual particles in high density particle flows. The phenomenon occurs because the particles are illuminated indirectly by the scattering of the others. These contributions are significant, since the intensity of light scattered at 90° is orders of magnitude smaller than 0° and 180° [32]. However, the density of particles must be chosen carefully, since large values of density may generate noises in the analysis of the images [32]. The same aspect is also present in spray droplets. This multi-scattering illumination influences the determination of geometrical measured properties of spray and is subject to study and discussion. For example, see [35] [36].

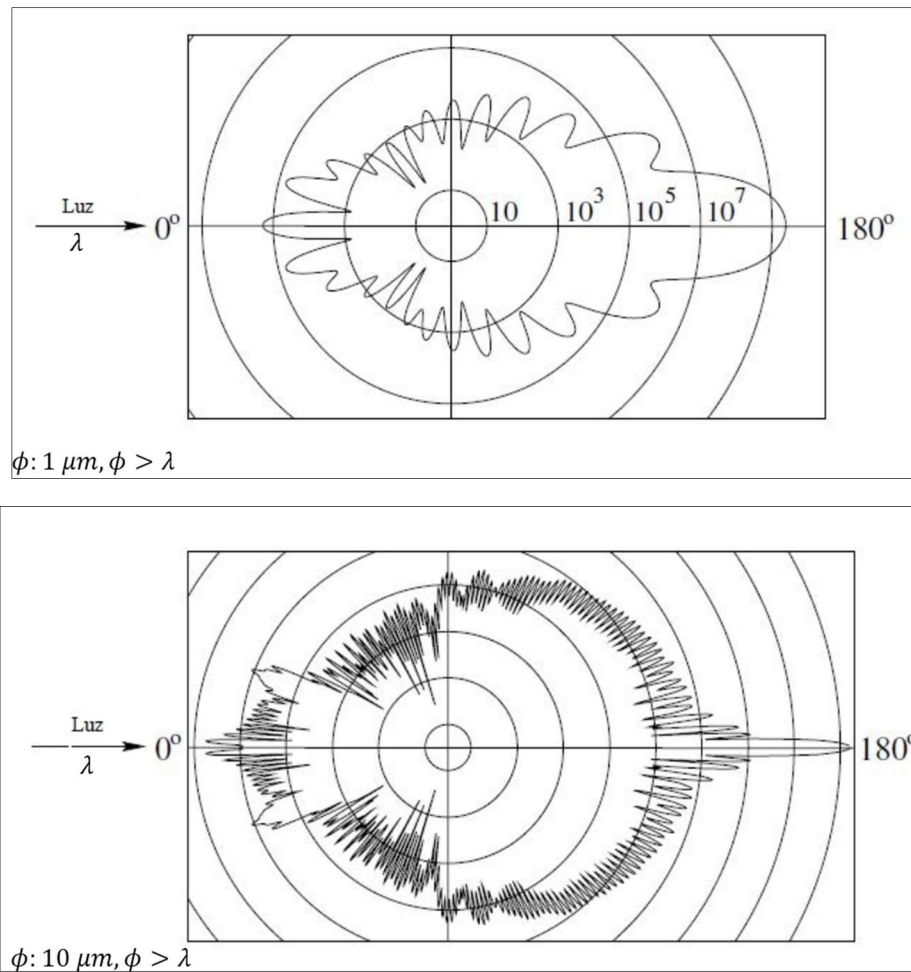


Figure 5.13 - Light scattering according to Mie theory for particles of oil in air with diameters of  $1 \mu m$  (superior) and  $10 \mu m$  (inferior image). Adapted from [32]

Figure 5.13 allows us to say that the intensity of light scattering, in general, increases with the diameter of the particle. In fact, there is a tendency for scattering efficiency to increase with particle diameter if all directions are observed. Considering a given fixed direction, this tendency does not occur, and there may be points of maximum and minimum with the increase of the diameter of the particle [32].

Light scattering is also described in terms of integral variables, as in Melling [37]. Considering scattering cross-section  $C_s$  as the ratio of scattered light power  $P_s$  to laser light intensity  $I_0$ , there is a correlation between  $C_s$  and particle diameter  $d_p$  (normalized by the incident light wavelength), as shown in Figure 5.14. However, for the PIV technique, the light scattering should also be evaluated in terms of the scattering at  $90^\circ$ :  $I_{s90}$ . In general terms, the ratio  $I_{s90}/I_{s0}$ , where  $I_{s0}$  is the total intensity of the scattered light, decreases with the increase of  $d_p$  [37]. Despite the

opposite trends of  $C_s$  and  $I_{s90}/I_{s0}$ , larger particles still have stronger signals. In terms of light scattering efficiency, the conclusions in [37] are in agreement with Raffel et al [32], since even taking into account the strong dependence on position, the increase in particle diameter tends to increase the light scattering efficiency.

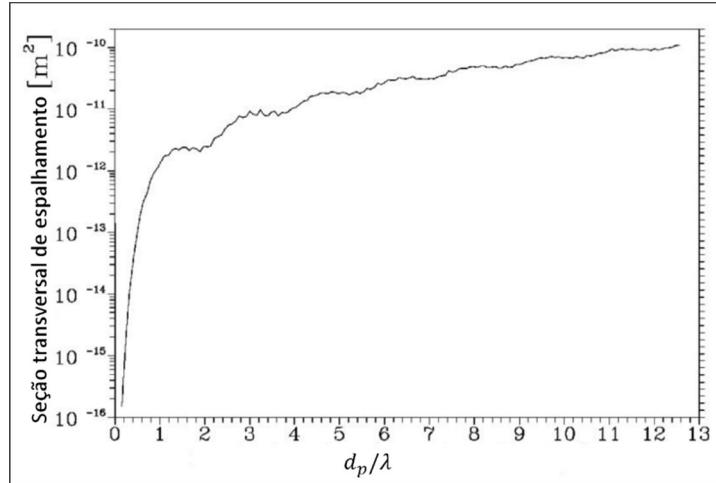


Figure 5.14 - Scattering cross-section as a function of normalized particle diameter. Adapted from [37]

The particles must also be chosen in function of their ability to represent the flow. This requirement can be interpreted as the response time of the particle to an acceleration of the fluid, which may be an acceleration of the mean flow or a fluctuation of velocity inherent to the turbulence. The complete equation of this response time is a difficult task if all the variables affecting the movement of particles, such as the interaction between particles, the inertial and the field forces, are considered. For simplicity, only characteristics such as diameter, particle density, specific mass and viscosity of the fluid are considered. The response time is evaluated in terms of the Stokes number - the ratio between the response time of the particle and a characteristic time scale of the flow. If we consider the case of a flow with spherical particles of low Reynolds number based on particle diameter, the response time of the particle is given by [32]:

$$\tau_s = d_p^2 \frac{\rho_p}{18\mu} \quad 5.1$$

Where  $d_p$  is the particle diameter,  $\rho_p$  is the particle density and  $\mu$  the dynamic viscosity of the fluid. Equation 5.1 shows that the response time of a particle decreases with the diameter and with the density. For PIV technique applications,

$\tau_s$  should be as small as possible. In general, a good representation of the flow is assumed when the number of Stokes ( $S_k$ ) is very small -  $S_k \ll 0.1$  [38] [34].

Although the criterion is conservative for considering the drag in a Stokes flow [32], the method does not consider the behavior of particles with velocity fluctuations present in a turbulent flow. Melling [31] evaluates the response time of the particles from the Basset equations of motion in the case of an air-particle turbulent flow in a pipe. The results are calculated as a function of two turbulence characteristic frequencies ( $f_c$ ) and are reproduced in Table 5.1. Note that for olive oil, diameters between 1  $\mu\text{m}$  and 3  $\mu\text{m}$  are sufficient for flows with characteristic frequencies between 1 and 10 kHz. The choice of the frequencies value was made by Melling [37] according to his experience. Another way is by determining the Kolmogorov time scale which depends on the rate of local dissipation, not known in many cases. For further details on the formulation and hypotheses, the reader is referred to Melling [37].

<b>Particles</b>	$\rho_p$ ( $\text{kg}/\text{m}^3$ )	<b>Gas</b> ( $10^5 \text{Pa}$ )	<b>Density</b> <b>ratio s</b>	<b>Viscosity</b> $\nu$ ( $\text{m}^2 \text{s}^{-1}$ )	$f_c$ ( $\text{kHz}$ )	$S_k$	$d_p$ ( $\mu\text{m}$ )
<b><i>TiO<sub>2</sub></i></b>	3500	Air (100 K)	2950	$1.5 \times 10^{-5}$	1	0.0295	1.44
					10		0.45
<b><i>Al<sub>2</sub>O<sub>3</sub></i></b>	3970	Flame (1800 K)	20250	$3 \times 10^{-4}$	1	0.0113	2.46
					10		0.78
<b><i>Glass</i></b>	2600	Air (300 K)	2190	$1.5 \times 10^{-5}$	1	0.0342	1.67
					10		0.53
<b><i>Olive oil</i></b>	970	Air (300 K)	617	$1.4 \times 10^{-5}$	1	0.0645	3.09
					10		0.98
<b><i>Micro</i></b> <b><i>Baloons</i></b>	100	Air (300 K)	84.5	$1.5 \times 10^{-5}$	1	0.1742	8.50
					10		2.69

Table 5.1 – Minimum particle diameter according to the flow characteristic frequency and  $\eta = 0.99$ .  
Adapted from [37].

In this project, propylene carbonate was used as the oil for generating the tracer particles. The choice was made based on the properties of the oil and since it is a solvent for the fluorescent dye Rhodamine B. The dye used in the two-phase PIV technique is explained in section 5.7.2. The determination of the maximum particle diameter should guarantee a Stokes number smaller than 0.1 and be in accordance with the criteria of frequency response according to Melling [37]. Table 5.2 shows the calculated values:

<b>Particle</b>	$\rho_p$ ( $kg/m^3$ ) <sup>1</sup>	<b>Gas</b> ( $10^5 Pa$ )	$s$	$\nu$ ( $m^2 s^{-1}$ ) <sup>2</sup>	$f_c$ ( $kHz$ )	$S_k$	$d_p$ ( $\mu m$ )
<b>Propylene</b>	1198	Ar	928.7	2.08	1	0.05	0.96
<b>Carbonate</b>		(300 K)		$\times 10^{-6}$	10	2	0.30

Table 5.2 - Maximum particle diameter for propylene carbonate in air according to criterion developed in [37].

The production of the propylene carbonate particles suspended in the air is made by a piece of equipment called the Laskin generator. Figure 5.17 shows a schematic drawing of the principle of operation for these generators. The system consists of a tank with two intakes of compressed air and one outlet for the aerosol. Four closed-bottomed tubes penetrate the liquid inside the container, which is the oil that will form the aerosol. A circular disc is placed inside the container, forming an annular region between the disc and the inner wall of the container. Air is introduced by the inlet and bubbles are formed in the liquid through the holes in the submerged tubes. The shear stresses induced by the air jets form droplets of the liquid which are transported towards the outlet. Droplets larger than a certain diameter are blocked and the others are directed to the outlet. The flow rate of the aerosol is controlled by the valve in the second air supply of the generator. According to Raffel et al [32], oils generally produce distributions with an average diameter of about  $1 \mu m$ , which is sufficient for the use of propylene carbonate. For the Laskin generator used in these experiments, previous phase-Doppler interferometry measurements reveal a particle Gaussian distribution with a Sauter mean diameter of  $3 \mu m$ .

<sup>1</sup> 298,15 K. Data extracted from [67]

<sup>2</sup> 298,15 K. Data extracted from [67]

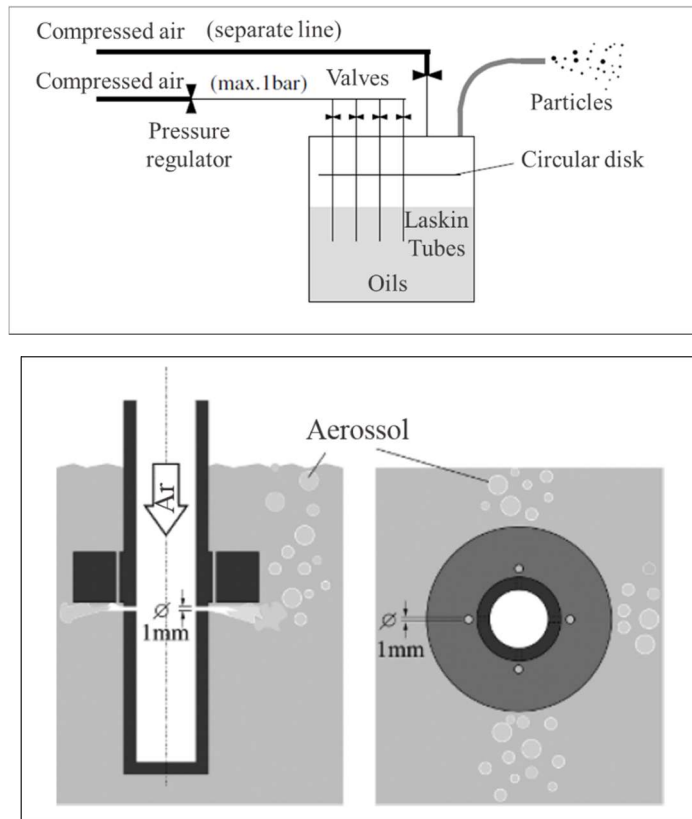


Figure 5.15 – Schematics of the working principles for Laskin generators. Adapted from [32].

Figure 5.16 illustrates the effects of the relaxation period and particle diameter on the relative velocity between the flow stream and the particle. The normalized relative velocity is the difference between the particle velocity and flow stream velocity normalized by the flow stream velocity,  $\frac{u_f - u_p}{u_f}$ . The relaxation period is calculated considering constant flow velocity and zero initial particle velocity. Equation 5.2 shows the relation between the relaxation period, particle response time and the normalized relative velocity.

$$\frac{u_f - u_p}{u_f} = e^{-t/\tau_s} \quad 5.2$$

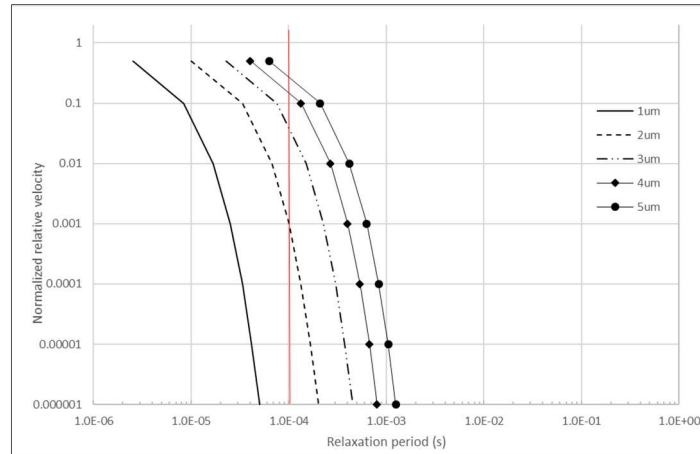


Figure 5.16 - Normalized relative velocity as a function of the particle diameter and relaxation period.

Although the hypothesis considered in equation 5.2 are restrictive, the results shown in Figure 5.16 provide an estimation of the ability of the particle to follow the flow. For example, consider the situation where the particle is subjected to a sudden flow acceleration. This force is translated to a relative velocity between fluid and particle. The time interval needed for the particle to achieve the new flow velocity is represented by the relaxation period.

Since the Laskin nozzle generates a particle size distribution rather than a unique particle diameter, it is important to evaluate the different response characteristics. Larger particles require longer relaxation periods. The difference between the size of the particles may affect the uncertainty of the velocity calculations. An estimation of these uncertainties is discussed in section 5.8.3.

In order to reduce the tracer particles path length and concurrently ensure a homogeneous mixing with the main flow, a device is designed to be installed at the entrance to IESC. The distance from the injection of the particles into the chamber is approximately 100 mm. This passageway allows the particle flow to enter the centerline of the pipe, which reduces oil deposits on the downstream walls and improves mixing with the air flow. Figure 5.17 shows a sketch of this device.

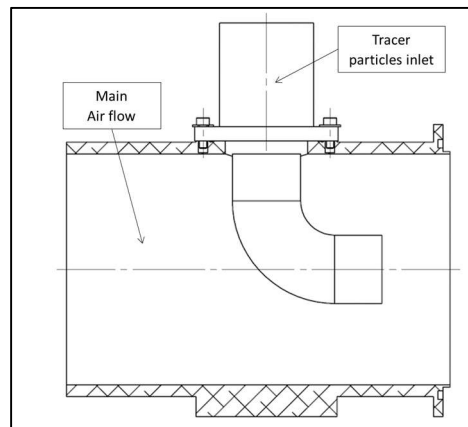


Figure 5.17 - Detail of the tracer particles inlet on IESC. The injection is performed at the center line of the main air flow pipes close to the optical access section.

### 5.7.1.2 Laser system

In this section, the system responsible for particle illumination is described. Lasers are equipment consolidated as light sources for use in PIV, mainly because of the capability of emitting monochromatic coherent light of elevated energy density. The light generated by the equipment can easily be transformed into a sheet of light, since it produces a light beam with low divergence.

The laser system used in the experiments of this project, model LDY 302 PIV, from Litron Lasers, is a diode pumped solid state laser (DPSS) with two cavities, which allows controlling and reducing the time interval between two consecutive pulses. The laser beam is generated by  $Nd^{3+}$  ions embedded in yttrium and lithium fluoride (Nd: YLF) crystals, allowing high energy pulses with repetition rates of up to 10 kHz [32]. The laser beam has wavelength  $\lambda = 527 \text{ nm}$  with 4.5 mJ of energy at 5 kHz. The system can operate with frequencies from 1 to 5 kHz in double-frame mode.

In the PIV technique there are three parameters of the laser system that must be adjusted according to the conditions of the experiment:  $f_l$ , the frequency at which each pair of laser pulses is supplied;  $\delta t_l$ , the duration of a single light pulse;  $\Delta t_l$ , time interval between the two pulses forming the pair. Figure 5.18 is an example of the laser event diagram in the acquisition of two pairs of images. The acquisition of images occurs at each produced light pulse. Therefore, for each pair of pulses, a couple of images is acquired. This pair is correlated to providing the velocity fields.

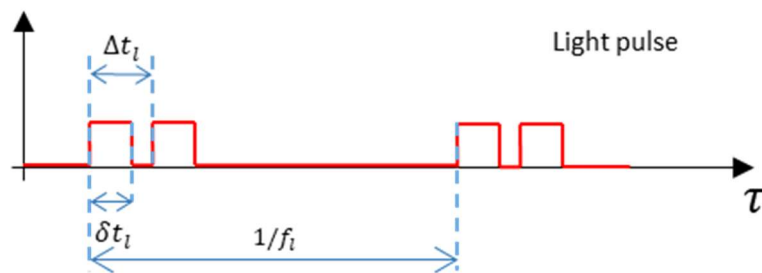


Figure 5.18 - Example of the event diagram for the laser system between two consecutive acquisition pairs.

The first of them,  $f_l$ , is related to the temporal resolution between the velocity fields. In the high speed PIV technique, the laser system acquisition frequency can reach 10 kHz, which results in a period  $\tau_l = 1/f_l$  of 100  $\mu s$  between two consecutive instantaneous velocity fields. In phenomena whereby the smallest time scales of the turbulence are greater than  $\tau_l$ , the measurements are said to be correlated (or resolved) over time. The width of the laser pulse ( $\delta t$ ), which is also related to the camera exposure time, will determine whether the particles will be recorded as points or lines. Ideally the particles should be recorded as if they were “frozen in time” ([32] [34]). With  $\delta t$  of the order of nanoseconds and flows with a velocity magnitude of the order of 100 m/s, the displacements will be very small - smaller than the spatial resolution of the camera for most experiments. For most laser systems, this requirement is well met.

The interval between two consecutive pulses,  $\Delta t_l$ , must be chosen according to the following characteristics:

- a. Perpendicular movement to the measurement plane. In 2D PIV, particles that cross the light sheet may not be visible in either image of the pair, depending on the time interval between them. This phenomenon is called loss-of-par and is a source of uncertainty for measurement [39] [32] [34]. In this case,  $\Delta t_l$  must be minimized.
- b. During the estimation of the velocity of the particles from the two consecutive images, they are assumed not to accelerate from one frame to another. The greater the  $\Delta t_l$ , the less appropriate the hypothesis is [32]. Second order effects, such as curvature of the particle trajectory between the images, are not taken into account, either.
- c. Considering a constant error of measuring the particle position in the image, the larger the particle displacement, the smaller the relative error is. Therefore,  $\Delta t_l$  should be increased to obtain greater displacements. However, large displacements may not respect the Nyquist theorem when performing the correlations. This restriction is discussed in section 5.7.1.4.

The use of laser beams for illumination depends on the set of lenses to transform the beam into a plane of light of small thickness. In the experiments with IESC, light sheets were formed from a three-lens set mounted in the same device. This set is formed by cylindrical lenses to allow constructing a light plane of constant height and minimum thickness according to the focal length of the last lens. The device can move the last lens relative to the other two lenses; this allows changing the position of the plane focal line. In this case, the focal length of the third lens is 500 *mm*. The height of the laser sheet is 50 *mm* and the thickness of the order of 1 *mm*. Figure 5.20 shows the arrangement of the lenses as well as the focal lengths of each lens and dimensions of the light sheet.

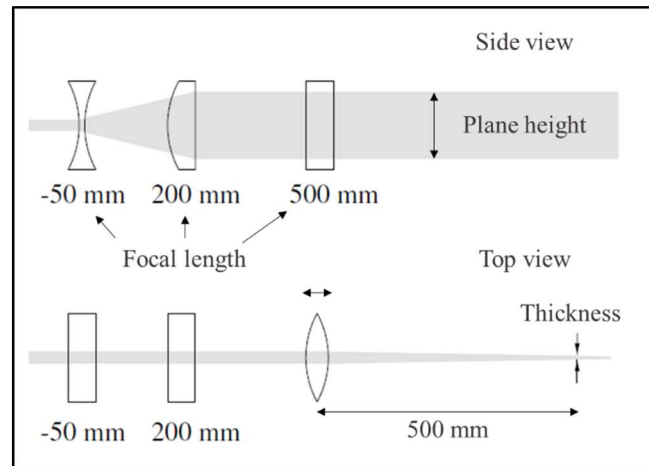


Figure 5.19 - Lenses set for the generation of the laser light sheet. Adapted from [32].

### 5.7.1.3 Image acquisition system

In order to perform the PIV technique with temporal resolution, in addition to the high repetition rate laser, a high frequency acquisition image capture system is required. In experiments with the IESC, the illuminated particles are recorded by a v311 model camera, from Vision Research Inc. This camera is equipped with a semiconductor complementary metal oxide sensor (CMOS). One of the advantages of this type of sensor is the possibility of defining only one sub region as active during the recording, allowing an increase of the acquisition rate in detriment to resolution [32]. The sensor contains an array of 1280 x 800 pixels of 20  $\mu\text{m}$  by 20  $\mu\text{m}$  in size and 12-bit dynamic range. At maximum resolution, the camera is capable of recording up to 3,250 fps (frames per second). The maximum frequency occurs at the lowest resolution of 128 x 8 pixels - 500,000 fps

Coupled to this camera is the Planar 1.4 / 50 ZF lens set, from Carl Zeiss, with a focal length of 50 mm and a minimum  $f_n$  number of 1.4. An 8mm ring extension - Nikon PK-11A is used to decrease the minimum focal length of the lens and to magnify the image obtained. Some particularities of the lens assembly should be considered for being used in the PIV technique. The choice of the number  $f_n$  (relation between the focal length and the shutter aperture diameter) directly affects two properties:

- The diameter of the particle image. It is important that the particles image diameters are kept small and well defined so that the images have high contrast and good definition. Differentiation of the background particles from the image directly affects the signal-to-noise ratio of spatial correlation peaks.
- Due to the low light-scattering efficiency of the tracer particles, it is generally necessary to use large aperture diameters to collect more light. However, larger apertures imply smaller depths of field (thickness of the region where the particles are recorded in focus). This becomes a significant problem in very small particle images [32]. Usually  $f_n$  is chosen as a compromise of focus depth, signal intensity and sensor exposure time. In cases in which the loss-of-pair plays a significant role,  $f_n$  is generally increased to resolve more particles with in-plane motion.

For the standard PIV, in addition to the set of lenses, a  $527 \pm 5 \text{ nm}$  bandpass filter is usually coupled to the lenses. This filter has the function of minimizing light interferences from other wavelengths coming from external lighting and other sources. For the case of two-phase PIV and applications with the presence of high density sprays, special aspects should be addressed. These characteristics are discussed in section 5.7.2.1.

#### 5.7.1.4 Image processing and cross-correlation estimations

This section presents the processing steps of the images captured during the operation of IESC to perform the standard 2D PIV. The cross-correlation method for the application of the PIV technique is briefly described. The procedures used in the pre-processing, the calculation of the velocity vectors and post-processing are also discussed. Additional processing steps required for applying the two-phase PIV technique are discussed in section 5.7.2.2.

As described previously, particle image velocimetry is a technique for estimating velocity by the estimation of the displacement of a particle or group of particles over a known time interval. The determination of the displacement vectors is treated statistically using cross-correlation methods. These are a measure of the degree of similarity between the correlated elements. In the case of the PIV technique, the intensity fields of the images resulting from the illumination of the tracer particles in the flow are correlated. These intensity fields are represented by an array of pixels - the value of each pixel is the value in the gray scale. The discrete cross-correlation function is shown on equation 5.3. It represents the cross-correlation between two pairs of images for single exposure / multiple frame PIVs (For further details on the formulation - Chapter 3 of [32]).

$$R_{II}(x, y) = \sum_{i=-K}^K \sum_{j=-L}^L I(i, j)I'(i + x, j + y) \quad 5.3$$

Where  $I$  is the matrix of the intensity values of an interrogation window from the first image and  $I'$  for the image of the next registered time instant. Figure 5.20 shows the process graphically.  $I'$  is shifted around the first region without exceeding the limits. For each position, the sum of all multiplications pixel-by-pixel corresponds to a value  $R_{II}$ . For the shifts in which the regions align, the value of  $R_{II}$  will be the maximum. This position is then used as an estimate of the image particles displacement.

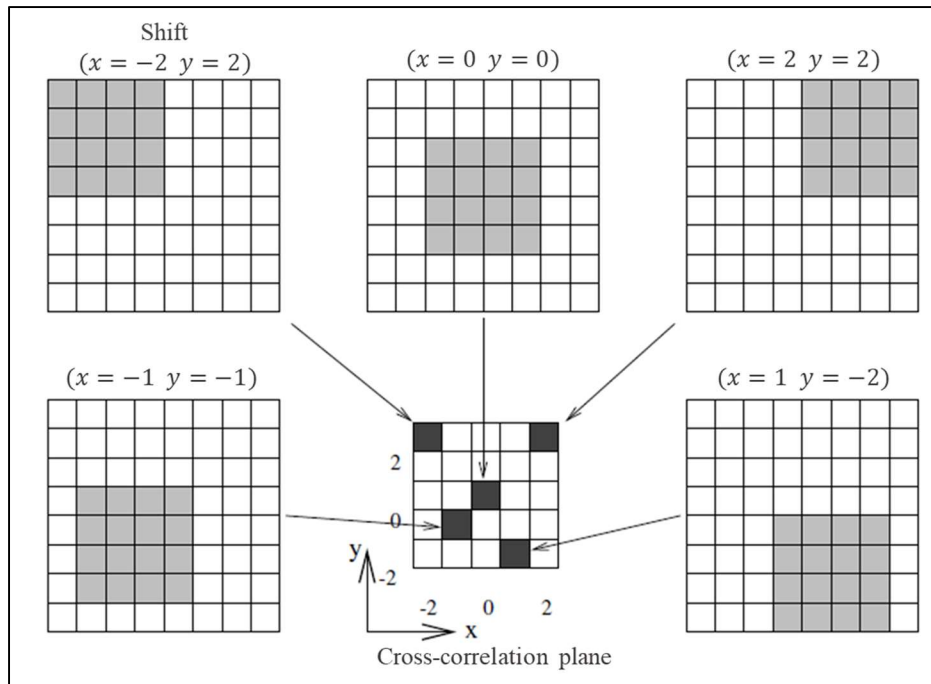


Figure 5.20 - Graphic illustration of the cross-correlation operation between two images. Adapted from [32]

An important observation is that the method is only capable of recovering the linear displacement between two regions. Any information about the curvature of the trajectory or acceleration between the two frames is lost. Thus, the size of the interrogation window should be small enough to ensure that the second order effects can be neglected.

Another disadvantage of the method formulated in the spatial domain is the computational cost. The shift procedure from one region to the other must be performed for each interrogation window that subdivides the images. Since these windows must be small, the number of operations for each pair of images is enormous. For this reason, cross-correlation is computed in the frequency domain. Using the correlation theorem, in which the cross-correlation of two functions over time is equivalent to the multiplication of the complex conjugate of the respective Fourier transform, the computational cost decreases considerably. If discrete Fourier transform algorithms are used, such as the fast Fourier transform - FFT, the number of required operations can be reduced from  $O[N^2]$  to  $O[N \log_2 N]^3$  [32]. However, the use of the Fourier transform assumes some

<sup>3</sup> Although the notions given in Raffel et al [32] are described for one-dimensional functions, the conclusions are also valid for two-dimensional functions (which is the case of a field of intensity of an image).

hypotheses that must be taken into account. An important hypothesis is the periodicity of the signals. The application of the Fourier transform requires that the signals have infinite domains. The use in finite domains is possible assuming that the signal is periodic. One consequence is the aliasing phenomenon.

If the images are considered periodic, the cross-correlations will also be. Thus, the Nyquist theorem must be respected. In this case, the displacement within a sample of size  $N$  must be smaller than  $N / 2$ . In practice the intensity of the peak correlation decreases with an increasing displacement [32]. Therefore, a common strategy is to limit the displacement of the particles to a quarter the size of the interrogation window - the so-called one-quarter rule. This parameter is controlled by decreasing the interval between consecutive images ( $\delta t$ ) or increasing the size of the window.

The first step in pre-processing is the removal of the static background image. The presence of objects in the image of the flow can cause reflection of the incident laser light, introducing noise in the calculation of the correlations. In this case the background image is removed by averaging the intensity fields for a large number of samples and subtracting it from the original images. This procedure was performed in the Dynamic Studio software - Dantec Dynamics A / S. Figure 5.21 shows an example of the process.

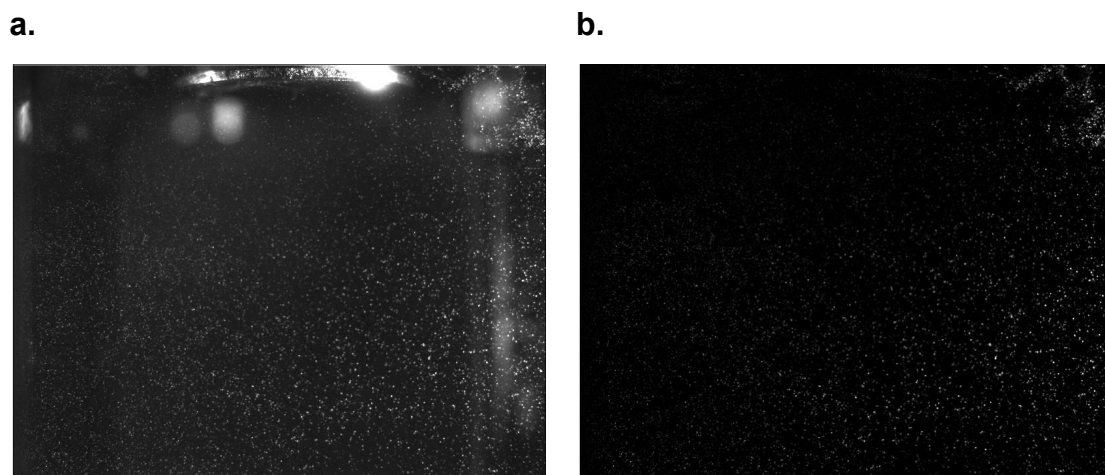


*Figure 5.21 - Example of pre-processing for background subtraction. Figure to the left is the acquired image. On the right is the resulting image after background subtraction*

After the first step, the images undergo a routine of uniformization of the field of intensities. Since the light plane crossing the flow does not cause uniform scatter intensity throughout the image, the values of the cross-correlation coefficients will be more influenced by the brighter particles than by the weaker particles. This balancing subroutine, which is established in the Dynamic Studio program, is used in this step. This is a two-step process. In the first one, a balancing map is constructed from factors extracted from the image set. Then this map is applied to each image [34]. Figure 5.22 is an example of the process.

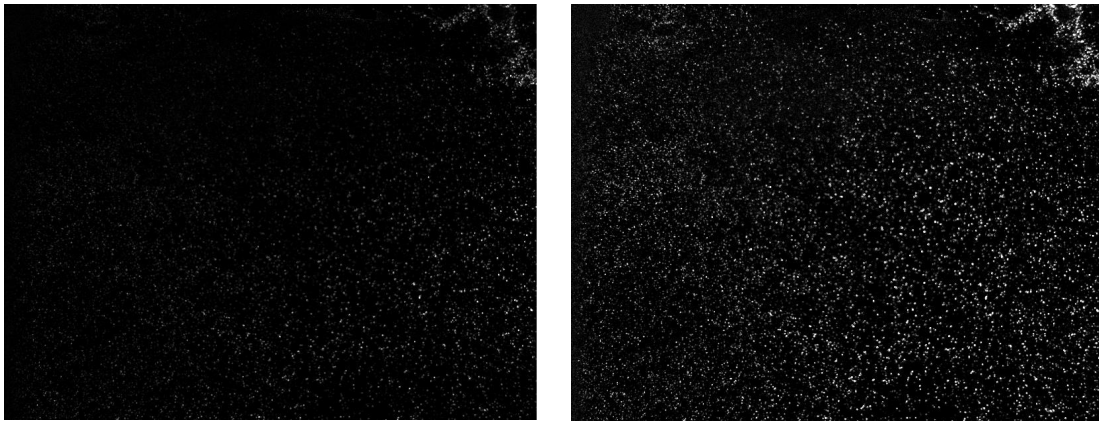


*Figure 5.22 - Example of the pre-process operation for balancing the pixel intensity fields. Figure to the left is the image after background subtraction. Figure to the right is the result of the image balancing operation.*

Finally, the balanced images pass through a filter that limits the maximum and minimum values in the grayscale scale. For example, as the particle images have low intensity, the maximum values in the gray scale do not exceed 40 (value from 0 to 255 for an image with 8-bit depth). Therefore, values above the limit in the set of images will be replaced with the limit, which in this case was used as 40.

After the pre-processing step, the velocity vectors are calculated with the algorithms based on cross-correlation in the frequency domain. The algorithm used in this project is based on an adaptive method in which the size and format of the interrogation windows are modified iteratively according to the local density of tracer particles and velocity gradients.

In the standard PIV method, cross-correlation is calculated using fixed size interrogation windows, thus assuming the hypothesis that the particles within the interrogation window move uniformly. In most cases, this condition is not verified. As a consequence, there is an increase in the cross-correlation peaks representing the displacements between the image pairs, which contributes to

the measurement uncertainty. In the adaptive method, the deformation of the interrogation windows reduces the loss of pairs for calculating the correlation, since its shapes changes to accommodate the different displacements of the particles from the initial area. Moreover, in the adaptive method the spatial resolution is up to two times as great as in the traditional method [28]. The method sequence occurs as follows:

- **Step 1:** Each image pair is pre-processed and subdivided into interrogation windows.
- **Step 2:** To reduce leakage, windowing functions are applied to the interrogation areas (IA) for the use of algorithms in the frequency domain. Additional filters are also applied to the signal.
- **Step 3:** The velocity vectors are computed iteratively. At each step the size and format of the interrogation window is modified according to the process control parameters. The cross-correlation field is firstly evaluated as a function of two factors: the field signal-to-noise ratio and peak height ratio. The displacement is rejected if the signal-to-noise ratio and peak-to-noise ratio is smaller than the predetermined value.

In each iteration a spurious vector detection algorithm is used - each vector is analyzed in comparison with its neighbors. The rejected vectors are replaced with an interpolation of the neighboring vectors. A filter is also applied to the velocity field to reduce propagation of errors between iterations.

- **Step 4:** At the end of the iterative process, the spurious vector detection algorithm and interpolation with neighbor vectors are utilized again

As stated earlier, algorithms based on Fast Fourier Transform (FFT) assume that the signals are periodic. Thus, when defining the image interrogation areas, the borders must be treated with care, since the loss of pairs and the cyclic behavior can influence the value of the calculated velocity. These problems are treated by applying window functions in the first iteration, which modify the weight given to the particles near the border and near the center of the interrogation area. In this work, a Gaussian window was used - a compromise between signal strength and cyclic behavior noise. For more details on the windowing function, the reader is referred to [40] [32].

A filter is also applied during the use of FFT algorithms. While the window is performed over the spatial domain, the filter is applied to the frequency domain. The use of a Gaussian low pass filter reduces the high frequency components, which can broaden the cross-correlation peak and thus reduce the pixel locking effect.

The control parameters of the iterative method are determined by two factors: Local particle density and velocity gradients. In the first, the interrogation window modifies its size until it reaches the desired local density of particles in the area. The approach to calculate the local density and the minimum volume of particles is adjustable. In the second factor, the interrogation window deforms according to the velocity gradients calculated from previous iterations. This process is controlled by limiting the modules of each gradient individually and the effect of the set of four gradients. The gradient modules in absolute values should be smaller than 0.1 individually and  $\sqrt{U_x^2 + V_x^2 + U_y^2 + V_y^2}$  must also be smaller than 0.1.

At the end of each iteration step, the cross-correlation field is evaluated as a function of two parameters: signal-to-noise ratio(SNR) and peak-height ratio. The signal-to-noise ratio is the relationship between the intensity of the highest correlation peak and the rms value of the negative correlation peaks, which represent the noise. For measurements with the IESC, the values for the SNR ratio greater than 6 have been used for the peak validation. For the peak height ratio, which is the ratio of the intensity of the highest peak to the second peak, its value must be greater than 1.2 for displacement validation [40].

The average displacement of the interrogation window is calculated by considering the position of the maximum cross-correlation peak. As the captured images are discretized according to pixel positions, the displacement can only be determined in integer pixel values, which would imply fixed spatial resolution of  $\pm 0.5$  pixel. However, the position of the correlation peak can be determined more precisely if the peak is approximated by some function. This type of strategy is called sub pixel level analysis. A common practice is to approximate the peak correlation by a Gaussian function, mainly because images of point particles are described by Airy functions. These in turn are well represented by Gaussian functions [32]. In the algorithm used in this work, the position at the sub pixel level is estimated by a 9-point Gaussian estimator [40]. However, care must be taken during the sub pixel level interpolation since it is directly linked to the pixel-locking phenomenon [34].

After the validation of the cross-correlation fields, the vectors are tested by the Universal Outlier Detection algorithm [41]. The operating principle is based on the median test of the analyzed vector when comparing it with the median of the neighbor vectors:

$$|U_{2D}(med) - U_{2D}(i, j)| < \varepsilon_{lim} \quad 5.4$$

The size of the neighborhood and  $\varepsilon_{lim}$  (test limiting value) are pre-defined by the user. When the test is normalized by the median of the residues  $r_i$ , where  $r_i = |U_i - U_{med}|$ , a single value of  $\varepsilon_{lim}$  can be used to effectively detect spurious vectors. The method as proposed by Westerweel and Scarano [41] is defined as:

$$\frac{|U_{2D}(med) - U_{2D}(i, j)|}{r_{med} + \varepsilon_0} < \varepsilon_{lim} \quad 5.5$$

Where  $r_{med}$  is the median of residues  $r_i$  and  $\varepsilon_0$  is a factor to account fluctuations in correlation analyses. In practice the value of  $\varepsilon_0$  will correspond to the mean value of the noise level in the PIV measurements - between 0.1 and 0.2 *pixel* [32]. In the measurements with IESC, a vector neighborhood of 5x5, with a limiting value of  $\varepsilon_{lim} = 2.0$  and a fluctuation value  $\varepsilon_0 = 0.1$  are used, as recommended by [41]. Figure 5.23 shows an illustration of a neighborhood of 5x5 vectors to be analyzed with the algorithm.

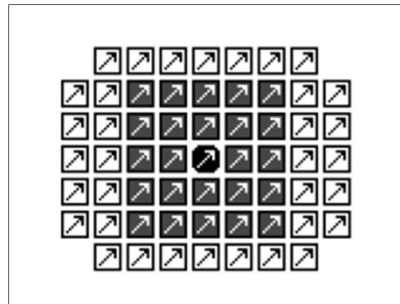


Figure 5.23 - Neighborhood of 5x5 vectors used in the universal outlier detection algorithm. The central vector is the vector under analysis. The gray vectors correspond to the neighbors of the central vector. [34]

When static features are present in the acquired images, this specific region should be properly treated. Even with the removal of the background image, the position where feature was present does not contain information about particle displacement, see for example Figure 5.24. The presence of this region in the cross-correlation calculations introduces uncertainty and noise in the velocity calculation. Therefore, this wall region must be removed or hidden from the image. However, if no special treatment is used in the regions near this wall, the calculated velocity will be higher than expected. This deviation occurs for interrogation windows containing the wall region. The particles distant from the wall, which are faster, have more influence on the correlation than the nearest particles and thus increase the velocity estimation on the interrogation window [40].

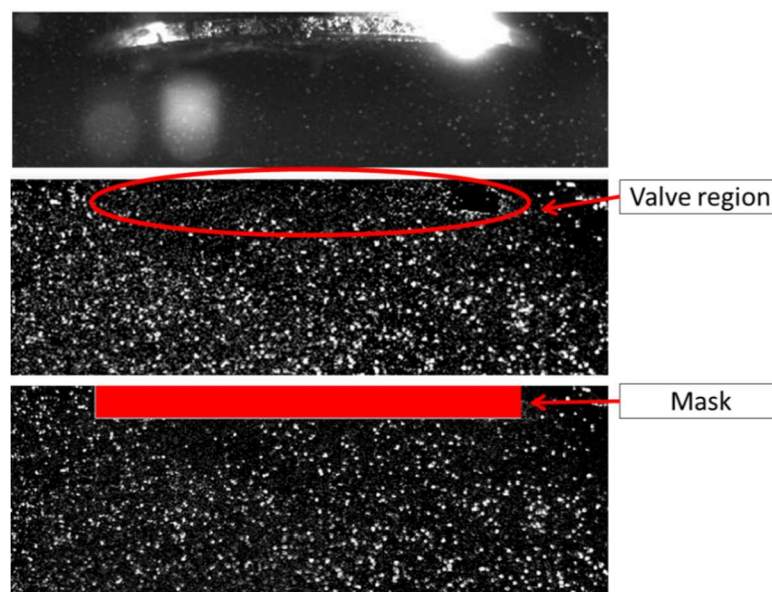
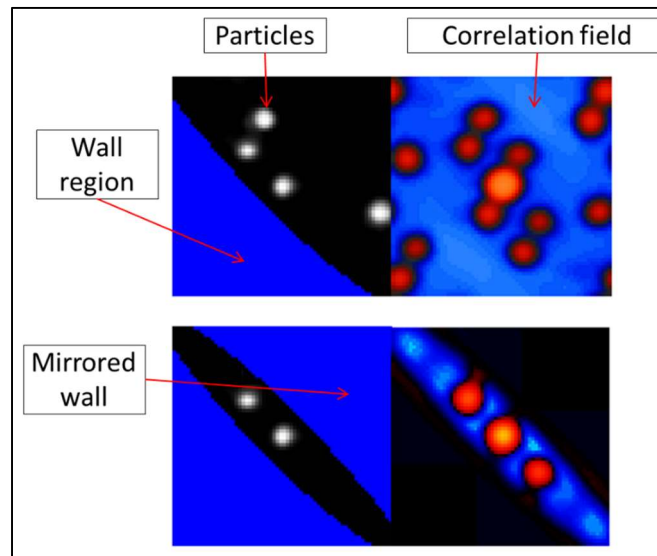


Figure 5.24 - Mask filter application to the region where the valve was present. The upper image shows the position of the valve in the image. In the middle figure, the region where the valve was located after pre-processing is highlighted. This region must be removed from the correlation calculations. The application of this mask (bottom image) defines the region where the wall treatment will be used.

One way to overcome the problem is to arrange the wall region symmetrically in the interrogation window, as shown in Figure 5.25. Therefore, the particles contained in the interrogation windows are symmetrically distributed in relation to the center of the interrogation area. Note, with the use of this method, the interrogation window may contain no particles depending on the particle density near the wall. These regions usually contain less particles due to the normal velocity gradient.



*Figure 5.25 - The use of the wall function in the adaptive PIV method [40]. The upper figure represents the area designated as the wall (in blue) and its correlation field. In the lower figure, the wall function is used. The symmetrical arrangement of the wall results in the field of correlations as shown in the lower right figure.*

With the brief statements of all the features and parameters that have significant influence on the velocity estimations by the standard PIV technique, the next section discusses the differences and additional aspects needed to perform the two-phase PIV technique. No common characteristics are mentioned in the next section since they were discussed in this section.

### 5.7.2 Two-phase particle image velocimetry (Two-phase PIV)

As seen in section 3, the concept of the two-phase PIV technique is the separation of flows present in the same sequence of images for the application of PIV algorithms. The flow phase separation can be conducted with post-treatment techniques, such as separation by intensities [3] or using different tracer particles for each flow [19]. For this research, the aim is to separate the spray evolution from the air flow. For some sprays, droplets may become natural tracer particles of the flow. In the case of air, an introduction of artificial particles is required, as described in section 5.7.1. Phase discrimination is achieved by doping artificial particles with a fluorescent substance. This substance is chosen by its laser light absorption properties and subsequent emissions in other wavelengths.

For this research project, the selected fluorescent substance was Rhodamine B. This dye is dissolved in propylene carbonate and the mixture is used to produce an aerosol with air as described in section 5.7.1.1. Figure 5.26 shows the absorption and emission spectra of rhodamine B. The absorption peak occurs at 542.75 nm, and the emission peak occurs at 565 nm. Also shown in the figure is the wavelength of the incident laser light, 527 nm. To enhance the distinction of the two phases, two cameras are used. One camera receives the light scattered by the droplets of the spray, which occurs at the laser wavelength. The other camera should only see the energy that fluoresces from the rhodamine B particles that represent the air flow. Using a long-pass optical filter, this camera should only be sensitive to wavelengths greater than 570 nm, thereby eliminating all laser light scattered by the spray. Thus, all the characteristics discussed for the PIV technique also apply to the two-phase PIV, since the separation of the flows happens before the application of the PIV algorithms.

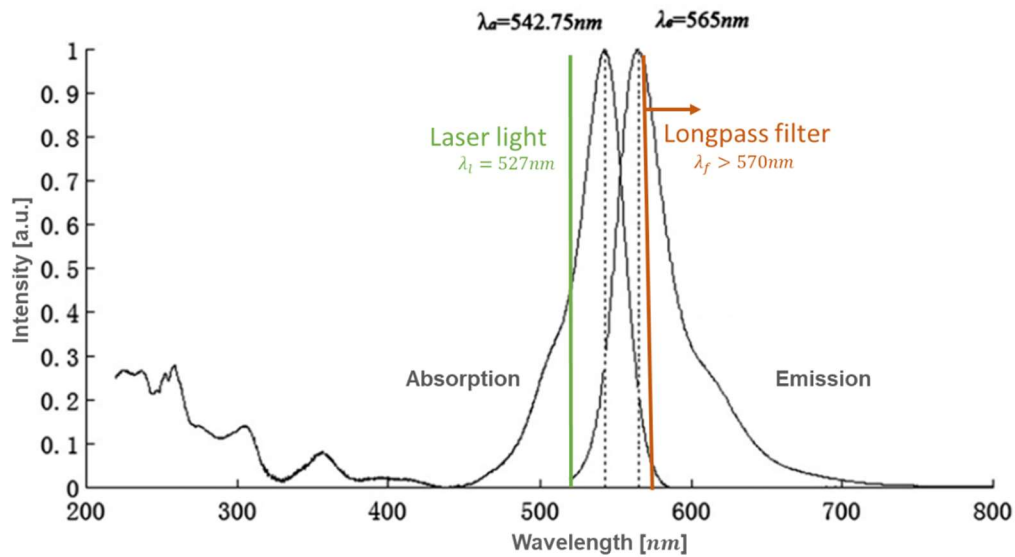


Figure 5.26 – Emission and absorption spectra of rhodamine B dissolved in ethanol. The green vertical line indicates the incident laser wavelength. The orange line represents the cut-off wavelength of the longpass filter used on the cameras. Adapted from [42].

### 5.7.2.1 Optical filters for two-phase PIV

The application of the proposed two-phase PIV technique on the experiments with ethanol DI sprays proved to be a challenge. The difficulties increase considerably mainly by two experimental conditions. The first factor is the spray density. DI multi-hole injectors are designed to produce compact and fast sprays. When these sprays are subjected to laser light sheets, most incident energy is scattered in the measurement volume. This creates a limitation on laser intensity and cameras sensitivity. The second factor is the fluorescence efficiency of the tracer particles. In some conditions, the Mie-scattered energy is about 60 times as high as the fluorescence signal [19]. With this low efficiency, incident laser energy should be high enough for the signal to be registered by the fluorescence camera. In the case of a continuous flow, the amount of necessary energy is even higher. Due to the lower particle residence time on the field-of-view, the fluorescence efficiency is lower when compared to quiescent environments.

A trade-off combination of laser light intensity, dye concentration and camera aperture have to be achieved to perform the measurements. The combination must allow enough energy to excite the fluorescence camera sensors but at acceptable levels for the camera that registers the spray Mie-scattering. These specific conditions demands optical filters with high performance on the rejection band, especially the longpass filters that should attenuate a significant amount of laser energy. In this case, a set of longpass filter were selected. This set was designed to reject most energy in the laser wavelength by reflection on a dichroic filter. The residual unwanted energy is filtered by the absorption filter sequence. Figure 5.27 shows an illustration of the filter set project. The first tilted filter, Brightline® Di02-R32 from Semrock Inc, is a dichroic beamsplitter with an optical density (OD) of 6 on the rejection band and a cut-off wavelength of 532 nm. The light angle of incidence is specified by the filter manufacturer. The next filters shown are longpass absorption filters. Following the sequence: RazorEdge® LWP Filter OD5 532 nm from Semrock Inc, Longpass OD4 570 nm generic filter and Longpass OD3 570 nm generic filter.

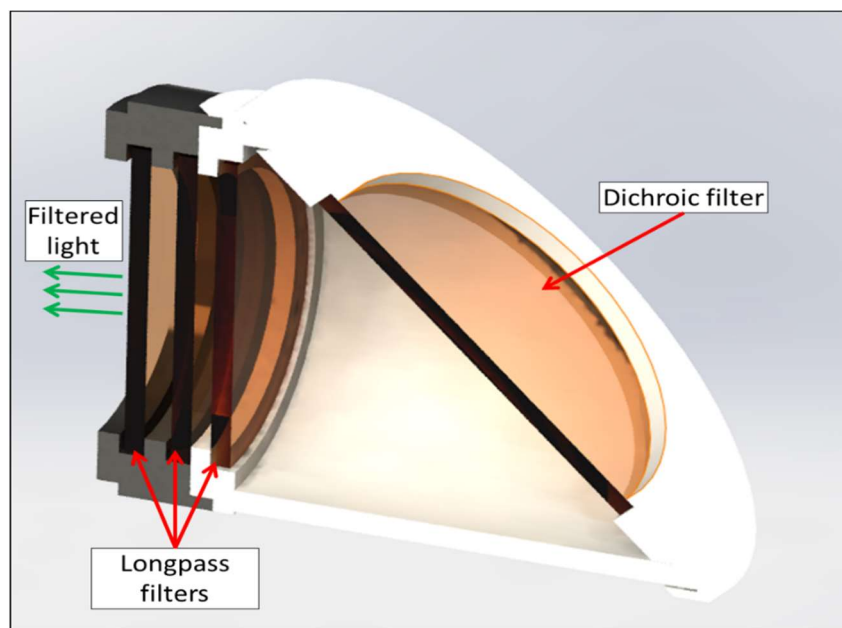


Figure 5.27 - Illustration of the filters assembly section view. The use of a set of filters was required due to the high levels of energy scattered from the spray during illumination.

For the case of the camera registering the Mie-scattering of the spray, another set of filters was selected – a bandpass filter centered at  $527 \pm 5 \text{ nm}$  was used together with neutral density filters for attenuating the visible spectra. Resultant optical density of 2 was obtained with the set.

### 5.7.2.2 Image enhancement for air vector field calculations

To enhance the separation between air field and spray, more image processing steps are necessary. For the fluorescence camera, a small contribution of the spray remains visible even by using the filters set. To overcome the problem, the images of both cameras are used simultaneously. Figure 5.28 shows the sequence of operations for enhancement procedure for the fluorescence images of the tracer particles. For the seeding particles raw images, a background subtraction is performed using the temporal mean of images acquired without the presence of spray and in the same measurement conditions. The same set of images is used to remove the background of the spray camera images. The next operation is the shift of the spray images coordinates to account for slight deviations between the fields of view of the different cameras. An image threshold is then performed to eliminate possible Mie-scattering signals from the air tracers. These images are used to remove the presence of spray in the seeding images with a subtraction operation. The resultant images are then processed using the standard procedure described in section 5.7.1 – operations of signal balancing, masking treatment of static walls and adaptive PIV algorithms.

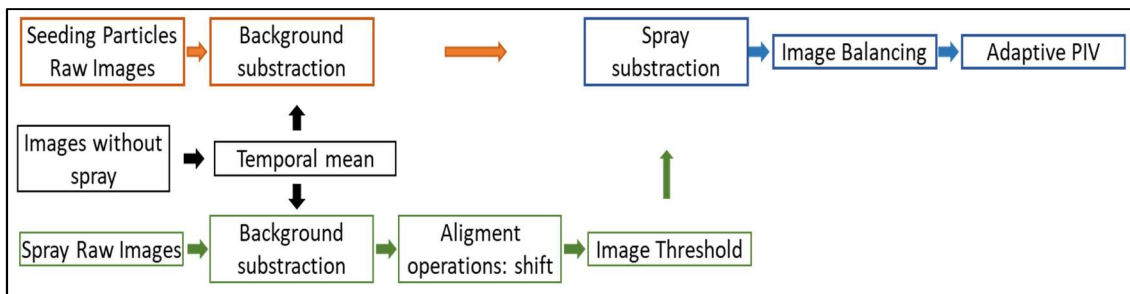
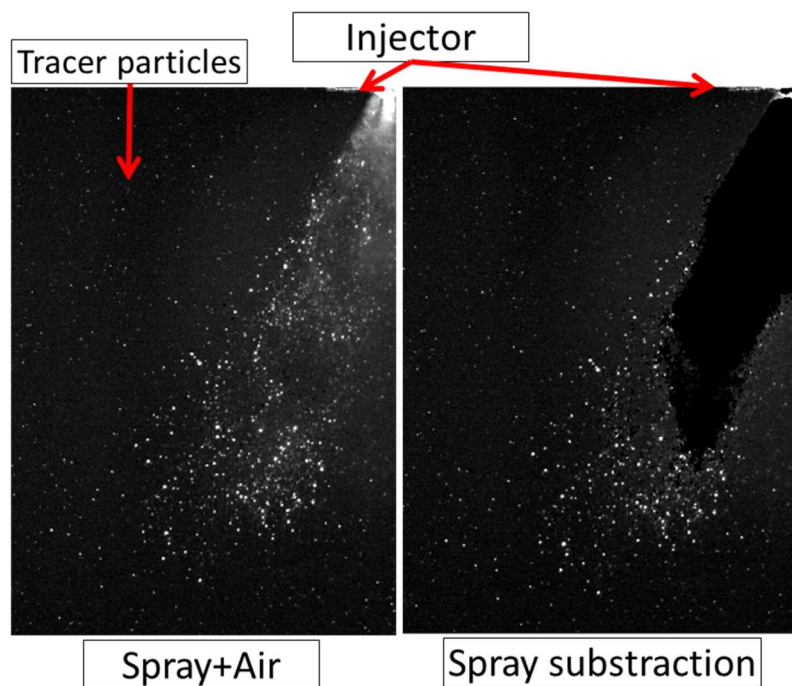


Figure 5.28 - Sequence of steps performed to enhance the velocity calculation for air field with adaptive PIV algorithm. The presence of spray in the fluorescence images is removed by subtraction of the synchronized Mie-scattering camera.

Figure 5.29 shows an example of the results from the enhancement procedure prior to the image balancing step. Figure allows observing the area occupied by the spray is shown by black values. Unfortunately, the region near the spray boundary is a highly active zone and the enhancement procedure cannot separate all droplets and clusters of ethanol from the spray particles. Many aspects can explain such difficulties, for example, time scales differences between spray and air, spatial resolution on the shear layer and light multi directional scattering. Therefore, this region should be evaluated with care during the analysis of the results. Nevertheless, the enhancement process and the information of both cameras allows improving the velocity estimations when compared to analysis without the proper treatment.



*Figure 5.29 - An example of the image enhancement procedure to remove remaining spray plume signals from the fluorescence images. The resultant images were used to perform the adaptive PIV algorithm.*

To perform the subtraction between the images of the synchronized cameras, it is important to describe the especial attention that should be paid during the acquisitions. These precautions are necessary since the subtraction is performed over the pixels intensity levels. First of all, the alignment of the camera should ensure field-of-views at the same spatial position in both cameras. Moreover, the same spatial resolution should be achieved for the pair. To ensure these requirements, a tailor-made image target was projected.

Figure 5.30 shows the illustration of the target. It consists of a transparent square-and-dot calibrator mounted on the alignment stand. This stand ensures a concentric assembly with the exit of IESC and a fixed known height of the calibrator center. Two features located on the calibrator mounting allow the alignment of the light sheet with the measurement plane and relative position between laser and cameras.

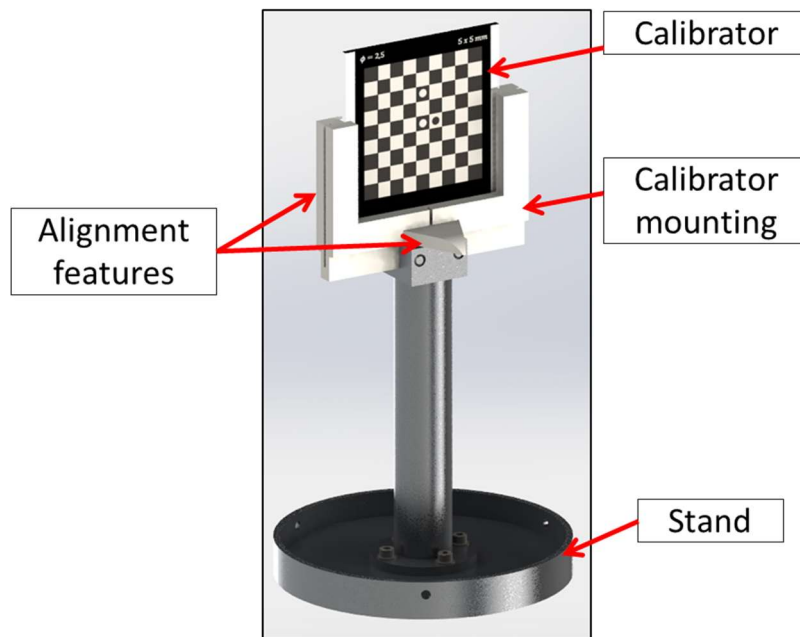


*Figure 5.30 - Tailor-made transparent target used to ensure the same field-of-view and resolution of the synchronized cameras.*

Figure 5.31 shows an example of calibration images to illustrate the procedure of spatial coordinates and spatial resolution match. The right image shows the position of the cameras and laser for the two-phase PIV measurement on IESC. The cameras are iteratively modified in order to maintain the same spatial coordinates in the respective field-of-views. At each modification, the cameras are refocused and the resolutions are verified. The procedure stops when the coordinates difference between cameras are of the order of 2 pixels and the pixel spatial resolution does not deviate by more than 5%.

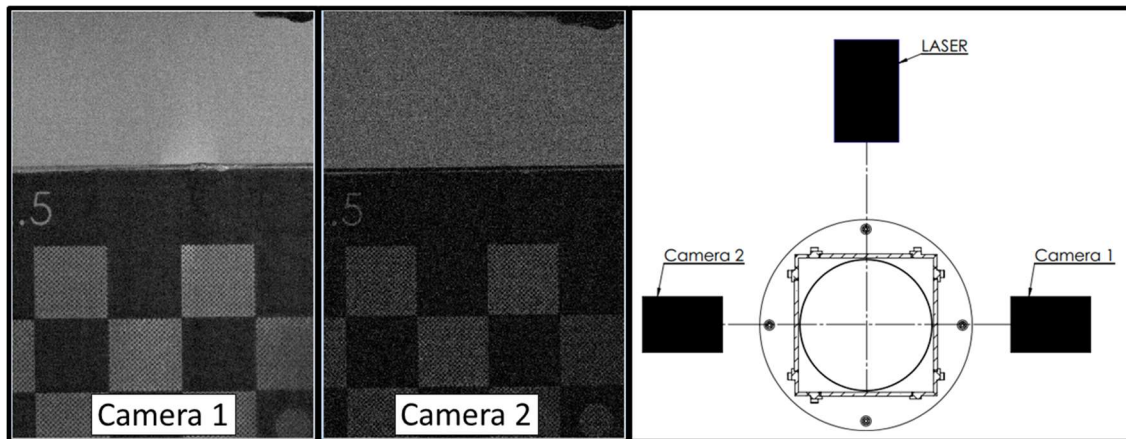


Figure 5.31 - Example of image calibration for spatial coordinates and magnification corrections between cameras.

The second critical point to the image subtraction is the threshold operation on the spray plumes. Since this operation depends on the choice of the limits, the size of the region the spray occupies on the image is also choice-dependent. In order to attenuate the problem, different threshold limits are tested until the visualized results have no significant variation. An advantage of this particular setup is the intensity difference between spray and tracer particles. Since the scattered signal from the sprays has higher intensity, the separation of background and spray can be performed with reasonable accuracy. Therefore, a low influence of thresholding is expected on the subtraction operations.

### 5.7.3 Velocity estimation by multiple planes acquisition

As described in section 5.7.2, the two-phase PIV technique devised for the air-spray interaction experiments is a 2D measurement technique. Due to geometrical features of IESC and time limitations, the technique could not be expanded to the acquisition of the third velocity component. Nevertheless, an approach to estimate the 3D velocity field of the stationary flow was designed and applied to IESC. This estimation is aimed to assess the magnitude of in-plane motion and its effects on the 2D velocity calculations.

The 3D velocity estimation technique is based on acquiring consecutive velocity planes. This set of 2D velocity fields is used to estimate the third velocity component by applying the continuity equation at each point of the measured planes. For a generic fluid element, the mass conservation or continuity equation can be written as in equation 5.6 [43]:

$$\frac{\partial \rho}{\partial t} + \nabla(\rho u) = 0 \quad 5.6$$

For incompressible stationary flow, the continuity equation can further be simplified. Figure 5.32 illustrates the respective fluid element considering incompressible stationary flow. The mass flow rate is accounted across the faces of the element and is described by terms at each boundary.

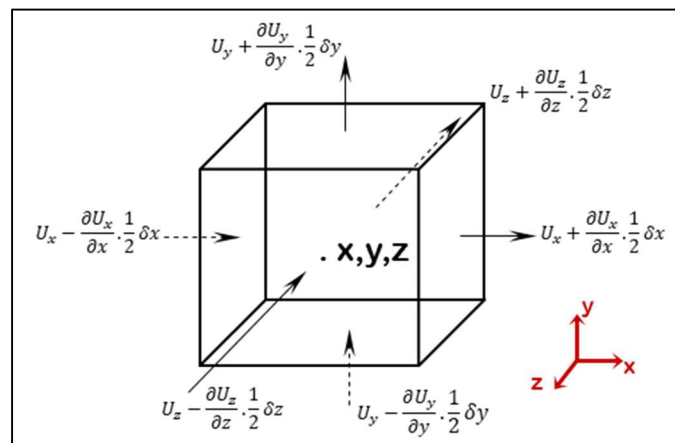


Figure 5.32 - Mass flow balance model for an incompressible stationary flow.

In this case, the mass conservation equation is independent of the non-zero fluid density:

$$\frac{\partial U_x}{\partial x} + \frac{\partial U_y}{\partial y} + \frac{\partial U_z}{\partial z} = 0 \quad 5.7$$

Where  $U_x$ ,  $U_y$  and  $U_z$  are the velocities in the coordinate system of Figure 5.32. The equation now can be rewritten in terms of variation of  $U_z$  over the  $z$  direction:

$$\frac{\partial U_z}{\partial z} = - \left( \frac{\partial U_x}{\partial x} + \frac{\partial U_y}{\partial y} \right) \quad 5.8$$

Using the approximation for  $\partial U_z / \partial z$ ,

$$\frac{U_{z,k} - U_{z,k-1}}{z_k - z_{k-1}} = - \left( \frac{\partial U_x}{\partial x} + \frac{\partial U_y}{\partial y} \right) \quad 5.9$$

Where  $k$  denotes the  $z$  coordinate of the measured plane. Finally, in terms of  $U_{z,k}$ ,

$$U_{z,k} = U_{z,k-1} - (z_k - z_{k-1}) \left( \frac{\partial U_x}{\partial x} + \frac{\partial U_y}{\partial y} \right) \quad 5.10$$

With equation 5.10, the third velocity component can be estimated by calculating the velocity variation over their respective coordinates.

The first derivative terms  $\partial U_x / \partial x$  and  $\partial U_y / \partial y$  are estimated using the five-point central-difference formulation [44] in fourth-order accuracy for a uniform spacing grid:

$$\frac{\partial U}{\partial x_i} = \frac{U_{i-2} - 8U_{i-1} + 8U_{i+1} - U_{i+2}}{12\Delta} \quad 5.11$$

Where  $i$  denotes the position index and  $\Delta$  the grid spacing. Figure 5.33 describes the positions of the elements used in the five-point differentiation scheme.

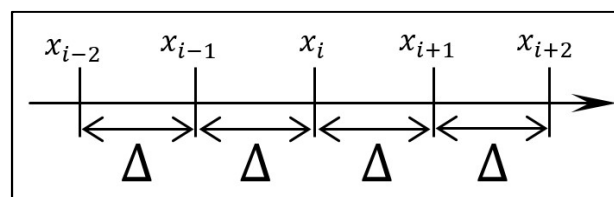


Figure 5.33 - The model to describe the five-point central-difference formulation for the first derivative.

From equation 5.11, note that the discretization considers a uniform spacing between the elements. For the case of the acquired PIV velocity fields this condition is already satisfied.

For elements near the boundaries of the sample space, the first derivatives are discretized as:

$$\frac{\partial U}{\partial x_i} = \frac{U_{i-2} - 4U_{i-1} + 3U_i}{2\Delta} \quad 5.12$$

$$\frac{\partial U}{\partial x_i} = \frac{-3U_i + 4U_{i+1} - U_{i+2}}{2\Delta} \quad 5.13$$

Considering equations 5.10 and 5.11, the third velocity component can be estimated with the acquisition of consecutive planar velocity fields. These 2D fields are acquired with standard TR-PIV technique described in section 5.7.1.

## 5.8 Uncertainty analyses

This section presents the uncertainty estimations of the three main quantities used in this work: the air mass flow rate, the injection pressure and the PIV velocity estimations. All the estimations are based in the recommendations of the Guide to the Expression of Uncertainty in Measurement (GUM - 1<sup>st</sup> Brazilian edition, 2008 [45]).

For each measurand, the Type B uncertainties are quantified. The Type B are those obtained by non-statistical procedures. They may include [45]:

- Data obtained from a calibration certificate.
- Scientific judgment.
- Manufacturer specification.
- Experience and personal judgment in the relevant phenomena.

The standard uncertainty of a given quantity  $y$  is calculated with equation 5.14:

$$\mu^2(y) = \sum_{i=1}^N \left( \frac{\partial f}{\partial x_i} \right)^2 \mu_i^2(x_i) \quad 5.14$$

Where  $f$  is the function describing the relation between the output  $y$  and the inputs  $x_i$ . The partial derivatives are called the sensitivity coefficients. The equation requires independence between the different inputs  $x_i$ . Although this condition is not always satisfied, the hypothesis greatly simplifies the estimations. To the purpose of this works, the hypothesis is satisfactory and the shown equation is used in all the uncertainties estimations.

### 5.8.1 Air mass flow rate

The inlet air mass flow in the experiments is a function of the measured volumetric air flow and of the fluid density. Equation 5.15 shows the relation.

$$\dot{m} = \rho \cdot \dot{V} \quad 5.15$$

Since there is no compressibility effects and the pressure loss across the IESC remained between 1 to 10 *mbar* in the experiments, the air density is only function of temperature. A linear curve is fitted in the values found in the literature [46] [47]. The following expression is used:

$$\dot{m} = (-4.38 \times 10^{-3} \cdot T + 1.2878) \cdot \dot{V} \quad 5.16$$

Where  $T$  is the measured temperature in °C. Thus, the standard uncertainty of Type B for the air mass flow rate is calculated using equations 5.14 and 5.15.

$$\mu_{\dot{m}}^2 = 19.18 \times 10^{-6} \cdot \dot{V}^2 \mu_T^2 + (19.18 \times 10^{-6} T^2 + 11.25 \times 10^{-3} T + 1.65) \mu_{\dot{V}}^2 \quad 5.17$$

Where  $\mu_t$  is the uncertainty of the temperature measurement and  $\mu_{\dot{V}}$  is the uncertainty of the volumetric flow measurement.

The air supply system is described in the section 5.5. The measurement instrument for the volumetric flow rate is a turbine gas meter, serial number IB-2055, model SMRIX G400 manufactured by Instromet. Since the supply lines were design with the recommendations of the manufacturer, the only source of uncertainties is the instrument calibration. The calibration certificate number 160 072-101 from 08/09/2017 states an expanded uncertainty of about  $\mu_{\dot{V}} = 0.33\%$  in the range of 33 – 650  $m^3/h$ .

The air flow temperature is measured with a thermocouple placed concentric to the supply line. The EC 584-1 complied, type T, class 3 thermocouple has a maximum permitted uncertainty  $0.5^{\circ}\text{C}$  for the range between  $0 - 100^{\circ}\text{C}$ . The measuring position and the heat transfer between the probe and air flow are sources of uncertainties. To reduce the uncertainty due to these effects, the following recommendations described in [48] were used :

- $\downarrow$  conduction :  $L/d \geq 6$ , where  $L$  and  $d$  are the length and diameter of the sensor. Also a low conductivity material should be selected.
- With a high  $L/d$  ratio, the heat transfer at the tip of the sensor is neglected. The used thermocouple is made of an Inconel alloy and the ratio  $L/d$ : 100.
- The probe is place at the isothermal line in the axys of the supply line.
- The sensor diameter should be as small as possible. In this case, the selected value as the smallest probe diameter considering the required mechanical strength,  $3\text{ mm}$ .

Considering these recommendations, the standard uncertainty for the temperature measurement is stated as 3%.

Using equation 5.17 for the two measured volumetric flow rates  $200 - 300\text{ m}^3/\text{h}$ , the standard uncertainty of the inlet air mass flow is show in Figure 5.34. Due to the low uncertainty in the volumetric flow rate, the standard uncertainty is insensitive to the temperature variations.

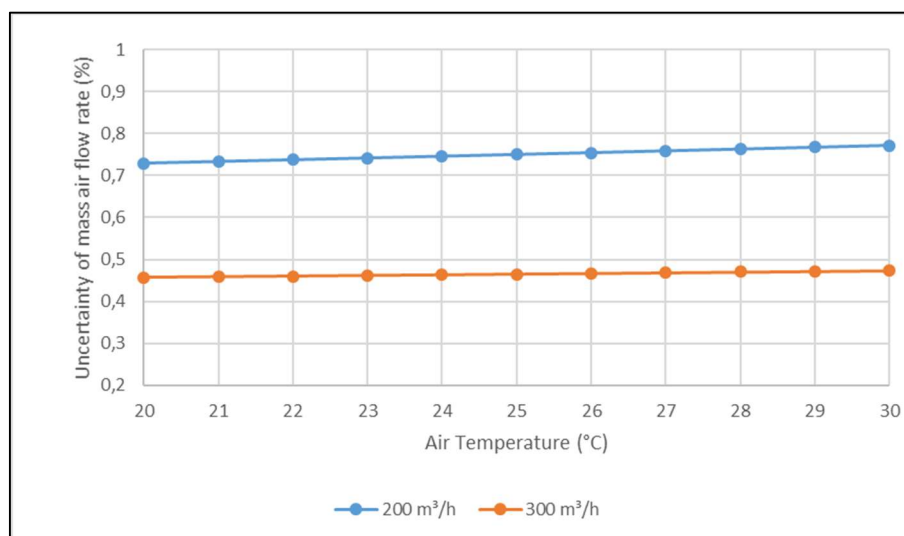


Figure 5.34 - The standard uncertainty for the inlet air mass flow rate as a function of the temperature and the volumetric flow rate.

### 5.8.2 Injection pressure

Section 5.4 describes the high-pressure fuel supply system. In this system, the control of a three-way valve generates the necessary fuel pressure according to the target value. An automotive piezo-resistive sensor measures the fuel pressure. Figure 5.35 shows the electrical response of the piezo-resistive sensor used in the experiments. With this response, the pressure and voltage have a linear relationship. Equation 5.185.8 shows the respective function

$$p_{fuel} = 39.47U - 19.73 \quad 5.18$$

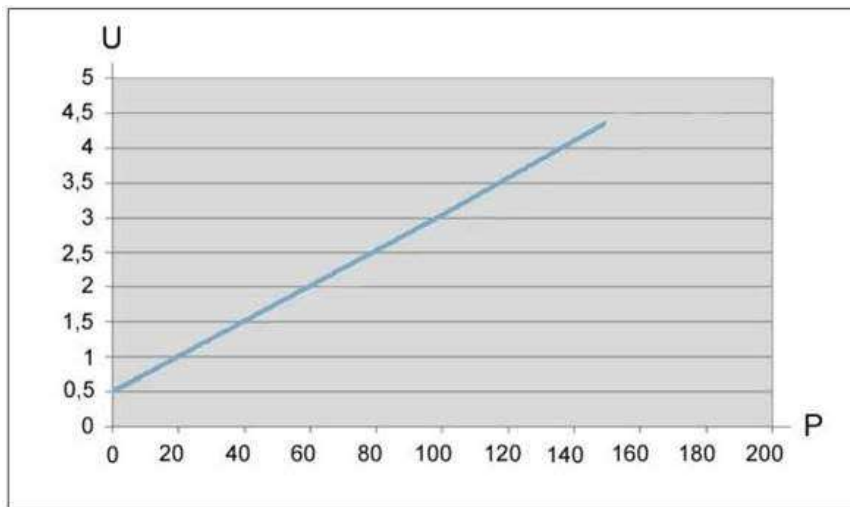


Figure 5.35 - The electrical response of the piezo-resistive sensor as a function of the static pressure. The vertical axis is the voltage between the terminals of the sensor in volts. The horizontal axis is the measured pressure in bars.

The tension between the terminals of the sensor is measured with NI9201 analog input module. The measurement uncertainty specified in the datasheet for uncalibrated modules is 0.67%. Therefore, the standard uncertainty for the injection pressure is:

$$\mu_{fuel}^2 = 39.67^2 \mu_U^2 \quad 5.19$$

In which  $\mu_U$  is the uncertainty of the NI9201 module. The equation 5.19 indicates that the uncertainty is independent of the measured pressure. Thus, the standard uncertainty of the fuel pressure is  $\approx 0,25\%$ .

Although the estimated Type B uncertainty is low, the Type A is more significant to the fuel pressure. Due to the fast response in the three-way in on-off mode, the pressure oscillations are high. A combined standard uncertainty of around 5% is estimated in the measurements.

### 5.8.3 PIV measurements

Uncertainties quantifications for TR-PIV are subject of study in numerous works [49] [39] [50] [37] [51] [52] [53] [54]. These estimations are strongly influenced by the adopted experimental procedure. The precautions described in this section were taken to minimize the deviations that the user had control. The PIV algorithms are also source of uncertainties to the experiments [49] [53] [52] [54]. The interrogation window size affects the velocity calculations In Sciacchitano et al [49], the planar PIV measurements are compared with Monte Carlo simulations. The obtained uncertainty in the velocity estimations remains between 0.02 0.38 pixels. In Xue at al [53], a relation between the uncertainty and metrics of the cross-correlation SNR are evaluated. The develop model estimates uncertainties of the order of 0.2 pixels in the velocity calculation. In Baum et al [54], Zentgraf et al [55], the combined uncertainty is stated as 5% for the 2D PIV measurements.

In section 5.7.1.1, the normalized relative velocity as a function of the relaxation period and particle diameter were calculated and shown in Figure 5.16. To estimate the uncertainties associated with the relative velocity, consider the time interval between two acquired consecutive velocity fields:  $1.25 \times 10^{-4} s$ . The value is depicted in red on Figure 5.16. If a particle is subjected to a sudden acceleration, after the time interval of  $1.25 \times 10^{-4} s$ , particles with less than  $3 \mu m$  have roughly 5% of velocity difference and particles between 3 to  $5 \mu m$  have 10~15%.

Thus, in measurements of this work, especially those associated with transient phenomena, an accumulated uncertainty of 15% is stated for the obtained velocities fields.

$$\mu_{PIV} = 0.15 \cdot u \quad 5.20$$

Another quantity widely discussed in this work is the turbulent intensity. The quantity is obtained with equation 5.21.

$$I_i = \frac{u'}{u} \quad 5.21$$

In which  $u'$  is the velocity fluctuation over the mean velocity  $u$ . The standard uncertainty in the turbulent intensity is shown in equation 5.22.

$$\mu_{I_i}^2 = \frac{I_i^2}{u^2} \mu_{PIV}^2 \quad 5.22$$

Finally, equation shows the standard uncertainty in the turbulent intensity.

$$\mu_{I_i} = I_i \cdot \left( \frac{\mu_{PIV}}{u} \right) \rightarrow 0.15 I_i \quad 5.23$$

Note that in the case of  $I_i$ , the standard uncertainty remains in the same levels of the velocity uncertainty estimations.

$$\frac{\mu_{I_i}}{I_i} = 15\%$$

## 6 Results

In this chapter, the results of the experiments with IESC are presented. The experiments were divided in two main types: the stationary flow analyses and the air-spray interaction analyses. The first type comprises all the investigations of the stationary air flows that are used during the spray events. Section 6.1.2 presents the turbulence characteristics of these stationary flows. A methodology for evaluating the integral turbulence characteristics of the air flows is presented. This method is based on the classical statistical turbulence theory. These obtained properties are used to analyze the effects of turbulence during the fuel injections. Section 6.1.1 shows the results for the third velocity component estimations for a stationary flow condition. The technique is based on the reconstruction of the 3D mean velocity field by the acquiring of multiple velocity planes. This analysis quantifies the normal velocity component that is not measured during the spray-air interactions. Finally, section 6.1.1 discuss all the results obtained for the investigation of the air-spray interactions in IESC. These interactions are evaluated in terms of velocity distributions and in terms of turbulence properties evolution with time. In section 6.2.7, a time-frequency method is used to calculate the spectrograms of the conditions studied. These analyses evaluate the effects of the injection events on the power density distributions.

## 6.1 Stationary flow analyses

The objective of this section is to characterize the non-homogeneous turbulence of the statistically-stationary flows in IESC. These constant-flows are the initial conditions in which the injections occur. The section also presents a detailed descriptions of the experimental procedure and special features required for the evaluation of power spectra distributions. The turbulent characteristics are calculated with the instantaneous velocity fields acquired with TR-PIV technique. Mean convergence is verified and space-depend variables are obtained by well-established methods for consistent estimations of random variables.

### 6.1.1 Setup and TR-PIV configuration

Figure 6.1 illustrates the experimental setup and TR-PIV configuration used to obtain the 2D planar time-resolved velocity fields. The air flow is supplied to the IESC by the blower kept in constant angular velocity of 600 *rpm*. The air flow enters the chamber as described in section 5.6 and discharges into a filter box. The nominal volume flow rate is  $245 \text{ m}^3/\text{h}$ , resulting in a Reynolds number of  $1.12 \times 10^5$  using IESC hydraulic diameter. Seeding particles of sebacate oil are generated by a Laskin nozzle with a mean diameter Gaussian-distribution of  $3 \mu\text{m}$  (see section 5.7.1.1). The laser, a frequency-doubled dual-cavity Nd:YLF Litron Lasers LDY302 -  $527\text{nm}$  with  $4.5 \text{ mJ}/\text{pulse}$  at a trigger rate of 5 kHz, is placed perpendicularly to the high-speed CMOS camera (v311 - Vision Research Inc.). The laser is equipped with a set of cylindrical lenses which creates a sheet with 50 mm high and thickness of the order of 1 mm.

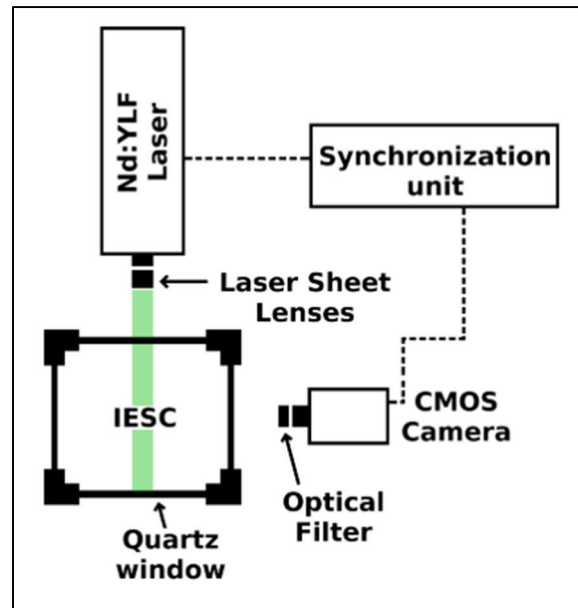


Figure 6.1 - Experimental arrangement for acquisition of images during the stationary flow analysis

The 8-bit camera is equipped with a sensor array of  $1280 \times 800$  pixels and  $20 \mu\text{m}$  of pixel pitch. The set of Carl Zeiss lenses of  $50 \text{ mm}$  focal length and 1.4 f-number coupled with a  $8 \text{ mm}$  extension ring is mounted on the high-speed camera. The image acquisition is performed with a  $527 \pm 5 \text{ nm}$  bandpass optical filter mounted on the lenses to reduce the interference of ambient light. Laser and camera are synchronized with the pulse delay generator model 575-8C (Berkeley Nucleonics Corporation) and controlled by Dynamic Studio® software (see section 5.7.1.4)

The TR-PIV experiments are performed in the symmetry plane of the IESC optical accessible section, which is also a symmetric plane of the injector cartridge. (see Figure 6.1). To ensure the alignment of laser sheet and focus plane of the camera, the tailor-made removable target described in section 5.7.2.2 is used. The seeding flow rate, laser intensity, camera aperture and focus fine-tuning are carefully adjusted to ensure a proper SNR, the number of particles per area, the particle-scattering sharpening and the spatial resolution. The time between the two consecutive pulses,  $20 \mu\text{s}$ , is chosen to limit the average particle displacement to  $1/4$  of interrogation window length, thus avoiding aliasing in the cross-correlation calculations and minimizing in-plane loss-of-pairs.

Before each measurement, the camera sensor is covered and calibrated to compensate for currents that may exist due to electrical potentials between the sensors. The field-of-view (F.O.V. ) of  $23.41 \times 23.41 \text{ mm}^2$ , captured with  $400 \times 400$  sensors and  $59 \mu\text{m}$  pixel resolution is illustrated in Figure 6.2. For this study, measurements are limited by the camera internal memory, resulting in 41513 image pairs obtained in double-frame mode with  $7491 \text{ Hz}$  of repetition rate.



*Figure 6.2 – The F.O.V. used for the stationary TR-PIV analyses in the IESC symmetric middle plane. The colormap illustrates the size of the F.O.V.*

The commercial software Dynamic Studio® is used for the PIV processing. A preprocessing phase is required to enhance the cross-correlation estimation. The acquired images are first treated to remove static background by average image subtraction. Next, a balance algorithm is used to compensate the light intensity loss through the images. A low-pass intensity filter is used to limit the dynamic range of the image to values near the particles scattering intensity.

The processing phase comprises the algorithms for velocity estimation. The calculated velocity vectors are validated by the universal outlier detection algorithm with a  $5 \times 5$  vector vicinity, a normalization level of 0.1 pixel and detection threshold of 2.0 (see section 5.7.1.4). The initial interrogation area of  $32 \times 32$  pixels is iteratively modified. The final interrogation window size of  $8 \times 8$  pixels results in a spatial resolution of 0.47 mm. Finally, a  $3 \times 3$  Gaussian smoothing filter is applied to reduce noise at small spatial scales. For the spectra estimations and calculations of other turbulent properties, a MATLAB® code was developed.

### 6.1.2 Integral scales and statistical treatment of turbulence

The current most acceptable approach for turbulent characterization uses statistical analysis in which the wide-sense stationary (WSS) hypothesis is extensively applied [56]. As stated by [56], a WSS process has finite variance and a convergent mean. The finite behavior of the variance is intrinsic to the studied physical phenomenon. To evaluate mean convergence, a criterion must be adopted. Unfortunately, the exact quantity of data cannot be known a priori since it depends on numerous factors, including the physical phenomena and the measurement equipment. The experimental setup described earlier allows acquiring 41513 image pairs, corresponding to a time interval of 5.54 seconds. The proposed methodology to evaluate mean convergence is defined in equation 6.1, in which  $\sigma_s$  is the estimated standard deviation,  $M_{(s)}^{i,j}$  is the evolving mean velocity field as a function of sample size,  $M_{tot}^{i,j}$  is the mean velocity field using the entire data and  $N_p = i \times j$  is the total number of random variables. The  $i$  and  $j$  variables are the coordinates of each velocity vector inside the measurement plane.

$$\sigma(s) = \frac{\sum_{i,j} \sqrt{\left( M_{(s)}^{i,j} - M_{tot}^{i,j} \right)^2}}{M_{tot}^{i,j}} \quad 6.1$$

$$\sigma(s) = \frac{N_p}{N_p}$$

Figure 6.3 illustrates the evolution of  $\sigma_{(s)}$  along sample size. Observe that after 3000 images,  $\sigma_{(s)}$  is as small as 0.1 and thus twice the equipment resolution limit.

Thus, all the average values could be considered converged with 5000 samples. However, due to the large amount of available data, all the average fields are calculated considering the entire measured sample.

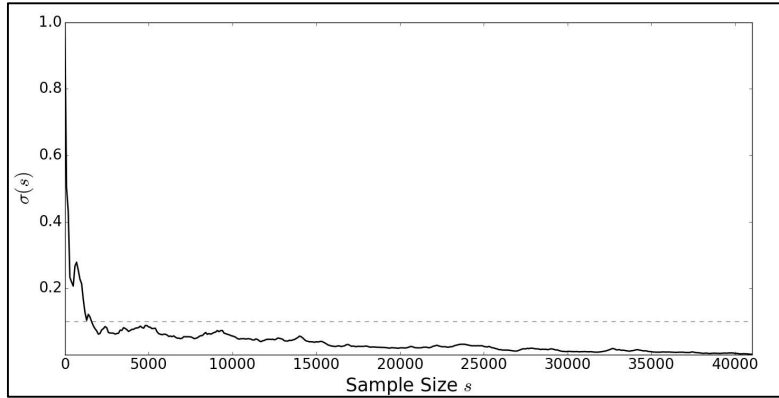


Figure 6.3 – Error estimation of the mean normalized by the number of pixels.

Figure 6.4 shows the mean velocity fields. A typical bluff-body recirculation structure, as seen in [57], is present in IESC stationary flow field. Note the difference in the velocity scales between directions. While the mean  $x$  coordinate component remain near by zero, the  $y$  coordinate velocity reaches  $10 \text{ m/s}$  in the region far from the shear layer and  $2 \text{ m/s}$  inside the recirculation zone.

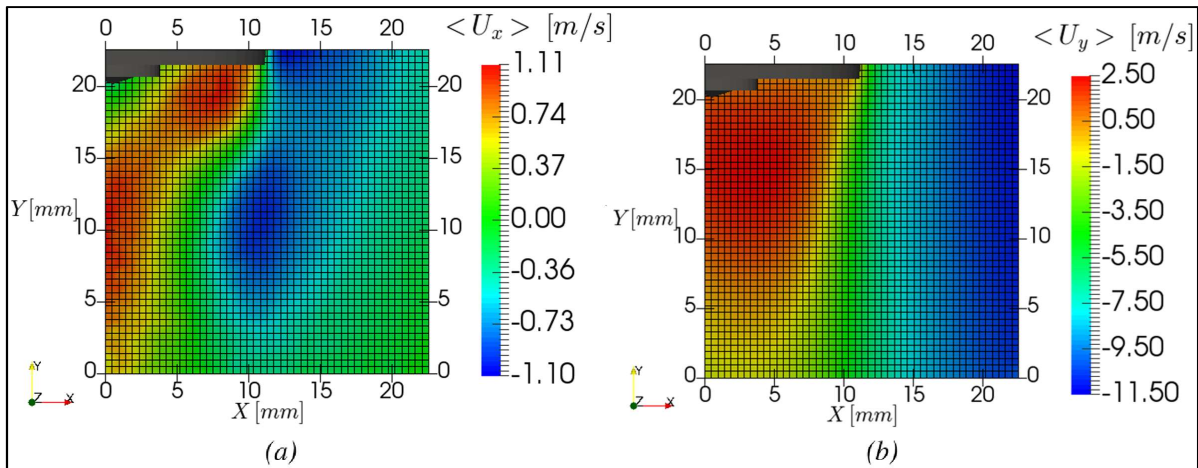


Figure 6.4 - Mean velocity fields over the measurement plane for  $x$  and  $y$  coordinates

Figure 6.5 and Figure 6.6 shows the two calculated components of the Reynolds stress tensor in the measuring plane. Since the components are not equal, the isotropy hypothesis is not applicable. Moreover, each component has a non-uniform distribution. The turbulent nonhomogeneous behavior of the flow field is evident.

By observing the magnitude of the  $\langle u_i u_i \rangle$  components, turbulence in the shear layer has a major contribution of the  $\langle u_y u_y \rangle$  component. Below the injector, a small region tends to the HIT hypothesis, since the normal components are approximately equal and the cross components are close to zero. The cross component, related to the rotational motion as stated by [55], indicates a strong rotational effect in the shear layer that diminishes along the  $+x$  direction of the field (after  $x > 12\text{mm}$ ). In the measured space, this component is dominated by the vortical structure of the bluff-body.

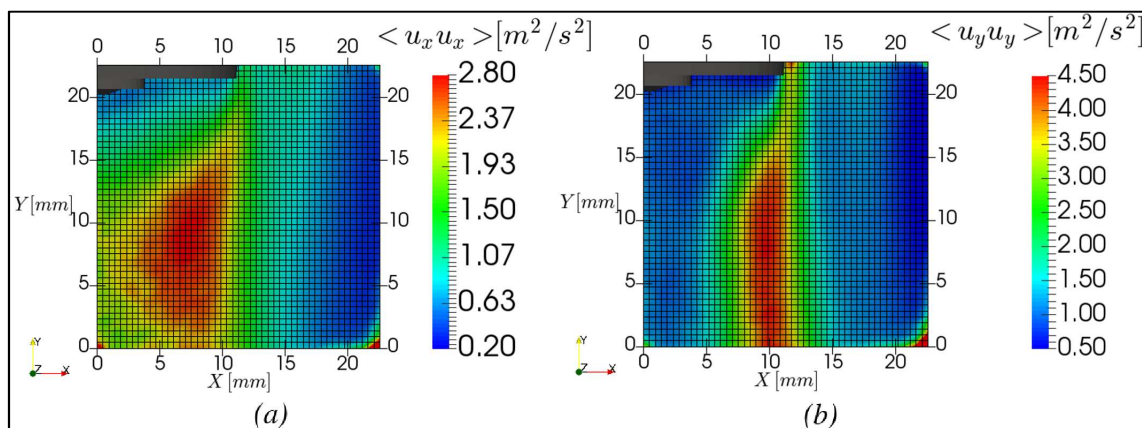


Figure 6.5 - Reynolds stress components  $\langle u_x u_x \rangle$  (a) and  $\langle u_y u_y \rangle$  (b) obtained for the stationary conditions on the measurement plane.

Figure 6.6b shows the distribution of the approximated turbulent kinetic energy  $k = \frac{1}{2} \langle u_i u_i \rangle$ . The property was calculated for the entire field considering the normal velocity component as  $u_z = u_x$ . Again the non-homogeneity of the flow is evident. Most of the turbulent kinetic energy in the measurement space originate inside the shear layer. A small contribution from the inlet flow is visible. This air flow carries the turbulence induced by the perforate plates.

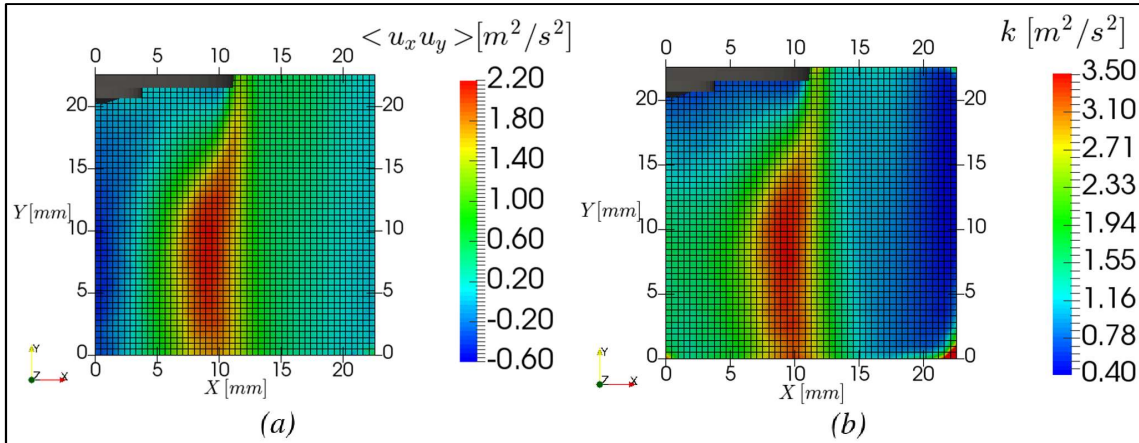


Figure 6.6 - Reynolds stress component  $\langle u_x u_y \rangle$  (a) and turbulent kinetic energy  $k$  (b) obtained for the stationary conditions in the measurement plane.

### 6.1.2.1 Power spectra estimations and integral scales

The assumption of the velocity field as a random process in turbulent flows leads to a convenient form of statistical description. However, care must be taken when acquiring and evaluating the random processes. Since a random process is a sequence of random variables, the observation leads to an estimation and not the true value of the parameter. The question whether this estimation is satisfactory or not will depend on how it is manipulated.

To assess the degree of confidence of the estimation, it is necessary to consider bias and consistency of the estimator. Bias, as described in [56], is the difference between the expected value of the estimate and true value of the parameter. An estimate is said to be *asymptotically unbiased* if bias goes to zero as the number of observations goes to infinity. However, bias is not the only property necessary to an estimator to converge. The variance of the estimation must also go to zero with increasing number of observations. In this sense, the estimator is called a *consistent estimator* in a mean-square sense [56].

An important set of parameters to be estimated in a turbulent flow is the correlation functions. These second-order statistical moments provide the relationship between two random variables. For the case of the temporal autocorrelation, the two random variables belong to the same random process. In turbulence, the autocorrelation functions are useful in describing the behavior of the flow by integral scales. The temporal autocorrelation estimation for a WSS

ergodic process at each point in sample space is calculated with equation 6.2, where  $N$  is the total sample size,  $s$  the lag variable,  $\langle u_i^2 \rangle$  the variance of estimate and  $\langle U_i \rangle$  is the mean velocity component.

$$\rho(s) = \frac{1}{\langle u_i^2 \rangle} \frac{1}{N-1} \sum_{n=1}^{N-1} (U_i(n) - \langle U_i \rangle)(U_i(n+s) - \langle U_i \rangle) \quad 6.2$$

Figure 6.7 shows the autocorrelation estimations of three different points in the measurement space. Note the difference in the behavior of the estimations. For point 2 located near downstream injector tip, a sinusoidal characteristic related to vortex shedding from the bluff body is presented. The same pattern is not visible at point 3 far from injector tip. In this case, the region is influenced by the inlet air flow. The point 1 indicates an intermediate behavior, in which the effects of vortex shedding are comparable to the inlet air flow characteristics.

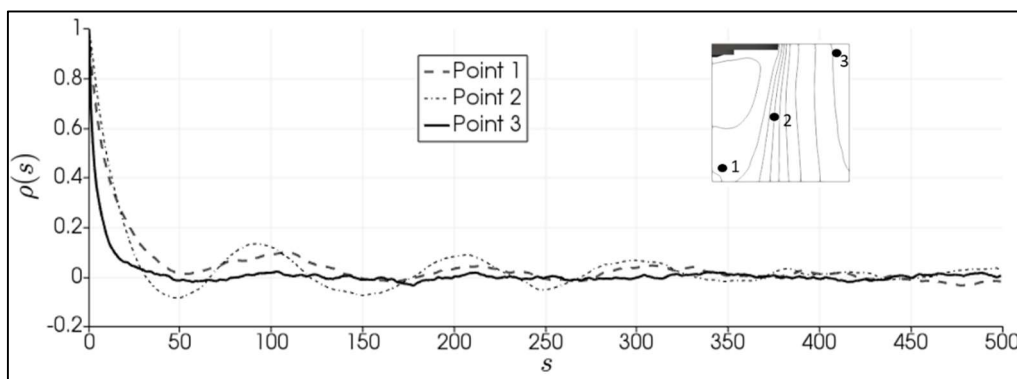


Figure 6.7 – The autocorrelation function estimation for three different points. The function characteristics are related to local differences in the flow field.

When assuming the HIT conditions, an estimation of a unique autocorrelation function can be calculated by space-averaging the autocorrelation functions obtained for each measured point [58] [59] [60]. In this case, performing the space-average of the functions leads to a *consistent estimator* of the true autocorrelation function of the process. For the nonhomogeneous case of IESC, space-averaging is not applicable. Since each point has different characteristics, there must be an autocorrelation function for each measured point in space. However, when just one realization is used to calculate the estimator, this would not lead to a consistent estimator. A direct consequence is observed when calculating the integral time scale  $\bar{\tau} = \int_0^{\infty} \rho(s) ds$  as stated by [61].

Figure 6.8 shows the result for integral length scales as a function of the number of observations. With a *non-consistent estimator*, increasing the number of observations do not enhance convergence. The calculated integral time-scale tends to the true value but with high variance. The value of the integral is very sensitive to its limits. Note that, for example, for some values of  $n$ , the function results in negative integral scales, which is physically impossible. The variation of the integral scale result is not related to the numeric method used to perform the operations but to the role of choosing a consistent estimator to assess the random variable. Although not shown in Figure 6.8, different numeric methods were tested and resulted in the same conclusions.

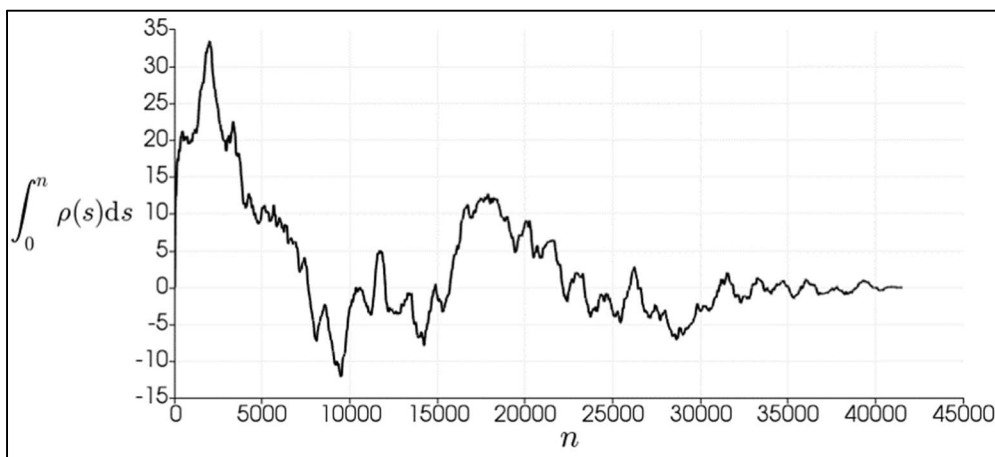


Figure 6.8 – The integral of the autocorrelation estimation as a function of the integral limits. The behavior is related to the non-consistency of the estimator

Another perspective to study the autocorrelation functions is by calculating its frequency domain representation - the power spectrum. For a discrete and limited data, the power spectrum must be estimated. A first estimator for the power spectrum is the so called Periodogram. As stated by [56], the power spectrum is calculated by simply taking the square of the discrete Fourier transform of the data set  $|X_N(e^{jw})|^2$  and performing a normalization by the number of samples  $N$ . However, as demonstrated by [56], the Periodogram is also a *non-consistent estimator* of the power-spectrum. A consolidate nonparametric method for a WSS ergodic process that results in a *consistent estimator* of the power spectrum is the Welch's Method. To exemplify the effects of consistency in the frequency domain, Figure 6.9 shows power spectra estimations for a point obtained with the Periodogram and with the Welch's method. Although the tendencies for both

cases are similar, for the non-consistent estimator, variance between points is significantly larger when compared with the consistent case.

The idea behind Welch's method is to segment the single realization of  $N$  events into sets of  $L$  points. These segments are obtained by partially overlapping each other and considering a window function to control leakage. For each new segment, a periodogram is calculated. The power spectrum estimation will be the ensemble-average of these *modified* periodograms.

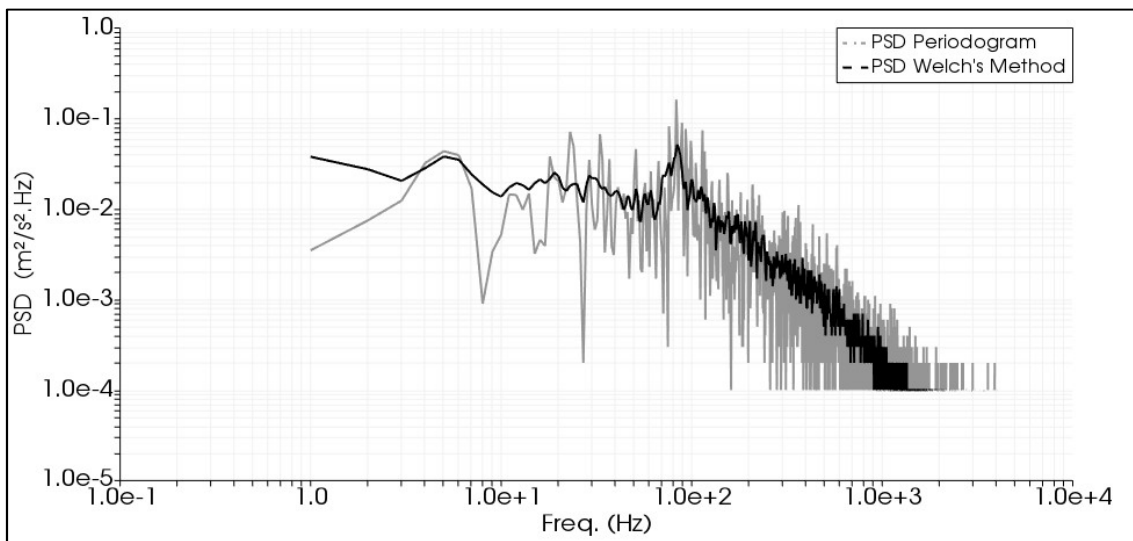


Figure 6.9 – The power spectrum density estimation for a particular point in measurement space. Comparison between the Periodogram and the Welch's method.

Figure 6.10 shows the calculated power spectrum for a point inside the measured velocity field. The frequency domain representation is obtained by the Welch's Method, resampling the entire data into sets of 5000 events computed with a Nuttall window to reduce leakage and 50% overlap between the resample data. The energy distribution through the low frequency range is observed. The visible part of the inertial sub-range also shows a good agreement with the  $-5/3$  inertial rule depicted in the red dashed line. As the frequencies approaches the high measurement limits, the variance of the estimate tends to increase. This increase in the variance can be affected by the absence of an anti-aliasing filter as highlighted by [62] and by the frequency response capability of the tracer particles as stated by [37].

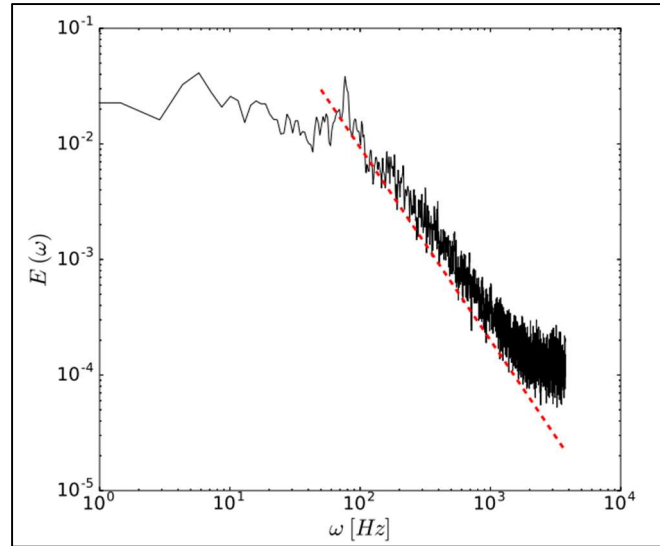


Figure 6.10 - An example of the power spectrum estimation for a point inside the measured region (continuous line) following the  $-5/3$  inertial sub-range rule (dashed line).

For a random variable acquired in time-space, the turbulence integral time scale  $\bar{\tau}$  can be calculated with equation 6.3 [61], in which the first value of the power spectrum  $E(0)$  and the velocity variance  $\langle u^2 \rangle$  are employed.

$$\bar{\tau}_i = \frac{\pi E_i(0)}{2 \langle u_i^2 \rangle} \quad 6.3$$

Since both the velocity variance and the power spectrum are obtained for each velocity component  $u_x$  and  $u_y$ , two turbulence integral time scales can be calculated. This directional dependence is represented in equation 6.3 with the  $i$  index. Considering each point as a series of random variables in the sample space of the TR-PIV measurements, one power spectrum is obtained for every location. With the space-dependent power spectra, equation 6.3 results in a spatial distribution of  $\bar{\tau}$  for each direction  $x$  and  $y$ , as illustrated in Figure 6.11.

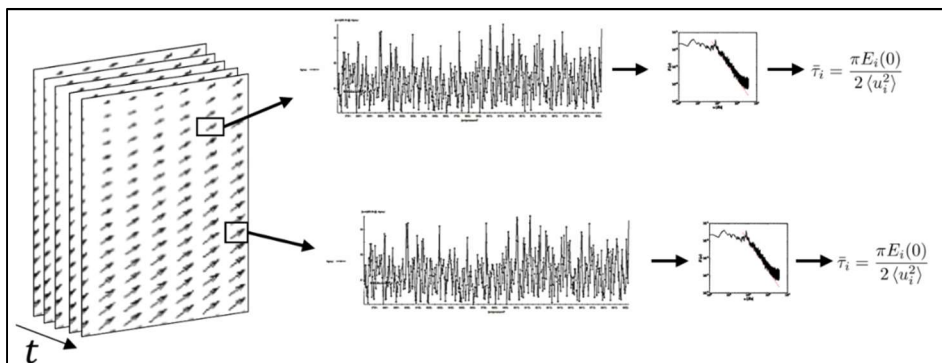


Figure 6.11 - Illustration of the procedure to calculate the space-dependent Integral time scales  $\tau$ . A sequence of the velocity fields is acquired over time interval  $t$ . For every location, a PSD is calculated. The integral time scale is then determined.

Figure 6.12 shows the turbulence integral scales calculated with the described procedure. Clearly, isotropy conditions are not globally applicable in this study since different turbulence integral time scales are present in the  $x$  and  $y$  coordinates. The nonuniform distributions in both directions also reinforces the non-homogeneous characteristic of the turbulence. Below the injector,  $\bar{\tau}$  shows the highest values and thus low frequency eddies. Near the perforated plates,  $\bar{\tau}$  is lowest and approximately uniform. This is expected for the small holes and indicates its success in providing a controllable inflow without the influence of the entire air flow preparation section.

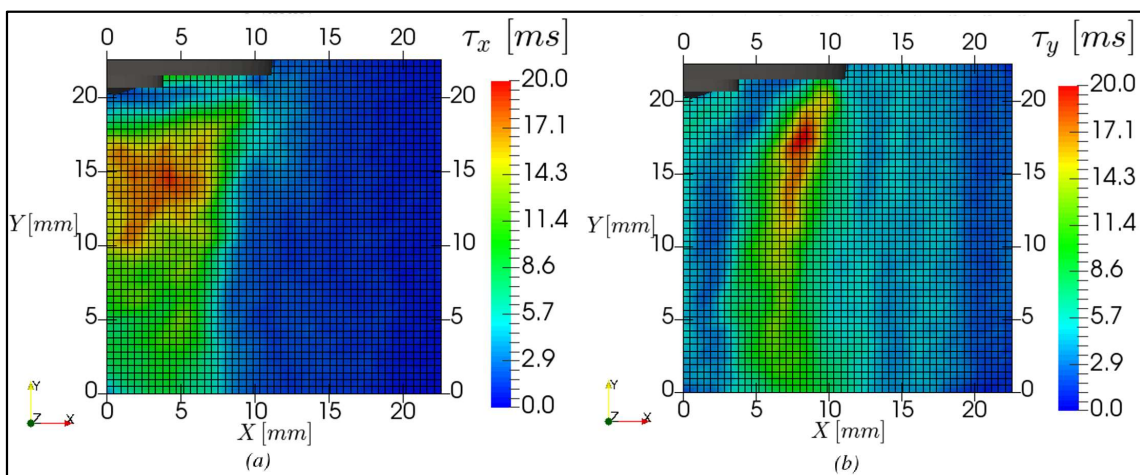


Figure 6.12 - Integral time scales  $\tau$  in the  $x$  coordinate (a) and  $y$  coordinate (b) obtained with the values of the PSD for every measurement point.

With the obtained time scales distributions, turbulence integral length scales  $L$  are estimated with equation 6.4.

$$L_i = \bar{\tau}_i |u_i| \quad 6.4$$

Figure 6.13 shows the spatial distributions of the integral length scales for the  $x$  and  $y$  directions. The same non-homogeneous behavior of  $\tau$  is present for  $L$ . Near the perforated plates, the turbulence integral length scales for  $y$  direction remains between 3.3 to 6.5 mm, scaling with the 4 mm holes of the perforated plates. Below the injector, scales of the order of 20 mm are present which is of the order of the injector cartridge diameter.

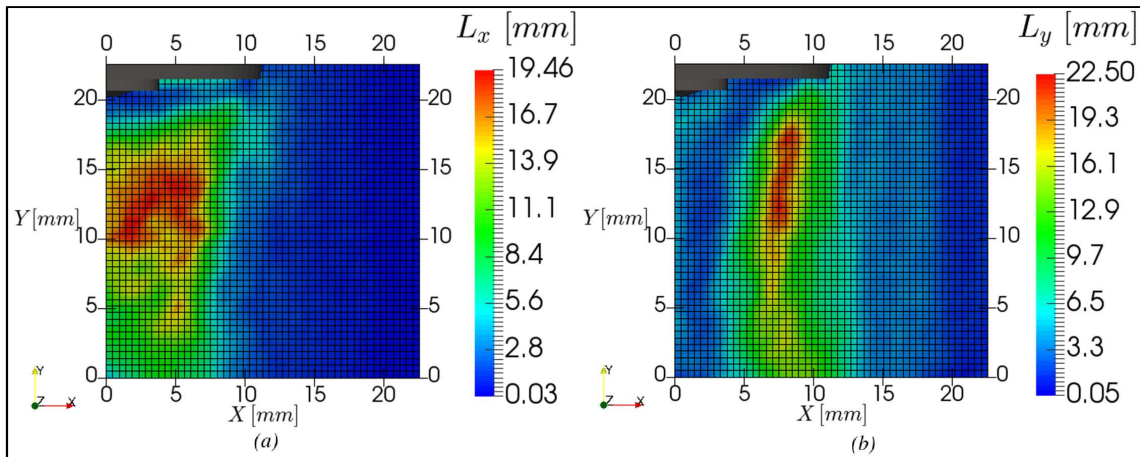


Figure 6.13 - The Integral length scales for the  $x$  and  $y$  coordinates.

With these distributions, a detailed description turbulence characteristics of a stationary flow is obtained. The description of an integral length scales distributions rather than a single value allows investigating the local effects of turbulence. For the case of IESC experiments, these distributions are important for a careful correlation with the effects of turbulence on the initial instants of the spray development.

### 6.1.3 Effects of perforated plates sets

As described in section 5.1, the IESC apparatus allows using three different pairs of perforated plates. These sets are designed to limit the turbulence integral scales inside the chamber. The effects of the sets are compared using the methodology developed in section 6.1.2.

The experiments are conducted with the procedure described in section 6.1.1. For each set of perforated plates, the air supply system maintains the volumetric flow rate of  $200 \text{ m}^3/h$ . A set of 14000 image pairs were acquire at  $8000 \text{ Hz}$  for each condition. For the three cases, the F.O.Vs with  $29.4 \text{ mm}$  height and  $20 \text{ mm}$  width are placed in approximately the same physical coordinates. The resultant vector spatial resolution is  $0.458 \text{ mm}$  using the algorithm described in section 6.1.1.

Figure 6.14 shows the results of the mean velocity fields for the conditions studied. The formation of a recirculation structure is observed below the injector tip similar to the condition of a flow around a bluff body. For the perforated plates sets of 2 mm and 4 mm, these structures have comparable sizes and shapes. Slightly differences are observed in the position of the recirculation centers. For the perforated plates set of 6 mm, the recirculation center is closer to the shear layer in left portion of the image. By observing the velocity magnitude distributions for all the three cases, the recirculation zone for the set of 6 mm is smallest.

In the air flow out of the recirculation zone, velocity gradients on the  $x$  direction are present due to the shear layer effects, as highlighted in section 6.1.2. In the outer regions unaffected by these gradients, the velocity magnitude gradually increases from about 10 m/s in the 2 mm set to 12 m/s in the 6 mm set.

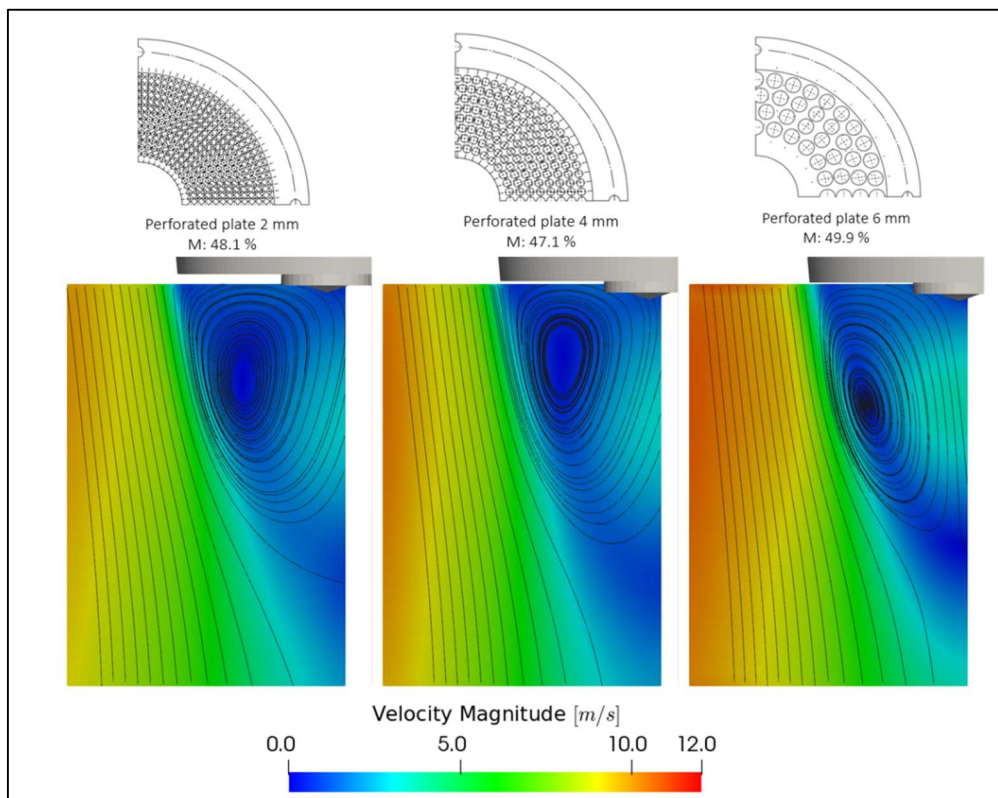


Figure 6.14 - The mean velocity fields of the stationary conditions for the three sets of perforated plates.

Figure 6.15 shows the results of distributions of the Reynolds stress tensor component  $\langle u_x u_x \rangle$  for the three perforated plates sets. Note the similarity between the cases. For the three sets, the major contribution for this tensor component is generated in the recirculation zone below injector tip. The magnitude of  $\langle u_x u_x \rangle$  in the region out of the recirculation zone increases from the plates set of 2 mm to the set of 6 mm.

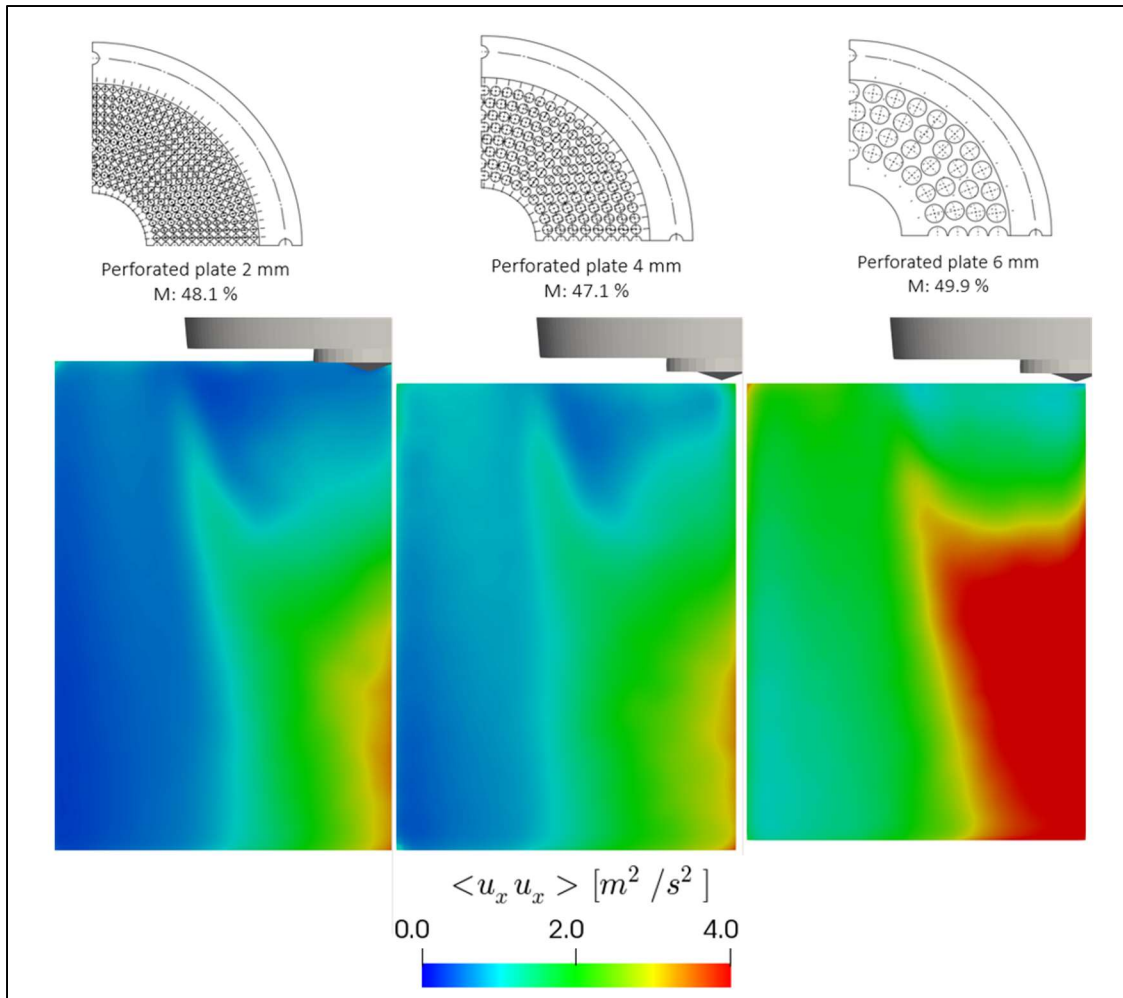


Figure 6.15 – The Reynolds stress tensor component  $\langle u_x u_x \rangle$  comparison between the different sets of perforated plates.

The same observations are made for the Reynolds stress tensor component  $\langle u_y u_y \rangle$ . Figure 6.16 shows the distribution of  $\langle u_y u_y \rangle$  for the three considered cases. The recirculation zone is responsible for the major production of  $\langle u_y u_y \rangle$ . Below the injector cartridge, the  $\langle u_y u_y \rangle$  distributions increase from the 2 mm set to the 6 mm set. The contribution of the air flow out of the recirculation zone increases from  $\approx 1 \text{ m}^2/\text{s}^2$  in the plates set of 2 mm to  $\approx 3 \text{ m}^2/\text{s}^2$  in the plates set of 6 mm.

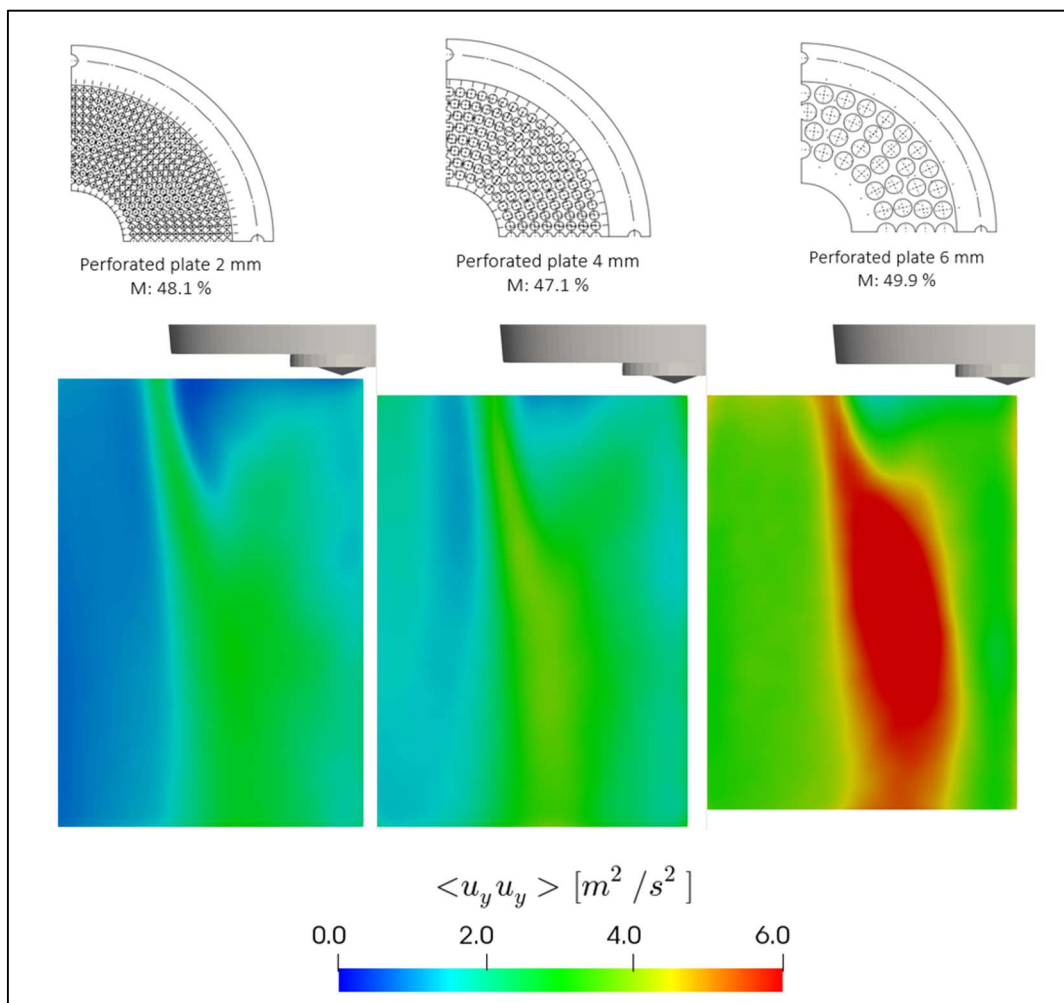


Figure 6.16 – The Reynolds stress tensor component  $\langle u_y u_y \rangle$  - comparison between the different sets of perforated plates.

Figure 6.17 shows the distributions of the component  $\langle u_x u_y \rangle$ . In the outer region, the magnitudes are roughly equal for all the conditions, indicating that the region is unaffected by the change of the perforated plates set. The production of  $\langle u_x u_y \rangle$  is due to formation of the recirculation zone. Observe the high values of  $\langle u_x u_y \rangle$  below the injector cartridge for the set of 6 mm holes. This distribution indicate a stronger rotational effect when compared to the previous cases and it is consistent with the velocity magnitude distributions.

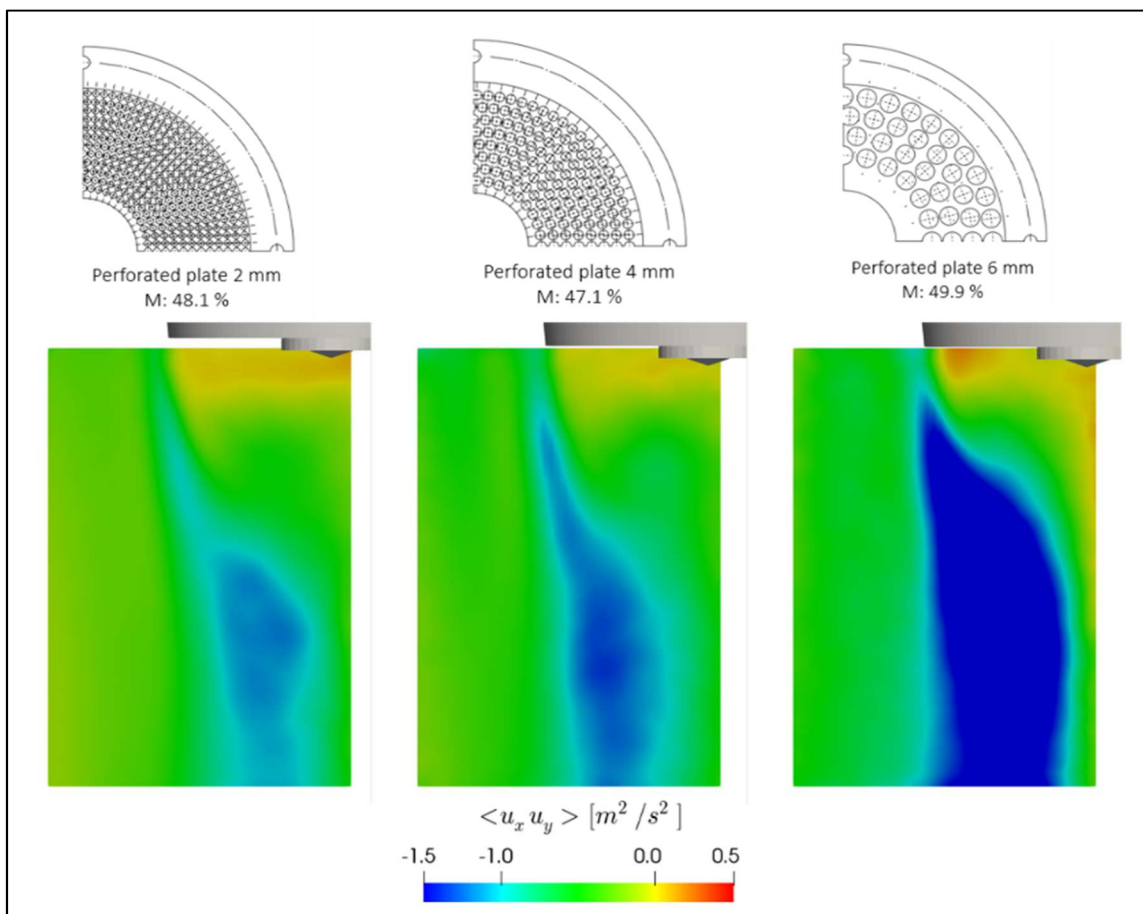


Figure 6.17 – The Reynolds stress tensor component  $\langle u_x u_y \rangle$  - comparison between the different sets of perforated plates.

Figure 6.18 shows the distributions of turbulence intensity for the three conditions studied. The color range was adjusted to highlight the effects in the region out of the recirculation zone. With the set of smallest diameters – the 2 mm set – the turbulence intensity magnitudes of the inlet air flow are smaller when compared to the other cases. As the diameters of the perforated plates increases, the turbulence intensity also increases, reaching 20 % for the 6 mm plates set. Inside the recirculation zone, the turbulence intensity is higher than in the outer region. In some points, the turbulence intensity reaches more than 100%. Since the presence of the injector cartridge produces the recirculation structure, the turbulent intensity distributions in the zones are similar to all the three cases.

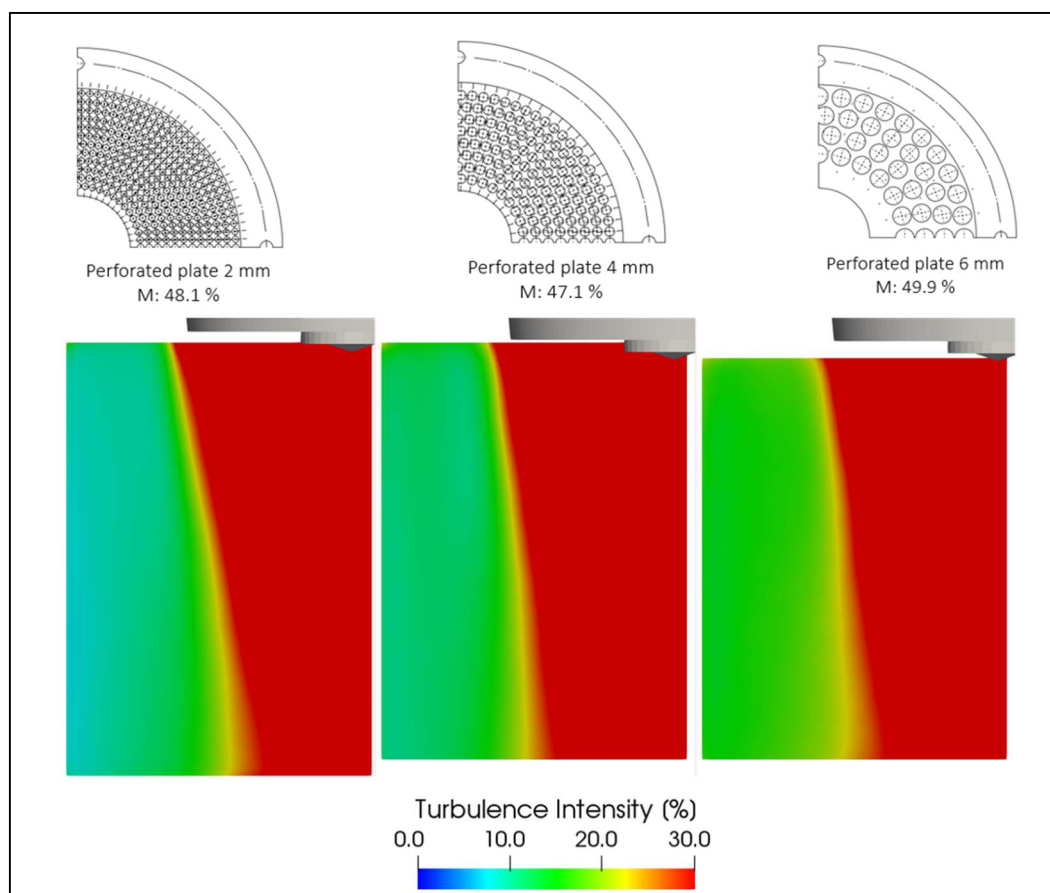


Figure 6.18 – The turbulence intensity distributions for the three perforated plates set. The color range was adjusted to highlight the effects of the perforated plates on the region out of the recirculation zone.

The results for integral length scales distributions in  $y$  direction are shown in Figure 6.19. Note the effects of the perforated plates on the turbulence development in the entire distributions. In the region below the injector tip, the integral length scales are consistent to the development of the recirculation zone. By comparing the positions of the recirculation centers with the highest values of integral scales, both properties occurs in the same spatial coordinates. At the center of these recirculation zones, the integral scales assume the highest values due to the low velocity fluctuation. The  $L_y$  values decrease from the center of the recirculation structures to the outer region. In the plates sets of 2 mm and 4 mm, since the recirculation structures are formed on similar positions, the integral scales have similar spatial distributions but with different magnitudes. From the plates set of 2 mm to the 4 mm set, the integral length scales increases from  $\approx 10$  mm to  $\approx 20$  mm. A different distribution of the integral length scales occurs for the 6 mm set due to the position of the recirculation structure. In this case, the highest values of the integral scales are concentrated near the shear layer.

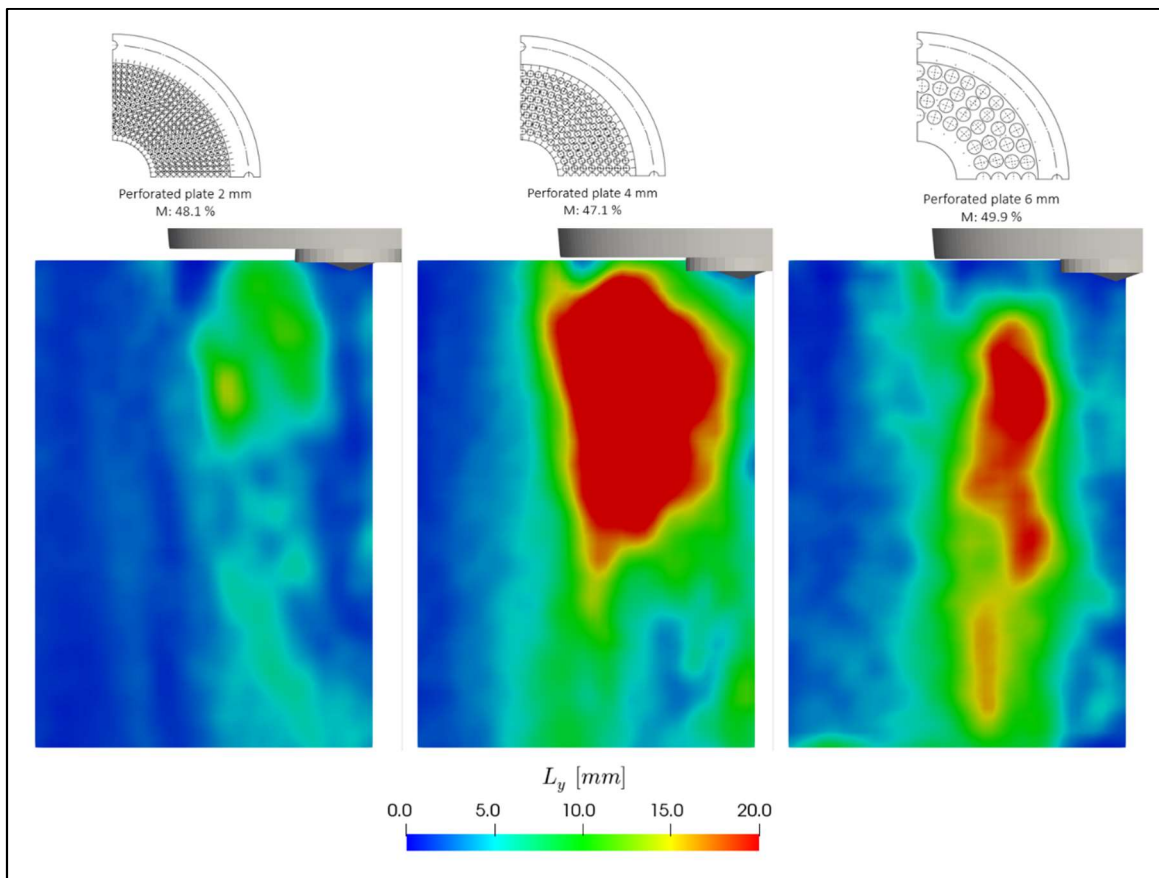


Figure 6.19- The integral length scales distributions  $L_y$ , obtained with the velocity in the  $y$  direction for the three perforated plates set.

The integral scales distributions in the regions out of the recirculation zone are also modified with the perforated plates set. For the perforated plates set of 2 mm, the integral scales assumes values closer to 2 mm. With the increase of the sets, the integral scales also increases to 3.5 mm with the 4 mm set and to 5 mm with the 6 mm set.

Figure 6.20 shows the results for the integral scales distributions considering the velocity fluctuations in the  $x$  direction. The integral length scales in the recirculation structure increase the change of the perforated plates set. For the case of 2 mm, the highest values of  $L_x$  are located near the center of the recirculation zone. With the plates set of 4 mm and 6 mm, the highest values of integral scales increases until the region where vortex shedding occurs. In the velocity fields unaffected by the recirculation zone, the integral scales increases from  $\approx 2$  mm with the 2 mm set to values of the order of 4 mm for the plates set of 6 mm.

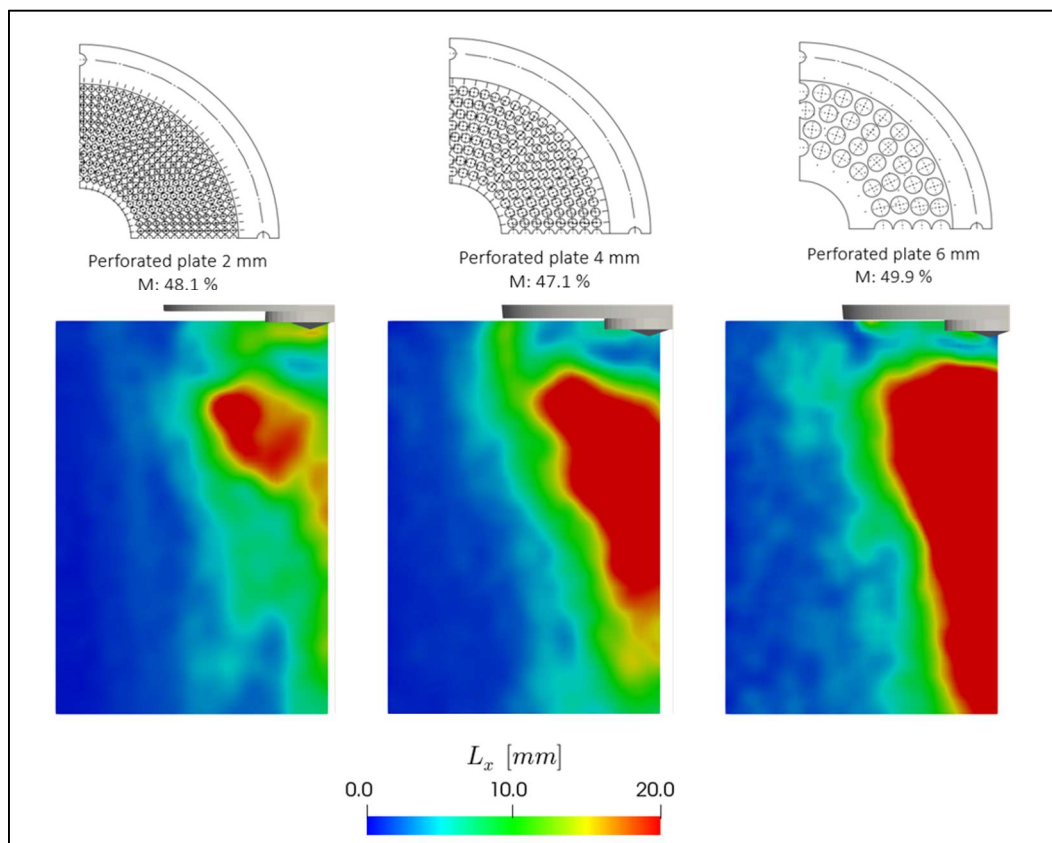


Figure 6.20- The integral length scales distributions  $L_x$  obtained with the velocity in the  $x$  direction for the three perforated plates set.

The results for the velocity distributions and turbulence properties such as turbulent intensity, Reynolds stress tensor components and integral length scales indicate that turbulence is more sensitive to the change of plates set than the velocity distributions. In order to evaluate the effects on different turbulent scales, the power spectra density distributions are estimated for the three sets. The procedure to obtain the PSDs is the same described in section 6.1.2.1. The Welch's method is used with segments of 1400 samples obtained with a nuttall window to minimize leakage. An overlap of 50% is used to increase convergence. These PSDs are obtained for each point in the measurement plane. For clarity reasons, three points are chosen to represent the different behaviors in the flow fields.

Figure 6.21 shows the PSDs in Point 1 for the three sets of perforated plates. The illustration in lower left portion of the figure represents the position of Point 1. This point represent the air flow unaffected by the recirculation structure. The overall behavior of the power density distributions are similar in the three sets. The tendency is consistent with the expected in turbulence field distributions. The integral region and part of the inertial subrange are visible. As described previously, at higher frequencies, the distributions are subjected to frequency response capabilities of the tracer particles. This can explain the modification of the decay rate. In point 1, the power content in roughly all the computed frequencies increases with the change of the perforated plate set. This power content modification is more pronounced from the 4 *mm* set to the 6 *mm* set.

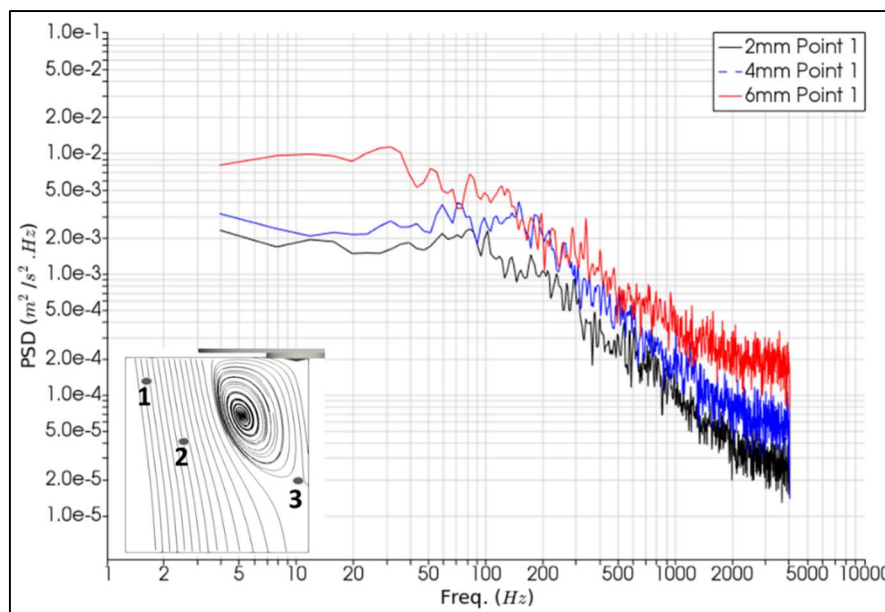


Figure 6.21 - Power spectra density estimation for a point inside the measurement plane – point 1. The distributions are consistent estimations obtained with the Welch method.

Figure 6.22 shows the power spectra density distributions for a point closer to the shear layer between the recirculation zone and the external air flow – Point 2. For this region, the differences between the plates set of 2 mm and 4 mm are minimal. For the case of 6 mm, the power density distribution is similar to Point 1. This behavior is consistent with the velocity distributions. Since the position of the recirculation zone for the 6 mm set is slightly different, the effects of the inlet air flow are still present at Point 2.

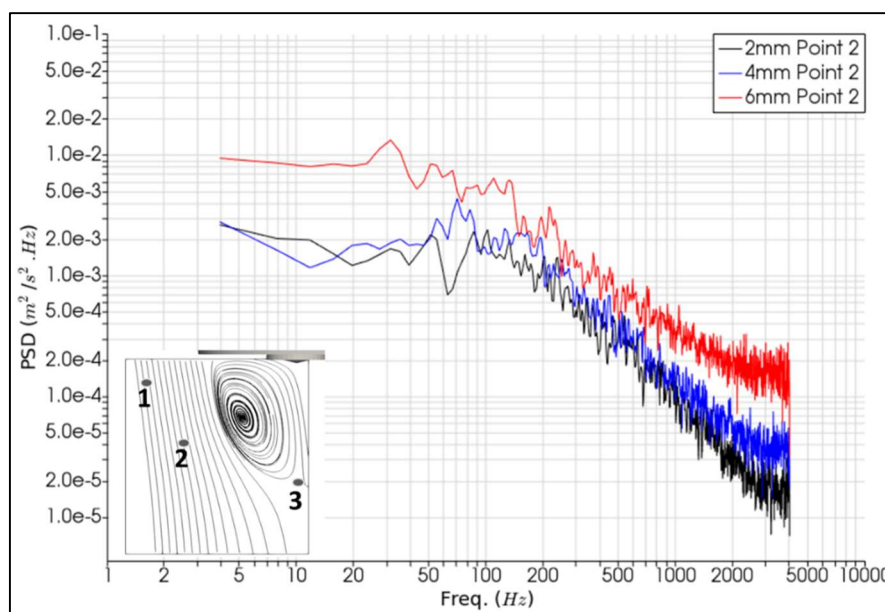


Figure 6.22 - Power spectra density estimation for a point inside the measurement plane – point 2. The distributions are consistent estimations obtained with the Welch method.

A different behavior is observed for Point 3. This point is located near the edge of the mean recirculation zone. Figure 6.23 shows the PSDs for this point. In all the three plates set, the power contents have similar distributions. This characteristic indicates that turbulence in this region is not significantly affected by the change of the perforated plates set. Both integral and inertial subrange have similar distributions with differences only in the higher frequencies.

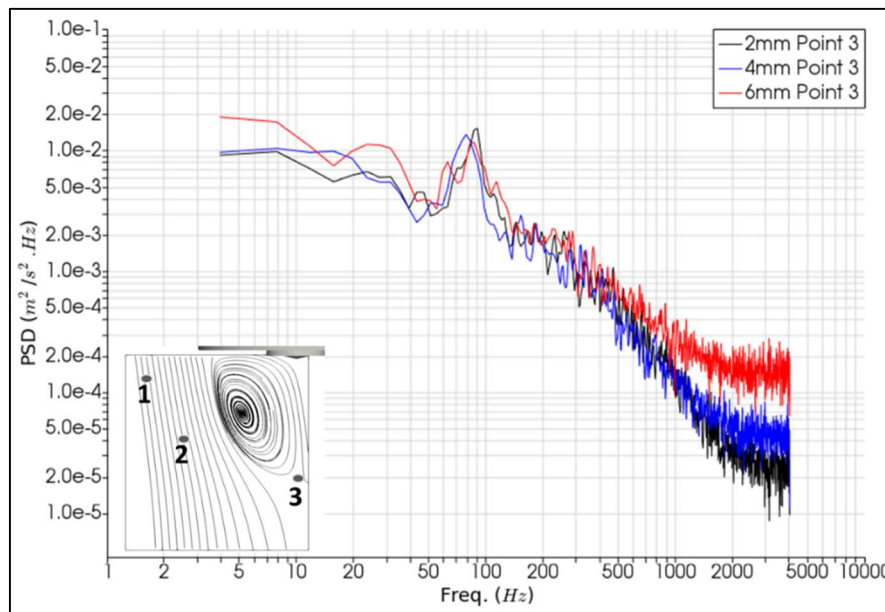


Figure 6.23 - Power spectra density estimation for a point inside the measurement plane – point 3. The distributions are consistent estimations obtained with the Welch method.

When compared to the previous cases, the overall power level in point 3 is higher for all the three sets. This higher power content is consistent with the results of the turbulent intensity and the integral length scales.

Observe the power content in the interval of 50-100 Hz. The power content at this interval has experience a sudden increase in point 3. One possible explanation for this increase can be the vortex shedding from the injector cartridge. The Strouhal number can be used to evaluate the presence of this vortex shedding in the power density spectra.

Considering the reported universal Strouhal number between  $\approx 0.1$  and  $0.2$  [63] for flows around cylindrical bluff bodies, the vortex shedding frequency can be calculated by equation 6.5.

$$St = \frac{fL}{V} \quad 6.5$$

Where  $f$  is the vortex shedding frequency,  $V$  is the mean characteristic velocity and  $L$  is the characteristic length. With a velocity  $V \approx 10 \text{ m/s}$  for the inlet air flow,  $L \approx 33 \text{ mm}$  for the injector cartridge diameter and a Strouhal number of  $St \approx 0.2$ , the expected frequency is  $f \approx 60 \text{ Hz}$ . This value is consistent with the power density distributions that shows an increase in the interval around  $60 \text{ Hz}$ .

The analyses of the stationary conditions for the perforated plates set indicate that these are capable of modifying the turbulence properties of the flow field with few effects on the mean velocity distributions. The results of calculated Reynolds stress tensor components and the turbulent intensities indicate that the turbulence energy distributions increase with the perforated plates sets. The recirculation zones formed below the injector cartridge present a significant role in the energy distribution but are less affected by the perforated plates set. In terms of the turbulence integral scales, an increase is observed with the change of plates set. Values on the external air flow scales with the holes diameters of the different plates. The power density distributions are also consistent with the results, indicating a higher power content for the set of  $6 \text{ mm}$  in all the frequency scales. With these characterized air flows, the injection events can be analyzed with well-defined boundary conditions. The perforated plates sets are able to provide different turbulence conditions with approximately the same mean flow. Therefore, the effects of the incoming turbulence in the spray development can be properly studied.

### 6.1.1 Velocity estimation by multiple planes acquisition

In order to evaluate the magnitude of the in-plane motion during the acquisition of the 2D velocity fields, the third velocity component is estimated with the approach described in section 5.7.3. This methodology requires the acquisition of different planar velocity fields to perform the estimation. Figure 6.24 shows a schematic of the measurement planes inside IESC. The experimental arrangement is the same used for the WSS stationary analysis in section 6.1.1. Thus, if not stated, only the differences between the experimental procedures are highlighted.

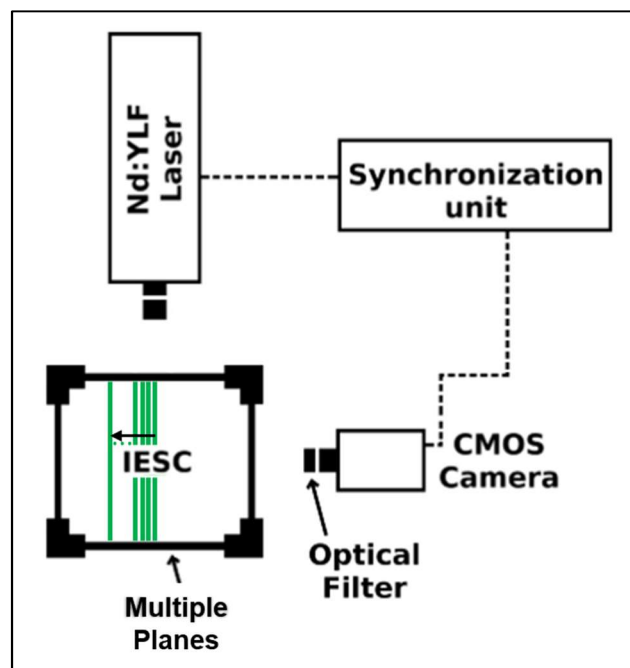


Figure 6.24 - Experimental arrangement used for the 3D velocity estimation. The arrangement is the same of the WSS stationary analysis.

The 2D velocity fields are acquired in 21 different planes. The planes are parallel to the quartz windows and perpendicular to the CMOS camera, as can be observed in Figure 6.24. The measurements started in the symmetric middle plane until the distance of 20 mm with a 1 mm uniform spacing between consecutive planes. The resultant F.O.V. is illustrated in Figure 6.25. The measured region encompasses the flow around the injector cartridge. This F.O.V. also comprises the region where the spray-air interactions are studied with the two-phase PIV technique.

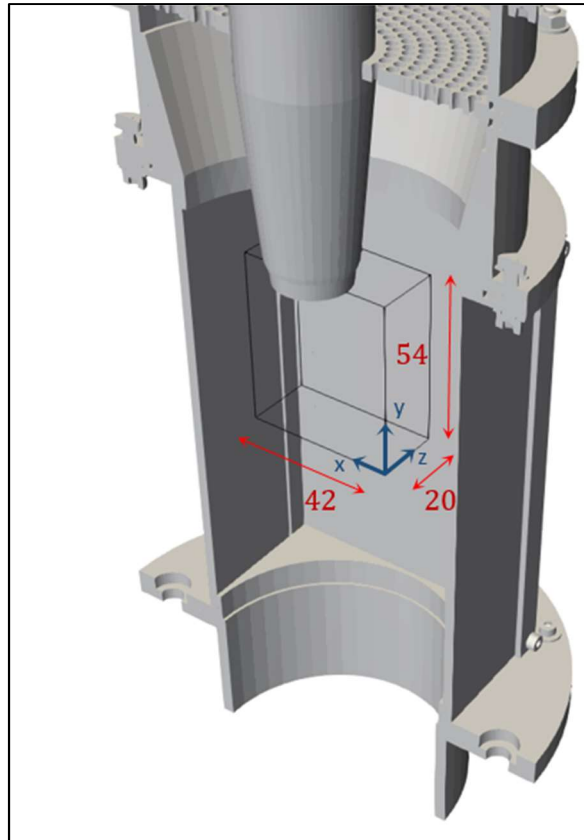


Figure 6.25 - The F.O.V. comprising the acquisition of the consecutive planes used in the estimation of the third velocity component. The dimensions are in millimeters.

The results of this section are obtained for a stationary condition without injection events. The air mass flow rate is kept at  $0.06538 \text{ kg/s}$ , resulting in a Reynolds number of  $4.18 \times 10^4$  using IESC hydraulic diameter. For each measured plane, the F.O.V. of  $42.2 \times 54.1 \text{ mm}^2$  are captured with  $1024 \times 800$  sensors and  $53.2 \mu\text{m}$  of pixel spatial resolution. 10,000 image pairs are acquired at each position with a sampling rate of  $2 \text{ kHz}$  in double-frame mode. The used PIV algorithm and the image processing were the same described in section 6.1.1. The final achieved vector resolution with the adaptive PIV method is  $0.5 \text{ mm}$ .

The in-plane velocity estimation is carried out with the approach described in section 5.7.3. Since the consecutive planes were acquired with a separation distance of  $1 \text{ mm}$ , the third velocity component was estimated with a spatial resolution of  $1 \text{ mm}$ . Two different boundary conditions are evaluated: The first boundary condition defined that the in-plane velocity ( $U_z$ ) has zero magnitude in the far most plane ( $z = 20 \text{ mm}$ ) using the coordinate system on Figure 6.24. The second used condition defined the  $U_z = U_x$  at the far most plane ( $z = 20 \text{ mm}$ ).

Since the velocity magnitudes in the vertical direction  $U_y$  are significantly higher than the horizontal component, as seen in the results of section 6.1.3, the two boundary conditions provided estimations with similar results. Minor differences were found on the estimations only near the plane  $z = 20 \text{ mm}$ . Thus, the results with second boundary condition are present since it provides an inhomogeneous velocity distribution at  $z = 20 \text{ mm}$ .

Figure 6.26 shows the results for the mean velocity distributions of the flow around the injector cartridge. The streamlines and the iso-volume are colored by the velocity magnitude. As expected, there is a formation of the recirculation structure downstream the injector cartridge. The effects of this low velocity region is still present further downstream. In the inlet air flow outside the recirculation zone, the velocity field has preferential vertical direction. Note the curvature of the velocity streamlines. This curvature resulted from the external air flow being pushed towards the axis of the recirculation zone. The same characteristic is noted in Figure 6.27.

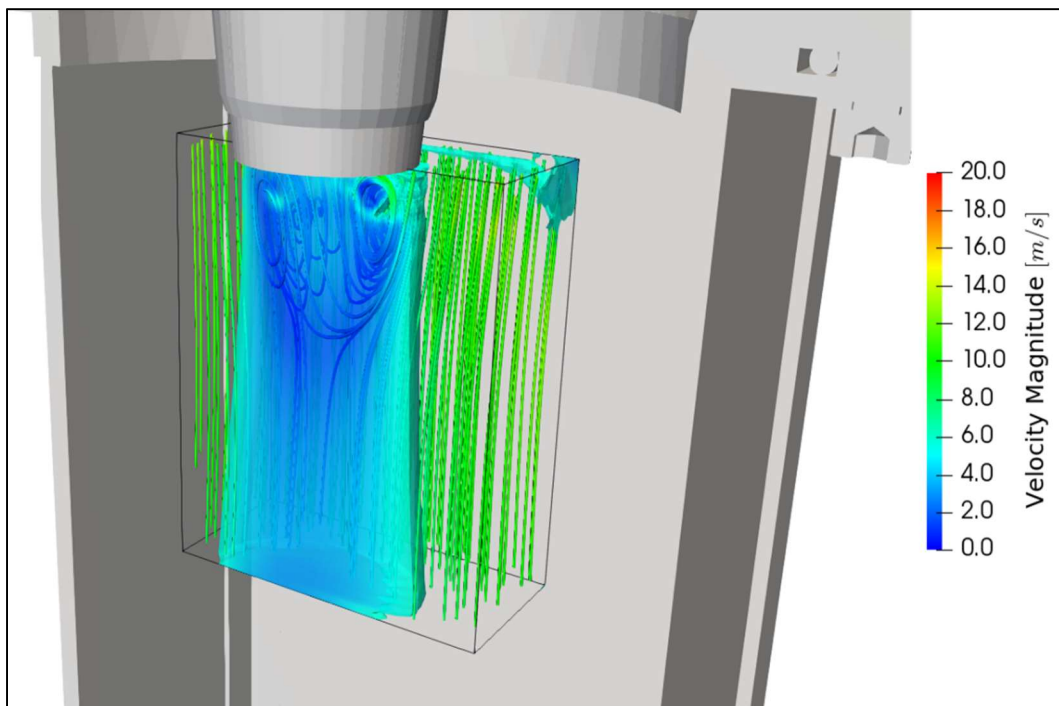


Figure 6.26 – The mean velocity field of the flow around the injector cartridge.

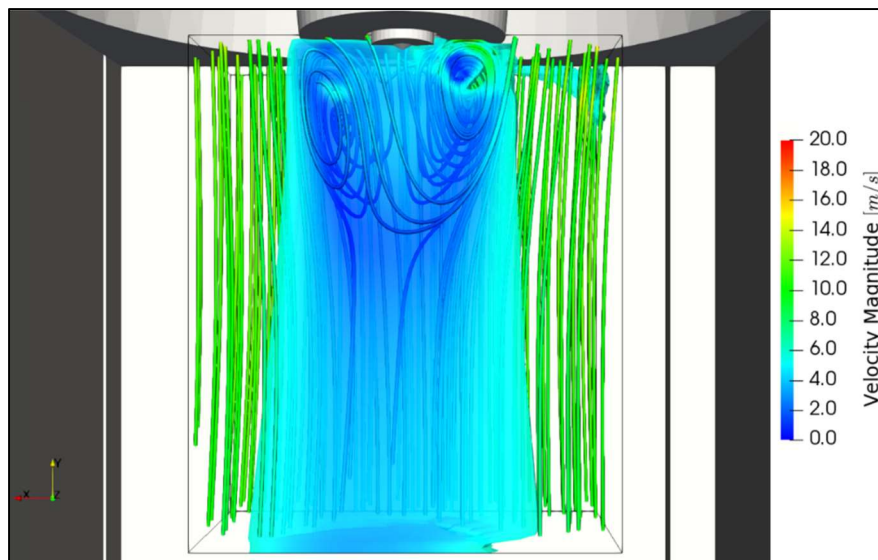


Figure 6.27 – The volumetric representation of the velocity magnitude of the flow around the injector cartridge.

Figure 6.28 shows the mean velocity components in the horizontal directions,  $U_x$  and  $U_z$ . The distributions present a half of the measured volume. This representation allows visualizing the flow behavior in the middle planes of IESC. Figure 6.28a shows the distributions of  $U_z$ . A low velocity magnitude can be observed throughout the volume. Magnitudes of the order of  $1.5 \text{ m/s}$  are found inside the recirculation zone. In the external flow, the  $U_z$  velocity magnitudes are of the order of  $-0.5$  to  $0.5 \text{ m/s}$ .

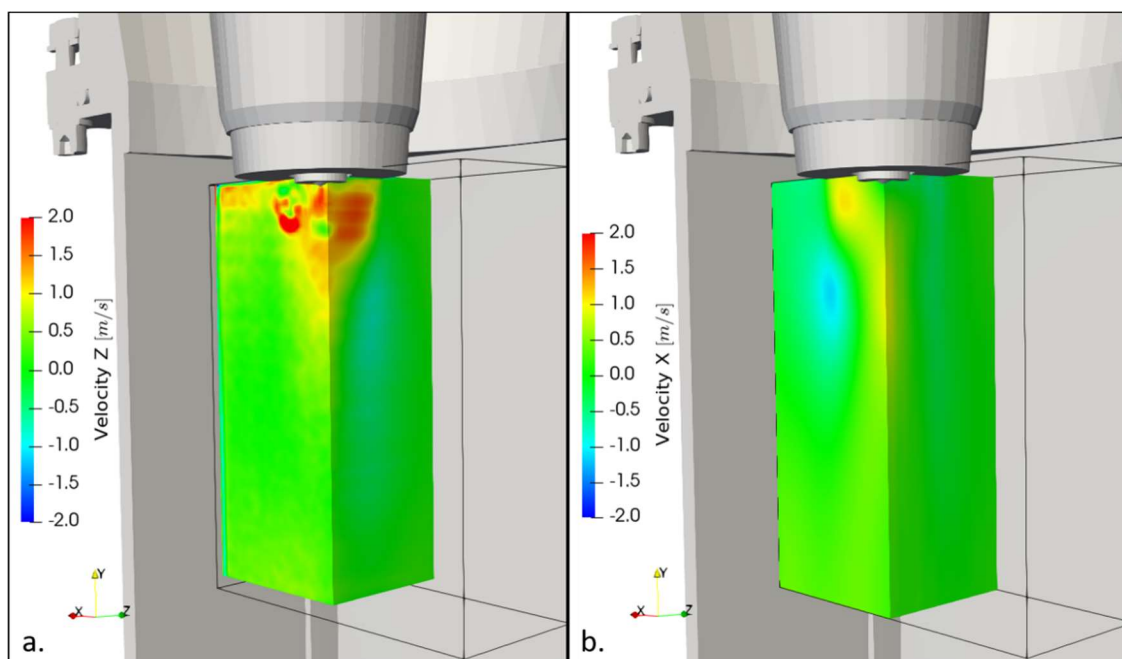


Figure 6.28 – The horizontal velocity components of the air flow in the measured volume. Figure a. – the  $U_z$  component and figure b. the  $U_x$  component.

Figure 6.28b shows the  $U_x$  velocity distributions over the measured volume. The  $U_x$  presents low magnitudes in the sample space similar to the  $U_z$  distributions. In the recirculation zone, the velocity magnitudes reaches  $1\text{ m/s}$  with distributions consistent with the recirculation structure. Immediately below this zone, the velocity magnitudes are also of the order of  $1\text{ m/s}$  but with the opposite sign. The same characteristic also appears in the  $U_z$  distributions and it is consistent with the observations of the streamlines curvatures. Outside the recirculation zone, the  $U_x$  magnitudes remains between  $\pm 0.5\text{ m/s}$ .

The estimation of the third velocity components allowed the evaluation of the in-plane motion. The results shown that the magnitudes of the third component are low when compared to the magnitudes in the vertical direction. In the recirculation zone, the horizontal components increase their magnitude in accordance to vortex formation. In the external air flow, these velocity components assume distributions closer to zero magnitude. Therefore, no significant influence of the in-plane motion is expected during the spray-air interaction analyses.

## 6.2 Sprays-air interaction analyses

In the spray-air interaction analyses, three different types of parameters are evaluated: one to control the air flow properties, one to control spray properties and one for the air flow turbulence characteristics. The air flow is controlled by the air mass flow rate in the inlet of IESC. The spray is modified by injection pressure. The air flow turbulence characteristics are changed with the sets of perforated plates. Table 6.2 shows the values of these parameters for the cases studied. The Reynolds number calculated with IESC hydraulic diameter is also reported. The integral length scale is estimated with the results of section 6.1.3 considering the air flow region not affected by the recirculation zone.

The experiments are organized by the sets of perforated plates. For each set, the air mass flow and the injection pressure are changed independently. For the air mass flow, two values are possible: The value of  $0.06536 \text{ kg/s}$ , which is the same air mass flow used in the stationary analyses, and the value 50% as high:  $0.09786 \text{ kg/s}$ . The values of the air mass flow represent the expected average air mass flow of a 1.4 liters DISI turbo-charged engine operating in mid-high loads between 2000 to 3000 rpm. Although the inlet air pressure is not at atmospheric conditions, the pressure effects are expected to be low at these conditions. The uncertainties in the air mass flow rate are the combined standard uncertainties (Type A + Type B). In the case of the injection pressure, the are 60 and 100 bar, which are common injection pressures in small DISI engines operating in middle loads. In all the case conditions, the injection time is fixed at  $3 \text{ ms}$  and the same the injector current profile is used. This injection time is in accordance to the conditions used to estimate the air mass flow rates. The experiments comprise nine cases, allowing the comparison of each parameter individually.

Since the analysis are focused in the air velocity fields during the spray event, the spray major characteristics were estimated using the classical spray formation theory. The liquid jet break-up regimes for the experimental conditions are depicted in red Ohnesorge diagram of Figure 6.29. Since the air velocity and injection pressure are modified during the experiments, the relative velocity between the liquid jet and airflow is not constant. Thus, different Reynolds number based on the liquid jet are obtained as a function of the relative velocity,

which was varied from 20 m/s to 65 m/s. The chosen values are representative of the expected relative velocities. Since the physical properties of the fuel, such as surface tension and density, are roughly the same in all case conditions, similar Ohnesorge numbers are expected. For all the experimental conditions, the liquid jet break-up is the Atomization regime. Thus, no significant effects of the boundary on the droplets formation and distribution are expected during the experiments. The values used in the estimations of the Ohnesorge and Reynolds numbers are shown in

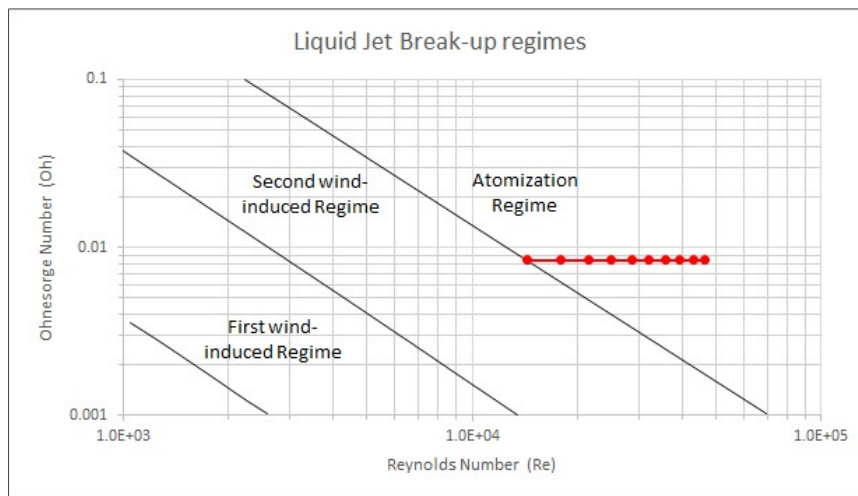


Figure 6.29 -The liquid jet break-up regimes in the experimental conditions.

Table 3 - Properties used to estimate the liquid jet break-up regimes during the experiments.

Properties	
Ethanol Fuel Density (kg/m <sup>3</sup> )	784.074
Ethanol Surface Tension (N/m)	0.02182
Ethanol Dynamic Viscosity (Pa.s)	0.001095
Injector orifice diameter (mm)	1.0
Relative velocity (m/s)	20~65

Table 6.2 - The conditions of the cases in the spray-air interaction analyses

Perforated plate		<i>PP2</i>			Integral length scale
	Air mass flow [kg/s]	Injection Pressure [bar]	Reynolds number [ ]	From inlet [mm]	
Case PP2-01	$0.06536 \pm 0.00080$	$100 \pm 5$	$4.18 \times 10^4$	2	
Case PP2-02	$0.06539 \pm 0.00088$	$60 \pm 3$	$4.18 \times 10^4$	2	
Case PP2-03	$0.09786 \pm 0.00095$	$100 \pm 5$	$6.25 \times 10^4$	2	
Perforated plate		<i>PP4</i>			
	Air mass flow [kg/s]	Injection Pressure [bar]	Reynolds number [ ]	From inlet [mm]	
Case PP4-01	$0.06614 \pm 0.00082$	$100 \pm 5$	$4.23 \times 10^4$	3.5	
Case PP4-02	$0.06568 \pm 0.00081$	$60 \pm 3$	$4.22 \times 10^4$	3.5	
Case PP4-03	$0.09674 \pm 0.00091$	$100 \pm 5$	$6.19 \times 10^4$	3.5	
Perforated plate		<i>PP6</i>			
	Air mass flow [kg/s]	Injection Pressure [bar]	Reynolds number [ ]	From inlet [mm]	
Case PP6-01	$0.06552 \pm 0.00078$	$100 \pm 5$	$4.19 \times 10^4$	5	
Case PP6-02	$0.06553 \pm 0.00083$	$60 \pm 3$	$4.20 \times 10^4$	5	
Case PP6-03	$0.09664 \pm 0.00092$	$100 \pm 5$	$6.18 \times 10^4$	5	

### 6.2.1 Acquisition of spray events

To investigate the interaction between air and spray development, the time-resolved air flow vector fields are obtained by means of the two-phase PIV technique described in section 5.7.2. Figure 6.30 shows the experimental apparatus. Two cameras are used. A bandpass filter centered at  $527 \pm 5 \text{ nm}$  is attached to the Spray camera to capture the scattered light from the spray. The Air camera captured the fluorescence signal from the doped tracer by coupling the set of low-pass filters to the camera lenses.

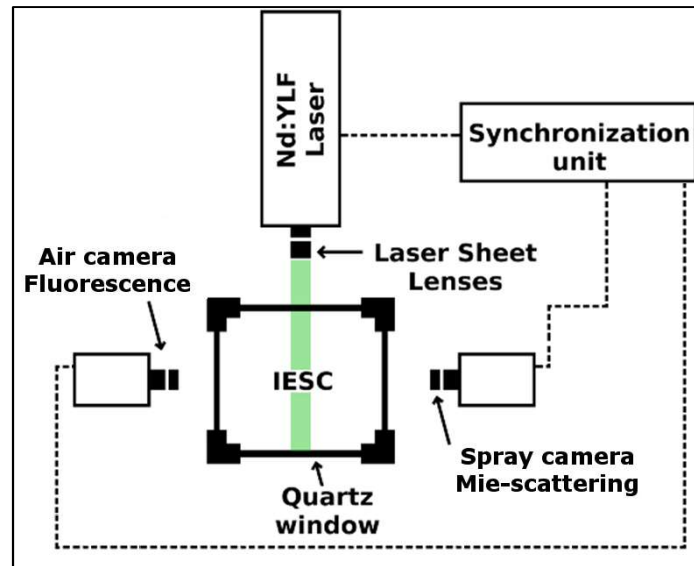


Figure 6.30 – The experimental arrangement for the two-phase PIV measurements.

The results presented in this section are sampled in the middle plane of IESC, as illustrated in Figure 6.30. In all runs, both cameras operated with the active pixel array of  $360 \times 512$  pixels. The resultant field-of-view (F.O.V.) is of  $20.4 \times 29 \text{ mm}^2$ . The regions are positioned at left portion of measurement plane and below injector tip, as shown in Figure 6.31. The position and size of the F.O.V are a tradeoff between visualization of the spray-air interaction zone and the maximum system acquisition rate.

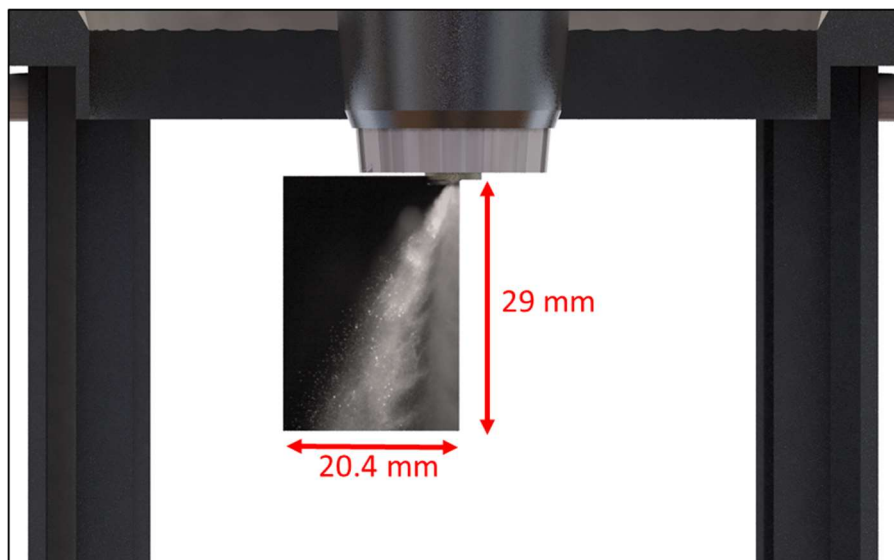


Figure 6.31 – The F.O.V. in IESC for spray-air interaction analyses.

The acquisition rate is fixed at 8000 Hz for all the case conditions. The time between pulses is fixed at 20  $\mu s$ . As described in section 5.6, the fuel injections are synchronized in the acquisition system. Thus, all the electric SOI had a known time instant related to the measurement. Figure 6.32 illustrates the event sequence of the measurements. The period between the subsequent injections is adjusted to ensure air flow stabilization after injection. The procedure to establish this period is discussed in the subsection 6.2.2. For each run, the PIV system captured a fixed number of instants. The amount of timestamps is adjusted as a multiple of the period between injections.

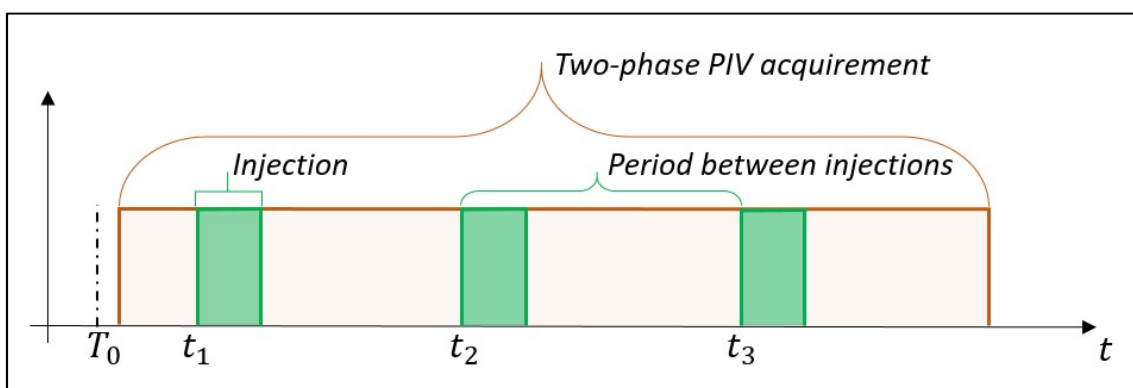


Figure 6.32 - The timing box representing the sequence of events during the two-phase PIV experiments

In each case, 255 injection events were capture. This value, as high as the common procedure [13] [8] [17] [3] [16], is chosen to improve convergence of the statistical properties. Due to camera memory limitations, the experiments were divided into runs of 17 injection events, resulting in 15 runs for every case. 360.000 image pairs were captured at each case condition. For all the cases studied, the amount of raw images reached 3.24 million. The adaptive PIV approach is used to calculate the velocity fields. The initial interrogation window of  $32 \times 32$  pixels is iteratively modified. A final interrogation window of  $8 \times 8$  pixels is achieved with a vector spatial resolution of 0.45 mm . The methodologies of image processing, air velocity fields calculations and post processing are described in sections 5.7.1.4 and 5.7.2.2.

## 6.2.2 Statistical description of the spray event

Since the development of the spray and its interaction with surrounding air are time dependent statistical random processes, it is necessary to analyze their properties as statistical variables. Therefore, all the results are based on the ensemble-average of the temporal evolution of sprays, named as the spray event.

Figure 6.33 shows the temporal evolution of the velocity in a point inside the measurement plane for one of the cases studied. The temporal evolution can be divided in three different regions. The first region, before SOI, the velocity is marginally stable. During the injection, the velocity magnitude changes. After the injection, the velocity decreases to its initial level. This procedure is repeated for each case condition and different points in space are analyzed. A time window is properly chosen to ensure velocity stabilization for the most critical case. The time window of 100 ms is considered sufficient for the spray events. This fixed value are used in all case conditions.

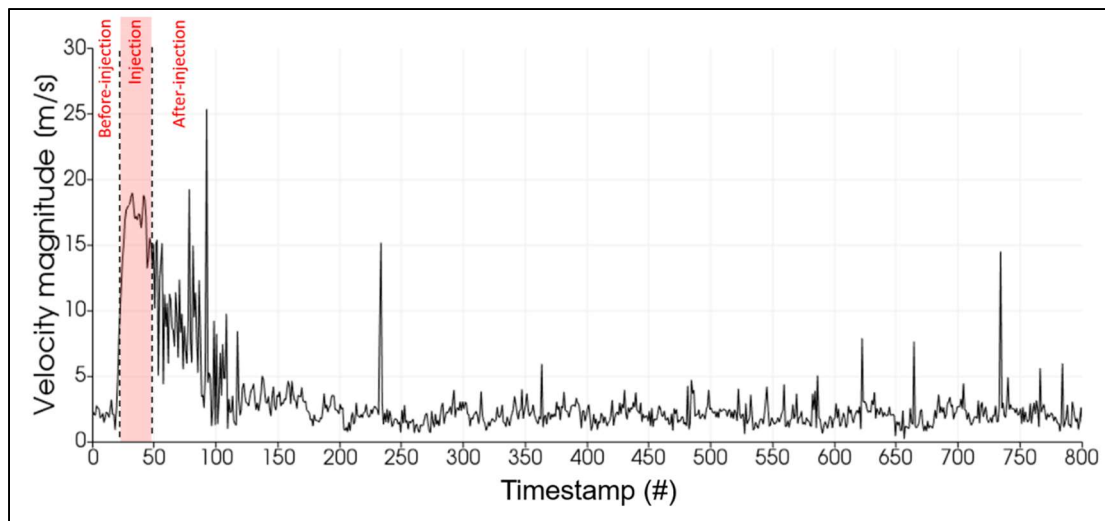


Figure 6.33 – The velocity magnitude evolution for a particular point in the sample space. A proper choosing of time window is necessary to evaluate the spray ensemble-average temporal evolution.

The ensemble-averages of the variables of interest, denoted as  $x_i(t)$ , are calculated with equation 6.6, where  $n$  is the number of captured spray events,  $(t)$  indicates the temporal dependence of the random variable,  $X_{i,n}(t)$  is the instantaneous value of the variable in the  $i$  direction for spray event number  $n$

$$x_i(t) = \frac{1}{n} \sum_{1}^n X_{i,n}(t) \quad 6.6$$

The variance over the ensemble-average, or the phase-average variance, is obtained with equation 6.7. Note that, due to the transient characteristics, the temporal dependence remains on the statistical variables.

$$x_i'^2(t) = \frac{1}{n-1} \sum_{1}^n \left( X_{i,n}(t) - x_i(t) \right)^2 \quad 6.7$$

For convenience, to any random variable mentioned in the text, it should be understood that the properties refers to its ensemble-average value. To the rest, a clear specification is used. For example, when referring to the variable velocity, discussion are drawn over the ensemble-average velocity of a point or set of points. The velocity of a specific event should be addressed as the instantaneous velocity.

With the definition of mean and variance, the statistical variables related to velocity are evaluated. The ensemble-average mean velocity and its variance are calculated with equations 6.6 and 6.7. The approximated mean kinetic energy distributions per unit of mass, named as mean kinetic energy for simplicity, are calculated at each point with equation 6.8.  $u_x$  and  $u_y$  denote the ensemble-average velocity components in the horizontal and vertical directions respectively. Since the measurements are obtained as 2D velocity fields, the component normal to measurement plane is considered equal to the horizontal component. Compared to the vertical velocity, the horizontal component is considered small. This approximation is expected not to significantly interfere in the analyses. The estimations of the third component with the tomographic stationary analysis are reported in section 6.1.1.

$$Ek(t) \cong \frac{1}{2} \left( 2u_x^2(t) + u_y^2(t) \right) \quad 6.8$$

The approximated turbulent kinetic energy per unit of mass or simply turbulent kinetic energy (TKE) is calculated with equation 6.9. An approach for the third component similar to the mean kinetic energy calculation is used. The variables  $u_x'^2$  and  $u_y'^2$  represent the velocity variance for the horizontal and vertical directions.

$$k(t) \cong \frac{1}{2} (2u_x'^2 + u_y'^2) \quad 6.9$$

The ensemble-average turbulent intensity is calculated with equation 6.9, where  $u_i'$  is the fluctuation of the  $i$  velocity component at a specific coordinate and instant.  $u_i$  is the ensemble-average velocity for the same point and instant.

$$I_i(t) = \frac{u_i'(t)}{u_i(t)} \quad 6.10$$

As discussed in section 6.1.2, the necessary number of samples to converge the statistical quantities is not known a priori. To evaluate if the number of acquired spray events is sufficient, the ensemble-average velocity and variance are calculated as a function of the number of samples. Figure 6.34 shows these quantities calculated in two points of one condition studied. The chosen time instant is 2.625 ms after SOI. The instant represents a condition in which fluctuations are expected to be high due to presence of the spray. In the case of the ensemble-average velocity, the values are stable after 50 samples. In the case of the ensemble-average variance, a higher number of samples is required. This quantity reaches stable conditions only after about 120 samples. Although not shown in the figures, the others conditions and other time instants were also analyzed. The 255 injection events are considered sufficient to converge the statistical variables in all the conditions studied.

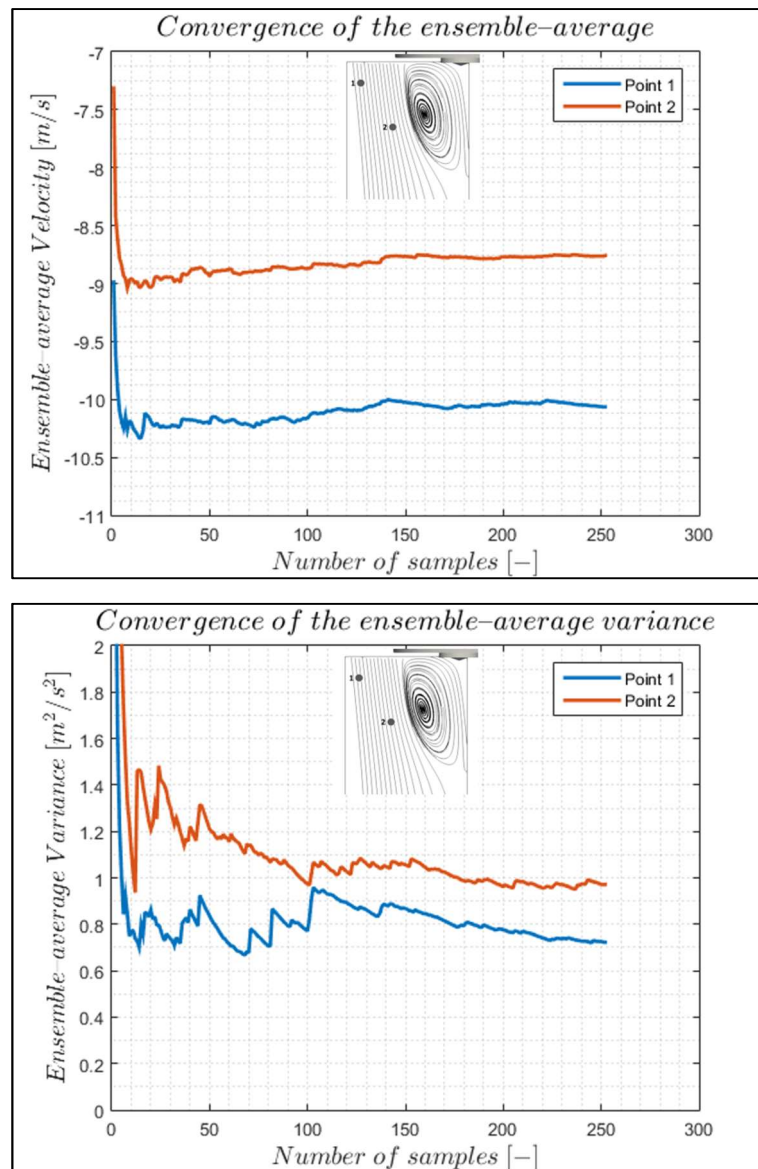


Figure 6.34- The ensemble-average velocity and variance as a function of the number of samples. The values are calculated in two point inside the velocity fields. The points are represented in the streamline illustrations.

## 6.2.3 Global development of the air flow velocity fields

### 6.2.3.1 Perforated plates set PP4: 4 mm

The phase averaged temporal evolution of the air flow velocity fields during the spray event for case PP4-01 is shown in Figure 6.35. The inlet air flow rate is  $0.06536 \text{ kg/s}$ . The fuel injection pressure is  $100 \text{ bar}$ . The object in the top of the images represents the injector tip position related to the F.O.V. Nine time instants were chosen to illustrate the spray event. The first instant shown corresponds to  $-0.125 \text{ ms}$ . The negative value in  $-0.125 \text{ ms}$  represents instants before SOI. In this instant, the velocity field presents features of to the stationary condition: a low-velocity recirculation structure below injector tip and the main stream with higher velocity. Images (2) to (6) comprise three different stages of air-spray interaction. In the first stage, the initial spray development, fuel is injected in the chamber and the velocity field is little affected. Note, for example in image (2), the recirculation structure below the injector tip is still present albeit the spray is in the early phase. Over the next instants, the spray destroys the recirculation structure and penetrates further in the air flow field. In image (4), the beginning of second stage, the spray reached the *quasi*-steady condition. At this instant, interaction affects not only the boundary between air and spray but the air flow field far from spray. By comparing images (1) to (4), the velocity field at the mainstream region altered significantly. The vectors changed from the vertical movement towards the direction normal to the spray boundary. A considerable acceleration of the air velocity vectors is observed during second stage (images (4) and (5)). This acceleration is related to high spray penetration velocity during injection, which causes a pressure gradient between air flow inlet and the region inside the fuel plumes. In some regions, the velocity magnitudes increases more than 50%. The last stage encompass the end of injection and the return to the stationary conditions. Images (7) to (9) shows the stabilization of the airflow field after injection.. Note that in image (7), the spray velocity was visible together with the air velocity fields. At the end of injection, the fuel plumes became less dense and the droplet clusters could be used as signal tracers. It was decided not to remove the signal from this instant and further since it could provide insights into the spray-air interaction after EOI.

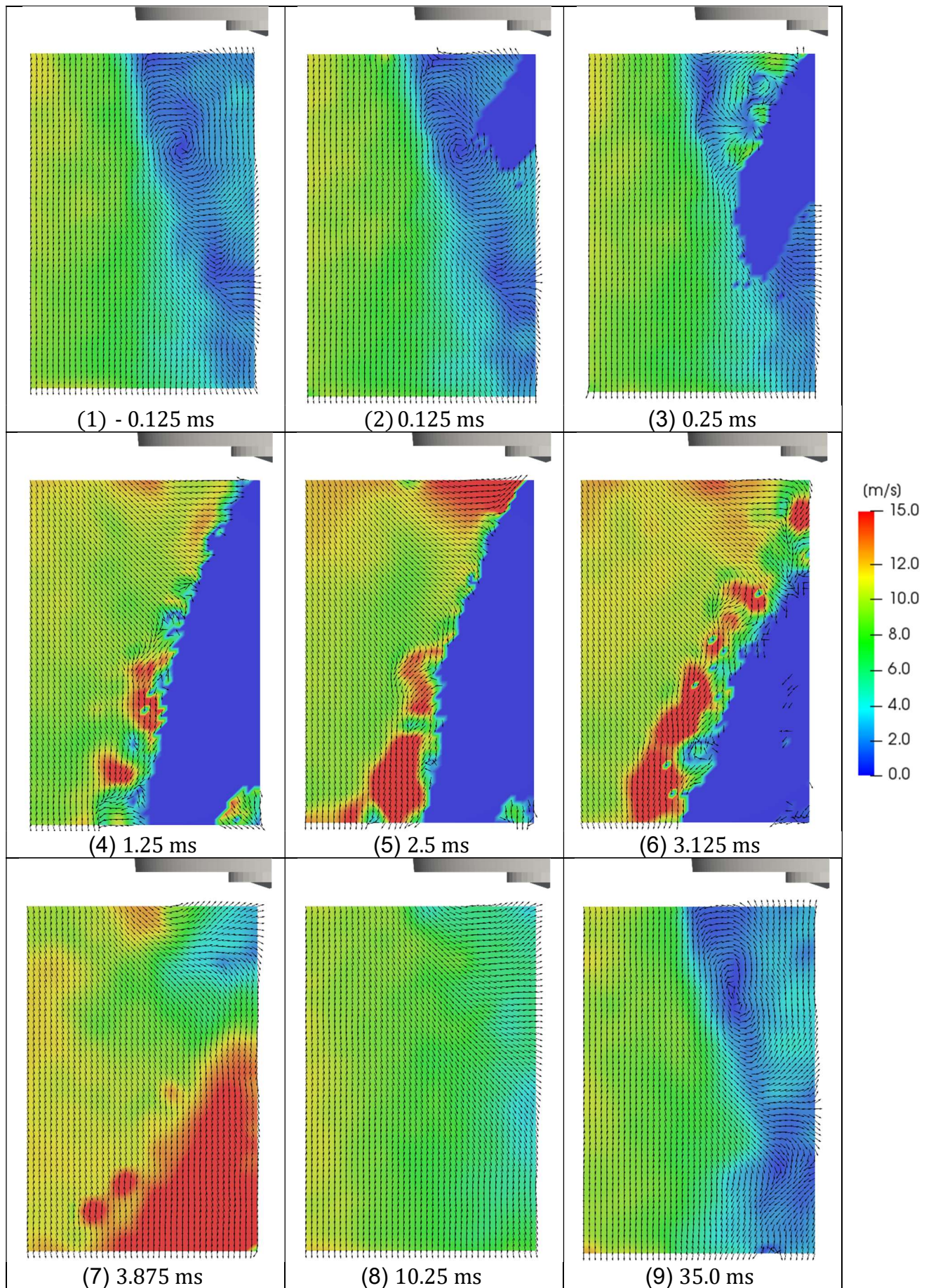


Figure 6.35 – The global development of the air flow velocity during spray event in Case PP4-01.

Figure 6.37 shows the ensemble-average temporal sequence for case PP4-02. In this configuration, the air mass flow rate is  $0.06536 \text{ kg/s}$  and the injection pressure modified from 100 to 60 *bar*. The same characteristics observed previously were also present at this case. The spray event also presents three stages: images (1) to (3) show the initial stage of spray development where the stationary structure is modified. From images (4) to (5), the spray development reaches the second stage in the *quasi*-steady condition. By comparing the cases PP4-01 and PP4-02, velocity distributions are observed to be similar throughout the temporal evolution. The difference lies in the acceleration magnitude. In the case PP4-02, with injection pressure at 60 bar, a lower pressure gradient was imposed between the inlet and the spray plumes. As a result, the velocity magnitudes at image (5) were lower near injection tip due to this acceleration decrease. Images (7) to (9) represent the third stage – the end of injection phase and stabilization of stationary conditions.

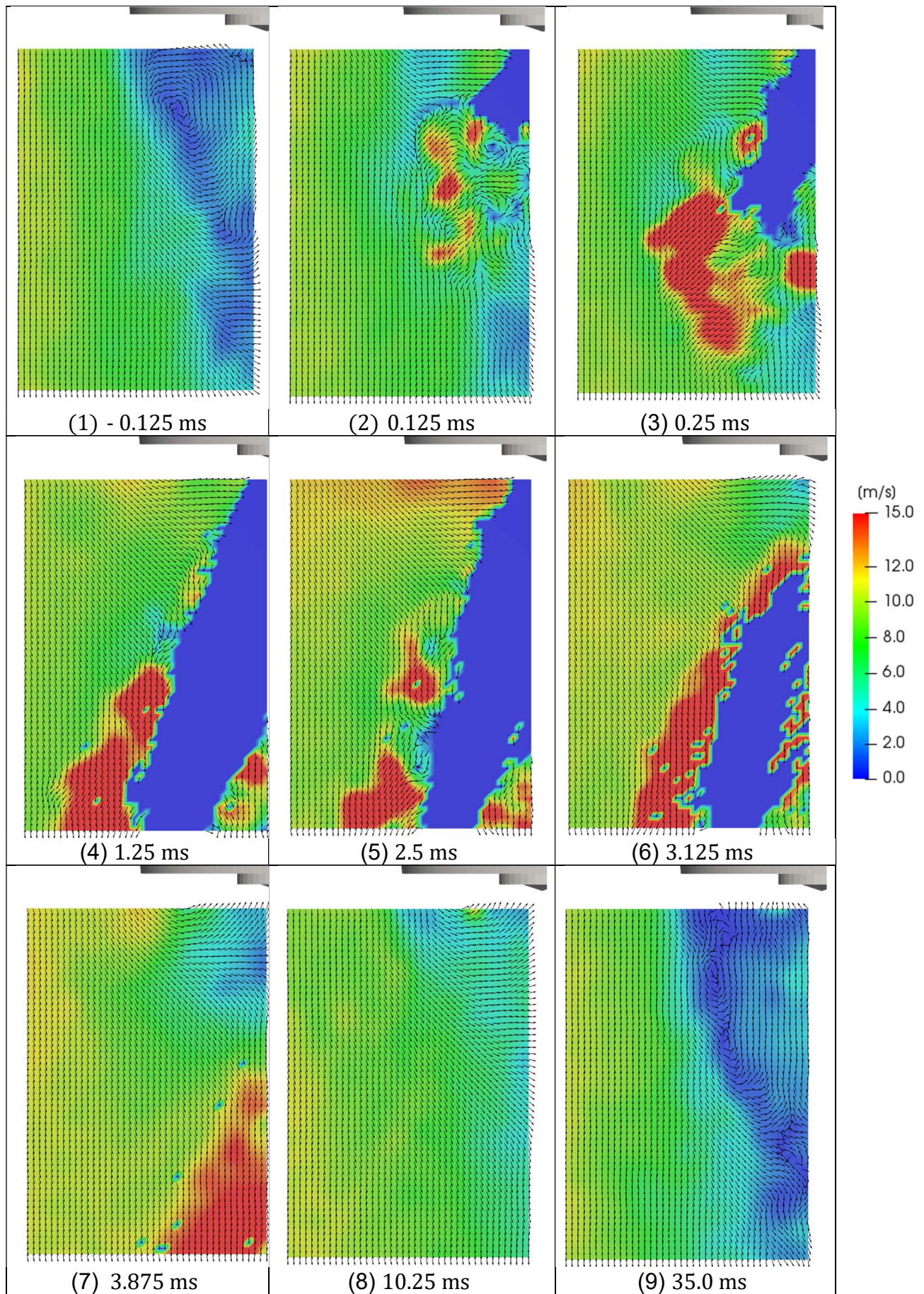


Figure 6.36 - - Global development of the air flow velocity during spray event for Case PP4-02

The ensemble-average temporal evolution of the spray event for case condition PP4-03 is shown in Figure 6.37. The air mass flow rate changes from 0.06536 to 0.09674  $kg/s$  and the injection pressure remains constant at 100  $bar$ . To allow the comparison between the image sequences, the color ranges for all the three cases are the same. In the case PP4-03, the velocity fields has higher magnitudes than the previous cases due to the elevated air mass flow rate. The same development behavior are observed for this case condition. Although not visible in the image sequence due to color range limitations, the velocity magnitudes near injection tip during second stage (image (5)) were higher than the overall air velocity field distribution.

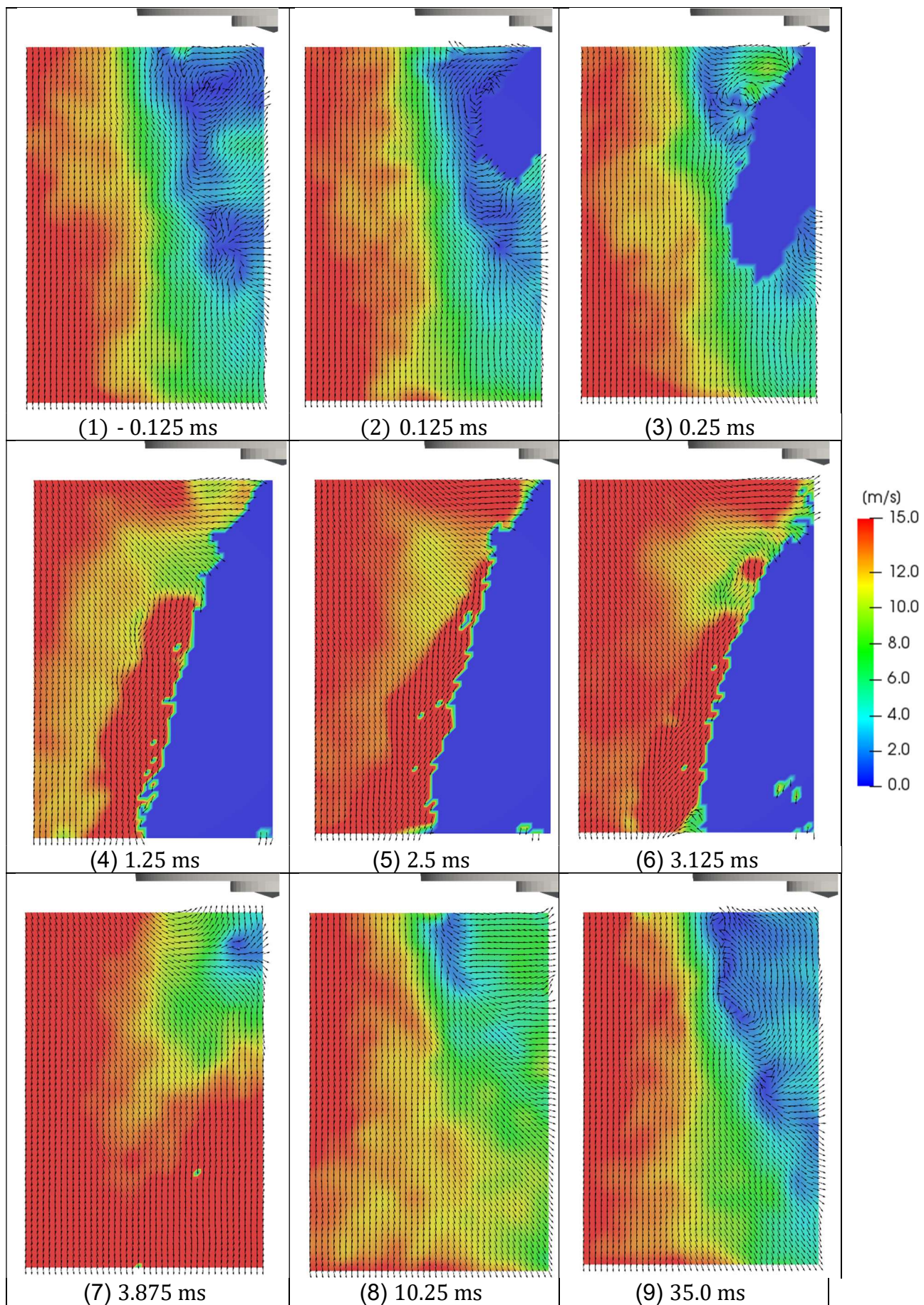


Figure 6.37 - Global development of the air flow velocity during spray event for Case PP4-03

### **6.2.3.2 Perforated plates set PP2: 2 mm**

Figure 6.38 shows the results of the case PP2-01. The air mass flow and the injection pressure are similar to the case PP4-01:  $0.06536 \text{ kg/s}$  of air and  $100 \text{ bar}$  of injection pressure. The instant (1) shows the last instant before SOI. As discussed in section 6.1.3, for these two perforated plates set, the mean recirculation structures assume similar shapes and positions. By comparing Figure 6.38 to Figure 6.35, the development for both conditions are very similar. In terms of the ensemble average velocities, there are no significant differences in the distributions during the first and quasi-steady stages. After the injection, at  $10,25 \text{ ms}$  after SOI, the recirculation structure is visible below the injection tip for the case PP2-01. This recirculation vortex is transformed and transported until the position of the recirculation on stationary conditions. Due to slightly differences between the F.O.Vs of the cases PP4 and PP2, this structure was not visible in the perforated plates set PP4.

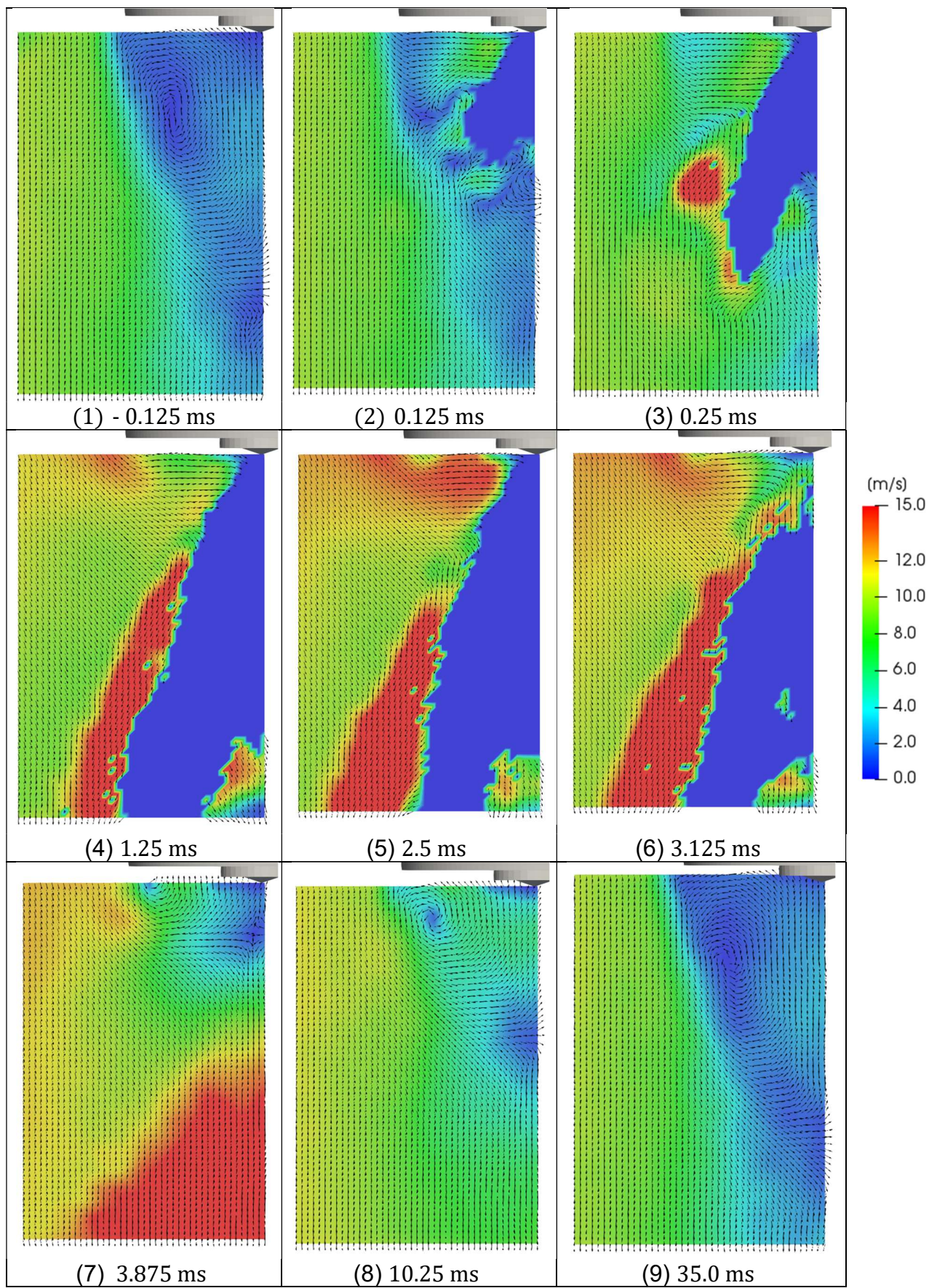


Figure 6.38 – The global development of the velocity distributions during spray event for Case PP2-01

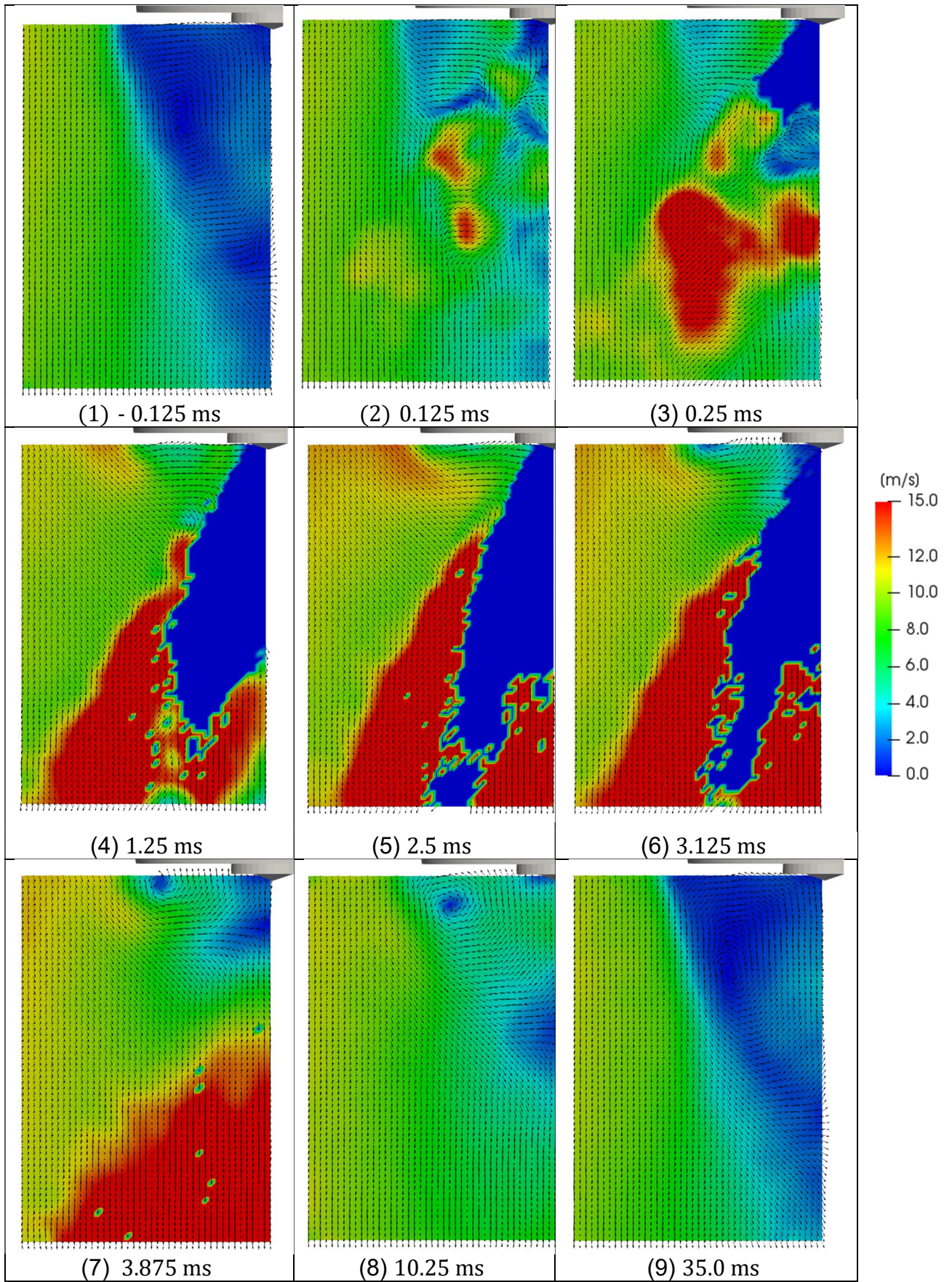


Figure 6.39 – The global development of the velocity distributions during the spray event for Case PP2-02

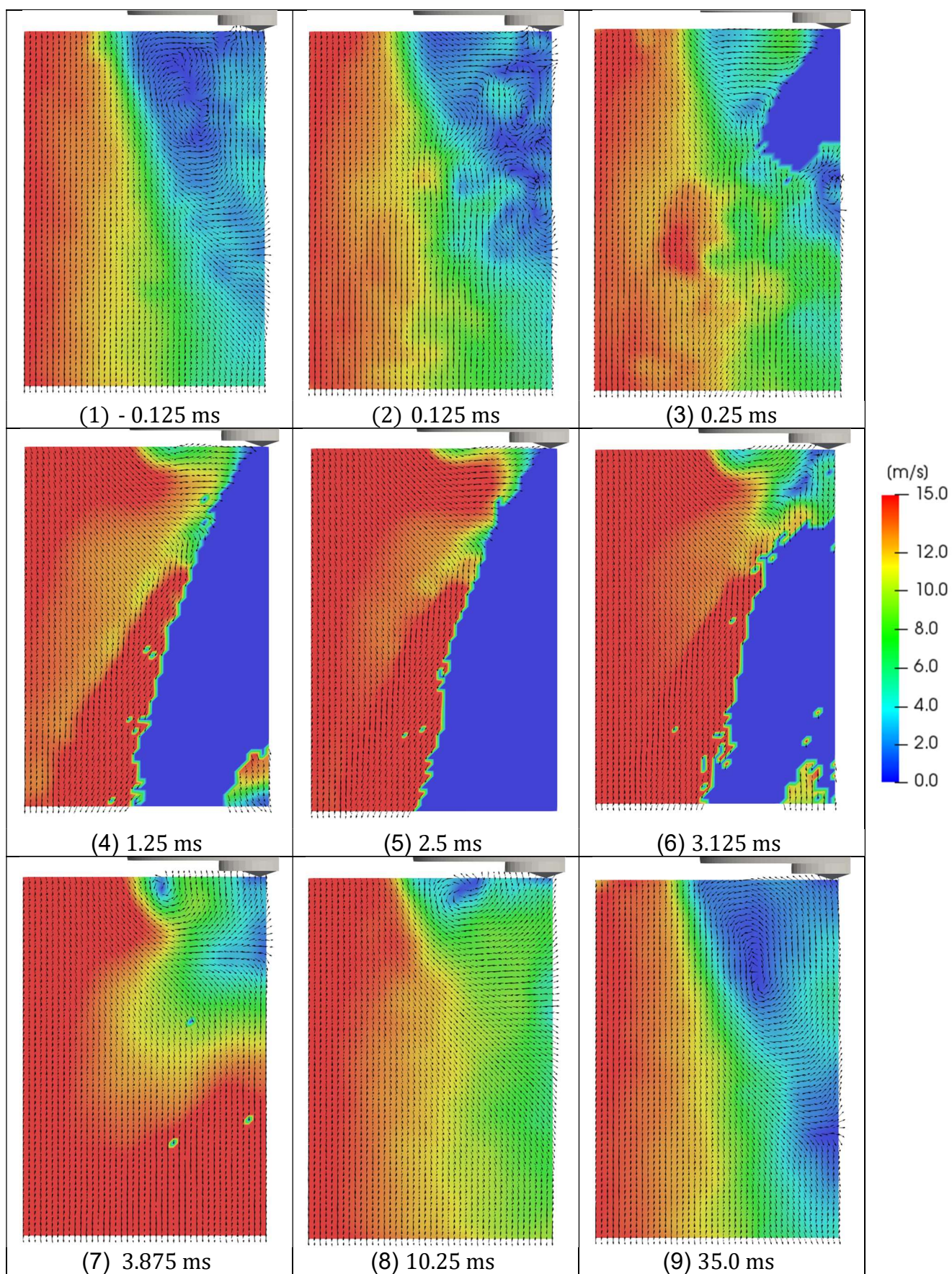


Figure 6.40 – The global development of the velocity distributions during the spray event for Case PP2-03

Figure 6.39 presents the global evolution of the velocity fields for case PP2-02. In this case, the air mass flow is similar to case PP2-01 and the injection pressure is reduced from 100 to 60 *bar*. The injection pressure reduction is not able to modify the major characteristics of the spray. The effects are similar to case PP4-02 – lower velocity magnitudes when compared to the case of higher injection pressure. The same pattern is formed throughout the injection – the initial settlement of the spray plumes, the quasi-steady regime where the surrounding air flow is accelerated and the stabilization of the stationary conditions.

For the case of highest air mass flow - PP2-03, the air flow field development during the spray event is also comparable to the evolution of case PP4-03. Figure 6.40 shows the results for this case. A minor difference between the cases occurs near the injector cartridge during the injection. For case PP2-03 there is a formation a low velocity region that remains until the end of injection. A recirculation vortex is formed after the end of the spray. As for the other cases of PP2, this vortex becomes the main recirculation structure during the stationary conditions, as can be observed from the instants 8 to 9.

### **6.2.3.3 Perforated plates set PP6: 6 mm**

Due to geometric limitations of the perforated plates set PP6, the injector cannot be placed with the same orientation of other two plates set. As result, the visible injector plumes are different from those of the previous cases. Nevertheless, this difference can be used to evaluate if the air flow fields developments in the spray surroundings have similar behaviors.

Figure 6.41 shows the results for case PP6-01. The last recorded instant before SOI shows the recirculation structure with the behavior of the stationary conditions. In this set of perforated plates, the recirculation center is positioned differently from the other two sets. By comparing the spray event with the previous cases, the velocity fields evolution present similar characteristics, regardless of the plumes orientation. During the first instants after SOI, the air flow field is modified – the velocity changes from main vertical movement to the direction normal to the spray boundary. As the sprays evolves inside IESC, the air flow field is accelerated due to the pressure gradient imposed by the spray. Near the injector cartridge, the air flow for case PP6-01 present a similar behavior of the cases from perforated plate set PP2: a low velocity region that creates a recirculation vortex after injection. At instants after  $10.25\text{ ms}$ , this structure becomes part of the recirculation structure that reaches the stationary conditions.

Figure 6.42 and Figure 6.43 shows the spray event development for the case conditions of PP6-02 and PP6-03. By observing both image sequence, it is clear that the behavior is consistent with the previous perforated plates set. No major differences between the cases are observed in the global development. The velocity magnitude are modified according to the injection pressure and the air mass flow respectively. At the end of injection, the air flow field behavior is also similar to the previous cases. After  $35\text{ ms}$ , the air flow fields resemble the stationary conditions in both cases.

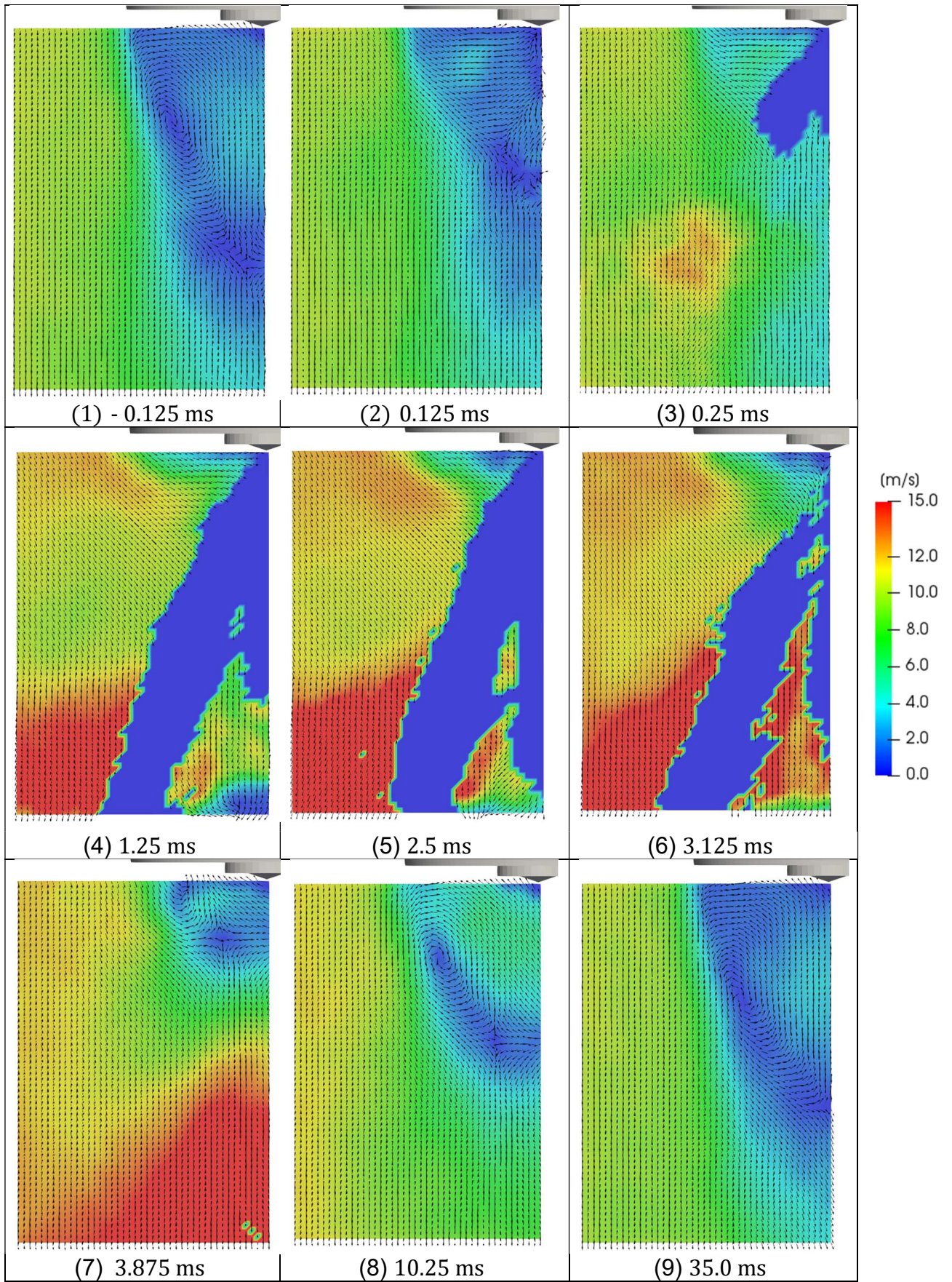


Figure 6.41 - Global development of the air flow velocity during spray event for Case PP6-01

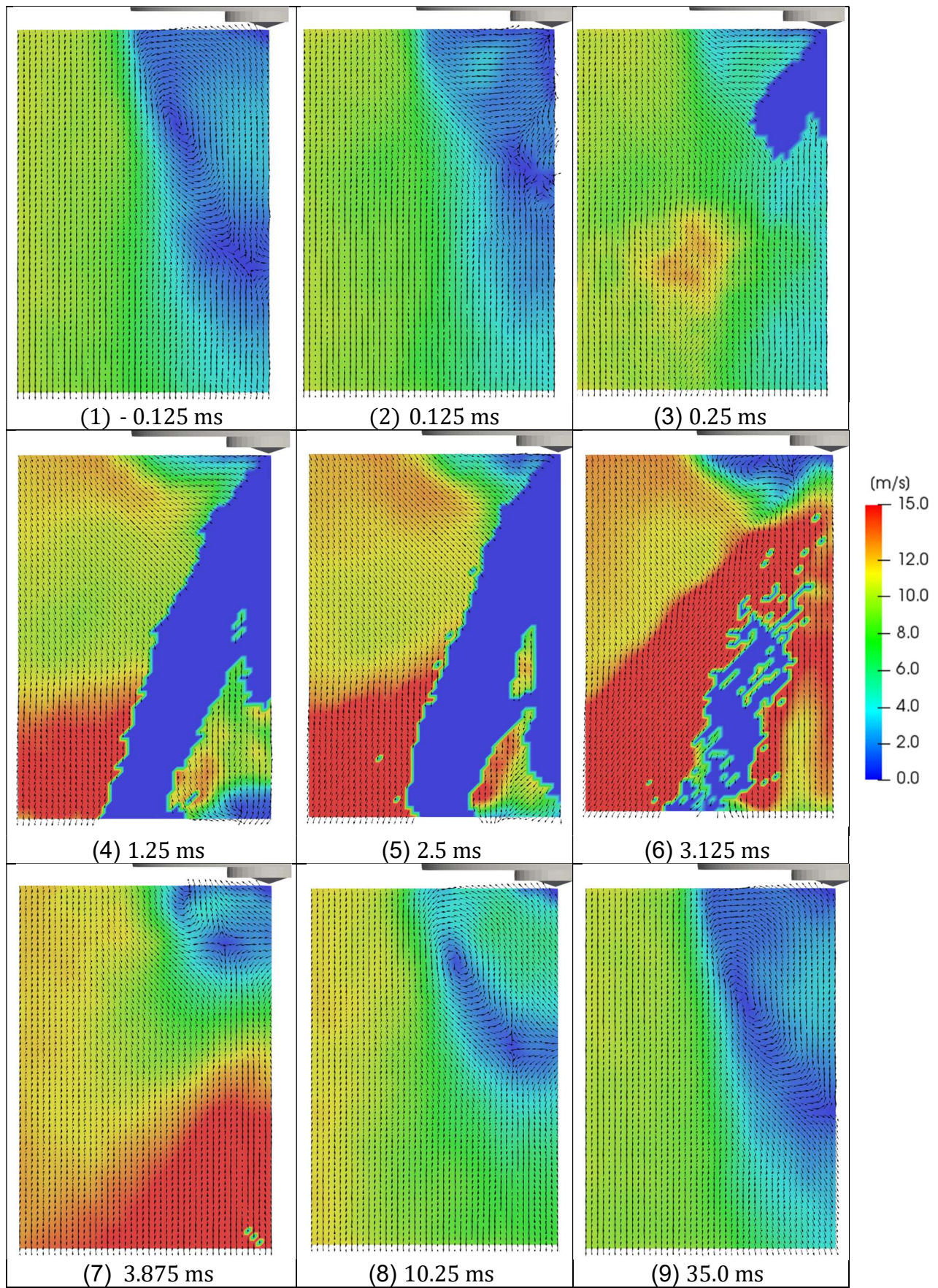


Figure 6.42 - Global development of the air flow velocity during spray event for Case PP6-02

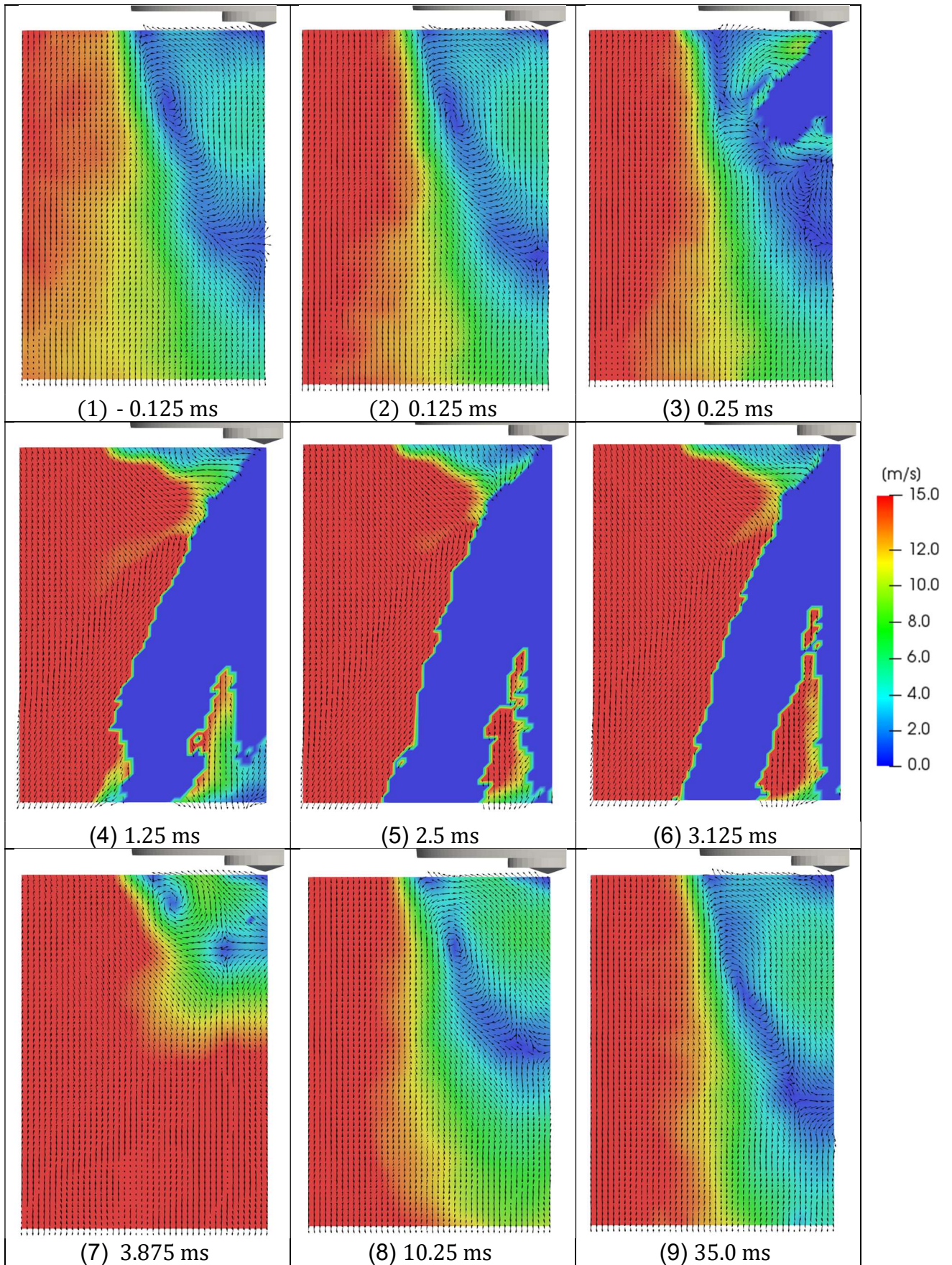


Figure 6.43 - Global development of the air flow velocity during spray event for Case PP6-03

In the global development of the spray events, the velocity fields evolve with the same mechanism regardless of the modification of the control parameters. During the first acquired instant after SOI, the velocity field is reorganized due to the rapid movement of the spray. In all the cases, the pressure gradient between the inner regions of the spray and surrounding air modifies the direction of the velocity fields near the plumes boundaries. The air suffers an acceleration during the quasi-steady phase of injection. This acceleration is present in all the case conditions. However, the magnitudes changes according to the injection pressure. The inlet air mass flow modifies the velocity magnitudes during the spray event, which may increase the air penetration in the inner region of the spray.

Different spray orientations, as observed for the cases of perforated plate set PP6 do not alter the evolution mechanism. After the end of injection, fuel is transported out of the measurement plane. The velocity field reaches the stationary conditions in roughly the same period for all the case conditions.

#### 6.2.4 Effects of the perforated plates set

In this section, the effects of the perforated plates set in the spray development are studied. The case conditions are compared in terms of the velocity and the turbulent intensity distributions. To isolate the effects of the perforated plates, the compared cases have similar values of the inlet air mass flow and the injection pressure.

Figure 6.44 shows the ensemble velocity fields for the cases PP4-01 and PP2-01 at the instant  $0.25\text{ ms}$  after SOI. At this stage, the fuel spray penetrates inside the recirculation zone formed during the stationary conditions. Since the velocity magnitudes in this region are low, a recirculating vortex develops over the spray boundary. This structure is responsible for the establishment of a feedback mechanism that modifies the velocity field near the spray plumes. This condition is similar to those found on the literature for the quiescent conditions ( [9] [10] [11] [4] and others). By comparing both case conditions, no significant difference in the velocity field is observed. The behavior is expected and it is consistent with the results for the stationary conditions. Since the initial recirculation structure for both cases are very similar, no major differences are expected at this early phase.

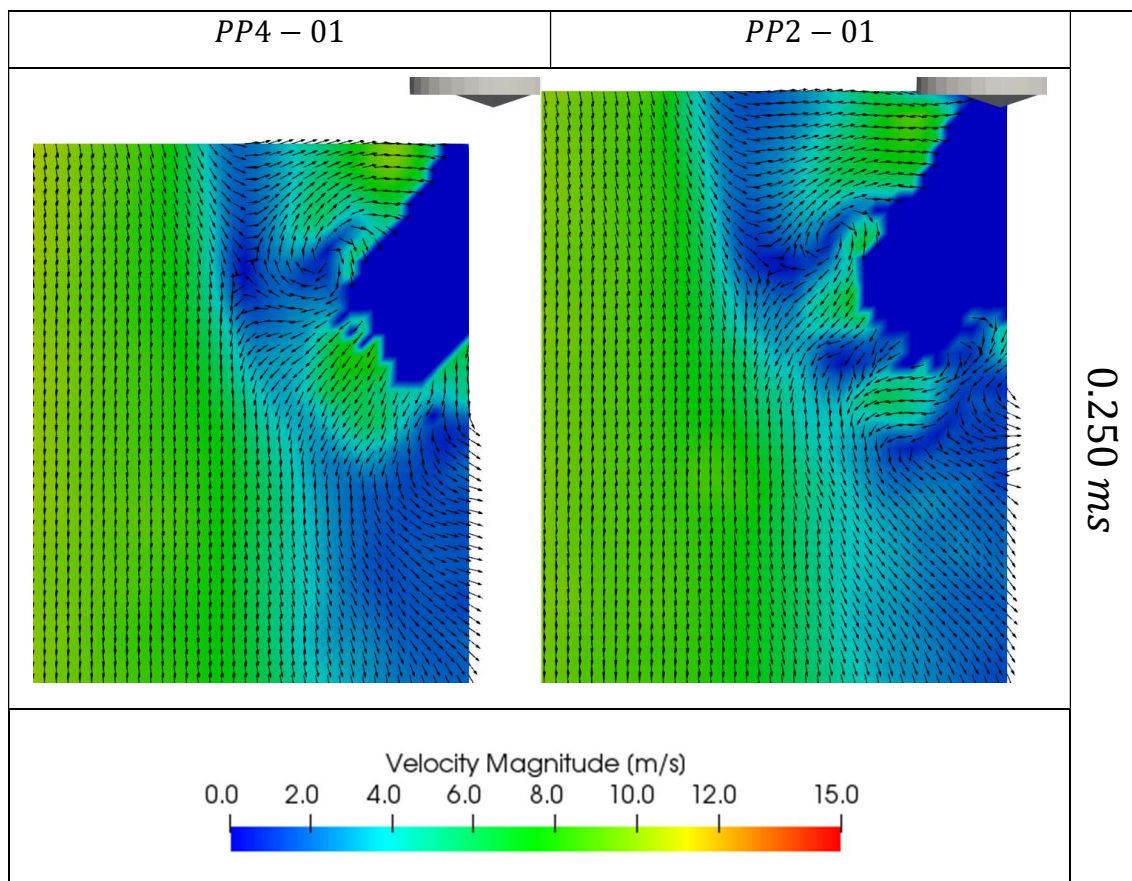


Figure 6.44 - Comparison of the case conditions: PP4-01 and PP2-01. The effects of the perforated plates set. Timestamp: 0.25 ms after SOI.

During the next acquired instant, the spray penetrates the velocity field out of the recirculation zone. Figure 6.45 shows the velocity fields for this instant. Differently from the previous instant, no recirculation structure can be observed over the spray boundary or below the injector tip in both cases. Thus, no feedback mechanism from the spray tip to the lateral boundary can be formed. The velocity distributions near the spray plumes are directed towards the spray boundary.

Note the presence of a high velocity cluster near the spray tip in both cases. By observing the time evolution, this cluster is the result of the previous recirculating vortex being removed from its initial position due to high-velocity fuel spray. Although not shown in the figures, this cluster propagates in the subsequent acquired instants.

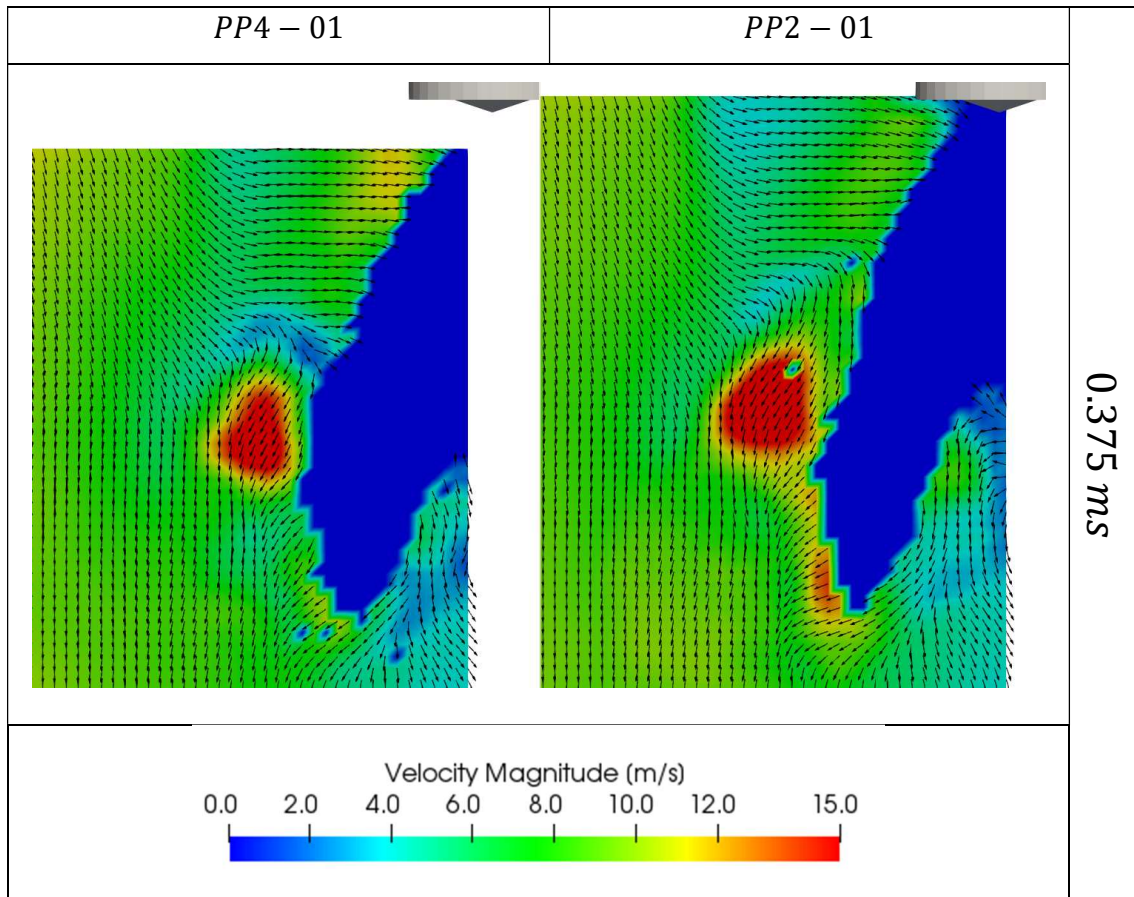


Figure 6.45 - Comparison of the case conditions: PP4-01 and PP2-01. The effects of the perforated plates set. Timestamp: 0.375 ms after SOI

Figure 6.46 shows the velocity fields distributions at 2.625 ms after SOI. During this stage, the spray development are in quasi-steady conditions. In both conditions, the velocity fields are oriented towards the spray boundary. The velocity near the injector tip increases, reaching roughly the same distributions in both cases. The velocity fields increased even for the region distant from the spray boundary.

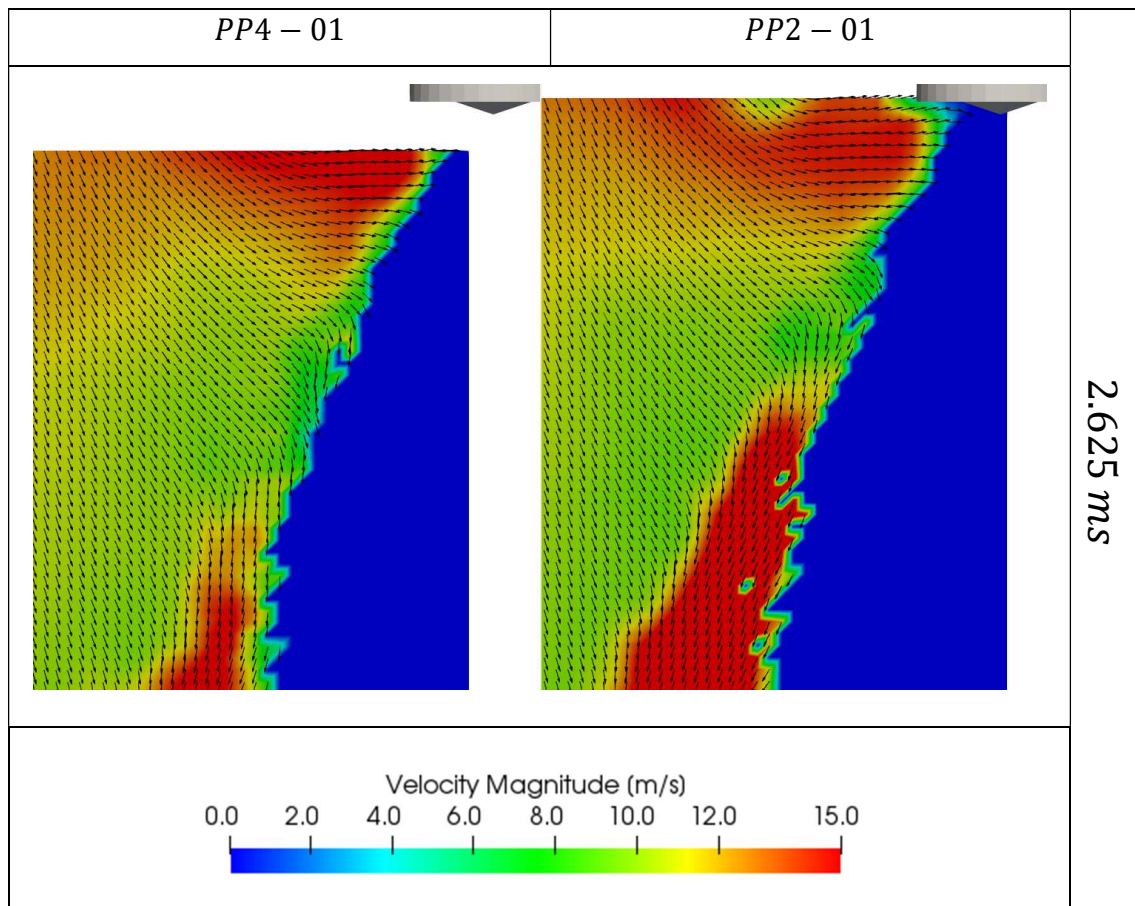


Figure 6.46 - Comparison of the case conditions: PP4-01 and PP2-01. The effects of the perforated plates set. Timestamp: 2.625 ms after SOI

The comparison for the instant 3.250 ms after SOI is shown in Figure 6.47. This stage represents the second acquired instant after the end of injection. By comparing both case conditions, no significant difference is noted in the ensemble velocity fields out of the spray region.

With the needle valve closing, a low velocity field is formed below the injector tip. Over the next instants, this low velocity region expands until reaching the stationary conditions. A high velocity region is formed on the upper part of the sprays to compensate the sudden decrease in the fuel mass flow over the region. This velocity increase is similar to the end-of-injection phenomenon and penetration waves described in the literature. Note that the high velocity region is present in both cases. The velocity magnitudes associated with the penetration wave are similar in the two cases.

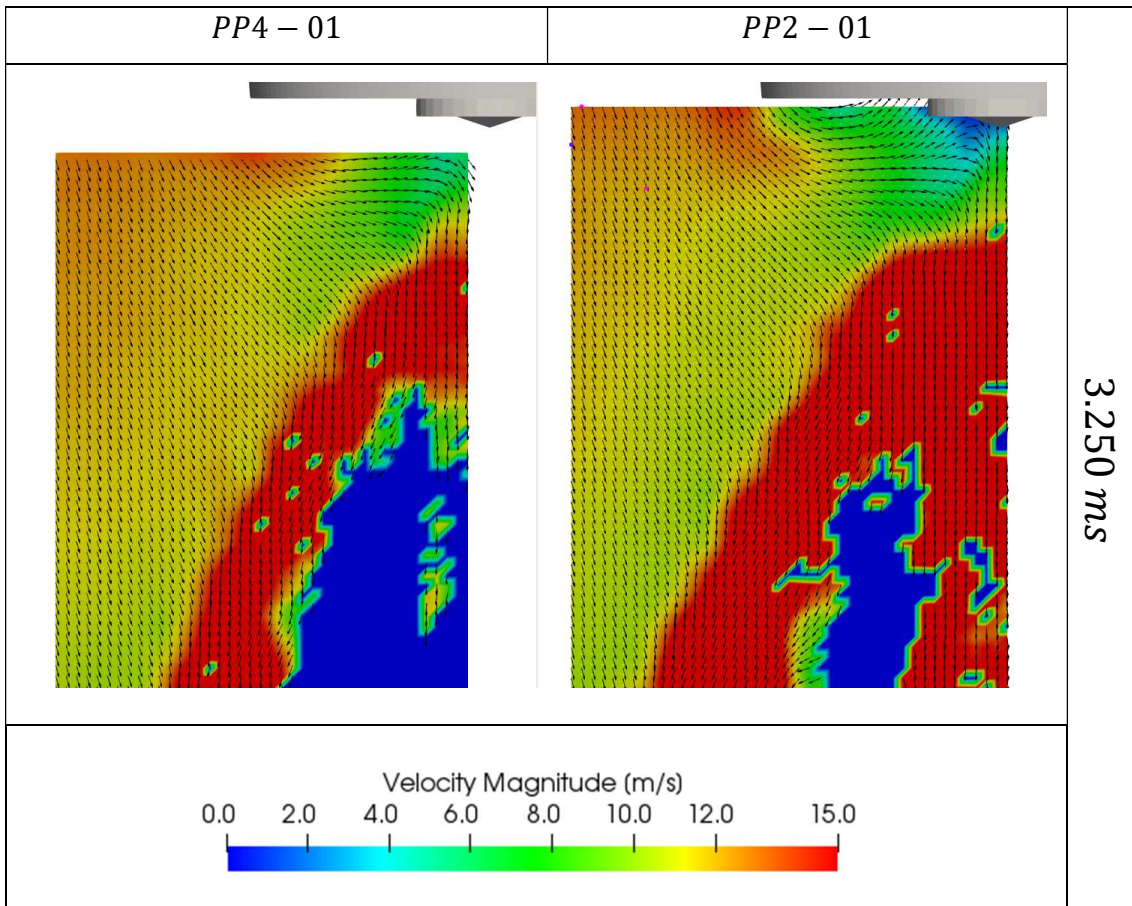


Figure 6.47 - Comparison of the case conditions: PP4-01 and PP2-01. The effects of the perforated plates set. Timestamp: 3.125 ms after SOI

The analysis with the ensemble velocity fields indicates that the velocity fields develop in a very similar pattern for both perforated plates set. The structures formed at each injection stage are present in both case conditions and their evolution are similar. No significant effects of the incoming turbulence integral scales can be observed on the ensemble velocity fields evolution.

To evaluate the effects in the turbulence field, the same two cases are compared with respect to their phase-average turbulent intensities. These are calculated with the vertical velocity component – the  $y$  direction (see section 6.2.2). Figure 6.48 shows the results for the instant 0.250 ms before SOI. Without injection, the turbulent intensity fields resemble the stationary conditions. Below the injector cartridge and further downstream, the values associated with the recirculation structure are high. In the air flow out of the recirculation zone, the values are lower and are consistent with the effects of each plates set. In the case PP2-01, the turbulent intensity in the outer region is lower when compared with case PP4-01.

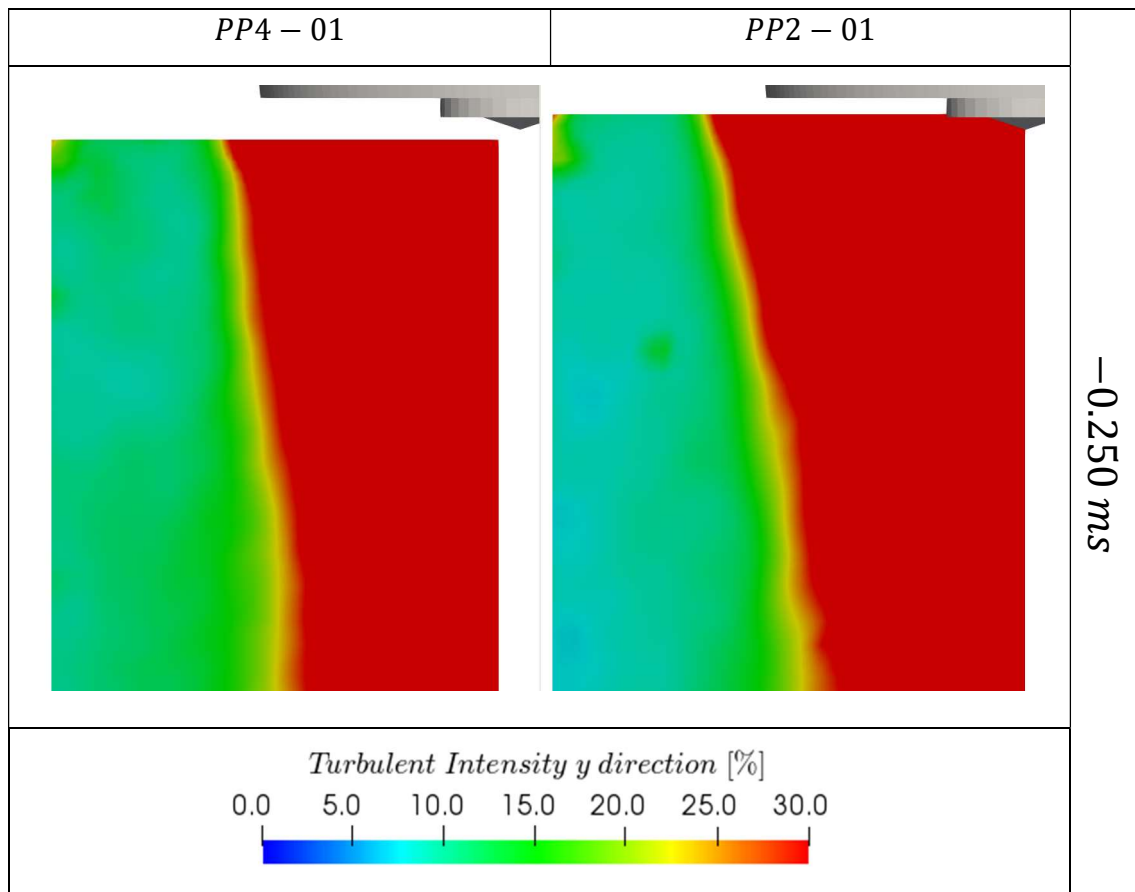


Figure 6.48 - Turbulent intensity calculated with  $y$  direction component. The comparison between cases conditions PP4-01 and PP2-01. 0.250 ms before SOI.

Figure 6.49 shows the turbulent intensity distributions for the 0.250 ms after SOI. During this stage, the spray plumes reached the recirculation zone. The effects on the turbulence intensity fields are observed near the tip of the sprays. Over the remaining regions, the distributions still resemble the stationary conditions.

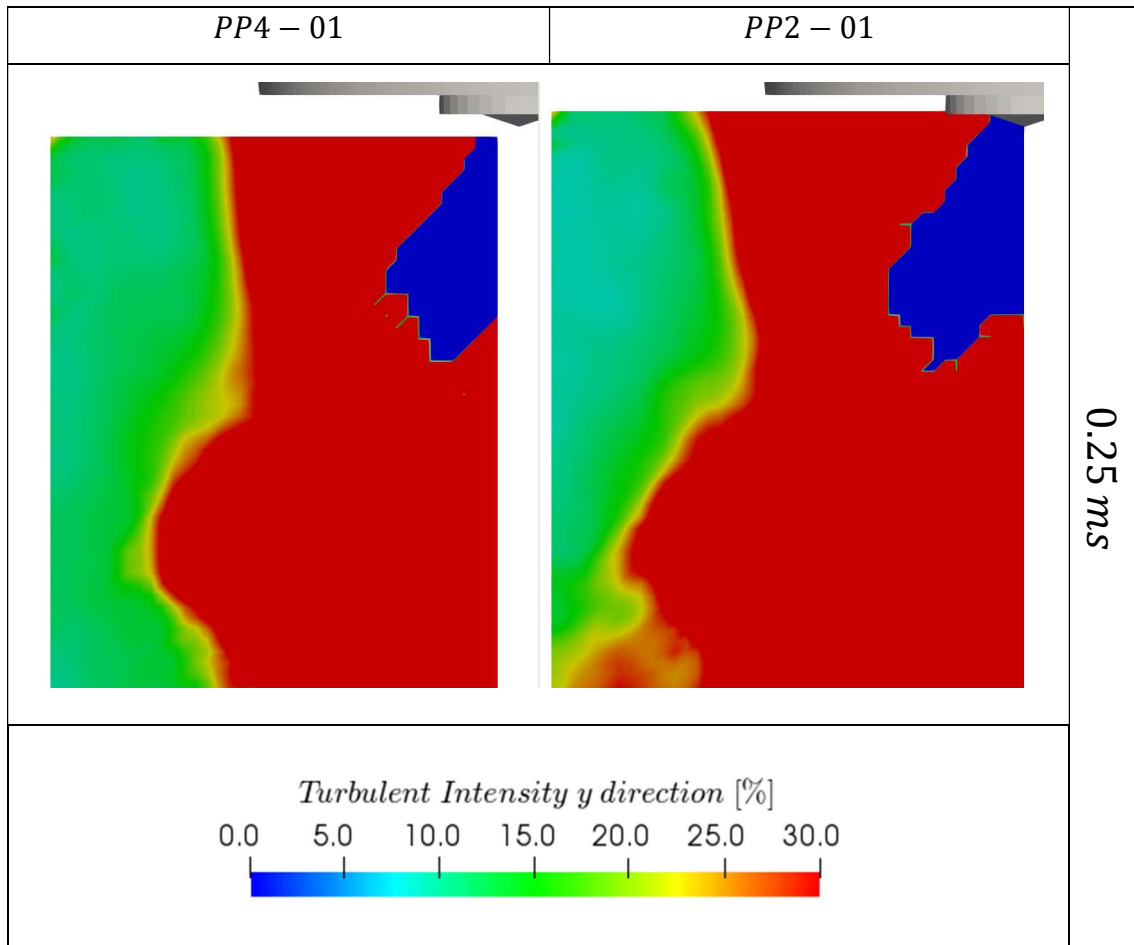


Figure 6.49 - Turbulent intensity calculated with  $y$  direction component. The comparison between cases conditions PP4-01 and PP2-01. 0.250 ms after SOI

The next acquired instant shows the spray plumes reaching the velocity fields out of the recirculation zone. Figure 6.50 shows the turbulent intensity distributions for this time instant. The region near all the spray boundaries presents an elevated fluctuation level. The spray boundary is a highly active zone where fuel droplets and the air flow are constantly interacting. Thus, close to the spray boundaries the velocity fluctuations are subjected not only to turbulence fluctuations but to spray variations and droplets interaction. These active zones are present during the injections in all the cases studied. For the regions outside the spray boundary, the turbulent intensity distributions are still unaffected. These results are consistent with the velocity distributions. In the same instant, only the velocity near spray boundary has been significantly modified.

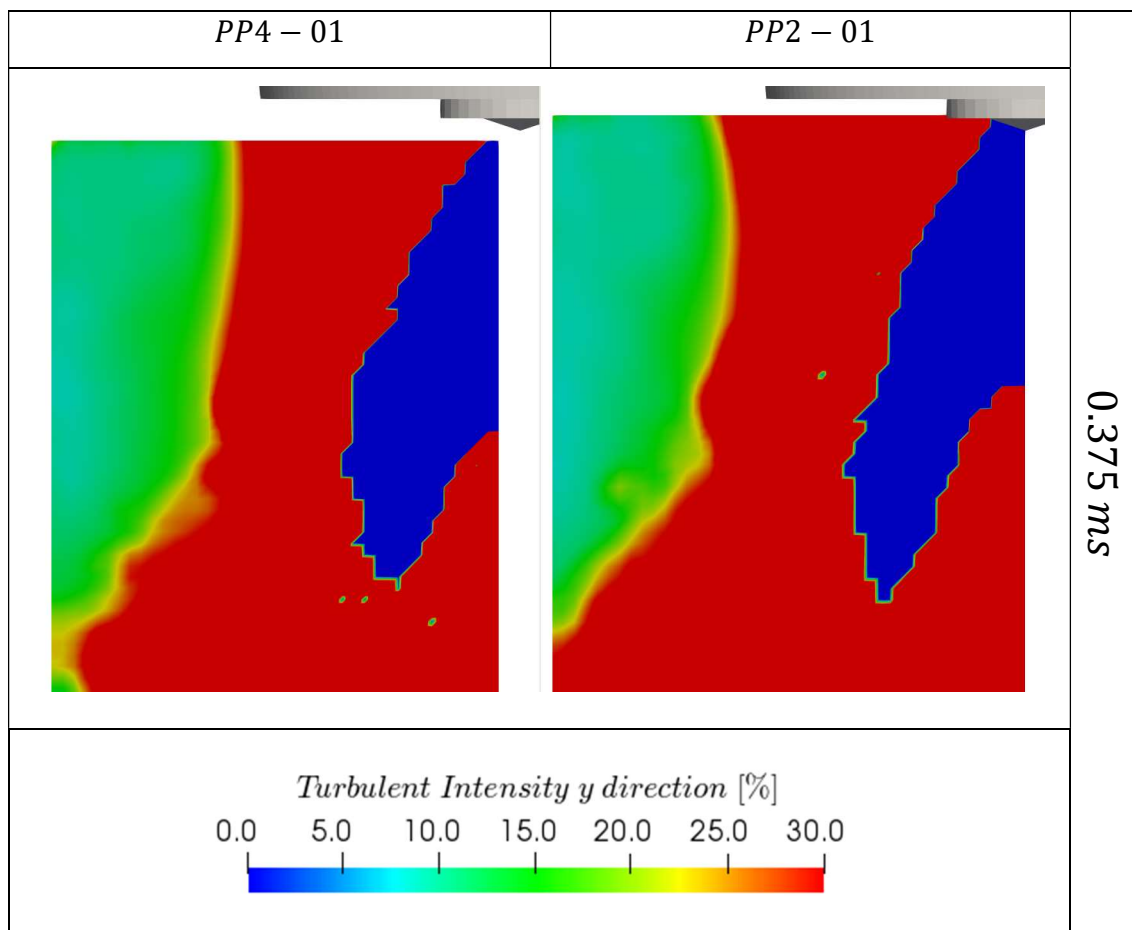


Figure 6.50 - Turbulent intensity calculated with  $y$  direction component. The comparison between cases conditions PP4-01 and PP2-01. 0.375 ms after SOI

The turbulent intensity distribution for the time instant 2.625 ms after SOI is shown in Figure 6.51. At this stage, the sprays are in the quasi-steady regime. In both cases, there is an overall reduction of the turbulent intensity levels for the velocity field outside the spray boundary. These reductions initiate at the beginning of the spray formation and continues throughout injection. By observing the velocity distributions in the same time instant, a relation is to be noted between the turbulent intensity levels and the velocity vectors. Due to the pressure gradient between the outer and inner spray regions, the velocity fields are reoriented towards the spray boundary. As seen on the velocity distributions, this pressure gradient is also responsible for accelerating the flow field around the spray. In the turbulent intensity distributions, an additional effect driven by this mechanism is observed. During the same instant, the velocity fluctuations decrease. With a higher velocity magnitude and a reduced velocity fluctuation, turbulent intensity levels are reduced. Since the pressure gradient occurs with every injection, the

turbulent intensity decrease in both conditions. The effects continues until the pressure gradient is ceased.

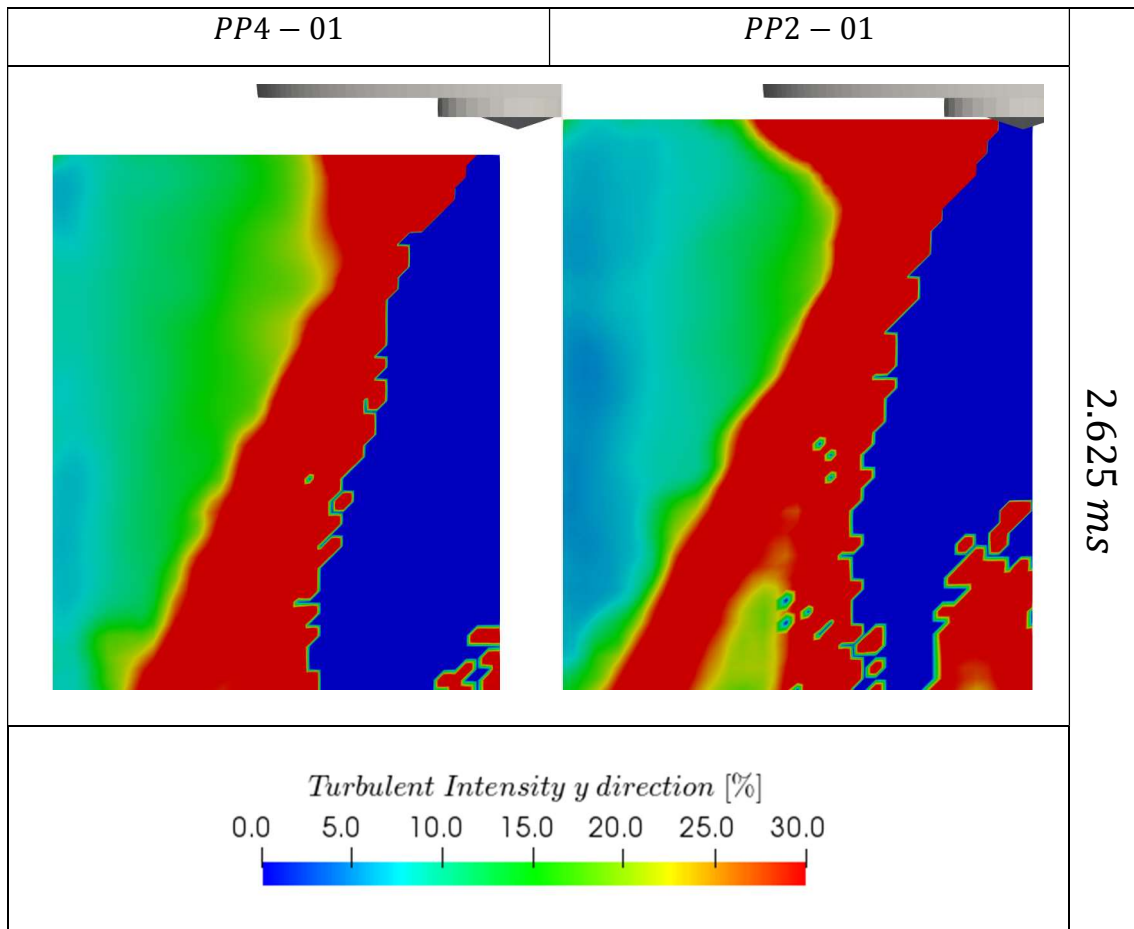


Figure 6.51 - Turbulent intensity calculated with  $y$  direction component. The comparison between cases conditions PP4-01 and PP2-01. 2.625 ms after SOI

By comparing the results for the two perforated plates set, different distributions are observed. In the case with higher inlet turbulence integral scales, case PP4-01, the turbulent intensity levels are higher at the velocity field when compared to the same region of case PP2-01. In the case PP4-01, turbulent intensity levels remains around 12% at this region. For the case PP2-01, these values are between 5 to 8%. In the regions near the spray tip and in the air flow at the left portions of the distributions, the turbulent intensity levels are roughly the same in both conditions.

Figure 6.52 shows the turbulent intensity distributions at the time instants  $3.125\text{ ms}$  and  $3.375\text{ ms}$  after SOI. These distributions correspond to the time instant  $0.125\text{ ms}$  and  $0.375\text{ ms}$  after the end of injection, respectively. With the needle valve closing event, the pressure gradient mechanism is no longer present. However, at the instant  $0.125\text{ ms}$ , the turbulent intensity fields have not changed significantly from the previous conditions. With the transport of the spray out of the field of view, the high levels of turbulent intensity near the injector tip are modified. The instant  $3.375\text{ ms}$  after SOI shows the remaining levels of turbulent intensity below the recirculation structure where the spray was present. These regions are continuously modified until reaching the stationary conditions. Higher levels of turbulent intensity are observed around the fuel spray after the injection. These values are associated with the EOI phenomenon also visible in the velocity distributions.

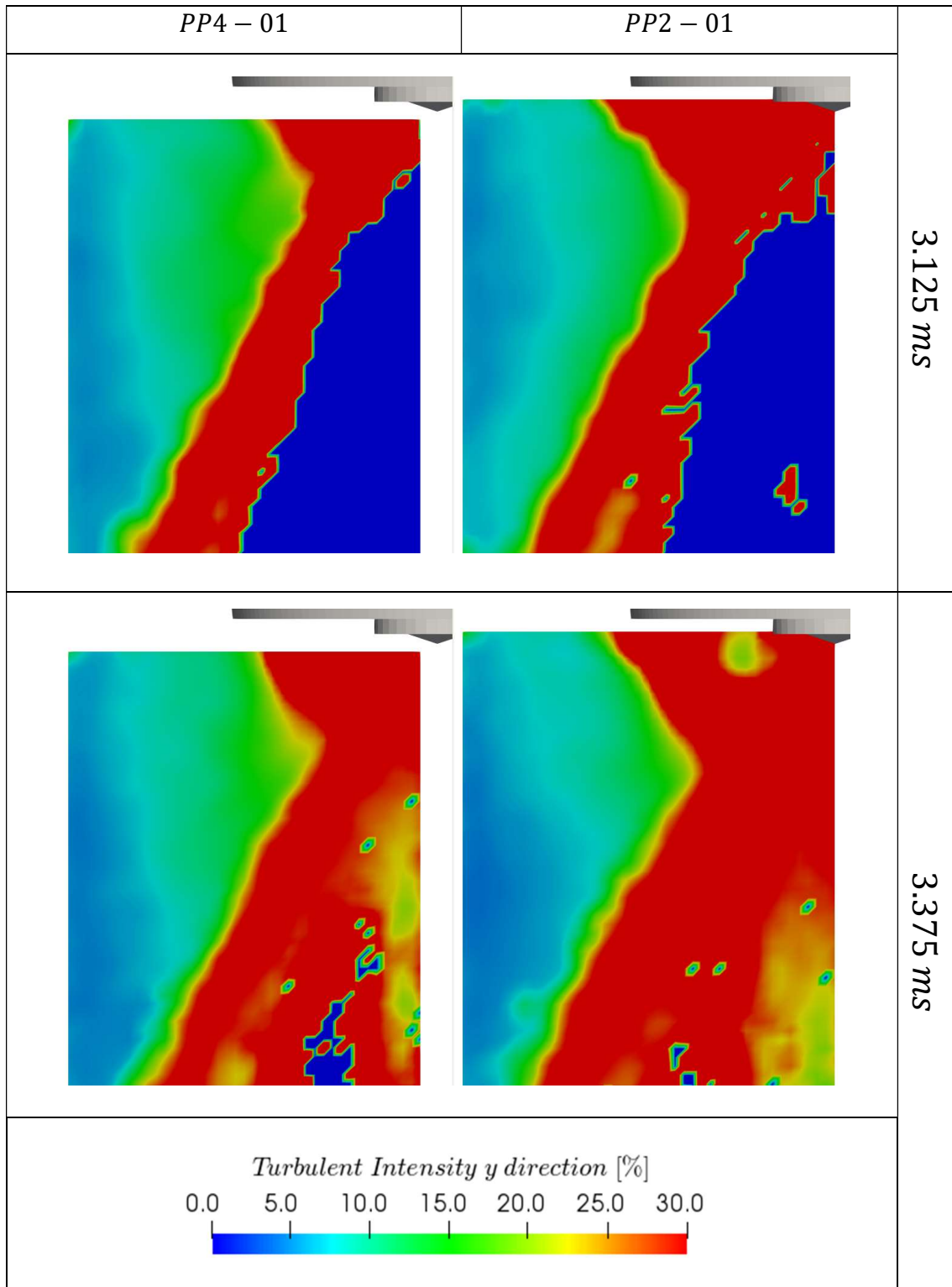


Figure 6.52 - Turbulent intensity calculated with  $y$  direction component. The comparison between cases conditions PP4-01 and PP2-01. Two different timestamps are show: 3.125 ms after SOI and 3.375 ms after SOI.

Figure 6.53 shows the results for the turbulent intensity fields calculated with the horizontal component – the  $x$  direction. The first shown instant corresponds to 0.250  $ms$  before SOI. Since the velocity field during the stationary conditions are mainly vertical, the velocity magnitudes in the horizontal directional are low. Thus, turbulent intensity levels are very high at this time interval.

During the instant 2.625  $ms$  after SOI, the same described mechanism also modifies the turbulent intensity fields in the horizontal direction. Comparing the results for each direction, a stronger reduction is observed in the horizontal component. The turbulent intensity levels around 100 % in stationary conditions reduce to levels between 0 to 25 % during the injection phase. With the exception of the region closer to the injector tip, no significant difference between the two distributions is observed. After the end of injection, the turbulent intensity distributions are gradually modified until the stationary conditions.

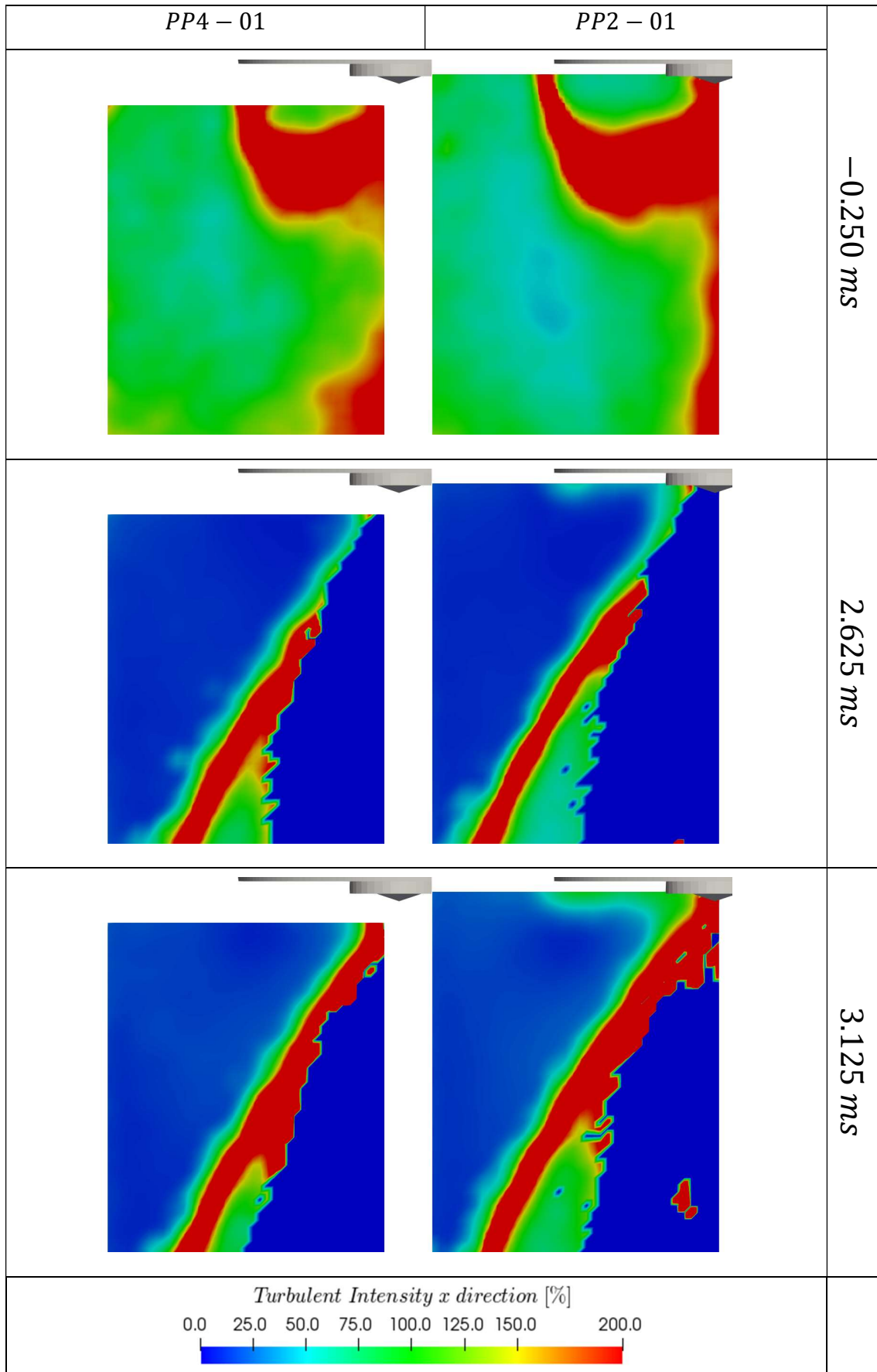


Figure 6.53 - Turbulent intensity calculated with *x* direction component. The comparison between cases conditions *PP4-01* and *PP2-01*.

To investigate if the effects of perforated plates sets are not conditioned to the cases PP4-01 and PP2-01, the same analysis are performed on the other measured conditions. Figure 6.54 shows the comparison between the ensemble-average velocity fields of the cases PP4-03 and PP2-03. No significant difference is observed in the initial injection stages. The recirculation vortex is present during the early injection. This vortex is destroyed and the remaining structure is transported over the spray boundary while the spray penetrates further down the chamber. The velocity field is accelerated and reoriented towards the spray boundary.

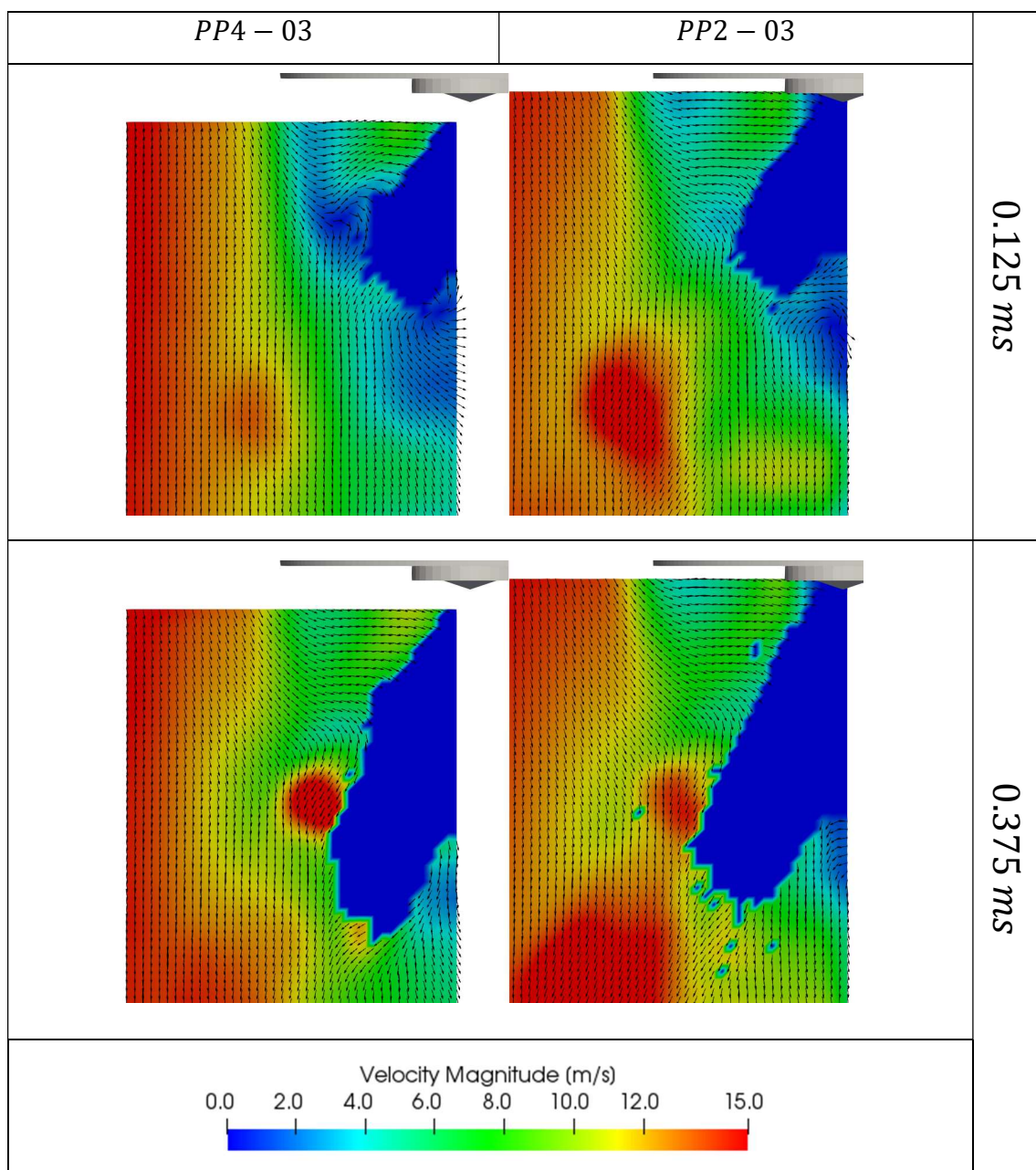


Figure 6.54 – The comparison of the case conditions: PP4-03 and PP2-03. The effects of the perforated plates set. Timestamps: 0.125 ms and 0.375 ms after SOI.

Figure 6.55 shows the ensemble-average velocity fields at the instants  $2.625\text{ ms}$  and  $3.125\text{ ms}$ . During the quasi-steady conditions, the velocity magnitudes around the spray increased due to stabilization of the pressure gradient mechanism. Near the injector cartridge tip, the velocity magnitudes are lower. After the end of injection, the recirculation vortex is formed at this region and it is transported until the stationary conditions. No significant difference can be observed between the two case conditions.

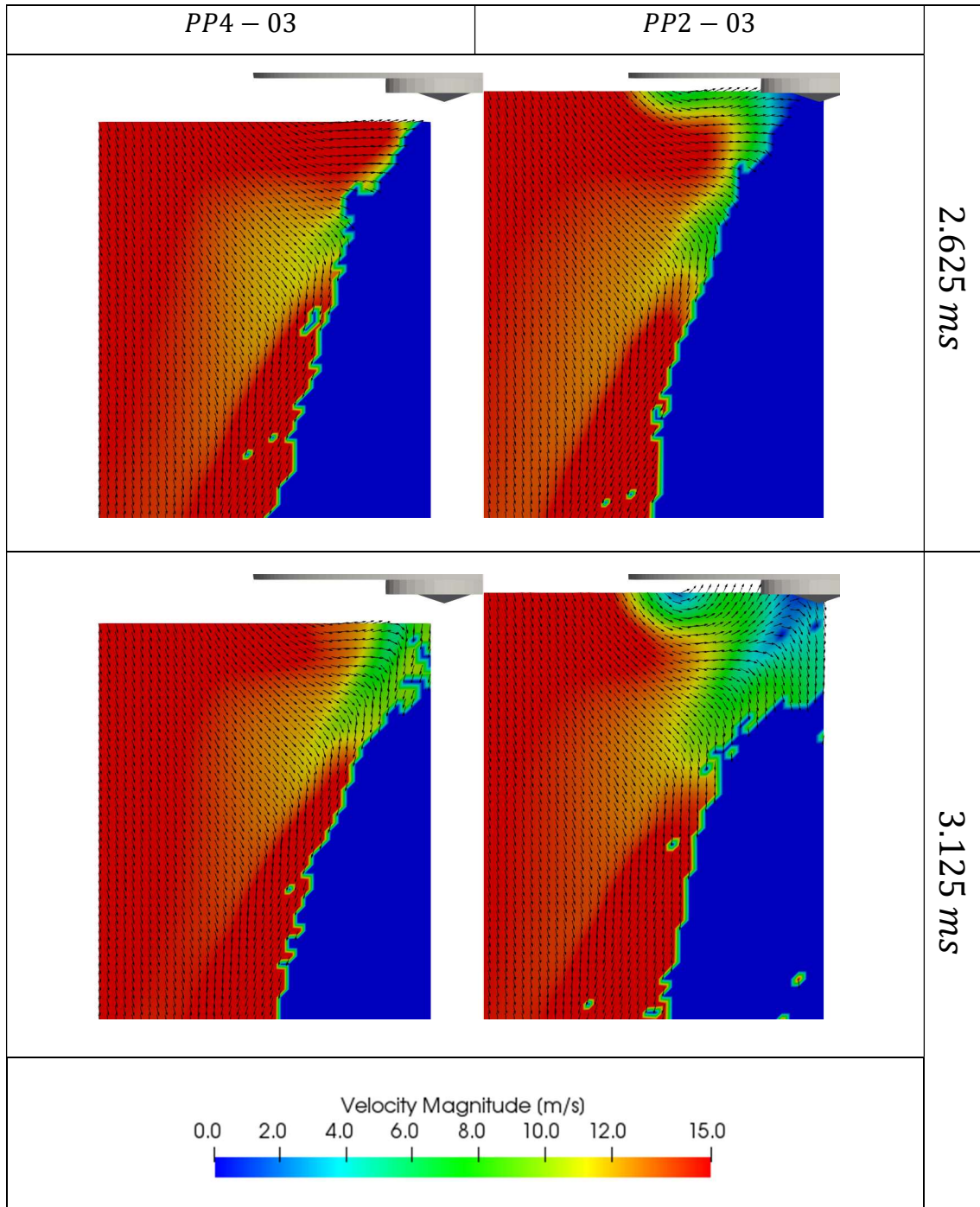


Figure 6.55 – The comparison of the case conditions: *PP4-03* and *PP2-03*. The effects of the perforated plates set. Timestamps:  $2.625\text{ ms}$  and  $3.125\text{ ms}$  after SOI.

Figure 6.56 shows the comparison of the turbulent intensity distributions between cases PP4-03 and PP2-03. The development of the turbulent intensity distributions in these cases is similar to the previous analysis. The cases PP4-03 and PP2-03 experience a reduction of the turbulent intensity levels during the injection phase. For the condition with low integral length scales, case PP2-03, a stronger reduction can be noted on the region near the spray boundary. The same conclusions are drawn for the comparison between case conditions PP4-2 and PP2-02. The turbulent intensity fields for cases PP4-02 and PP2-02 are shown in Figure 6.57.

Figure 6.58 shows the results of the ensemble-average velocity fields and turbulent intensity distributions in the case PP6-01. Although these results of the perforated plates set PP6 cannot be directly compared to the other case conditions due to the difference in the injector mounting position, the cases that can be used can be indicated if the development mechanisms are modified. The velocity field developments are consistent with the observations of the other perforated plates set. No significant difference is to be noted in the velocity development. During the injection, the turbulent intensity fields are also modified. However, since the observed spray plume is different from the other cases, a different distribution is formed. For this case, the turbulent intensity reduction is less intense when compared to the previous conditions.

In this section, to evaluate the effects of the perforated plates set, different cases were compared. The results indicate the formation of a mechanism that depends on the pressure gradient created between the inner and outer regions of the sprays. The velocity fields are reoriented and accelerated towards the spray boundary due to this mechanism. Regarding these distributions, no significant differences were observed in the change of the sets PP4 and PP2. With the same boundary conditions of air mass flow and injection pressure, the velocity distributions are similar even with the spray development.

During the initial injection stages, a vortex structure forms in the spray boundary similar to those found in quiescent environments. This structure is responsible for a feedback mechanism that accelerates the air flow around the spray. This structure is stable only in regions with low air velocity magnitude. When the spray penetrates further in the velocity field out of the recirculation zone, this structure

detach from the spray boundary. In the next instants, this structure is not present in the spray boundary. The different turbulent boundary conditions do not seem to affect the formation and destruction of this vortex.

In the spray development, the velocity fluctuations are reduced. Hence, a decrease of the turbulent intensity levels is observed for all the acquired cases. Higher reductions of the turbulent intensity levels are noted for the cases with the lower incoming turbulence length scales - the perforated plates set PP2. However, since the velocity fields are unaffected, different inlet integral length scales and turbulent intensity scales do not affect the macro spray developments. This evidence is verified with the other acquired conditions. After the end-of-injection, the transient phenomenon observed regardless of the turbulence boundary conditions. The velocity magnitudes in EOI transient are little affected by the change of the inlet turbulence integral scales.

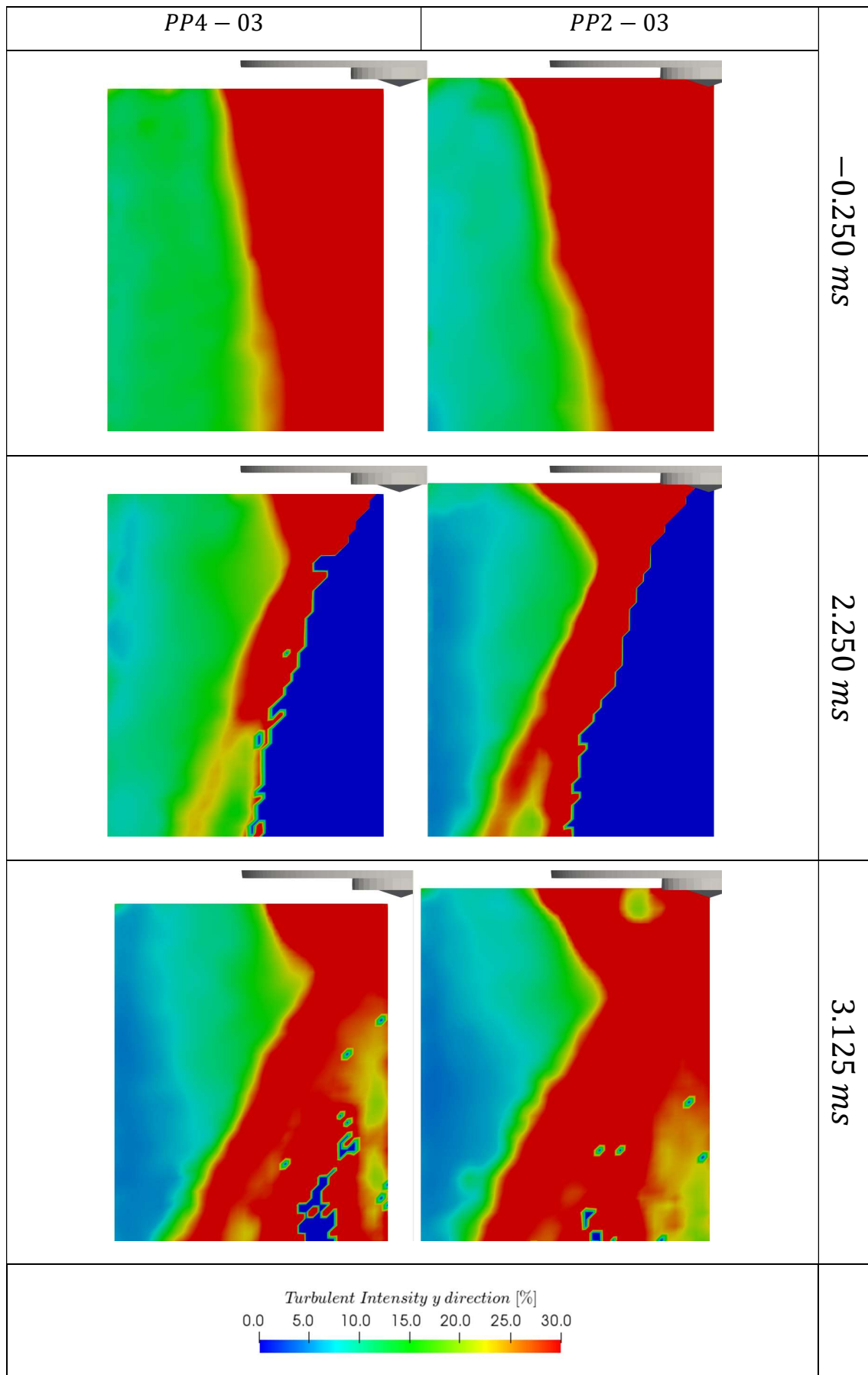


Figure 6.56 - Turbulent intensity calculated with y direction component. The comparison between cases conditions PP4-03 and PP2-03.

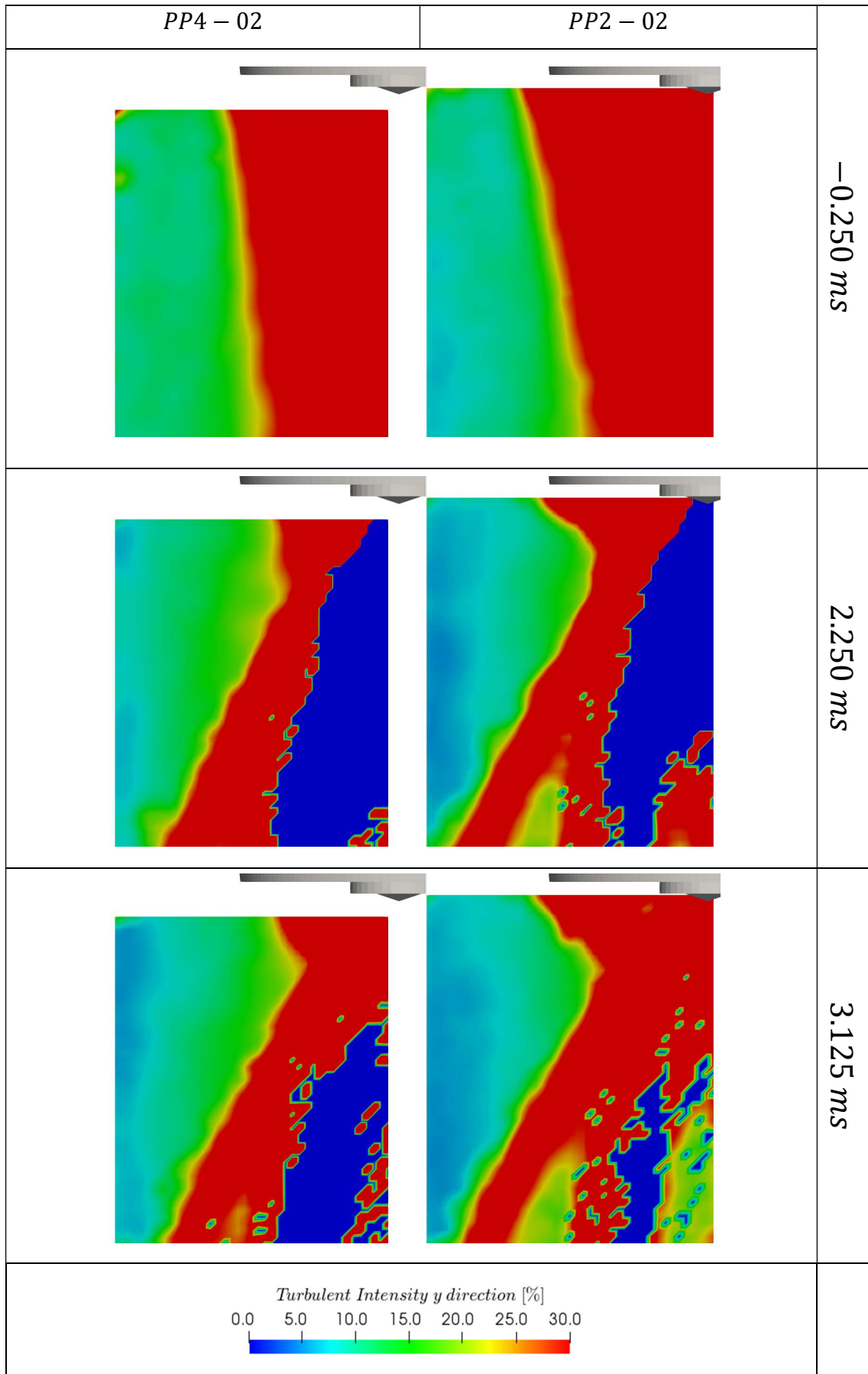


Figure 6.57 - Turbulent intensity calculated with y direction component. The comparison between cases conditions PP4-02 and PP2-02.

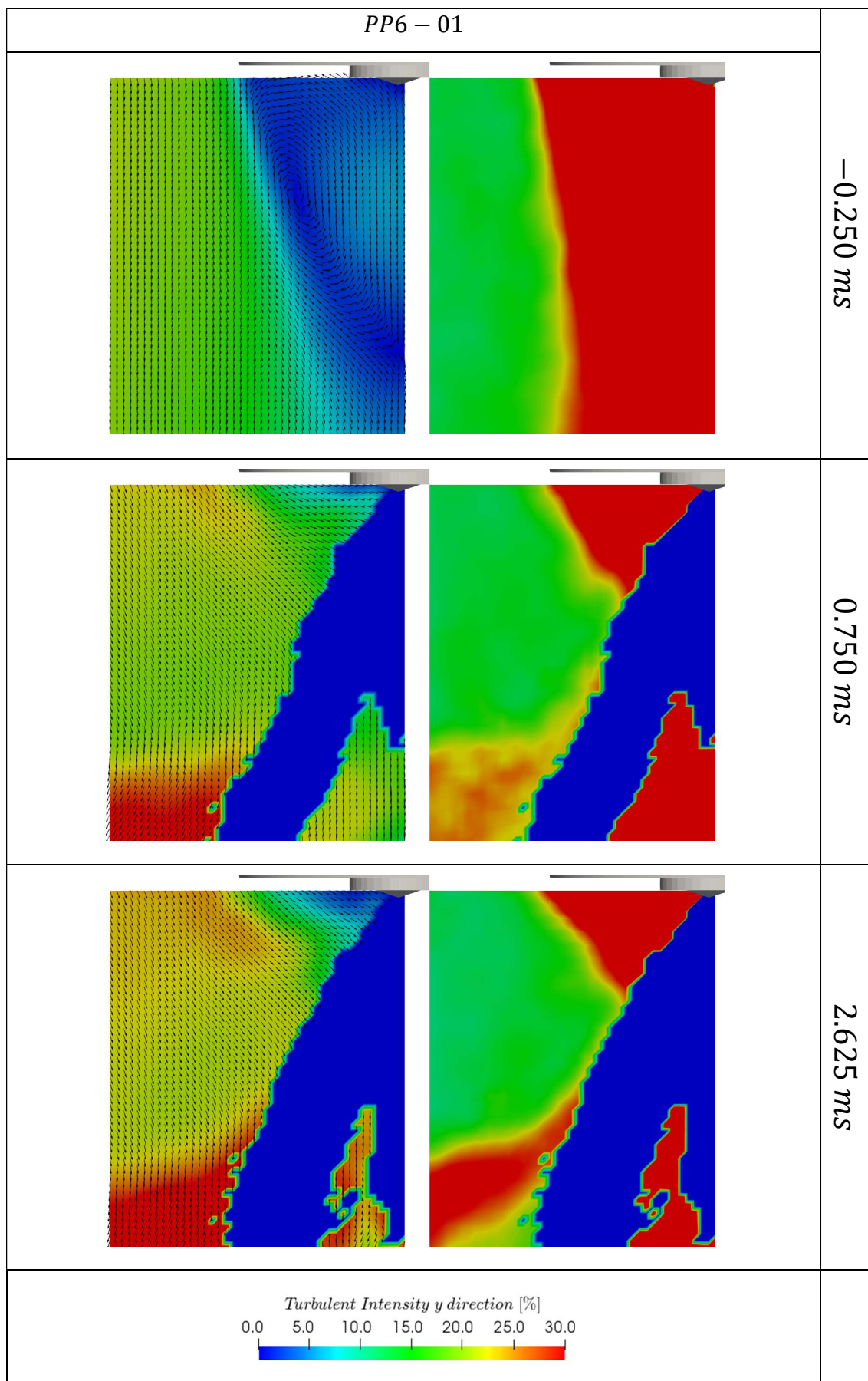


Figure 6.58 - The ensemble-average velocity fields and turbulent intensity calculated with *y* direction component for case condition PP6-01.

### 6.2.5 Effects of the injection pressure

The effects of the injection pressure in the development of the velocity fields are investigated in this section. For each perforated plates set, two cases are compared simultaneously. The air mass flow is kept constant while the injection pressure assumes two different values: 100 *bar* and 60 *bar*.

Figure 6.59 shows the ensemble-average velocity fields for cases PP4-01 and PP4-02 during the early injection phase. Since the cases are synchronized with the electric SOI, different penetration are observed in the time instant. In the case with the highest injection pressure, the recirculation vortex responsible for the feedback mechanism is noted over the spray boundary. In both cases, the air flow near the injector tip is accelerated towards the spray boundary. The recirculation structures of the stationary conditions are transformed due to the presence of the high velocity spray. In the case PP4-02, the spray pushed the remaining cluster further downstream.

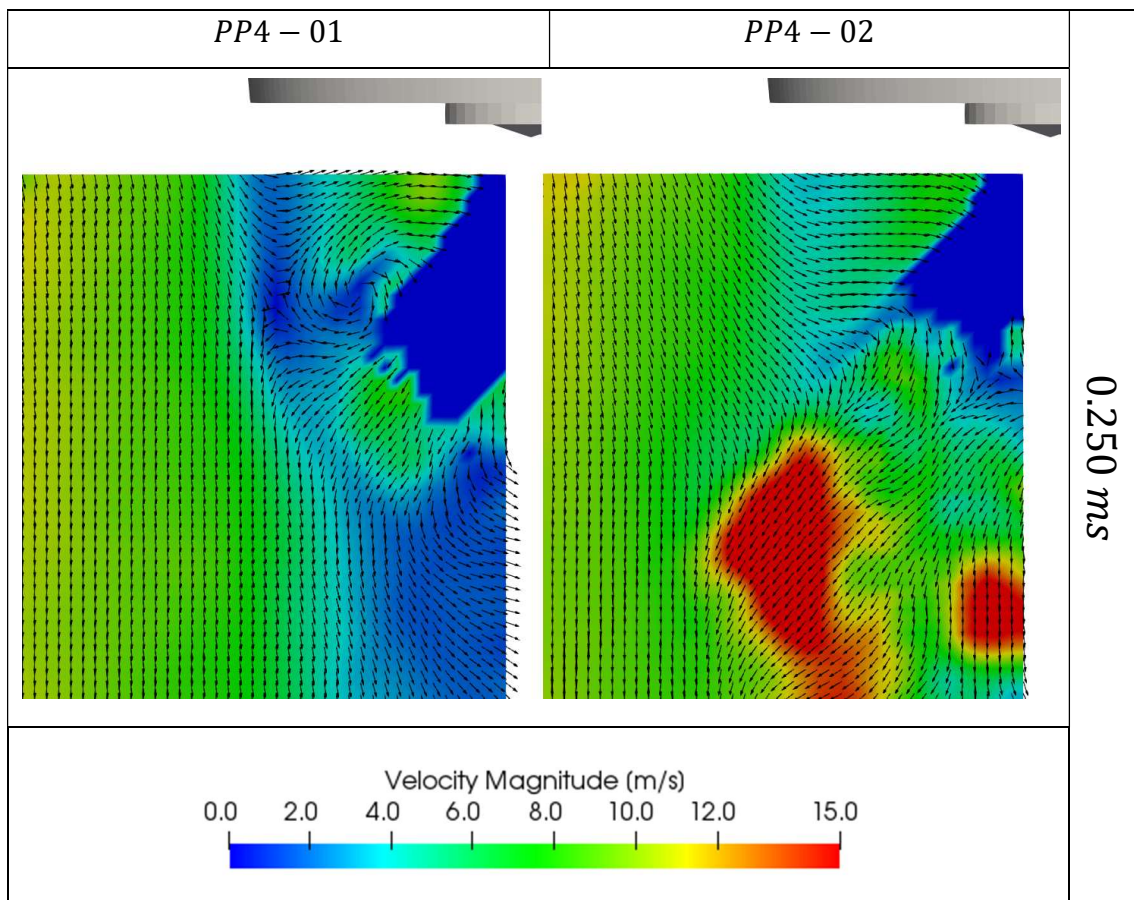


Figure 6.59 – The comparison of the case conditions: PP4-01 and PP4-02. The effects of the injection pressure. Timestamp: 0.250 ms after SOI.

During the next instants, the velocity fields are gradually modified. The pressure gradient mechanism actuates over the spray surrounding and the velocity fields are reoriented toward the spray boundary. Note that for the instant  $0.500\text{ ms}$  after SOI, shown in Figure 6.60, the velocity fields present similar distributions. Since the case PP4-02 has the lowest injector pressure, the spray penetration length is smaller.

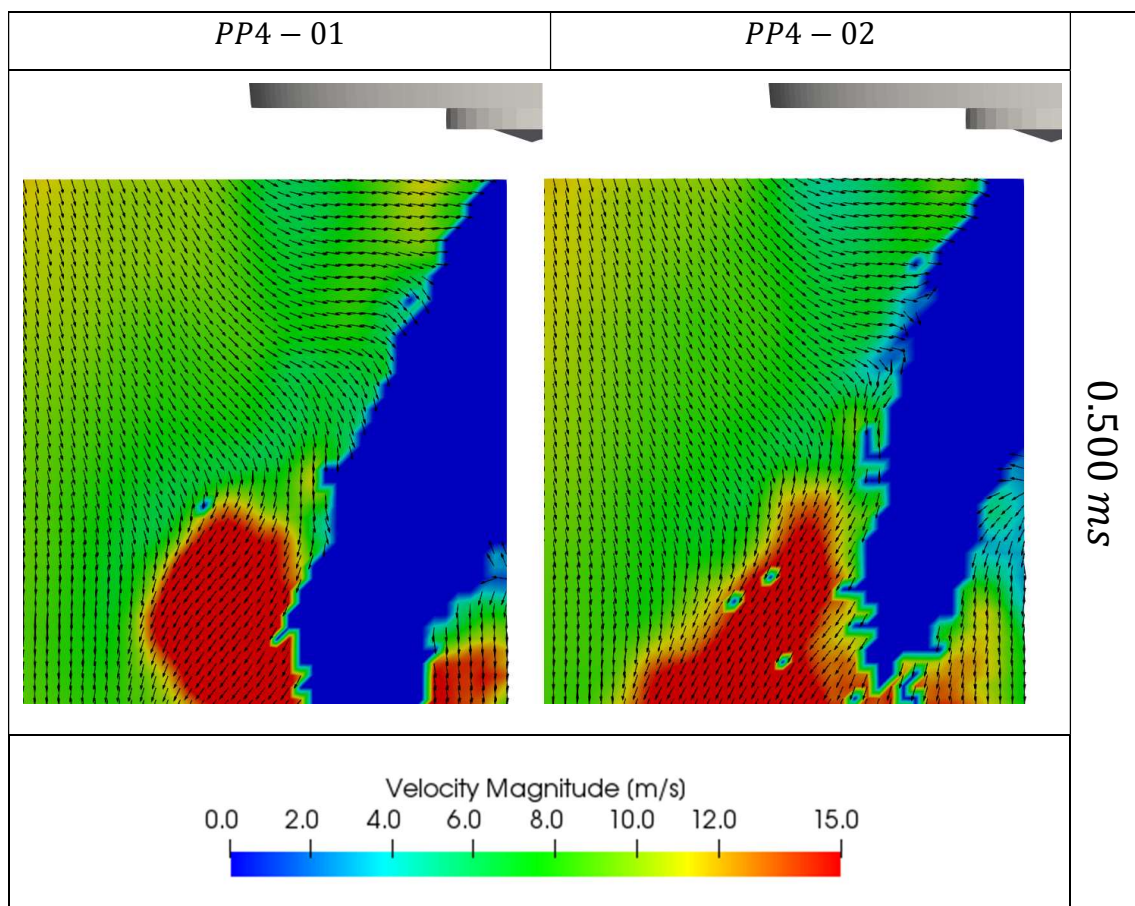


Figure 6.60 – The comparison of the case conditions: PP4-01 and PP4-02. The effects of the injection pressure. Timestamp:  $0.500\text{ ms}$  after SOI.

Figure 6.61 shows the ensemble average velocity fields for the instant  $2.625\text{ ms}$  after SOI. At this stage, the sprays are on the quasi-steady conditions. The velocity field magnitudes are different in the two conditions. With a higher injection pressure, the velocity magnitudes increase in near the injector tip. In the other regions, the velocity magnitudes are slightly higher in the case PP4-01.

Note that the velocity orientations in both conditions are very similar regardless of the differences in their magnitudes. Since the modification of the velocity fields is a result of the pressure gradient acting over the region, the same velocity orientations are expected. The highest velocity magnitudes observed in the case PP4-01 are consistent with the injection pressure variation. Since the sprays velocities are high, the pressure gradient is also higher. Thus, the velocity fields have higher magnitudes in case PP4-01, specially for region near the initial dense spray.

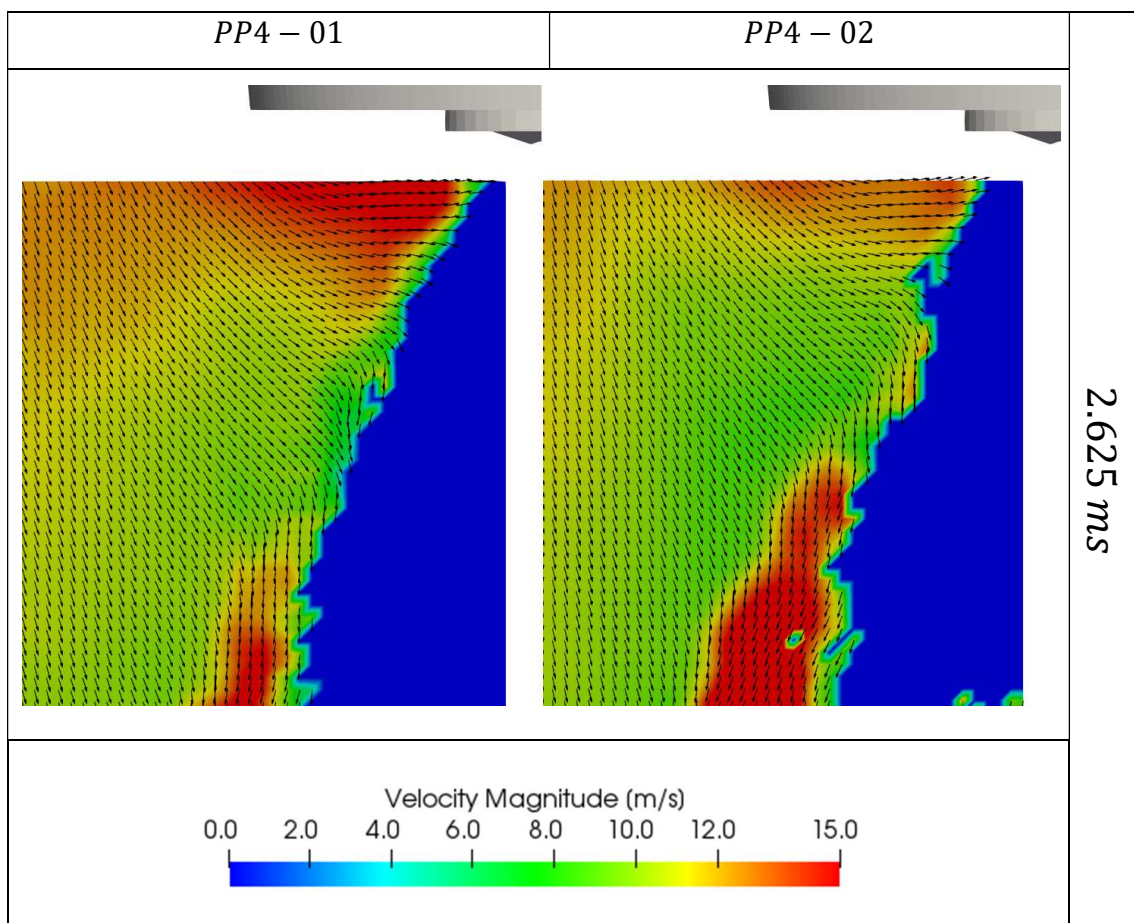


Figure 6.61 – The comparison of the case conditions: PP4-01 and PP4-02. The effects of the injection pressure. Timestamp: 2.625 ms after SOI.

Figure 6.62 shows the results of the ensemble-average velocity fields for the instant 3.125 ms. This instant corresponds to 0.125 ms after EOI. In the region below the injector tip, the velocity magnitudes decreased due to the absence of the spray. In the region far from the spray boundary, the velocity fields are still similar to the distributions during the quasi-steady phase. After the end of injection, regions with elevated magnitudes are observed near the spray boundary in both conditions. This increase in the velocity magnitude after the end

of injection is related to the EOI phenomenon. This feature is present at the end of injection regardless of the injection pressure and the perforated plates set. For the case of higher injection pressure, the EOI phenomenon is more pronounced. Since this effect is related to the mass conservation after the needle valve closing, a higher velocity magnitude should be expected for the case with higher injection pressure. These effects are in agreement with the works by Moon et al [12] [64].

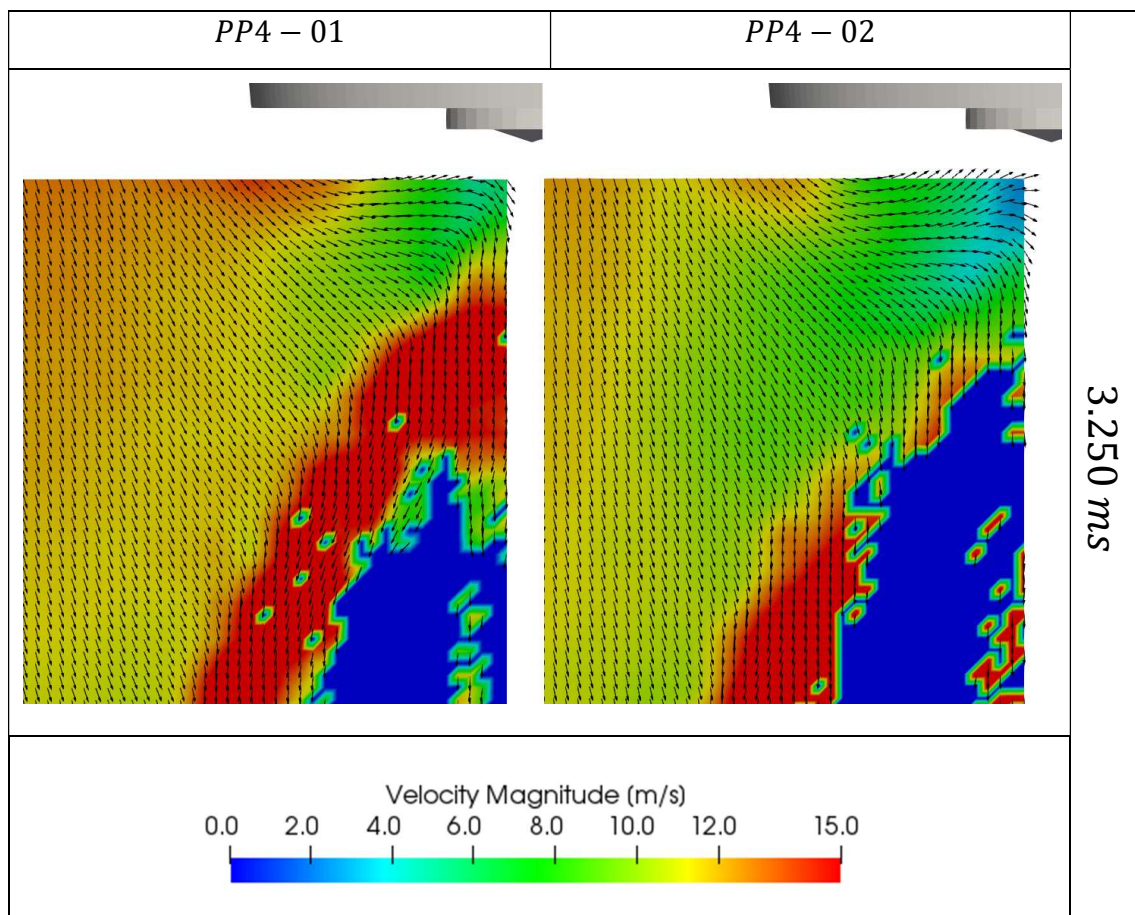


Figure 6.62 – The comparison of the case conditions: *PP4-01* and *PP4-02*. The effects of the injection pressure. Timestamp: 3.125 ms after SOI.

To analyze the effects in the turbulence fields, the ensemble-average turbulent intensity distributions are compared between the cases PP4-01 and PP4-02. These are calculated with the velocities for the  $y$  direction component. Figure 6.63 shows the turbulent intensity distributions in both cases at the instant  $0.125\text{ ms}$  before SOI. Since the air mass flow and the perforated plates set are equal, no significant difference is observed in the distributions prior to the injection phase.

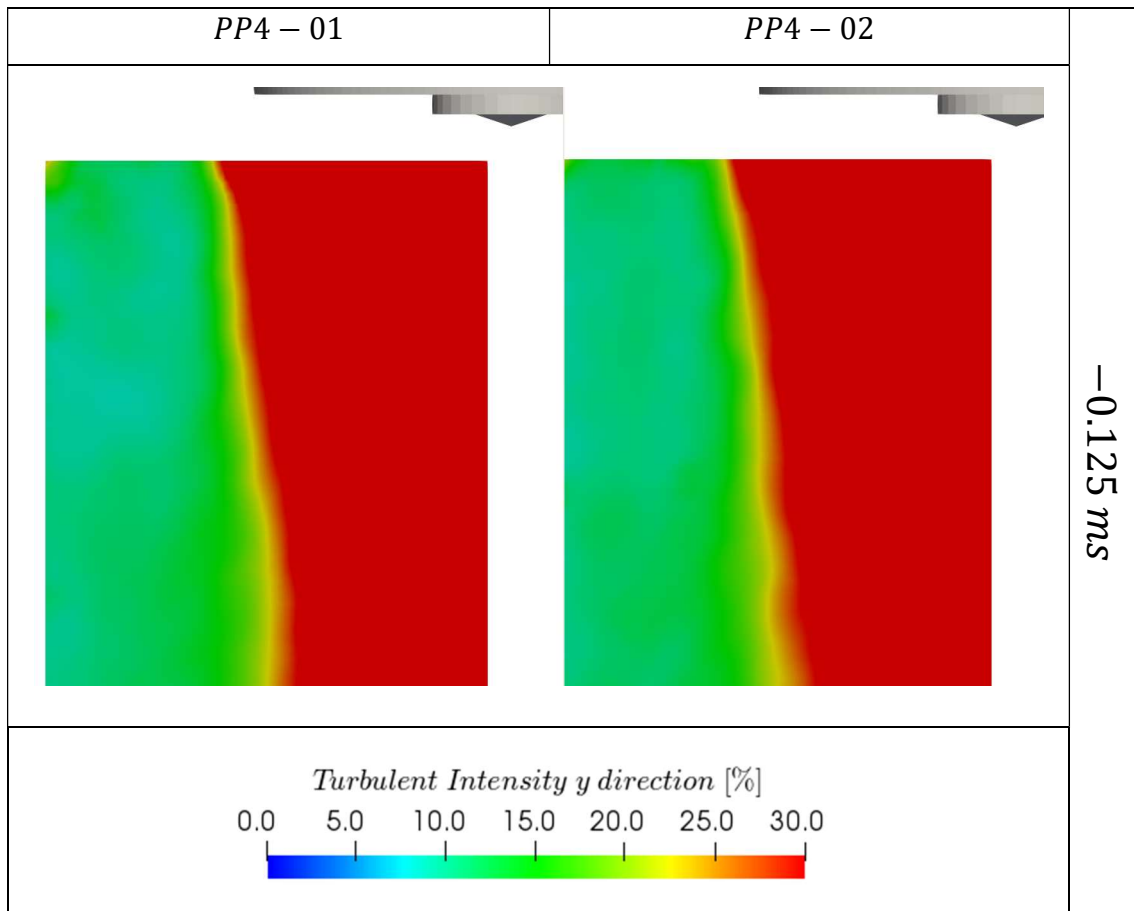


Figure 6.63 – The turbulent intensity distributions calculated with  $y$  direction component. The comparison between cases conditions PP4-01 and PP4-02.  $0.125\text{ ms}$  before SOI.

Figure 6.64 shows the distributions at the time instant  $0.250\text{ ms}$  after SOI. At this stage, the sprays penetrate the region occupied by the stationary recirculation structure. The velocity field far from the spray are little affected, with the exception of the region downstream the spray tip being pushed by the fuel front.

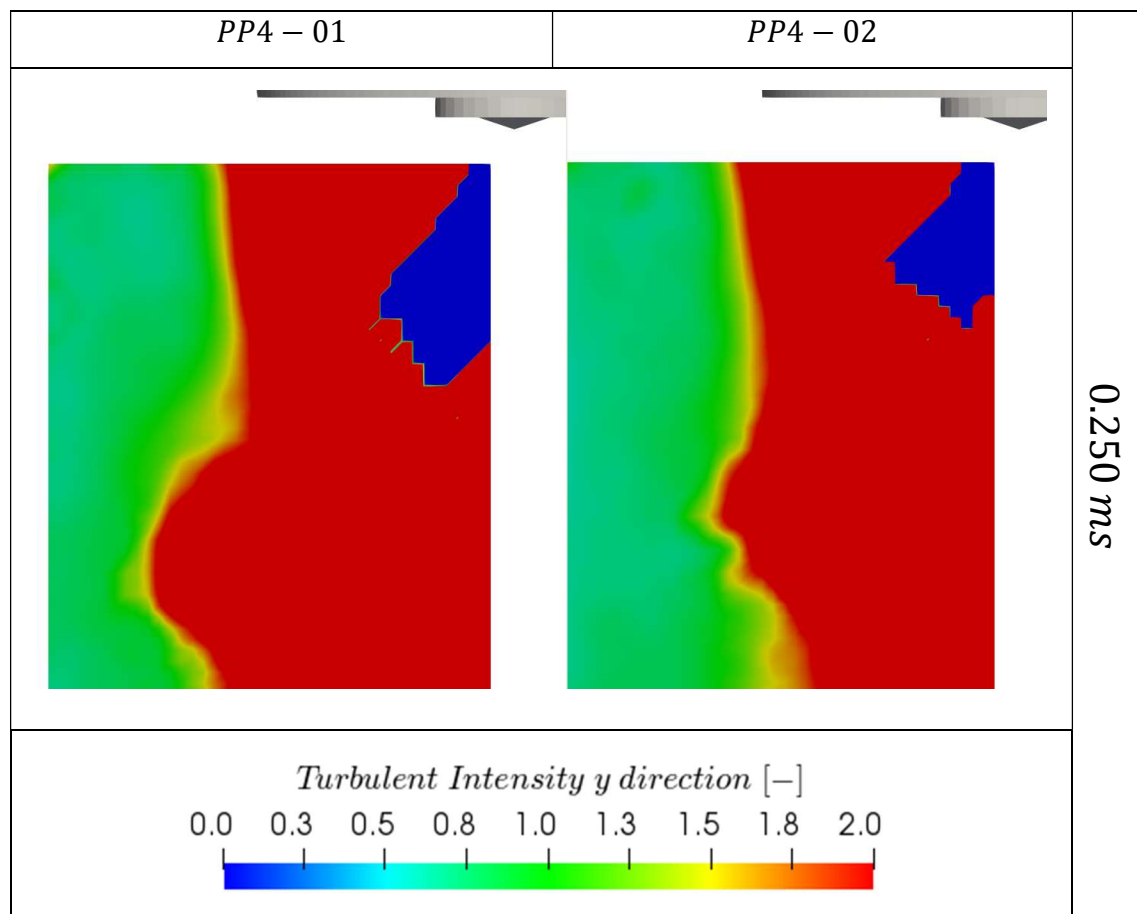


Figure 6.64 – The turbulent intensity distributions calculated with  $y$  direction component. The comparison between cases conditions PP4-01 and PP4-02.  $0.250\text{ ms}$  after SOI.

Figure 6.65 shows the spray evolution during the instants  $0.750\text{ ms}$  and  $2.625\text{ ms}$  after SOI. At the first instant, the formed distributions present similar characteristics. However, at this stage, the turbulent intensity levels are slightly lower in the case PP4-01 in the region out of the spray boundary. With the time progress, the sprays continue to develop and eventually reach the quasi-steady conditions. At the second instant,  $2.625\text{ ms}$  after SOI, the turbulent intensity levels are very similar in both cases. No significant differences are observed in the regions out of the spray boundaries. Although the region near the injector tip has different velocity magnitudes depending on the injection pressure, similar values in the turbulent intensity distributions are noted.

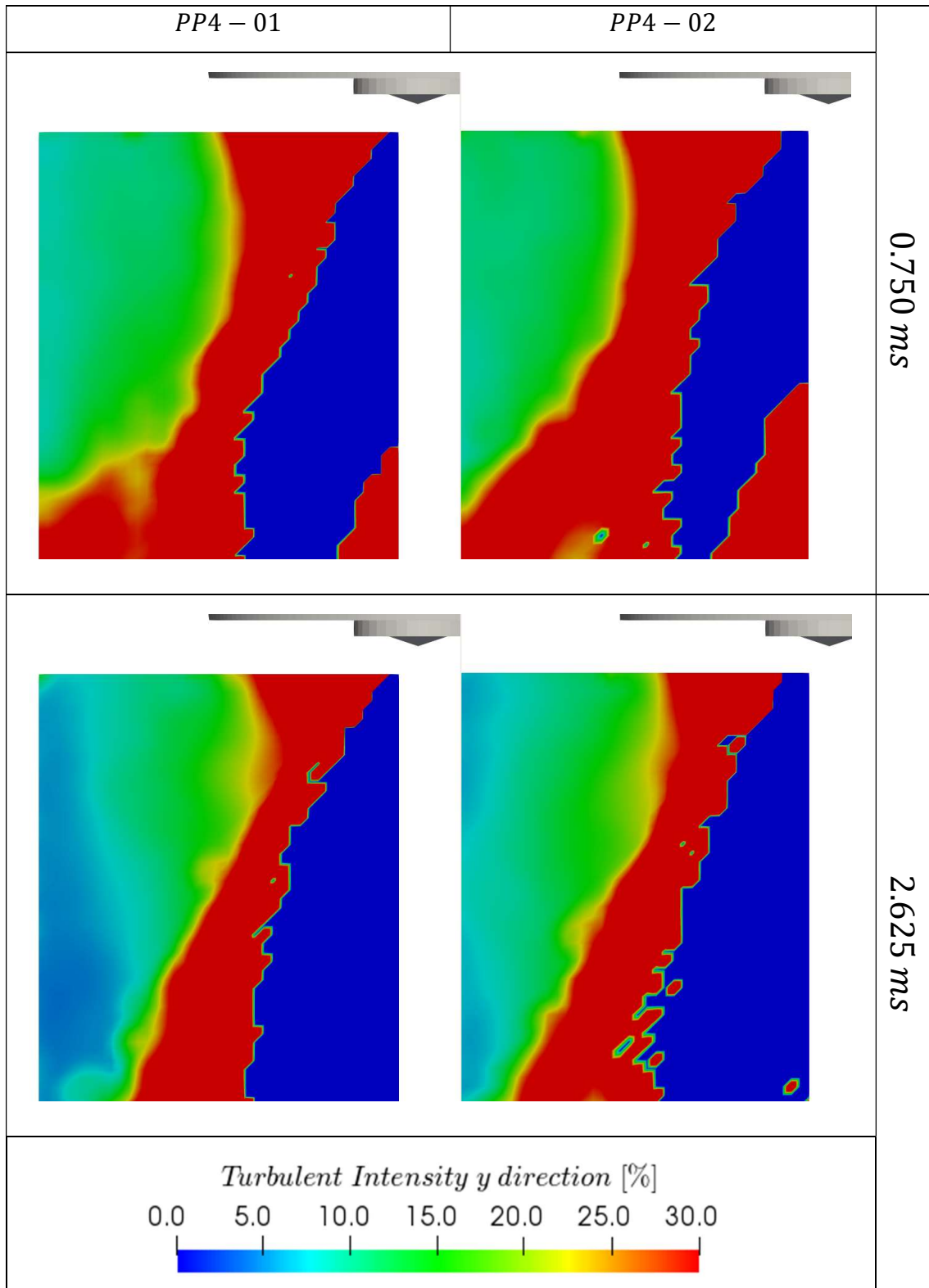


Figure 6.65 – The turbulent intensity distributions calculated with  $y$  direction component. The comparison between cases conditions PP4-01 and PP4-02. Two different instant are shown: 0.750 ms and 2.625 ms after SOI.

Figure 6.66 shows the turbulent intensity distributions in the time instant  $0.250\text{ ms}$  after EOI. In the case with lowest injection pressure, the turbulent intensity levels associated with the penetration wave are comparable to the case PP4-01. Considering the results of the velocity fields, a relation between the EOI phenomenon and injection pressure is observed. With higher injection pressure, the velocity magnitudes associated with the instability are higher. Thus, more air penetration is expected for this case. However, the turbulent intensity levels are comparable in both conditions.

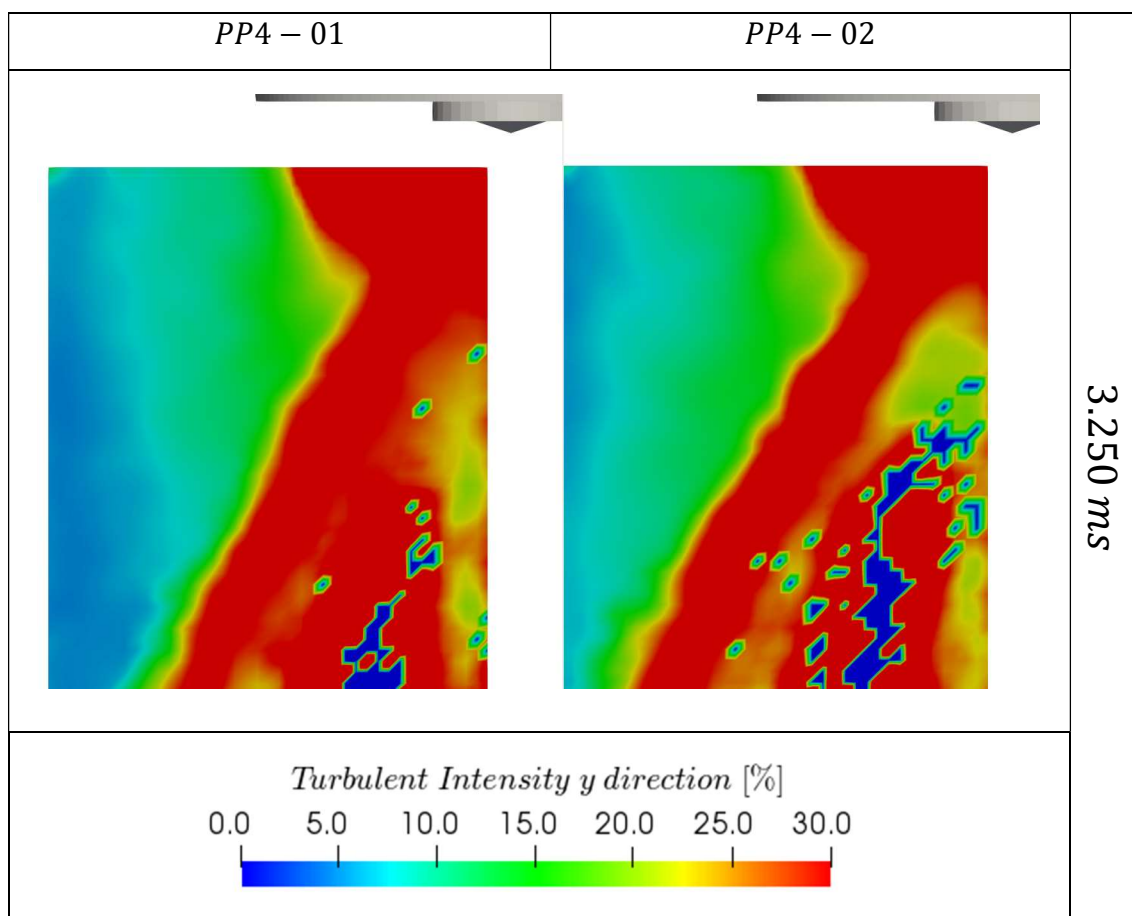


Figure 6.66 – The turbulent intensity distributions calculated with  $y$  direction component. The comparison between cases conditions PP4-01 and PP4-02.  $3.250\text{ ms}$  after SOI.

To investigate if the observed phenomenon also occurs in the other measured conditions, the turbulent intensity distributions are compared between the cases of PP2 and PP6. Figure 6.67 shows the comparison between the cases PP2-01 and PP2-02. The two conditions have similar inlet air mass flow. The injection pressure are 100 *bar* and 60 *bar*, respectively. The three shown time instants describe the turbulent intensity evolution with characteristics very similar to the cases of the perforated plates set PP4. At the early injection phase, slightly different distributions are formed depending on the injection pressure. With the spray development, these differences gradually diminish. At the instant 2.625 *ms* after SOI, the turbulent intensity distributions are similar throughout the measurement plane.

Figure 6.68 shows the ensemble-average turbulent intensity fields in the cases of the perforated plates set PP6. Although not directly comparable to the other sprays developments, the turbulent intensity evolutions also reach similar distributions in cases PP6-01 and PP6-02. The differences between the cases are more pronounced in the regions near the injector tips.

The comparison between the ensemble velocity fields developed with different fuel injection pressures indicate that the pressure gradient mechanism is present in both conditions. The mechanism is responsible for the velocity field modification throughout the injection. In both injection pressures, the air velocity field around the spray accelerates towards the interaction zone. With a higher injection pressure, the velocity magnitudes are higher near the injector tip. In the other regions, the velocity magnitude is marginally higher for the 100 *bar* case. With respect to the turbulence fields, the development of turbulent intensity levels depend on the injection pressure during the initial stage. At the quasi-steady conditions, these distributions assume similar values. These observations indicate that these values of injection pressure do not significant modify the turbulence properties during the final stages of injection. The characteristics were observed regardless of the inlet turbulence integral scales. At the end of injection, the EOI phenomenon is noted in both case conditions. The magnitude of the velocities associated with the transient behavior shown a relation with the injection pressure.

In the practical point of view, the mixture formation occurring after the end of injection would encounter different velocity field magnitudes depending on the injection pressure. In the turbulence level, the turbulent intensity distributions decreases during the injection when compared to the stationary conditions. However, these levels are not significantly affected by the injection pressure variation, neither near the spray during the EOI transient. Thus, the air penetration in the spray would be higher for the case with high pressure but the turbulence conditions would be roughly similar. After the end of injection, turbulence levels are roughly equal near the spray boundary but with higher velocity magnitudes in the case of the highest injection pressure.

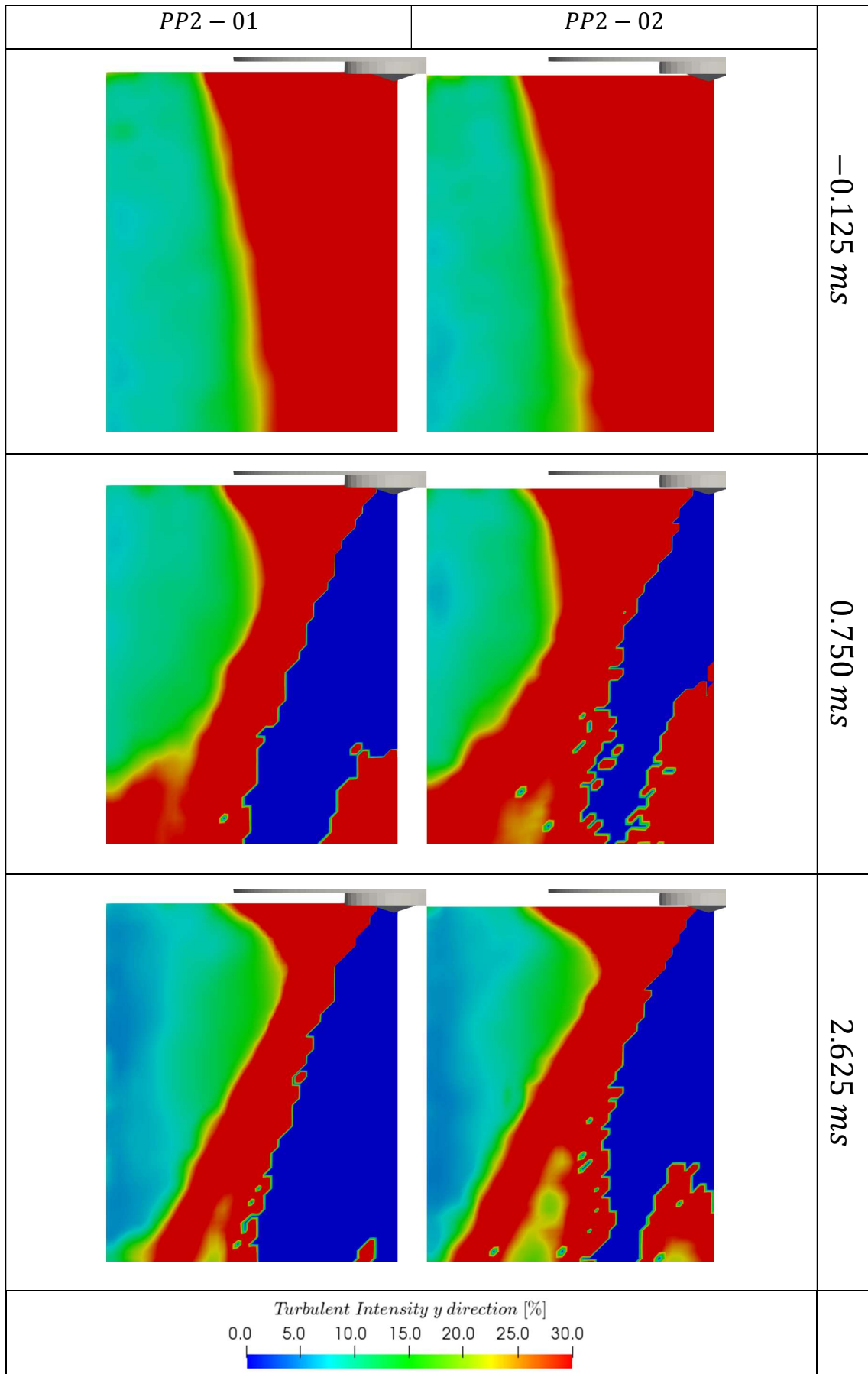


Figure 6.67 – The turbulent intensity calculated with y direction component. The comparison between cases conditions PP2-01 and PP2-02.

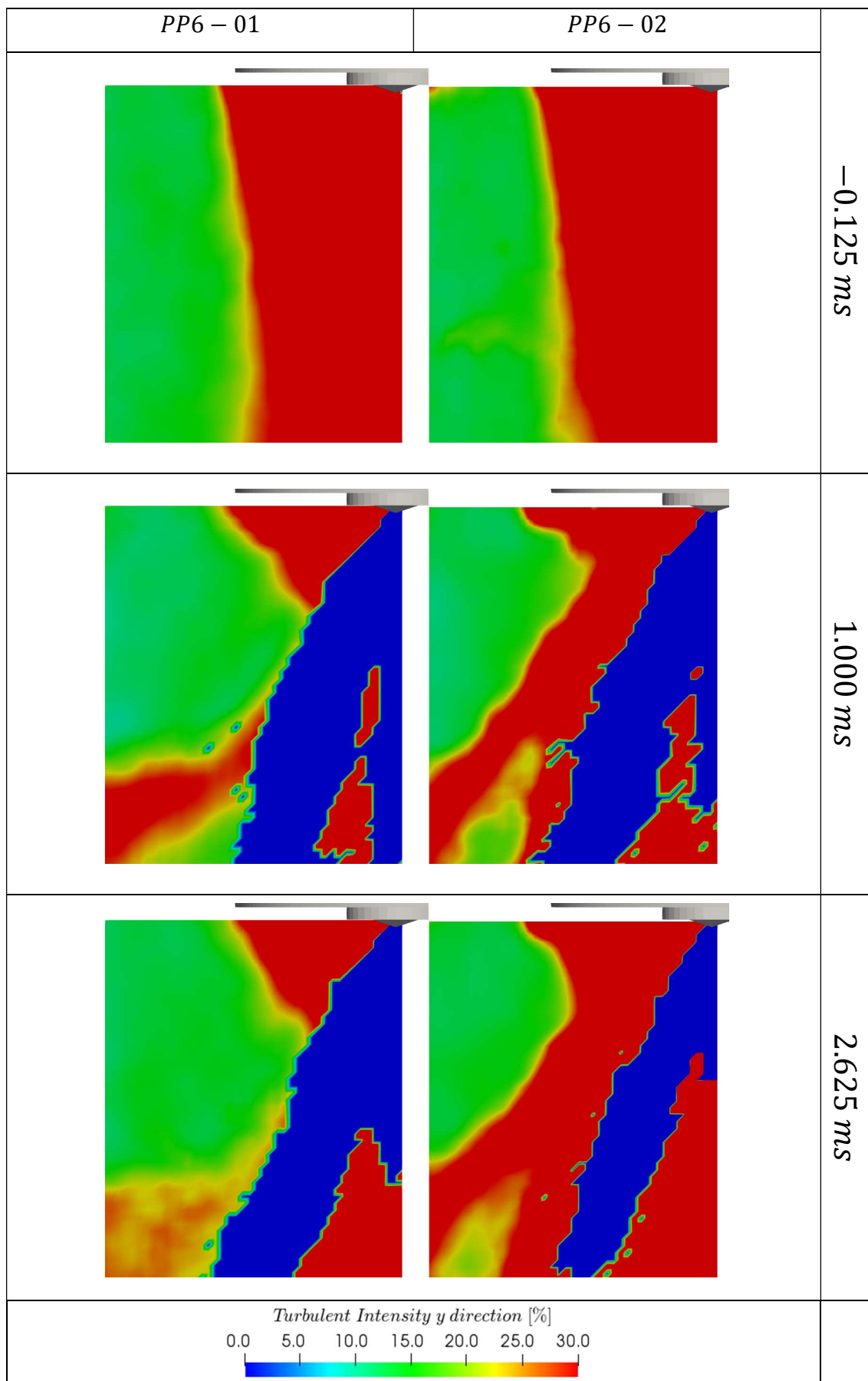


Figure 6.68 – The turbulent intensity calculated with y direction component. The comparison between cases conditions PP6-01 and PP6-02.

### 6.2.5.1 Near injector tip

An important area to investigate the spray-air interaction is the region near the injector tip. In this region, the primary spray break-up takes place. Ligaments, droplets cluster and droplets are being formed. This is usually a very challenging region to measure any property due to the elevated spray density. In this sense, the velocity field of the surrounding air can provide information of the spray progress over time.

To analyze the evolution of the velocity field near the injector tip, a region below the injector cartridge and near the high density area was chosen. A set of 8 points in the measurement plane was used to track the velocity time history. A space-average operation for the velocity of the 8 points was performed for each timestamp of the spray events. Figure 6.69 depicts the time sequence of this space-averaged velocity in the case PP4-01. The left figures show the velocity fields distributions below the injector cartridge. The black dots represent the points chosen to evaluate the region of interest. The right figures indicate the time history of the space-averaged velocity during the injection phase. The black line is the space-average value whereas the gray shade are the fluctuations over the mean for the set. The green vertical line marks the current instant been shown in the figures to left.

In the first time instant shown, at  $0.125\text{ ms}$  after SOI, the spray initial plumes are visible, but the distributions are still little affected by its presence. The magnitude of the average velocity is still low. A very fast modification of the velocity field occurs just  $125\ \mu\text{s}$  after. At instant (2), the orientation of the air flow field near injector tip changed. At instant (3), the spray growth accelerate the near tip flow. The average velocity magnitude reaches  $10\text{ m/s}$  in  $1\text{ ms}$ . At instant (4), the end of injection, the average velocity reaches the highest value of  $14\text{ m/s}$ . The deceleration begins after instant (4). At the time instants after EOI, the velocity enters the stabilization phase. The stationary condition is reached after  $35\text{ ms}$  (not illustrated in the pictures).

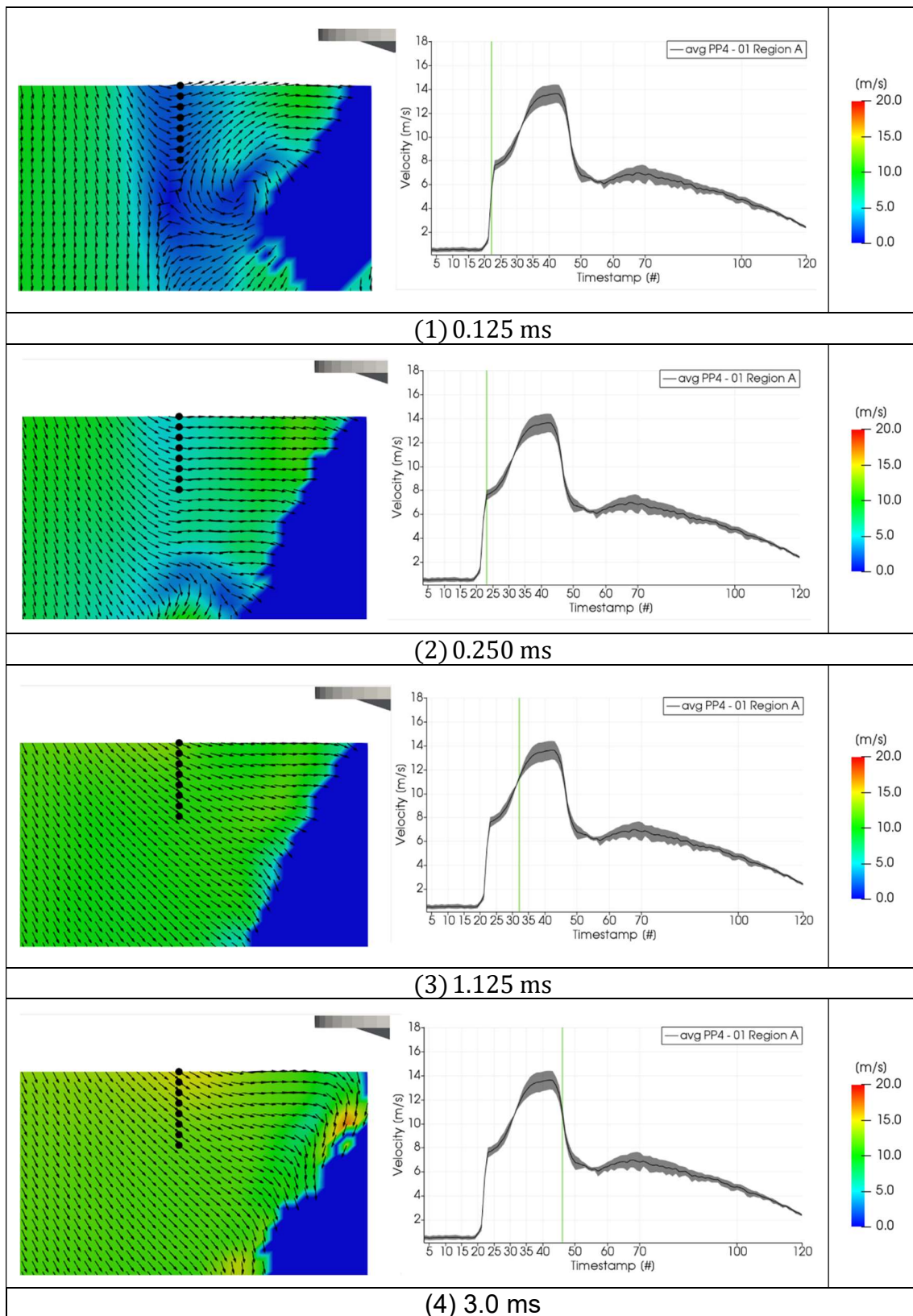


Figure 6.69 – The temporal evolution of space-average velocity near the injector tip (right figures) for case PP4-01. The space-averaging is performed considering the 8 points highlighted by the black dots (left figures).

Observe the response of the velocity fields to the forces and pressures generated in the spray evolution. The time history of the average velocity is divided in 3 stages, comprising the injection and after-injection events. The first stage occurs between timestamps #25 to 37. In this region, the air flow is subjected to a rapid acceleration. By comparing the instants (1) to (3) in Figure 6.69, two different patterns in stage 1 are noted: a steeper part of the curve and a second smoother part. In the first part, the flow field is reorganized. The spray penetration plumes affects the surrounding air flow, changing its direction very rapidly. The steeper representation of the first part is related to lack of the time resolution to track this variation. In stage 1, which occurs during 2 *ms* of the 3 *ms* injection period, the pressure gradient mechanism increases the average velocity magnitude by a factor of 7. The average acceleration is of the order of  $7000 \text{ m/s}^2$ . These acceleration forces are predominant in the velocity development. The fluctuations of the space-average velocity are considerable lower in this stage when compared to the rest of the time history. During the second stage, timestamps #38 to 44, the average velocity achieves a *quasi*-steady condition. At this stage, the air flow converges toward the spray plumes with roughly constant velocity. This effect in the air velocity field suggests that the spray is also at a *quasi*-steady phase. The third stage initiates at the EOI. Without the acceleration forces to maintain the high velocity, the average velocity decelerates significantly but do not reaches the same initial values. At this point, the inlet air flow is capable of interact with the flow below the injector cartridge. The deceleration rate changes and the average velocity decreases differently.

In order to evaluate the sensitivity of the previous analysis with respect to the choice of points, different sets near the injector tip were tested. An example of the effects of the selected points is shown in Figure 6.70. The black curve in the right figure is the same time history from the previous analysis. The blue curve represent the time history for the points set illustrated as blue dots on the left figure – region B. The fluctuations values are not shown in the curve for region B due to clarity in the graph. Note that the effects expected in stages 1 to 3 are essentially the same. Regarding the first stage, the acceleration rate for both regions are similar. The stage 2 behavior is comparable in both case but the magnitude value is lower in region B. In stage 3, both cases present a rapid

deceleration. In region B, the effects of the inlet flow are seen early. The final velocity in both cases are roughly equal.

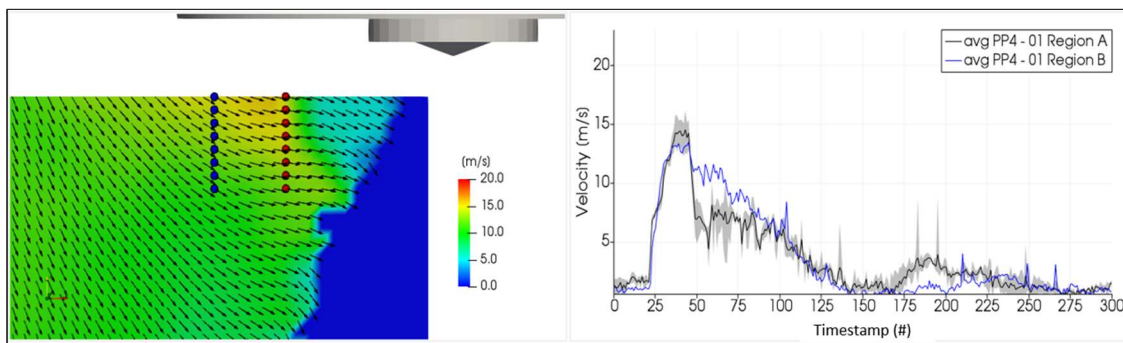


Figure 6.70 – The comparison between two space-average velocities in the region near injector tip. The red points indicate the ones used in the previous analysis (region A). The blue dots represent a second evaluated region B.

To evaluate the effects of injection pressure on the air flow field near injection tip, the space-averaging operation was performed in the case PP4-02 in the same physical coordinates of case PP4-01. The case conditions have the same boundary conditions except to the injection pressure. The injection pressure in case is 60 *bar*. Figure 6.71 shows the time history comparison between the two cases. The shade values indicate the fluctuation over the average value. During stage 1, the acceleration rate due to spray development is lower for case PP4-02. The lower injection pressure decrease the static pressure gradient between the inner region of spray and the surrounding air flow. Thus, the maximum velocity is the lowest to the case of the smallest injection pressure (PP4-02). However, this pressure gradient reduction does not noticeably affects the stage 2 duration – in both cases, stage 2 comprises roughly 1 *ms* of the 3 *ms* injection duration. The difference in stage 2 lies in the velocity magnitude reached during the *quasi*-steady condition. In stage 3, velocities are consistent with the injection pressures. Since the inlet air flow is at the same rate in both cases, the velocity magnitudes after EOI are at comparable levels. Both cases describes a similar temporal evolution.

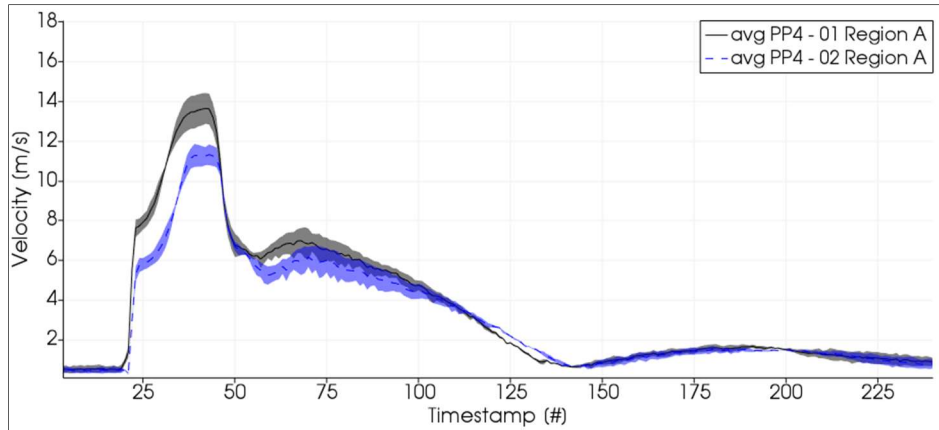


Figure 6.71 – The time history of the space-average velocity - the effects of the injection pressure.

### 6.2.5.2 Spray main boundary

To investigate the velocity field near the main spray boundary, a different approach was used. None set of points could be found whose properties have minimum independence of the chosen. By observing the velocity fields distributions, for example in Figure 6.37, it is clear that a single variable cannot represent the velocity of the entire distribution around the spray boundary. In this case, a profile plot was preferred to track the evolution. Figure 6.72 shows the temporal sequence of these velocity distributions. At each time instant, two plots are shown. The ensemble average velocity fields are shown in images to the left. The images to the right are the velocity profile over the line highlighted in the velocity field distributions. In the vertical axis of the profile plot, the line position  $0\text{ mm}$  is the most distant point from the injector cartridge.

At the instant (1) before SOI, the profile plot over the line captures the difference in the flow field below injector tip and the main stream. The velocities in the main stream region are roughly stable and of the order of  $9\text{ m/s}$ . In the point where the line intersects the recirculation frontier, the velocity magnitudes decreases. At  $0.125\text{ ms}$  after SOI, instant (2), the velocity distribution over the line still are not affected by the injection. With the evolution of the spray, the flow field is reorganized, as explained previously. At instant (3), the velocity in the near tip region changed significantly. The velocities near the spray boundary are less affected. In the velocity profile of instant (3), a relation is observed with the different regions of the spray. At  $y = 0\text{ mm}$ , the most distant part from injector

cartridge, the velocity magnitude and direction are roughly the same of the stationary conditions. With increasing  $y$ , the magnitude gradually increases. The velocity vectors direct towards spray boundary. As the line approximate to the injector cartridge, where the spray plumes are denser, the effects are even more pronounced. This tendency continues during the injection time until instant (5).

After EOI, at instant (5), a different velocity distribution develops. As previously shown, the near tip region decelerate with the EOI. To the rest of spray boundary, a sudden acceleration is observed. The transition is visible at instant (6). The velocity distributions shows a region of higher velocity near the main spray. The profile plot indicate higher velocities throughout the line. The acceleration after EOI is consistent with the results of the previous analyses. For instant (8), the effects of the spray injection are still visible. The next time instants reveal the stabilization of the stationary condition.

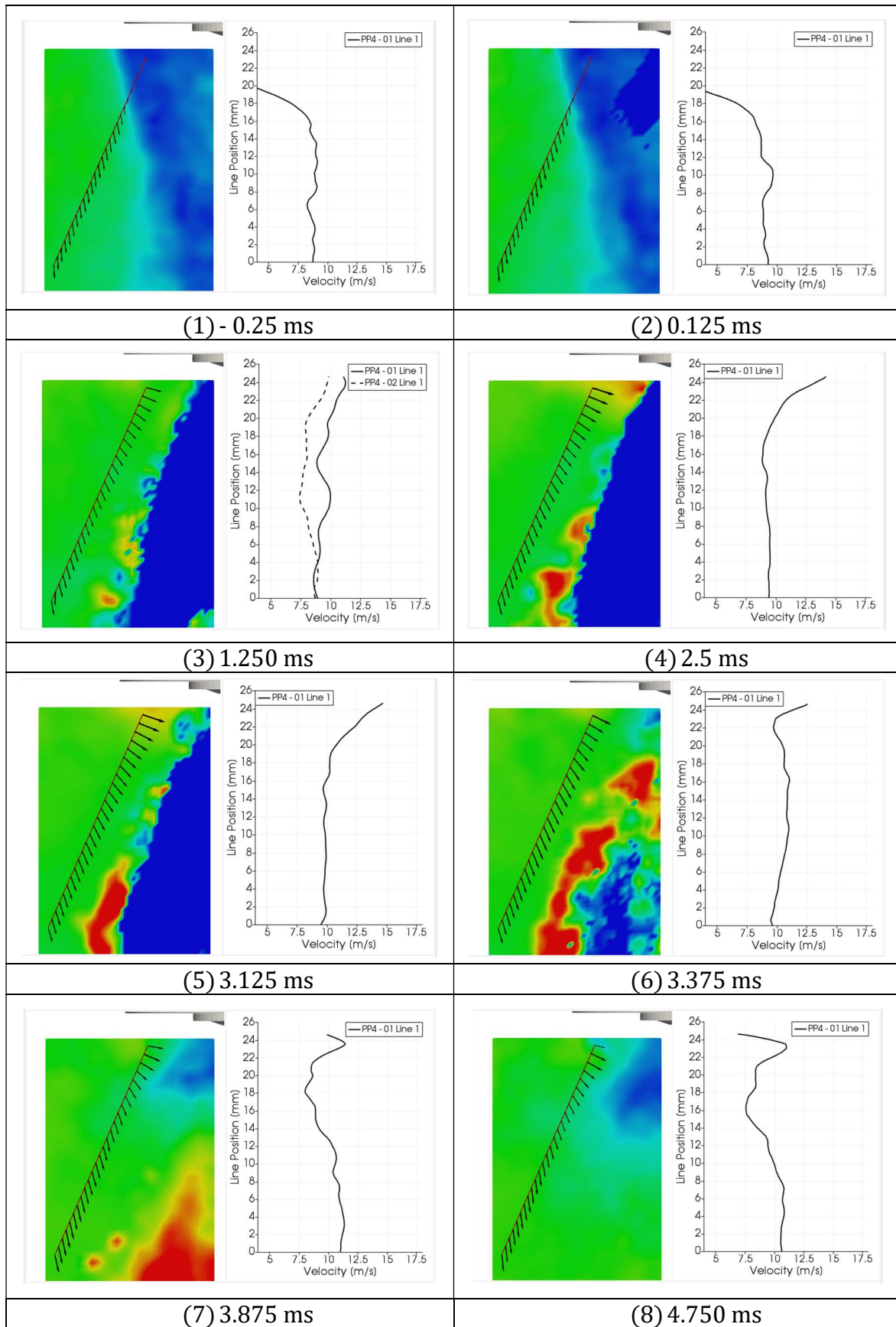


Figure 6.72 – The temporal evolution of velocity near the spray boundary (left figures) in the case PP4-01. The velocity magnitude over the highlighted line is shown in figures to the right.

The effects of injection pressure in the velocity field are investigated by comparing cases PP4-01 to PP4-02. The two cases have the same inlet air mass. The fuel pressure is changed from 100 *bar* in the condition PP4-01 to 60 *bar* in the condition PP4-02. Figure 6.73 shows the temporal sequence of the velocity fields in the case PP4-02. The velocity magnitude distributions at each timestamp are shown in the left figures. The comparison between velocity profiles in the cases PP4-01 and PP4-02 are shown in the right figures.

Instant (1) shows the distributions at the instant 0.125 after SOI. Different interactions are observed. Comparing the velocity magnitude distributions, the case PP4-02 with lowest injection pressure present larger effects in the interaction. The disturbance in the air flow field is clearly larger, especially in the near tip region and below the spray tip. The same characteristic is also visible in the profile plots. In the case PP4-01, the profile still resembles the stationary condition. In the case PP4-02, the velocity profile has changed. The higher degree of interaction for case PP4-02 is expected. At lower injection pressures, droplets and structures in the spray tip can achieve momentum magnitudes comparable to the air momentum near the spray boundary. At 0.25 *ms* after SOI, instant (2), a high velocity cluster is present over the sampling line, creating the observed peak in the profile plot.

At 1.250 *ms* after SOI, at instant (3), the velocity profiles remains stable until EOI. The regions far from injector tip are less affected. The near injector tip region presents the distinct increase in the velocity magnitudes. The velocity difference between the cases gradually reduces during injection. At the end of injection, the difference between the two profiles are more pronounced at the near tip region, as illustrated at instant (4).

At 0.375 *ms* after the EOI, instant (5) shows regions of elevated velocity similar to the case PP4-01. These regions are related to the EOI transient phenomenon. By comparing the velocity profiles at instant (5), the injection pressure can affect the transient phenomenon. In the case of higher pressure, the highest magnitudes are in the regions near the injector tip. At instant (6), the high velocity regions have been transported further down the chamber. The velocity profiles in both cases have similar tendencies.

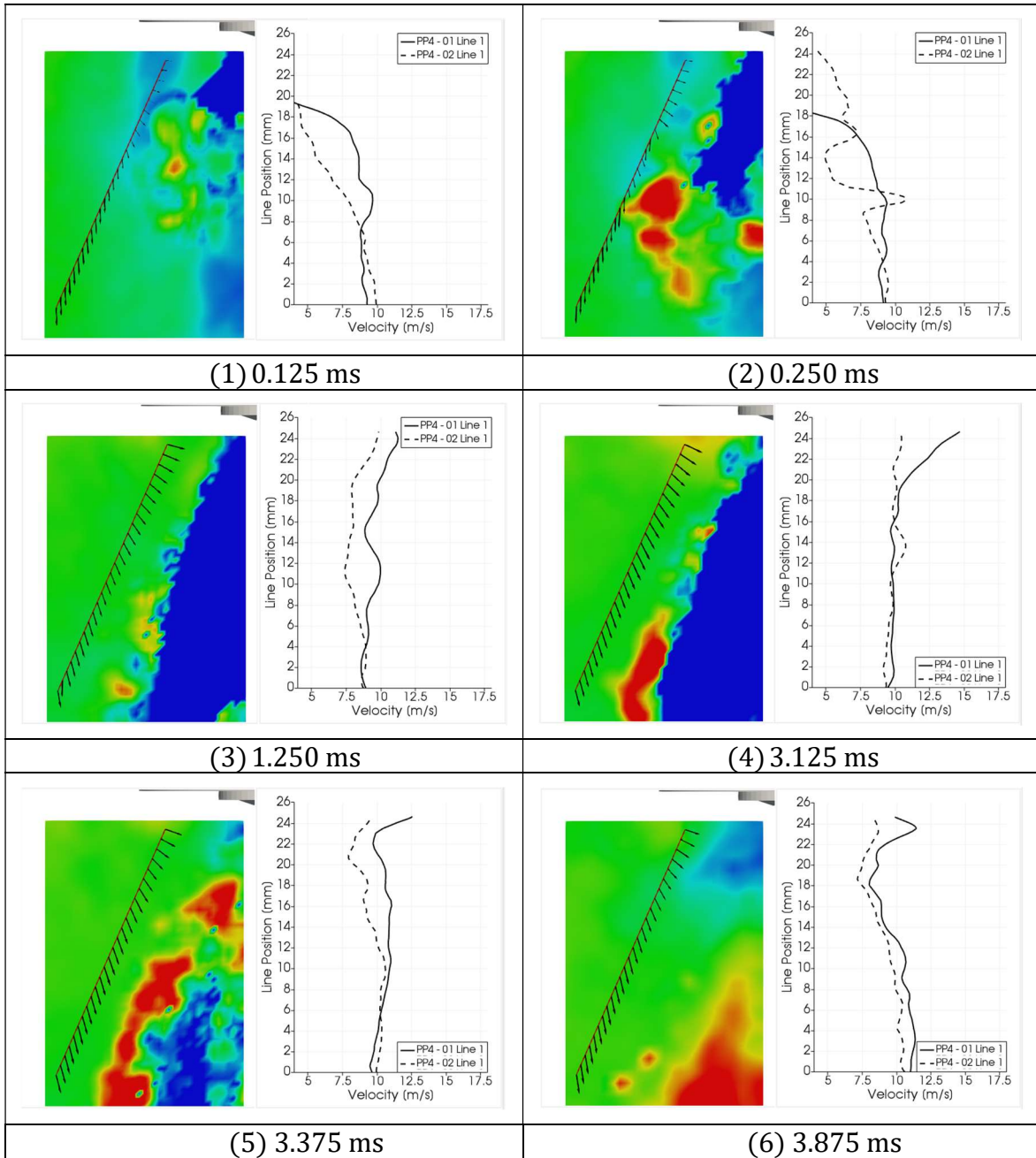


Figure 6.73 – The effects of injection pressure in temporal evolution of the velocity near spray boundary (left figures) in the case PP4-02. The velocity magnitude over the highlighted line is shown in figures to the right.

### 6.2.6 Effects of the inlet air mass flow

This section analyzes the effects of the inlet air mass flow in the spray development. Following the same approach of the other control parameters, the comparison are made in pairs. At each analysis, the same perforated plates set and the injection pressure is constant in both cases.

Figure 6.74 shows the comparison between the ensemble-average velocity fields of the acquired instant  $0.125\text{ ms}$  after SOI. The two compared cases are PP4-01 and PP4-03. Note that the color range is different from those shown in section 6.2.3. This range was chosen to enhance the differences between the two compared cases. Since the inlet air mass flow is higher in the case PP4-03, the velocity magnitudes in the outer region are higher than in the case PP4-01. At this instant, the sprays penetrates the low velocity region. In both cases, the recirculating vortex is formed. The velocities in the region near the injector tip increased due to the feedback mechanism of these vortices. At this instant, no effects are noted in the outer regions.

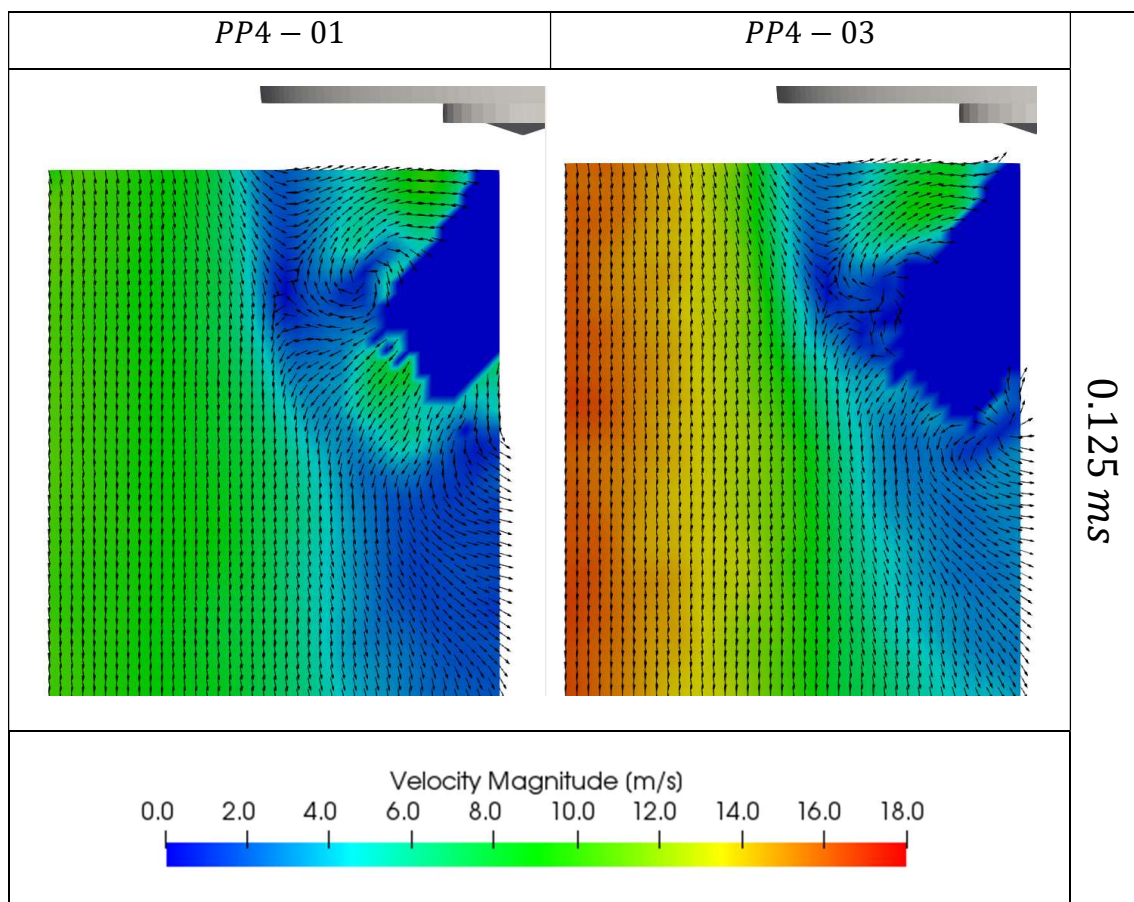


Figure 6.74 – The comparison of the case conditions: PP4-01 and PP4-03. The effects of the inlet air mass flow. Timestamp:  $0.125\text{ ms}$  after SOI.

Figure 6.75 shows the next acquired time instant, at  $0.250\text{ ms}$  after SOI. In these conditions, the sprays penetrated further down the chamber but the effects of the outer velocity regions are still not significant. Note that the velocity distributions around the main spray boundary and injector tip are similar in the two cases. The same high velocity cluster related to the previous stabilized vortex is observed near the spray main boundary.

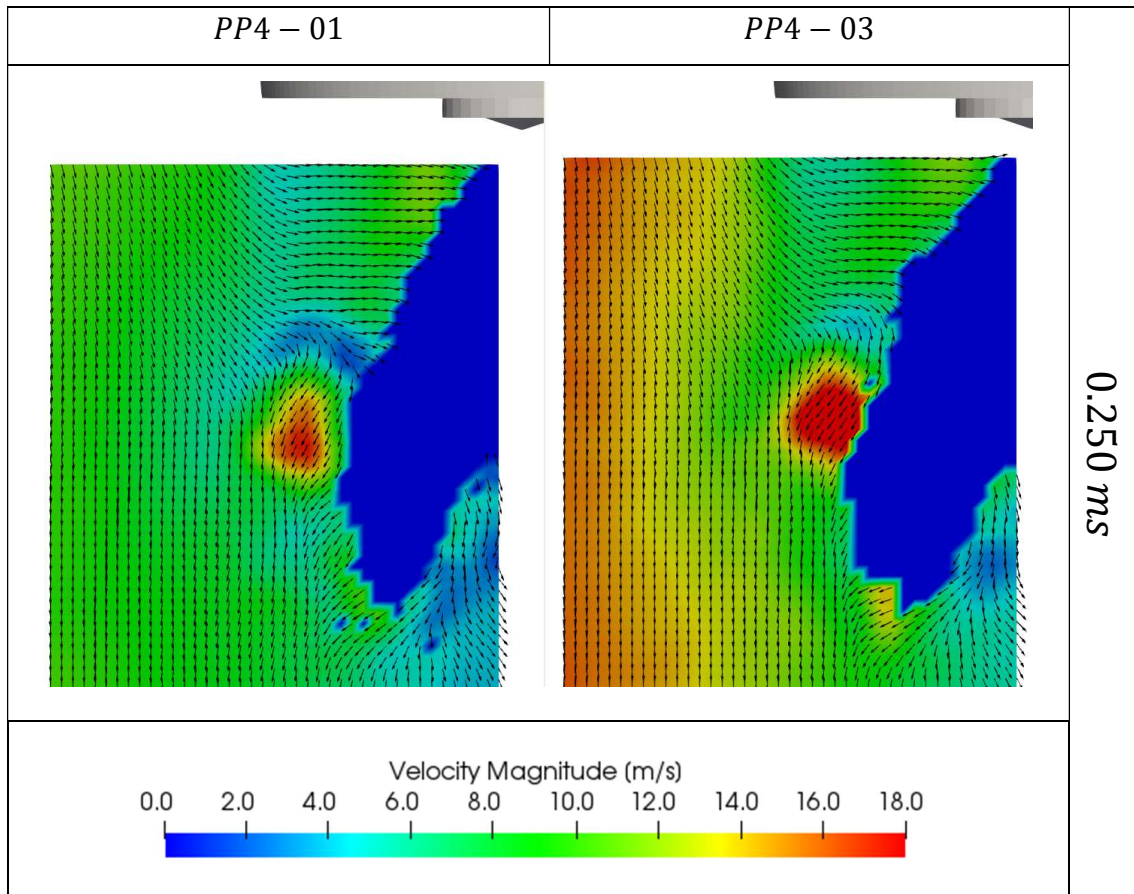


Figure 6.75 – The comparison of the case conditions: *PP4-01* and *PP4-03*. The effects of the inlet air mass flow. Timestamp:  $0.250\text{ ms}$  after SOI.

Figure 6.76 shows the velocity fields at an instant during the quasi-steady phase. At  $2.625\text{ ms}$  after SOI, the velocity distributions are different. In the case with lowest inlet air mass flow, the magnitudes are lower in the measured regions. The flow orientations are similar regardless of the inlet air mass flow.

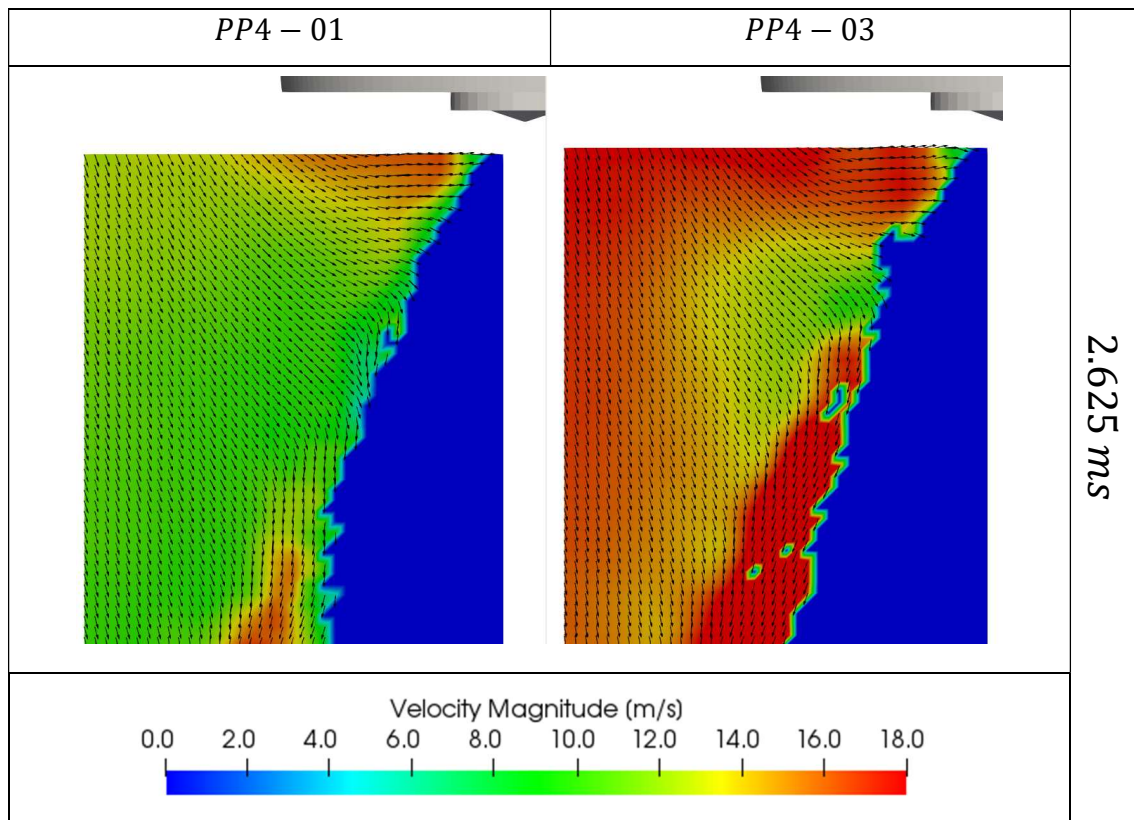


Figure 6.76 – The comparison of the case conditions: PP4-01 and PP4-03. The effects of the inlet air mass flow. Timestamp:  $2.625\text{ ms}$  after SOI.

The ensemble-average velocity fields at the instant  $0.250\text{ ms}$  after EOI are shown in Figure 6.77. After the end of injection, the velocity fields far from the spray boundary still resemble the conditions during the quasi-steady phase. The flow orientations are similar and the magnitudes are different. In the region near the injector tip, the velocity fields react to the needle valve closing and the magnitudes decrease in both cases. The penetration wave phenomenon is present in both case conditions. Note that the velocity magnitudes for these transient effects are roughly the same in the two cases. The observation suggests that the inlet air mass flow has little effect in the EOI transient phenomenon. Considering the results for the injection pressure variation and the observations of the works by Moon et al [64] [12], the EOI transient phenomenon is more sensitive to the spray parameters rather than the surrounding air flow boundary conditions.

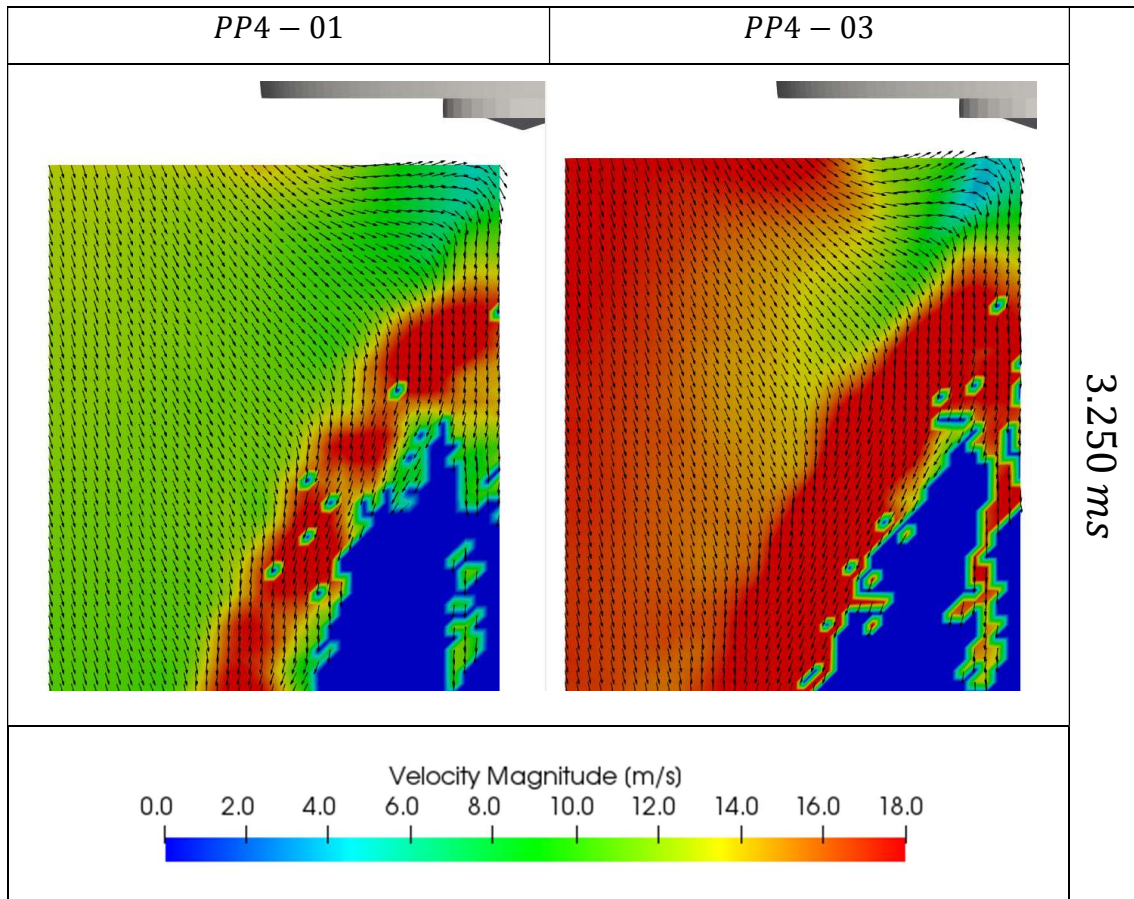


Figure 6.77 – The comparison of the case conditions: PP4-01 and PP4-03. The effects of the inlet air mass flow. Timestamp: 3.250 ms after SOI.

Figure 6.78 shows the ensemble-average velocity fields at three different instants during the spray development in the cases PP2-01 and PP2-03. A similar velocity evolution is observed. The behavior is consistent with the results in the cases PP4-01 and PP4-03: the flow fields have similar orientations and the magnitudes are higher for the case with the highest inlet air mass flow. After the end of injection, the velocity fields far from spray boundary resemble the conditions during injection. Near the injector tip, the velocity distributions decrease their magnitudes. The penetration wave develops in both case conditions with comparable magnitudes.

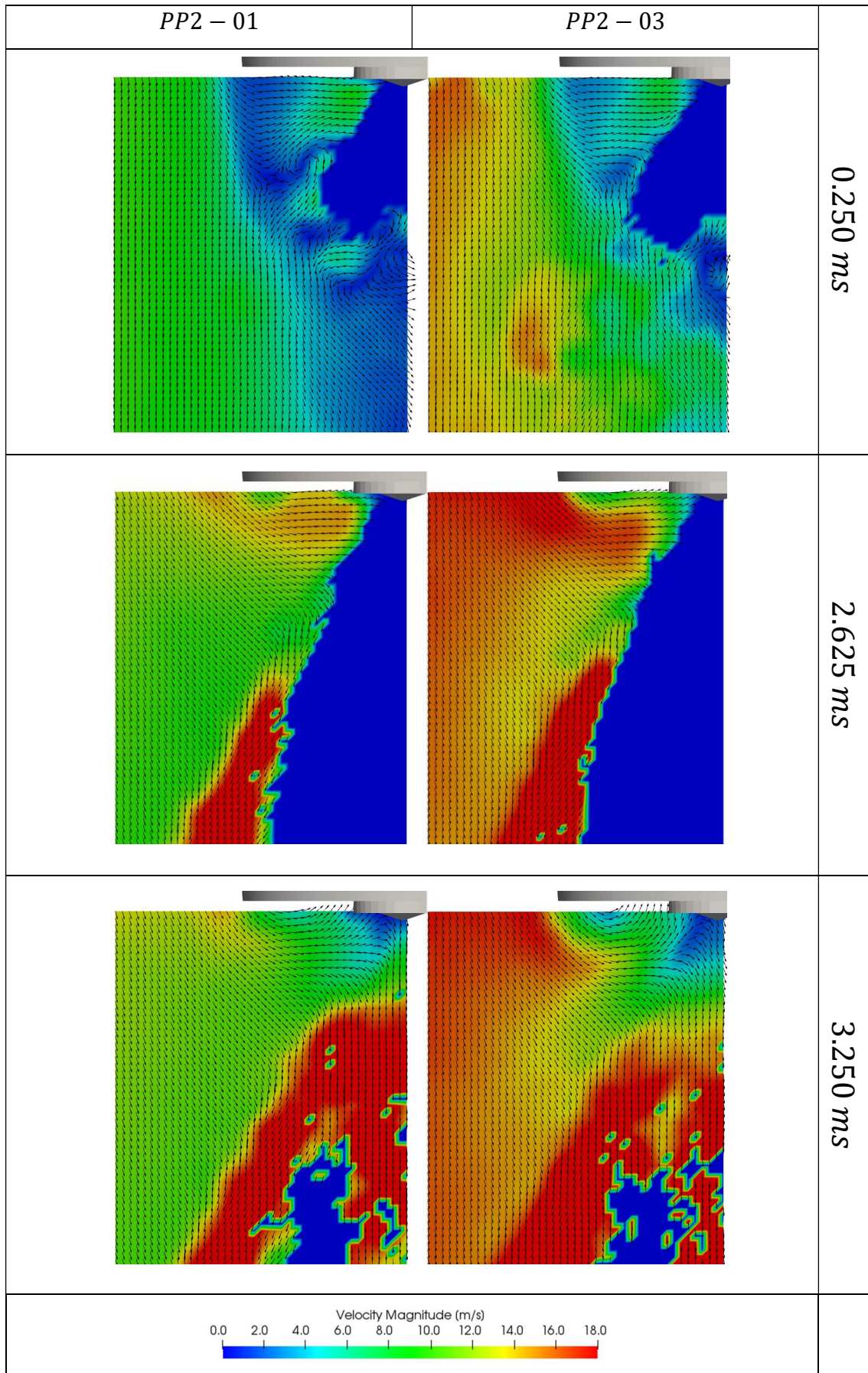


Figure 6.78 – The comparison of the case conditions: PP2-01 and PP2-03. The effects of the inlet air mass flow.

To investigate the effects of the inlet air mass flow in the turbulence development during the spray event, the turbulent intensity distributions were calculated with the same procedures described previously. For the comparison of cases PP4-01 and PP4-03, only the turbulent intensities obtained with the  $y$  direction velocity component are evaluated. The values calculated with the  $x$  direction components are not shown since the behaviors are similar and do not provide new information.

Figure 6.79 shows the results of the ensemble-average turbulent intensity distributions in the cases PP4-01 and PP4-03. The image represents the time instant  $0.125\text{ ms}$  before SOI. The distributions resemble the stationary fields. Higher values are found in the region below the injector cartridge and are associated with the stabilized recirculating structure. In the case of highest inlet air mass flow, the values of turbulent intensity are slightly higher in the region out of the recirculation zone.

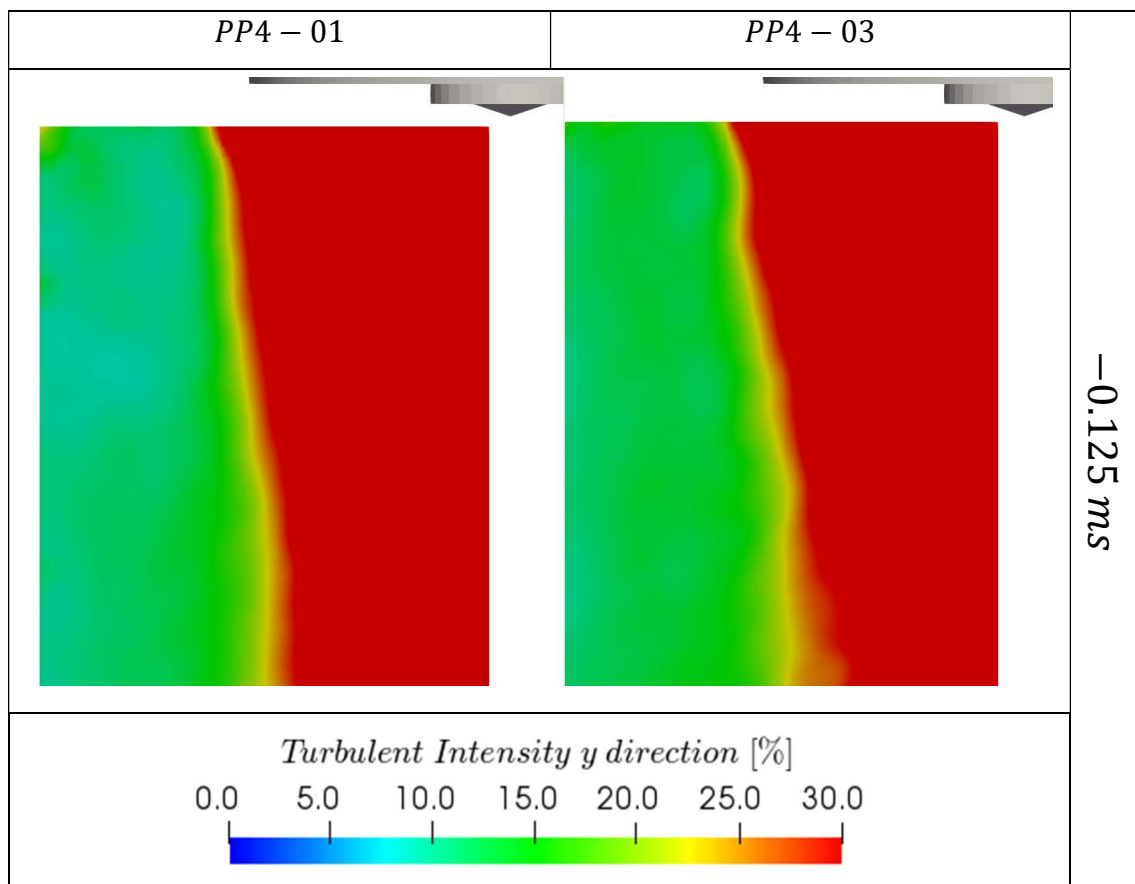


Figure 6.79 – The turbulent intensity distributions calculated with  $y$  direction component. The comparison between cases conditions PP4-01 and PP4-03.  $0.125\text{ ms}$  before SOI.

During the injection, at the instant  $0.250\text{ ms}$  after SOI, the turbulent intensity distributions are consistent with the velocity fields. The turbulent intensity levels changes only in the regions affected by the spray passage. Figure 6.80 shows the results for the specific instant.

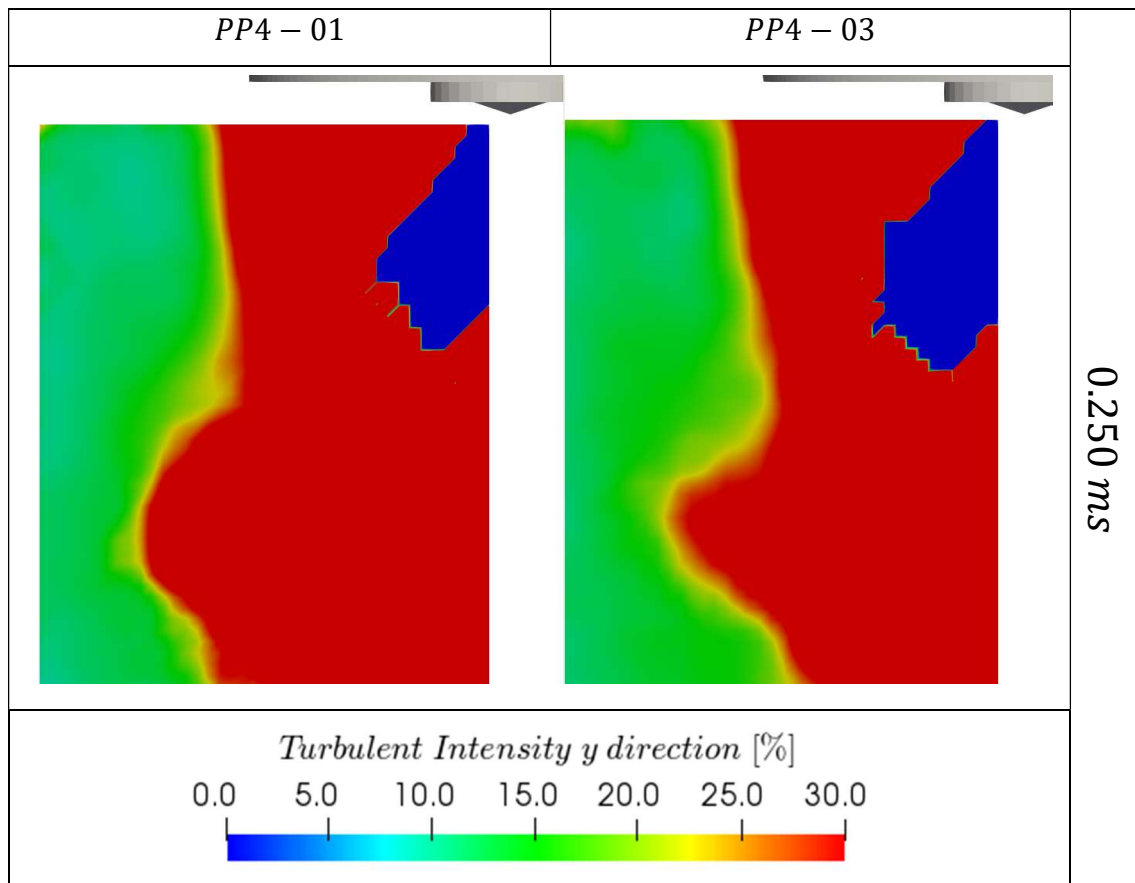


Figure 6.80 – The turbulent intensity distributions calculated with *y* direction component. The comparison between cases conditions *PP4-01* and *PP4-03*.  $0.250\text{ ms}$  after SOI.

During the early injection phase, at roughly  $0.750\text{ ms}$  after SOI, the velocity fields initiates the reorientation due to the pressure gradient mechanism. The turbulent intensity distributions are also modified. The levels are still higher for the case PP4-03 in the region out of the spray. Figure 6.81 shows the results for this time instant.

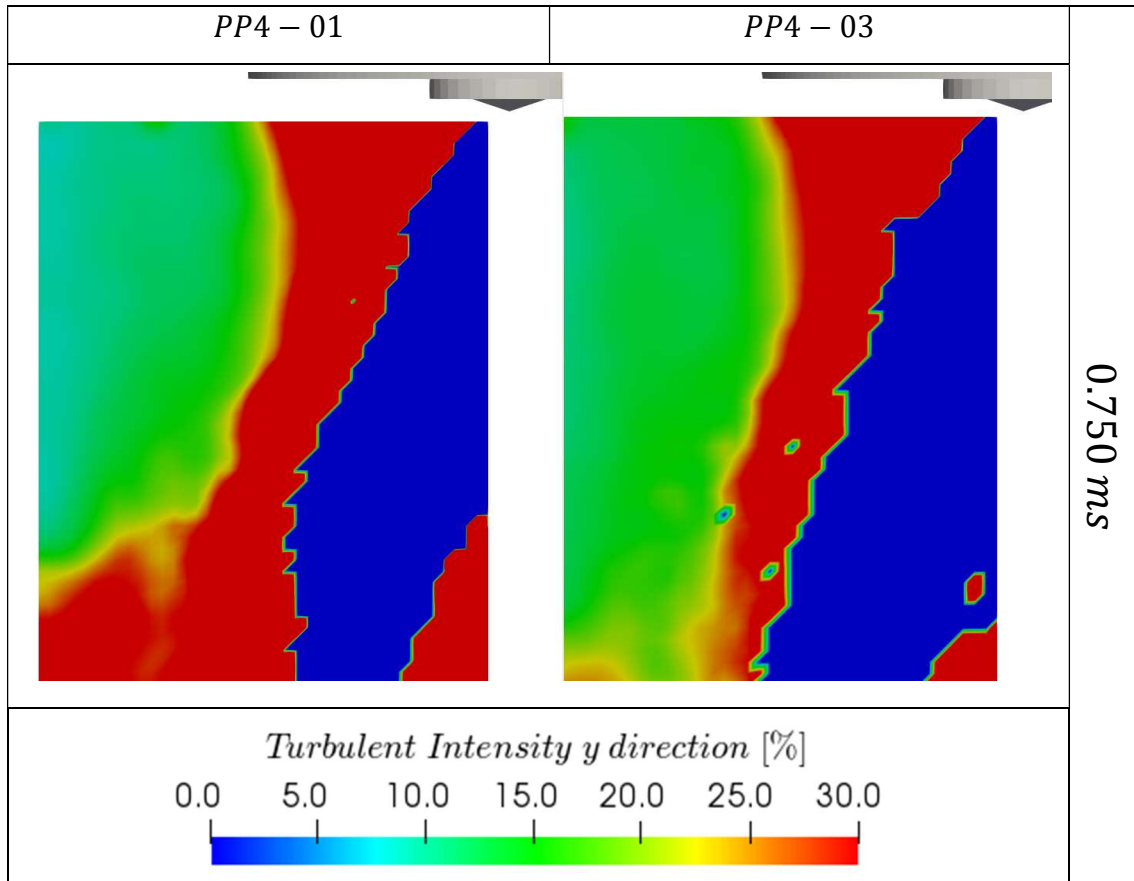


Figure 6.81 – The turbulent intensity distributions calculated with  $y$  direction component. The comparison between cases conditions PP4-01 and PP4-03.  $0.750\text{ ms}$  after SOI.

The spray development maintains the pressure gradient mechanism actuating in the surrounding air flow. The velocity fields are oriented towards the spray boundary and the turbulent intensity levels gradually decrease with time. Figure 6.82 shows the turbulent intensity distributions at 1.625 ms after SOI.

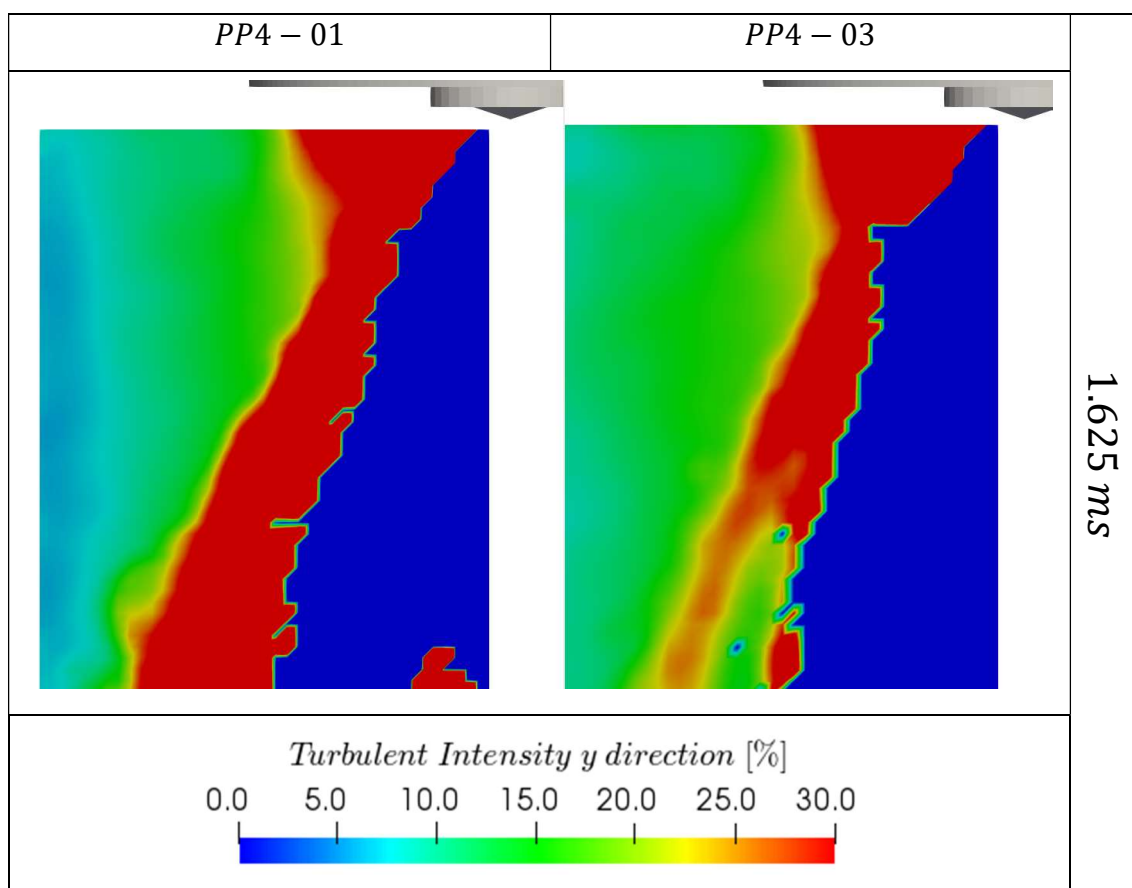


Figure 6.82 – The turbulent intensity distributions calculated with  $y$  direction component. The comparison between cases conditions PP4-01 and PP4-03. 1.625 ms after SOI.

Figure 6.83 shows the results for the instant  $2.875\text{ ms}$  after SOI. At near the end of injection, the turbulence intensity fields assume similar distributions for both conditions. In the region far from the spray boundary, the levels are lower in the case of the lowest inlet air mass flow. Near the injector tip, the values are at similar levels.

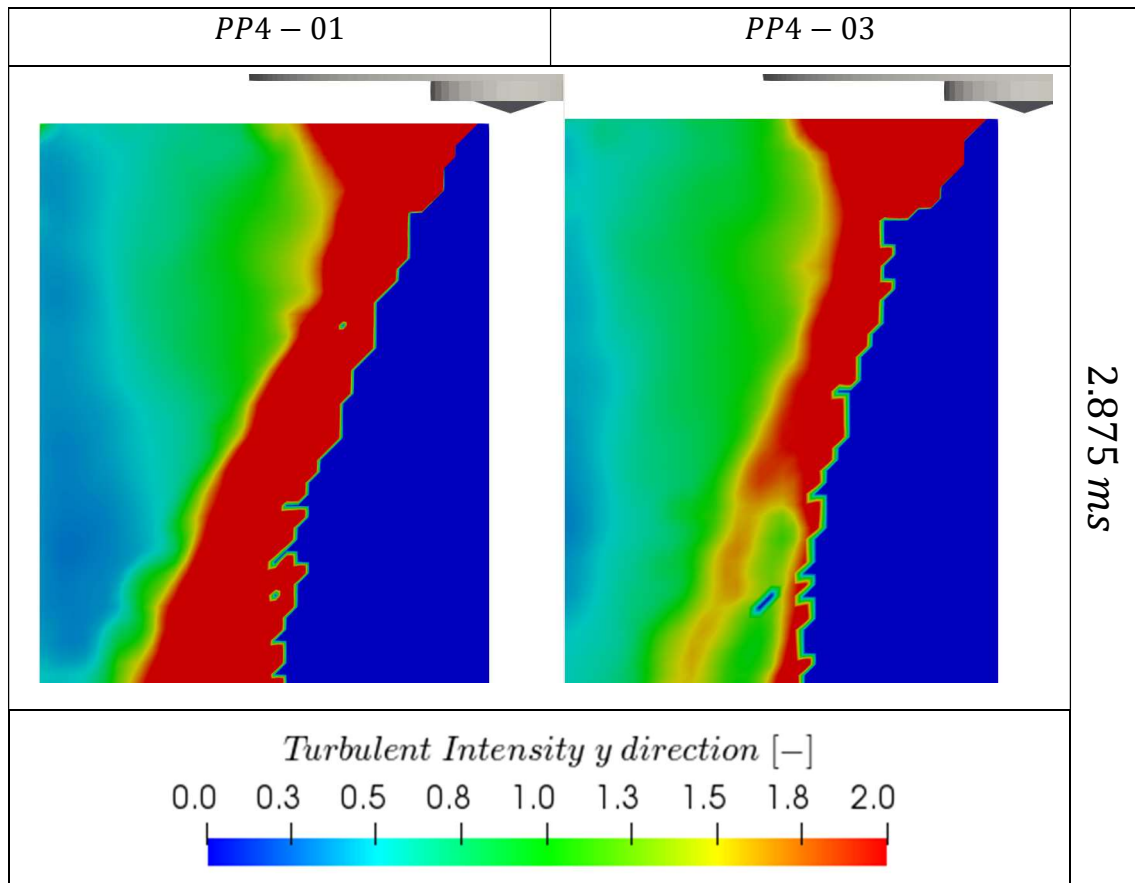


Figure 6.83 – The turbulent intensity distributions calculated with  $y$  direction component. The comparison between cases conditions PP4-01 and PP4-03.  $2.875\text{ ms}$  after SOI.

Figure 6.84 shows a time instant after the end of injection. The EOI transient phenomenon can be observed. At  $0.250\text{ ms}$  after EOI, the turbulent intensity distributions are consistent with observations of the velocity fields. In both cases, the levels far from the spray boundary are similar to the values found during injection. In the remaining regions, the values are similar in both cases. Slightly higher values are found near the spray boundary in the case PP4-03, suggesting that the inlet air mass flow do not significantly affects the EOI transient development.

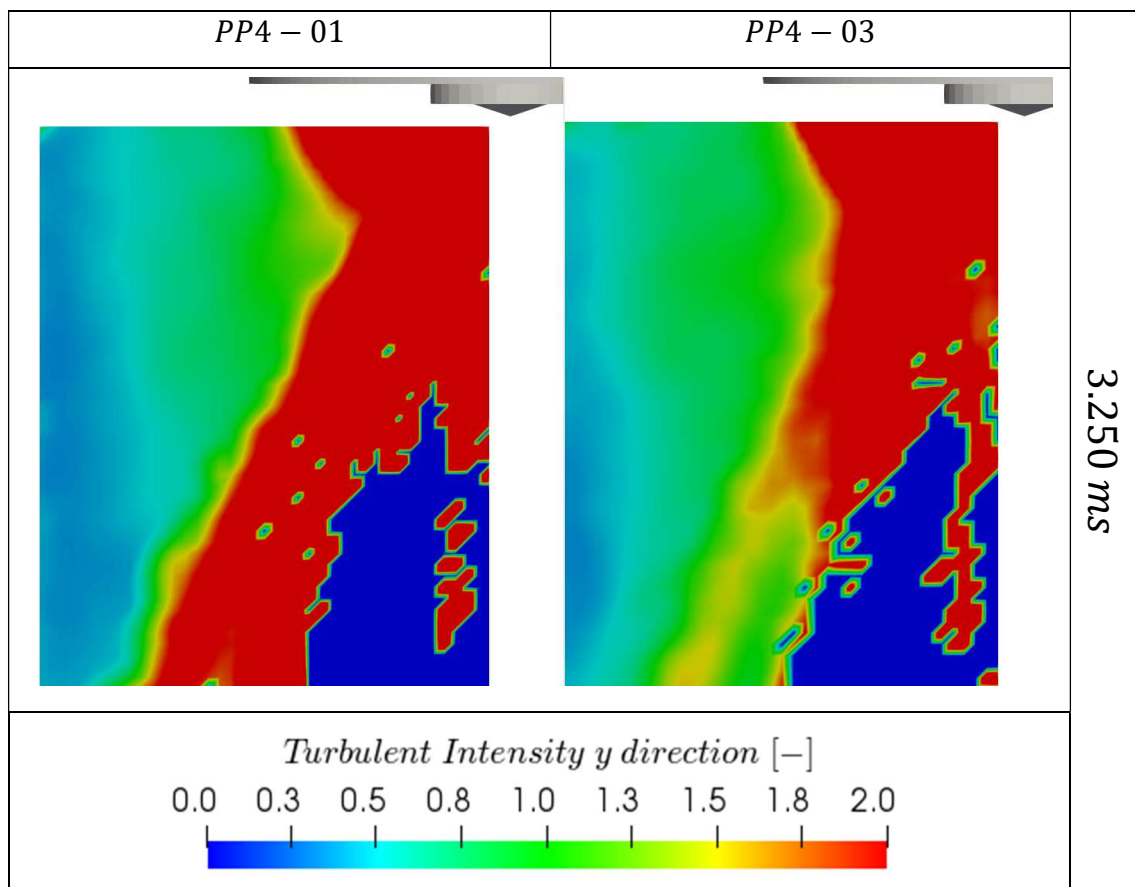


Figure 6.84 – The turbulent intensity distributions calculated with *y* direction component. The comparison between cases conditions *PP4-01* and *PP4-03*.  $3.250\text{ ms}$  before SOI.

Figure 6.85 shows the results for the turbulent intensity distributions in the cases *PP2-01* and *PP2-03*. At these time instants, the same characteristics are present. Near the end of injection and during the penetration wave, the turbulent intensity distributions are similar regardless of the value of the inlet air mass flow.

The evaluation of the inlet air mass flow effects indicates that the pressure gradient mechanism is present in both case conditions. With the same mechanism, the developed velocity fields direct towards the spray boundary during injection. For the region near the injector tip, the acceleration magnitudes are higher. The cases with higher inlet air mass flow present higher velocity magnitudes throughout the injection. The evolution of the turbulent intensity fields is different depending on the value of the inlet air mass flow. However, with the spray development, these distributions tends to similar levels near the end of injection. After the EOI, during the penetration wave, the velocity magnitudes are roughly similar in both conditions. The turbulent intensity levels are also similar. Considering the results for the injection pressure variation, the observations indicate that the penetration wave is more influenced by the spray boundary conditions than the air flow velocity distributions.

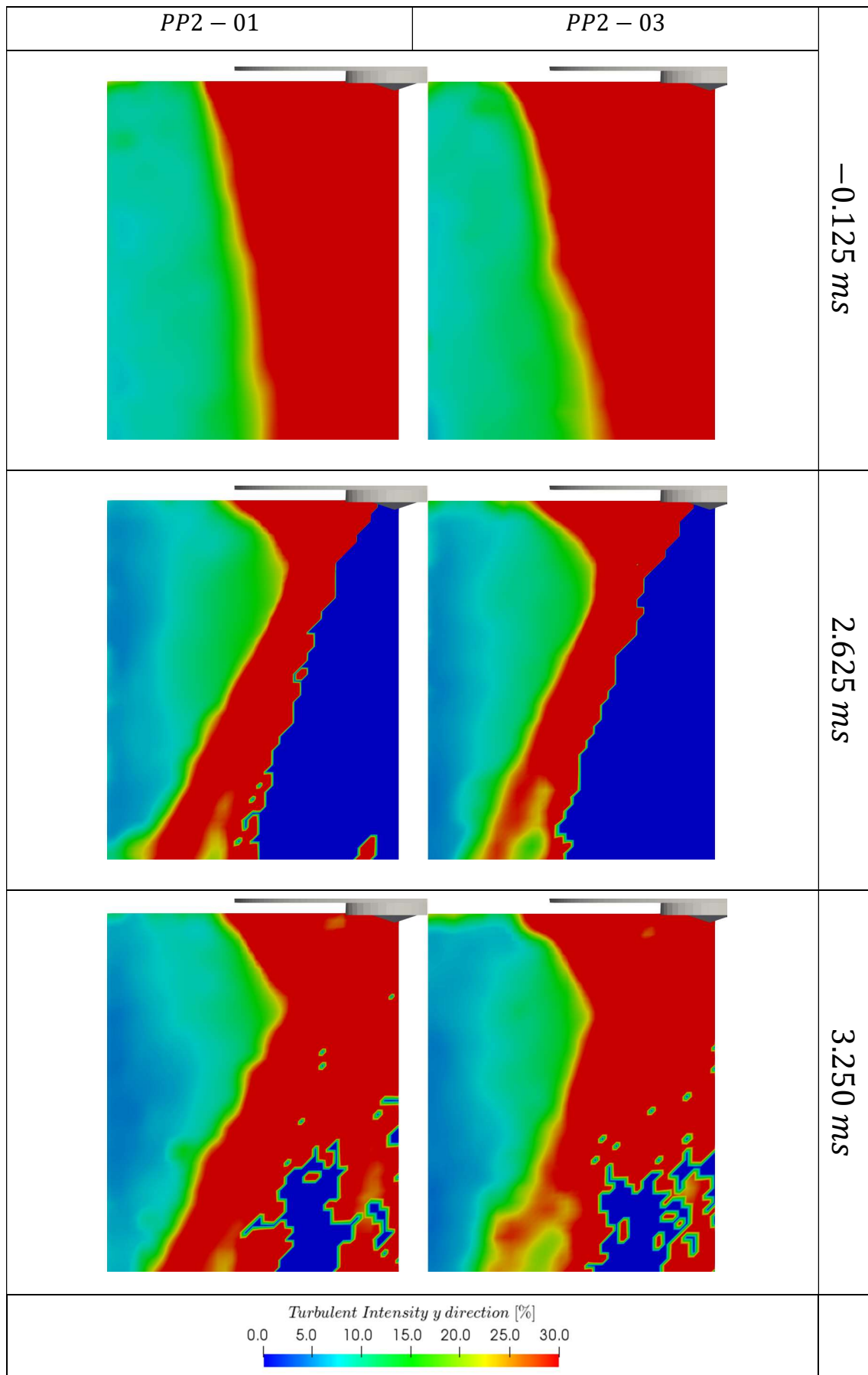


Figure 6.85 – The turbulent intensity calculated with y direction component. The comparison between cases conditions PP2-01 and PP2-03

### 6.2.6.1 Near injector tip

The influence of inlet air mass flow variation is examined in the cases PP4-01 and PP4-03. Figure 6.86 shows the comparison between the space-average variables of the two cases. The points are located at the same physical coordinates in both cases. Comparing stage 1, acceleration rate for both cases are similar during about the entire stage. The exception is at the end of stage 1. In the case of the highest inlet air mass flow, the velocity field is further accelerated. As a result, the magnitudes in the case PP4-03 reach slightly higher values. In the case PP4-03, the air and spray achieve the *quasi*-steady conditions significantly earlier. In fact, stage 2 in case PP4-03 is roughly 50% as long as in case PP4-01. Thus, this phase comprehend 1.5 *ms* of the 3 *ms* of injection period. This difference is illustrated in Figure 6.86.

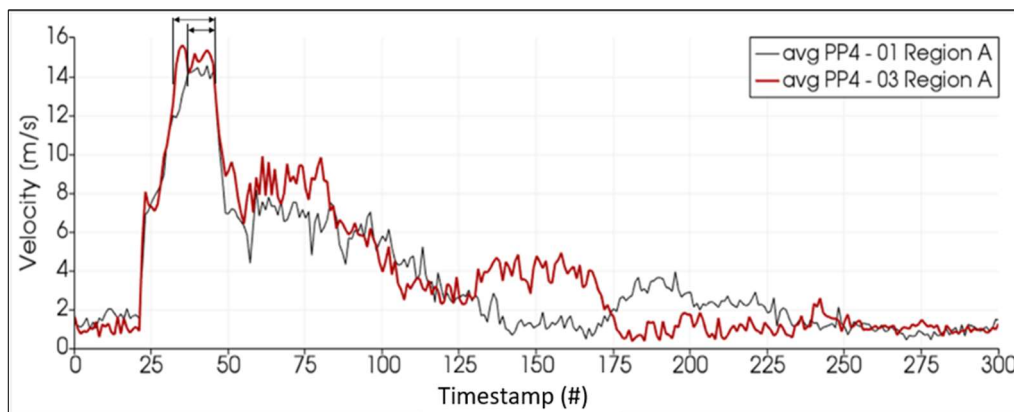


Figure 6.86 – The time history of the space-average velocity - the effects of the inlet air mass flow.

This longer period of *quasi*-steady injection is consistent with the highest inlet air mass flow. With the same injection pressures, the static pressure gradient that occurs near injector tip of case PP4-01 is also present in the case PP4-03. This would explain the same acceleration rate at about the entire stage 1. However, in the case PP4-03, the region near injector tip is constantly supplied with air flow with higher velocity and thus a greater initial dynamic pressure. This condition allows a faster spray stabilization when compared to the case PP4-01.

Note that the recirculation structure below the injector cartridge has roughly the same velocity distributions in case PP4-01 and case PP4-03 (see for example, Figure 6.35 and Figure 6.37). This characteristic provide initial conditions with similar behavior for both cases, allowing a proper comparison between cases.

### 6.2.6.2 Spray main boundary

Figure 6.87 shows the comparison between the cases PP4-01 and PP4-03. The two cases have the same conditions with exception of the air mass flow rate. The air mass flow rate is  $0.06614 \text{ kg/s}$  in the case PP4-01 and  $0.09674 \text{ kg/s}$  in case PP4-03. The injection pressure is maintained at  $100 \text{ bar}$  in both cases.

The overall development of the velocity distributions in case PP4-03 are consistent and follow the same tendency of the case with the lowest air mass flow. At the initial timestamps, illustrated by instants (1) and (2), the air velocity distributions are little affected. With the spray evolution, the velocity profiles are modified. At instant (3), the near injector tip region experiences a higher acceleration when compared to other regions. As mentioned, apart from the values of magnitude, the behavior of both velocity profiles curves is roughly the same.

At instant (4), the presence of the EOI transient phenomenon is also observed in the case PP4-03. Note that the velocity magnitudes after  $y = 20 \text{ mm}$  are approximately equal in the two cases. This indicates that the EOI transient is more dependent of the injection pressure than to the air mass flow. In both cases, the acceleration due to the end of injection is higher for the region near the injector tip. Instants (5) and (6) show the propagation of the air-spray structure through the measurement plane and the initial recovery of stationary conditions.

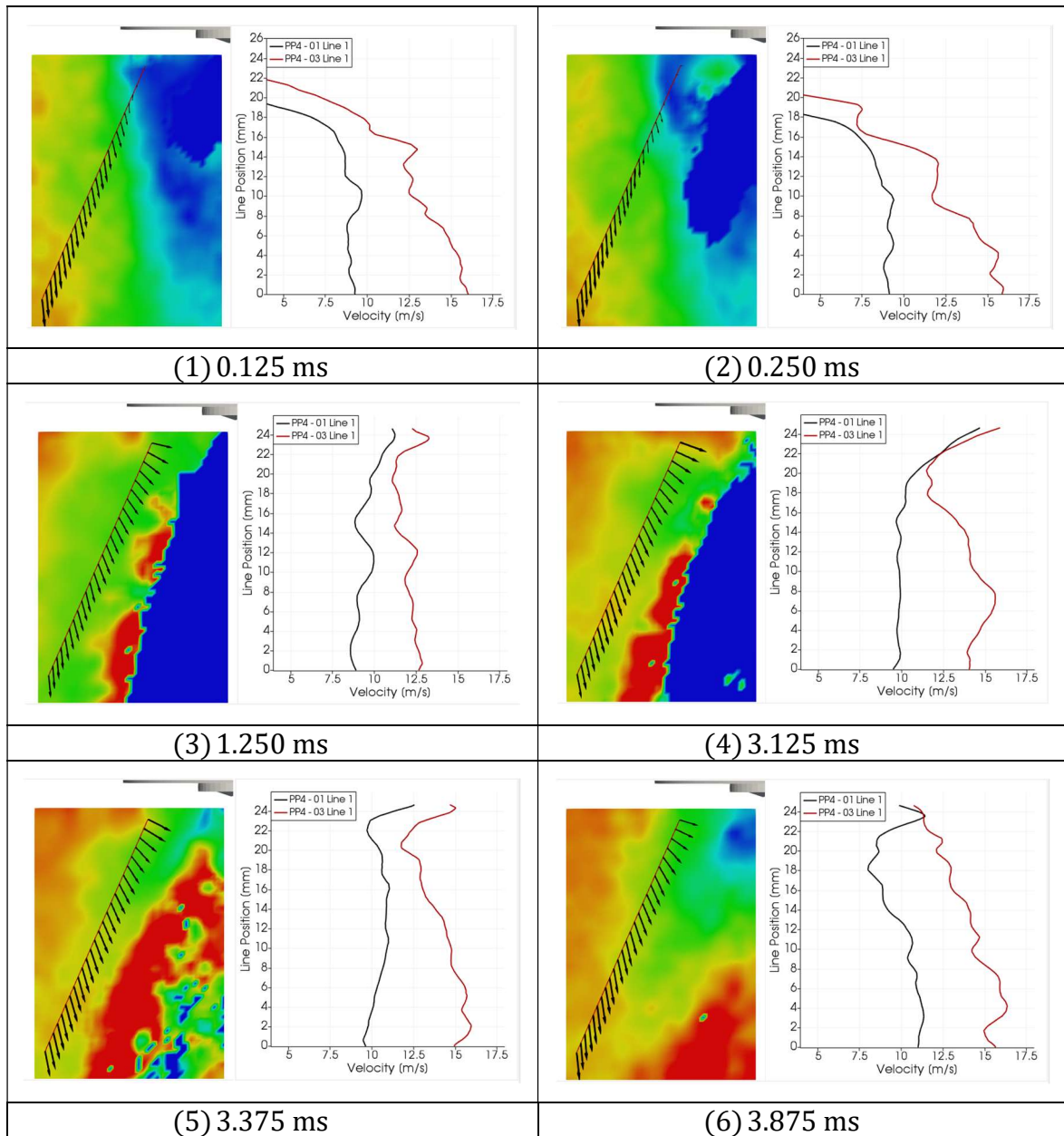


Figure 6.87 – The effects of the inlet air mass flow in temporal evolution of the velocity near the spray boundary (left figures) in the case PP4-03. The velocity magnitude over the highlighted line is shown on figures to the right.

### 6.2.7 Spectrogram analyses

In the previous sections, the turbulent intensity distributions are reorganized according to the pressure gradient mechanisms. The levels decrease during spray formation. This evolution is observed in all the conditions of injection pressure, of air mass flow and of turbulent integral length scales. However, these results do not provide any description of the energy distributions between the scales present in the flow. To assess this kind of information, a different approach is required.

If the studied phenomenon is at the *wide-sense stationary* conditions, then the Power Spectra Density can be estimated with the methodology described in section 6.1.2.1. In these situations, a time-invariant PSD is determined for each point in the sample space. However, in the case of the spray evolution, the events are not stationary and the same methodology cannot be directly applied. A different approach must be used to describe the time-transient behavior. For example, the time-frequency and time-scales methods.

One of the basic time-frequency method is the discrete-time short-time Fourier transform (STFT). The idea behind the method is to compute the Fourier transform, the discrete-time FFT, in local sections of the signal. These local segments are obtained with a window that slides through the long signal over time. At each segment, the signal is considered stationary or periodic. Although it is a basic time-frequency method, the STFT provides satisfactory results. Moreover, it is a non-parametric method, which greatly simplifies its use.

In this section, the STFT method is applied to all the acquired cases to assess the time evolution of the power spectra densities during the injection. The spectra time-evolution provide information of how the energy is distributed in the scales during the injection events. In all the case conditions, the STFTs are calculated in samples of 10 and with a segment overlap of 75%. A Hamming window is used to segment the entire velocity fluctuation signal to prevent leakage in the FFT computations. The STFT is computed using 128 discrete Fourier transform (DFT) points.

Figure 6.88 shows an example of the spectrogram estimation in a point inside the air flow in one of the conditions studied. As described previously, the spectrogram

is a time-variant representation of the power spectra density distributions. Thus, the image represents a tridimensional function that describes the power content in the frequencies scales and their variations over time. At each slice of the spectrogram, the power distribution and frequency range are similar to the expected turbulence PSD for a WSS condition.

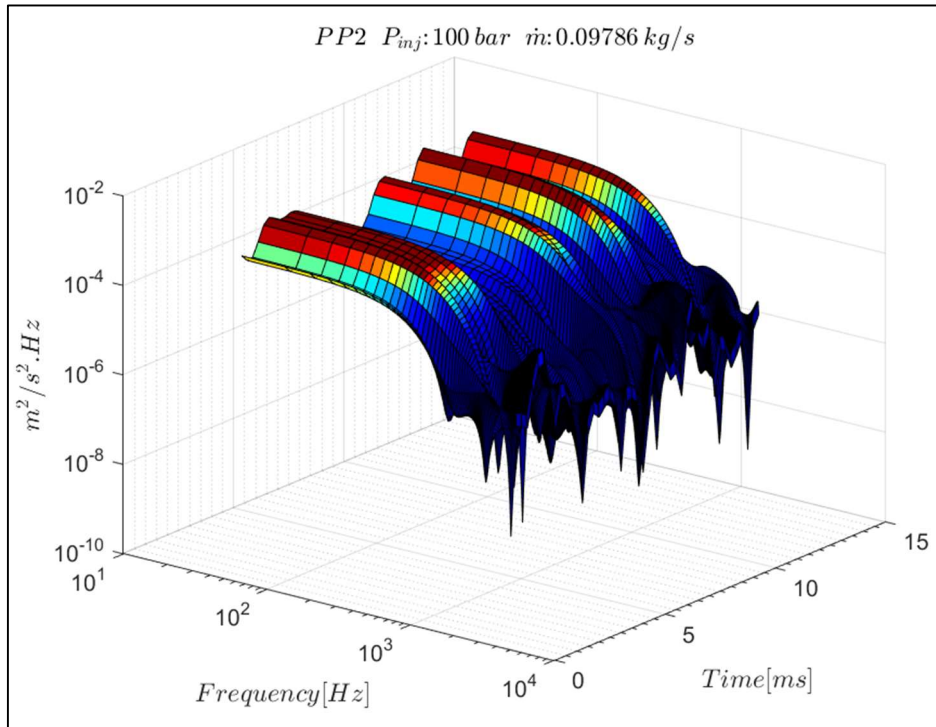


Figure 6.88 – The spectrogram estimation in a point inside the external flow. The spectrogram estimation is obtained with the STFT method.

### 6.2.7.1 Global development of the spectrograms

Figure 6.89 shows the evolution of the spectrogram of a point inside the air flow for the case PP4-01. The illustration in the left portion of the figure represents the point location. In this condition, the injection pressure is kept in 100 *bar* and the air mass flow at 0.006614 *kg/s*. The spectrogram is represented by its top projection view and the power density colors the map. The two vertical red lines indicate the start and the end of the injection event, respectively. Although the total ensemble-averaged period is 100 *ms*, only the evolution until 12 *ms* is shown due to clarity purposes.

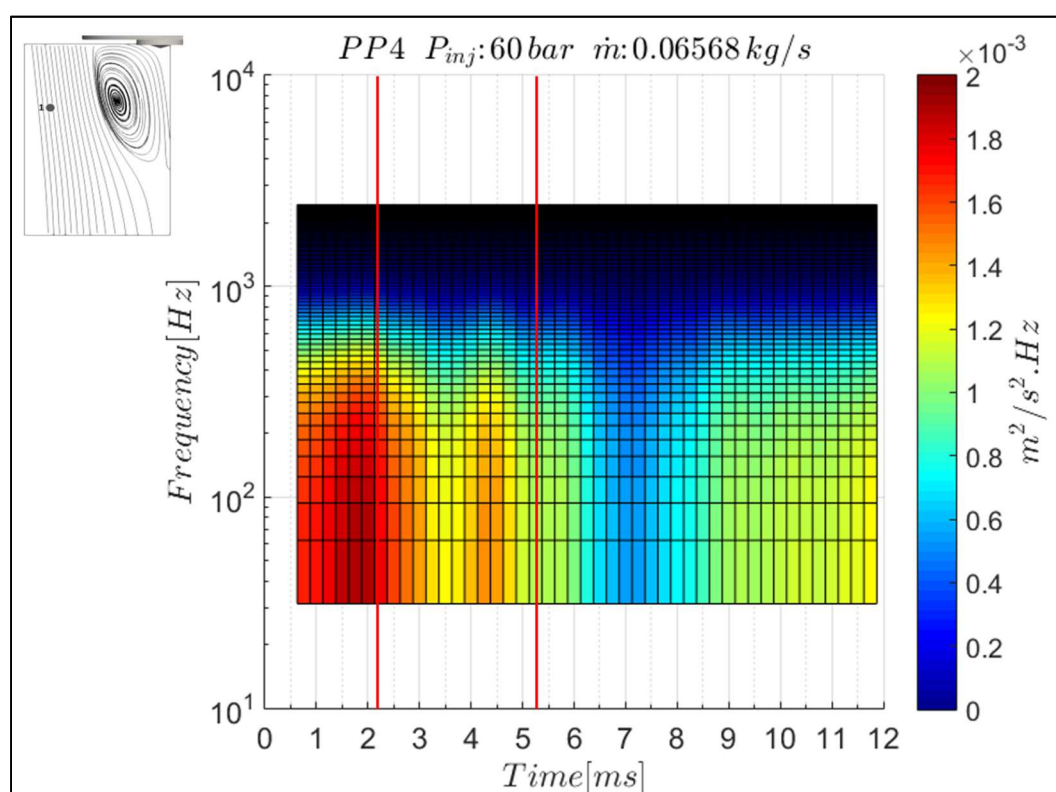


Figure 6.89 – The spectrogram evolution of point inside in the air flow during the injection event. The Case PP4-01. The red vertical lines indicate the SOI and EOI.

During the first instants of the spray formation, the air flow and fuel plumes interacts and modify the velocity distributions. As seen in section 6.2.3, the air flow field changes from the stationary velocity pattern to a distribution normal to the spray boundary. This velocity reorganization occurs at the first instants of the injection event and explains the decrease in the power distributions near SOI.

After the initial reorganization, while the spray is injected, the velocity fluctuations are reduced due to the pressure gradient mechanism created by the spray. Note the distributions during the injection event. The low levels of velocity fluctuations decreases the power content. This power reduction is present not only in the macro scales but in all the measured frequency scales. This decrease continues during injection, reaching the minimum values after EOI.

At a given instant, the power content distribution is again modified. The evolution of the power content in this stage is controlled by the passage of the structures in the probed point, as seen in the turbulence intensity distributions (see section 6.2.3). The power levels are significantly lower when compared to the initial conditions.

#### **6.2.7.2 Perforated plates effects**

Figure 6.90 shows the spectrograms of the cases PP2-01 and PP4-01. The air mass flow rate and the injection pressure are depicted in the images. Note the differences in the power content between the cases. The case with the lowest inlet turbulence integral scales also presents the lower power distribution before and during the injection. In both cases, the power decrease is consistent with the previous observations. The pressure gradient mechanism is present in both conditions. After the end of injection, even with a higher power content in the case PP4-01, the levels continue to decrease in all the frequency scales. Eventually, the distributions reach roughly the same levels regardless of the perforated plates set.

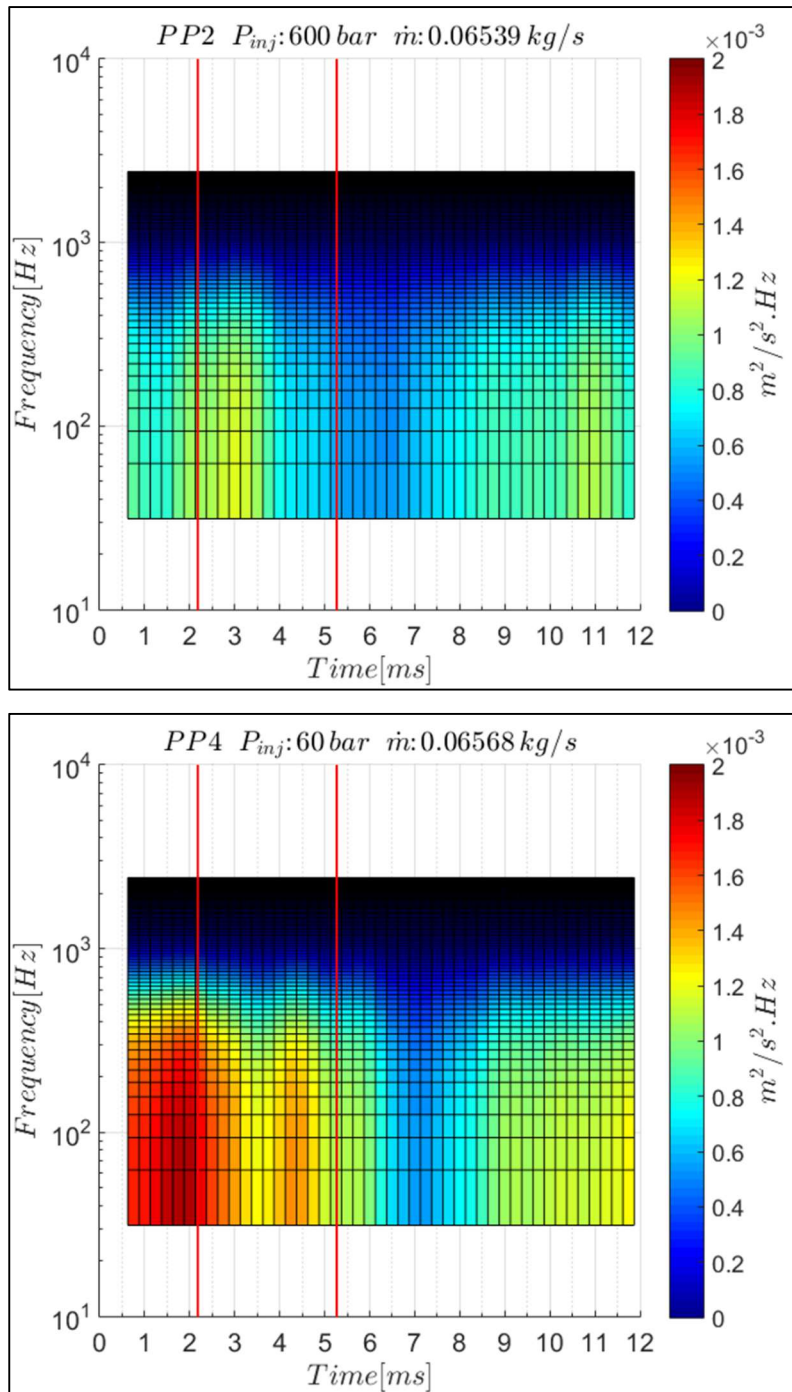


Figure 6.90 - The spectrogram analysis in a point inside the air flow field. The effects of the perforated plates set. Cases PP2-01 and PP4-01.

Figure 6.91 shows the results of the comparison between the cases PP2-03 and PP4-03. The same observations are drawn in this comparison. The behavior is also consistent with the analyses of the turbulent intensity distributions.

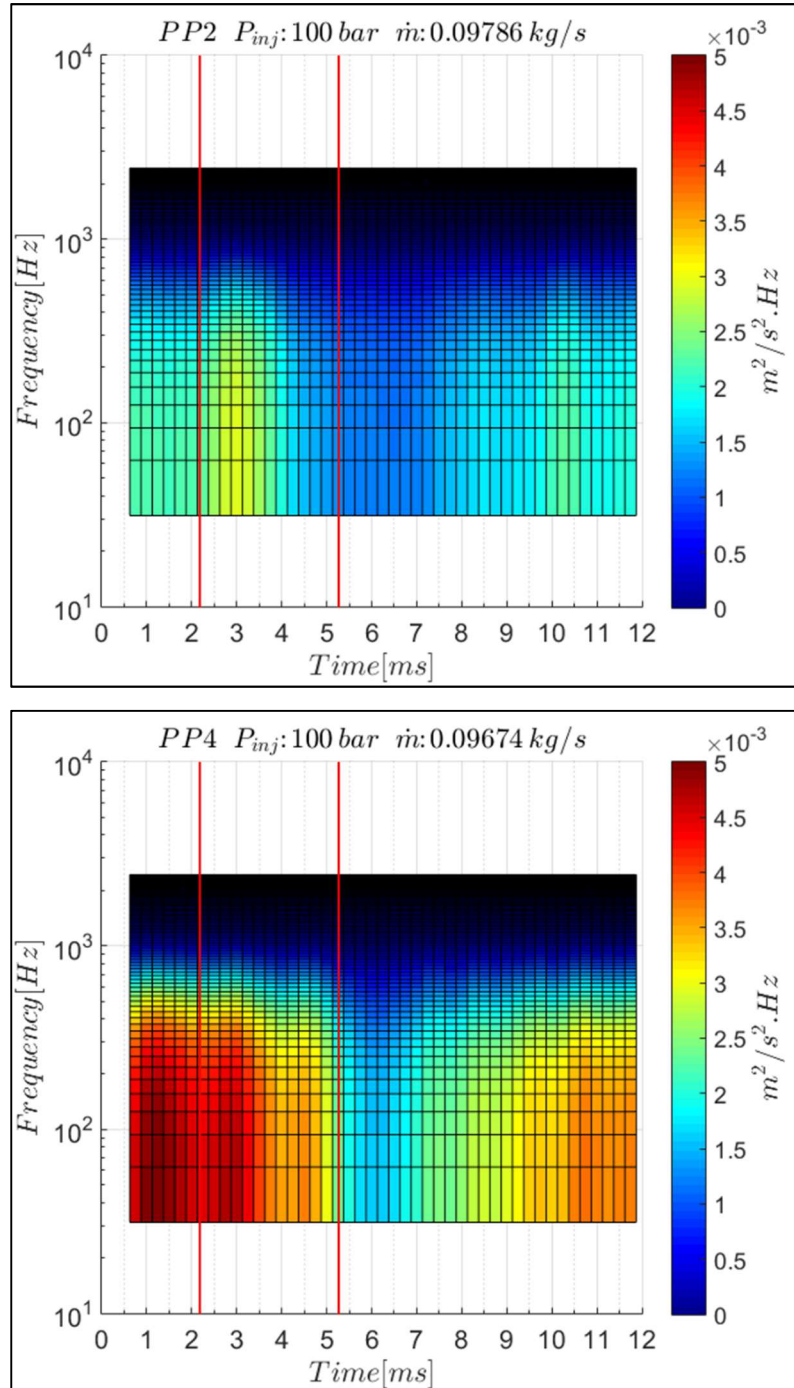


Figure 6.91 - The spectrogram analysis in a point inside the air flow field. The effects of the perforated plates set. Cases PP2-03 and PP4-03.

### **6.2.7.3 Injection pressure effects**

The effects of the injection pressure in the evolution of the power distributions are shown in Figure 6.92. In both cases, the instants after SOI modify the flow field structure and consequently reduce the power content in all the measured scales. In the development of the spray, the power distributions behave differently. In the case of the highest injection pressure, the power decrease in a higher rate than in the case PP4-02. This is consistent with the previous observations. The pressure gradient is higher in the case of the highest injection pressure. Thus, the velocity fluctuations reduction and the velocities reorientations occurs at a higher rate. At the end of injection, the power levels are higher in the case of the lowest injection pressure. At about 1.5 to 2 *ms* after EOI, the power distributions are similar in both cases.

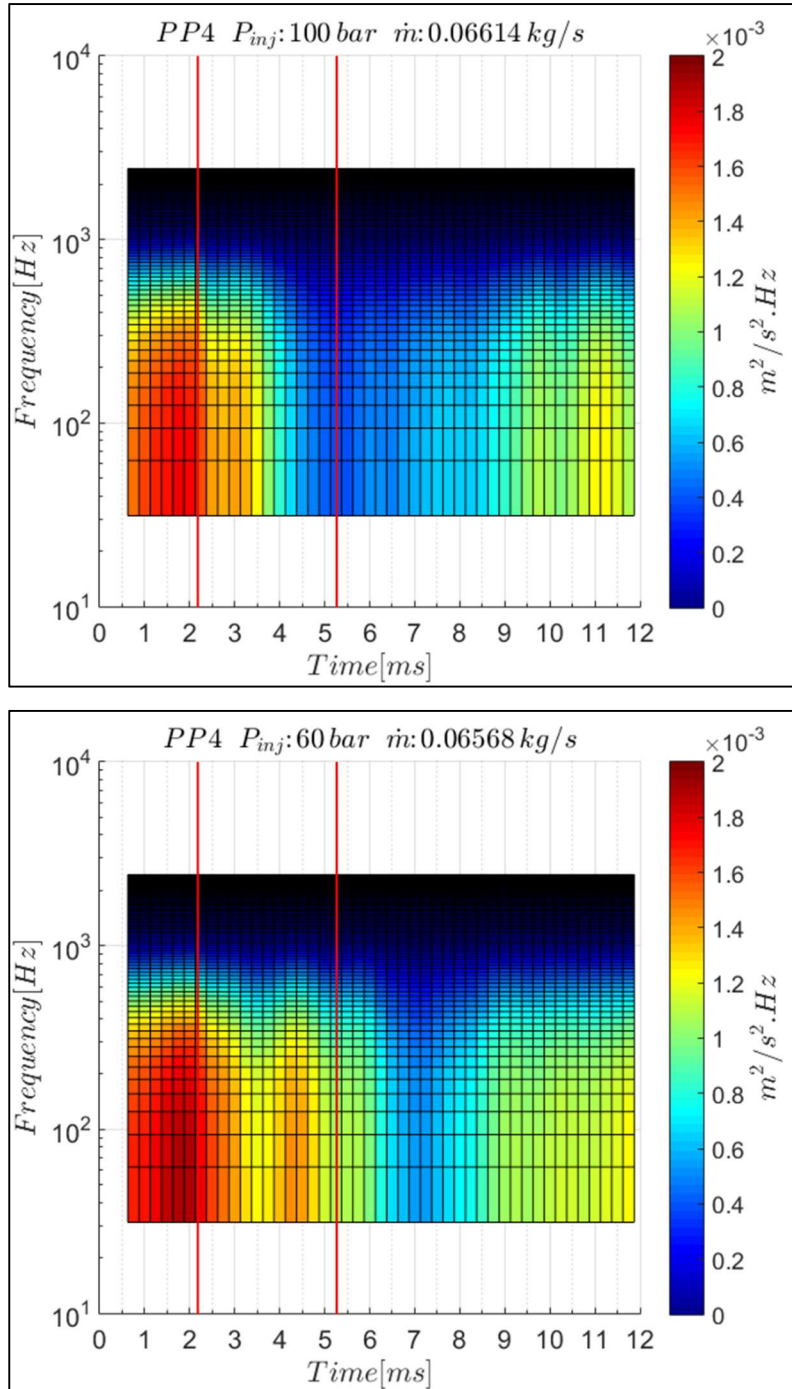


Figure 6.92 – The spectrogram analysis in a point inside the air flow field. The effects of the injection pressure. Cases PP4-01 and PP4-02.

#### 6.2.7.4 Inlet air mass flow effects

Figure 6.93 shows the comparison of the spectrogram calculated in the cases PP4-01 and PP4-03. In the case PP4-03, the power distributions are higher than in the case PP4-01 throughout the injection. Note the difference between the scales of the pictures. Although the power levels are different, the decrease rate is similar in both conditions. At the EOI the power distributions are significantly lower when compared to the stationary conditions.

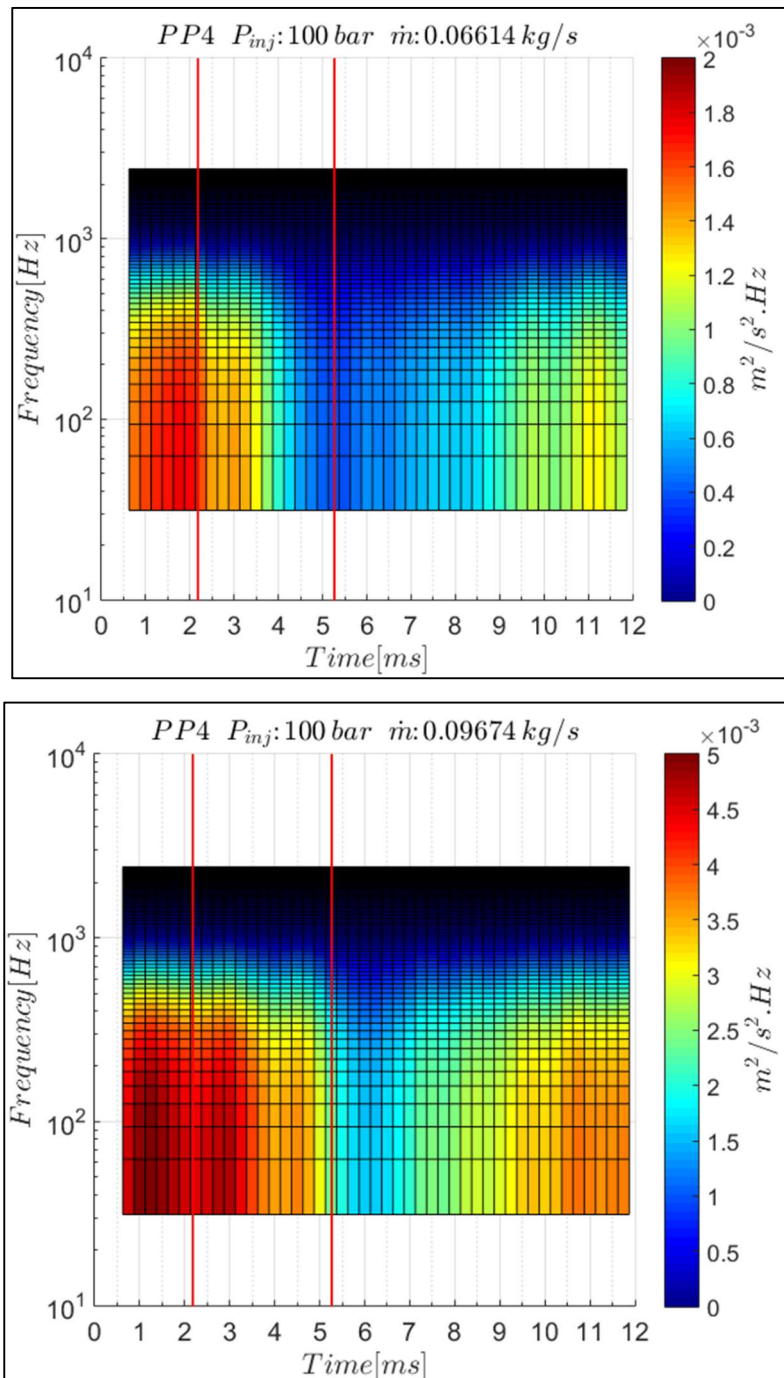


Figure 6.93– The spectrogram analysis in a point inside the air flow field. The effects of the inlet air mass flow. Cases PP4-01 and PP4-03.

The application of the STFT in the measured conditions allows the evaluation of the power content in the frequency scales present throughout the injection events. The same effects discussed with the turbulent intensity distributions are also observed in the spectrogram analyses. The results indicate a decrease in the power content not only in the integral scales. This power reduction is observed in all frequency scales. In all the conditions, the turbulence is reduced during injection. These effects are more sensitive to the injection pressure than to the inlet turbulence integral scales and the inlet air mass flow rate.

## 7 Conclusions and future works

The present work contributes to the field of spray development by studying how the air turbulence properties, the injection pressure and the air mass flow rate affects the evolution of the velocity fields in the presence of the sprays. The major conclusions and remarks which can be drawn from this study are summarized in this section.

In the experimental point of view, the use of a constant-flow chamber evaluated the effects of a continuous flow in the spray development. Few studies in the literature provide data in these experimental conditions. Regarding of the measurement technique, the two-phase PIV was enhanced to meet the experimental conditions. To the knowledge of this study, this technique had not yet applied in studies of sprays from multi-hole injectors in constant-flow conditions. The use of ethanol for the sprays analyses is also a significant contribution.

The large amount of acquired results, about 2.1 million velocity fields, comprises a significant data set. All the special considerations for the application of the PIV methodology and the necessary statistical treatment were taken to provide a comprehensive experimental database.

A detailed description was performed for the stationary flows in which the sprays were to be injected. A procedure was created to characterizes the non-homogeneity of these flow conditions. A consistent estimation of power-spectrum density function (PSD) is obtained. This PSD spatial distribution allows the calculation of integral scales for each measured point that are comparable to geometrical characteristic lengths. A methodology to obtain the spatial distribution of turbulence integral scales is described. The approach is also applicable to different fluid flows with geometrical features of interest.

The analyses of the stationary conditions for the perforated plates set indicate that these are capable of modifying the turbulence properties of the flow field with few effects on the mean velocity distributions. In terms of the turbulence integral scales, an increase is observed with the change of the plates set. Values on the external air flow scales with the holes diameters of the different plates. The power

density distributions indicate a higher power content for the set of 6 mm in all the frequency scales. The estimation of the third velocity components allowed the evaluation of the in-plane motion in the stationary conditions.

In the spray development analyses, the results indicate the formation of a mechanism that depends on the pressure gradient created between the inner and outer regions of the sprays. The velocity fields are reoriented and accelerated towards the spray boundary due to this mechanism. During the initial injection stages, a vortex structure forms in the spray boundary similar to those found in quiescent environments. This structure is responsible for a feedback mechanism that accelerates the air flow around the spray. This structure is stable only in regions with low air velocity magnitude. When the spray penetrates further in the velocity field, this structure detaches from the spray boundary.

Due to the pressure gradient mechanism, the velocity fluctuations are reduced during injection. Hence, a decrease of the turbulent intensity levels is observed for all the acquired cases. The effects of each control parameter are listed below:

- Regarding of the inlet turbulence scales, no significant differences in the velocity field development were observed. With the same boundary conditions of air mass flow and injection pressure, the velocity distributions are similar even with the spray development. Higher reductions of the turbulent intensity levels are noted for the cases with the lowest inlet turbulence length scales. However, since the velocity fields are unaffected, different inlet integral length scales and turbulent intensity scales do not affect the macro spray developments. After the end-of-injection, the transient phenomenon is observed. The velocity magnitudes in EOI transient are little affected by the change of the inlet turbulence integral scales
- The variation of the injection pressure indicated that the pressure gradient mechanism is present in both conditions. With a higher injection pressure, the velocity magnitudes are higher near the injector tip. The turbulent intensity levels depend on the injection pressure during the initial stage. The magnitude of the velocities associated with the EOI transient shown a relation with the injection pressure.

- The cases with the highest inlet air mass flow present higher velocity magnitudes throughout the injection. The evolution of the turbulent intensity fields is different depending on the value of the inlet air mass flow. These distributions tends to similar levels near the end of injection. During the penetration wave, the velocity magnitudes are roughly similar regardless of the inlet air mass flow conditions. The turbulent intensity levels are also similar.
- The use of a time-frequency method to track the power spectra evolution in the presence of the sprays allowed the evaluation of the power content in different scales of turbulence. The results indicate a decrease in the power content not only in the integral scales during the injection event. These effects are more sensitive to the injection pressure than to the inlet turbulence integral scales and the inlet air mass flow rate.

## **7.1 Two-phase PIV technique**

During the experiments and improvements of the two-phase PIV for applications with constant-flow and multi-hole injector, some challenges remain to be addressed. One particular issue is the boundary region between spray and the air stream. With the developed setup, the spatial resolution is not enough to resolve the interaction scales inside this region. Moreover, even the special optical filter set up was not able to complete separate the two phases if it is possible at all to separate them. Future works that evaluate and further enhance measurements of this region are necessary since there is lack of experiments capable of investigating such challenging region.

The use of two-fluorescence signals, one for doping the air tracer particles and another for the spray can be of interest. Visualization of the spray event phenomenon with less interference of light scattering enhance the spray contour and phase distinction.

Another improvement of the technique is to apply the two-camera stereoscopy method in order to obtain the normal velocity component. This approach can detail the tridimensionality of the spray event in terms of velocity, stress tensors and energy distributions.

In the field of image processing, an improvement on the phase distinction is particularly beneficial. It is well-known that the threshold procedure is sensitive to the user choice of parameters. Algorithms that optimize a transfer function between the intensity histograms of both cameras should give better results in phase of distinction procedures.

## **7.2 Air-spray interaction analyses**

The air-spray interaction presents a number of areas that still require further investigations. To the date, there is no single mechanism that describes the spray development. Considering the effects of ambient gas, the situation is even more unclear. To bring the results of air-spray interactions closer to the available theory, experiments that can characterize the states of the droplets during the injection are needed. With the droplets properties, such as diameter and velocity distribution can be used to link the state of atomization and break-up regimes with the ambient gas response to these conditions. However, the evaluation of the droplets time and space dependent variables with the results of the two-phase PIV analysis is a challenge task. In fact, most techniques for measuring droplets diameter are point-to-point acquisitions. The correlation of the air velocity distributions with these properties is even more difficult with the spray transient events.

Another important advance in the field of air-spray interactions would be with the measurement of the fuel vaporization properties during the spray events. An approach developed by Li *et al* [65] for example, can established relations between the fuel and fuel vapor phase. This kind of investigation in a constant-flow environment has not yet been performed and could give details of the interaction mechanism, especially at the boundary of the jets.

The devise of new experimental apparatus to account the effects of geometrical features and ambient pressure are also of great importance in the practical point of view. These devices should be designed to evaluate the combined effects of the results of this research on constant-flow interaction and the results for quiescent environments interactions. In fact, experiments with optical accessible ICE can be off particular interest but are more susceptible to variations of the boundary conditions.

## 8 References

- [1] C. Baumgarten, Mixture formation in internal combustion engines, Berlin: Springer-Verlag Berlin Heidelberg, 2006.
- [2] S. Soid and Z. Zainal, "Spray and combustion characterization for internal combustion engines using optical measuring techniques - A review," *Energy*, vol. 36, no. 2, pp. 724-741, 2011.
- [3] J. Rottenkolber, J. Gindele and R. e. al., "Spray analysis of a gasoline direct injector by means of two-phase PIV," *Experiments in Fluids*, vol. 32, no. 6, pp. 710-721, 2002.
- [4] S. Dankers and M. S. e. a. Gotthardt, "Two-phase PIV: Fuel-spray interaction with surrounding air," in *Particle Image Velocimetry: New Developments and Recent Applications*, Leipzig, Springer - Verlag Berlin Heidelberg, 2008, pp. 333-343.
- [5] P. G. Aleiferis, J. Serras-Pereira, C. J. van Romunde Z. and M. Wirth, "Mechanisms of spray formation and combustion from a multi-hole injector with E85 and gasoline," *Combustion and Flame*, vol. 157, no. 4, pp. 735-756, 2010.
- [6] R. Z. van Romunde, "Factors affecting the development of sprays produced by multihole injectors for direct-injection engine applications," Londres, 2011.
- [7] A. Wierzba, "Deformation and Breakup of Liquids Drops in a Gas Stream at Nearly Critical Weber Numbers," *Experiments in Fluids*, vol. 9, pp. 59-64, 1993.
- [8] M. Staudt, U. Meingast and U. Renz, "Experimental investigation of the turbulent flow field of vaporizing diesel-sprays," in *Proceeding of ICEF2002*, New Orleans, 2002.

- [9] M. Zhang, M. Xu and D. Hung, "Simultaneous two-phase flow measurement of spray mixing process by means of high-speed two-color PIV," *Measurement Science and Technology*, vol. 25, no. 9, p. 095204, 2014.
- [10] J. Zhu, K. K. O. Nishida and S. Moon, "Quantitative analyses of fuel spray-ambient gas interaction by means of LIF-PIV technique," *Atomization and Sprays*, vol. 21, no. 6, pp. 447-465, 2011.
- [11] J. Yeom, "Diagnosis of the behavior characteristics of the evaporative diesel spray by using images analysis," *Journal of Mechanical Science and Technology*, vol. 22, no. 9, pp. 1785-1792, 2008.
- [12] S. Moon, Y. Nishida, Y. Matsumoto and J. Lee, "Gas Entrainment Characteristics of Diesel Spray During End of Injection Transient," *Atomization and Sprays*, vol. 19, no. 11, pp. 1013-1029, 2009.
- [13] B. Prospero, G. Delay and R. Bazile, "FPIV study of gas entrainment by a hollow cone spray submitted to variable density," *Experiments in Fluids*, vol. 43, no. 2-3, pp. 315-327, 2007.
- [14] S. M. Begg, M. P. Hindle, T. Cowel and M. R. Heikal, "Low intake valve lift in a port fuel-injected engine," *Energy*, vol. 34, no. 12, pp. 2042-2050, 2009.
- [15] G. Cossali, "An integral model for gas entrainment into full cone sprays," *Journal of Fluid Mechanics*, vol. 439, pp. 353-366, 2001.
- [16] W. Sauter, J. Pfeil, A. Velji, U. Spicher, N. Laudenbach, F. Altenschmidt and U. Schaupp, "Application of Particle Image Velocimetry for Investigation of Spray Characteristics of an Outward Opening Nozzle for Gasoline Direct Injection," in *Powertran & Fluid Systems*, Toronto, 2006.
- [17] R. Stiehl, J. Schorr, C. Krüger, A. Dreizler and B. Böhm, "In-Cylinder Flow and Fuel Spray Interactions in a Stratified Spray-Guided Gasoline Engine Investigated by High-Speed Laser Imaging Techniques," *Flow Turbulence and Combustion*, vol. 91, pp. 431-450, 2013.

- [18] K. Driscoll, V. Sick and C. Gray, "Simultaneous air/fuel-phase PIV measurements in a dense fuel spray," *Experiments in Fluids*, vol. 35, no. 1, pp. 112-115, 2003.
- [19] D. Towers, C. B. C. H. Towers and M. Reeves, "A colour PIV system employing fluorescent particles for two-phase flow measurements," *Measurement Science and Technology*, vol. 10, no. 9, pp. 824-830, 1999.
- [20] L. Moyne, P. Guibert, R. Roy and B. Jeanne, "Fluorescent-PIV Spray / Air interaction analysis of high- pressure gasoline injector," *Sae Paper 2007-01-1825*, pp. 109-118, 2007.
- [21] B. Peterson and V. Sick, "Simultaneous flow field and fuel concentration imaging at 4.8 kHz in an operating engine.," *Applied Physics B*, vol. 97, pp. 887-895, 2009.
- [22] A. Omrane, P. Petersson, M. Alden and M. Linne, "Simultaneous 2d flow velocity and gas temperature measurements using thermographic phosphors," *Applied Physics B*, vol. 92, pp. 99-102, 2008.
- [23] M. Wells and D. Stock, "The effects of crossing trajectories on the dispersion of particles in a turbulent flow," *Journal of fluid mechanics*, vol. 136, pp. 31-62, 1983.
- [24] R. Liu, D. S. K. Ting and M. David Checkel, "Constant Reynolds number turbulence downstream of an orificed perforated plate," *Experimental Thermal and Fluid Science*, vol. 31, no. 8, pp. 897-908, 2007.
- [25] R. Liu, D. S. K. Ting and G. W. Rankin, "On the generation of turbulence with a perforated plate," *Experimental Thermal and Fluid Science*, vol. 28, no. 4, pp. 307-316, 2004.
- [26] Robert Bosch GmbH, "Technical Customer Information HDEV 5.1," 2009.
- [27] National Instruments, "NI 9751 Direct Injector Driver Module - User Manual," Austin, 2013.

- [28] Exxoster, Naylec et Aircraft Eletronic, "Support banc moteur pedagogique - Moteur essence Injection Directe Turbo," Chavanod, 2009.
- [29] National Instruments, "NI 9478 48 V Sinking Digital Output 16 Ch Module - User Manual," Austin, 2014.
- [30] National instruments, "NI 9201 10 V Analog Input 500 kS/s 8 Ch Module - User Manual," Austin, 2014.
- [31] National Instruments, "NI 9401 5 V/TTL Bidirectional Digital I/O 8 Ch Module - User Manual," Austin, 2014.
- [32] M. Raffel, C. E. Willert, S. T. Wereley and J. Kompenhans, Particle Image Velocimetry - A Practical Guide, Berlin: Springer-Verlag Berlin Heidelberg, 2007.
- [33] R. D. Keane and R. J. Adrian, "Optimization of particle image velocimeters. Part I: Double pulsed systems," *Measurement Science and Technology*, vol. 1, pp. 1202-1215, 1990.
- [34] A. Sciacchitano, *Uncertainty quantification in particle image velocimetry and advances in time-resolved image and data analysis*, Delft: Technische Universiteit Delft, 2014.
- [35] S. International, *SAE J2715 Gasoline Fuel Injector Spray Measurement and Characterization*, 2007, p. 104.
- [36] M. Bardi, R. Payri, L. M. Malbec, G. Bruneaux, L. M. Picket, J. Manin, T. Bazyn and C. Genzale, "Engine combustion network: comparsion of spray development, vaporization, and combustion in different combustion vessels," *Atomization and Sprays*, vol. 22, no. 10, pp. 807-842, 2012.
- [37] A. Melling, "Tracer particles and seeding for particle image velocimetry," *Measurement Science and Technology*, vol. 8, no. 12, pp. 1406-1416, 1997.

- [38] F. Picano, F. Battista and G. Troiani, "Dynamics of PIV seeding particles in turbulent premixed flames," *Experiments in Fluids*, vol. 50, no. 1, pp. 75-88, 2011.
- [39] D. P. Hart, "PIV error correction," *Experiments in Fluids*, vol. 29, no. 1, pp. 13-22, 2000.
- [40] Dantec Dynamics A/S, "DynamicStudio User's Guide," Skovlunde, 2015.
- [41] J. Westerweel and F. Scarano, "Universal outlier detection for PIV data," *Experiments in Fluids*, vol. 39, no. 6, pp. 1096-1100, 2005.
- [42] B. Yang, Y. Wang and J. Liu, "PIV measurements of two phase velocity fields in aeolian sediment transport using fluorescent tracer particles," *Measurement*, vol. 44, no. 4, pp. 708-716, 2011.
- [43] H. K. Versteeg and W. Malalasekera, *An Introduction to Computational Fluid Dynamics*, Glasgow: Pearson Education Limited, 2007.
- [44] T. Kajishima and K. Taira, *Computational Fluid Dynamics - Incompressible Turbulent Flows*, Springer International Publishing, 2017.
- [45] Instituto Nacional de Metrologia, Qualidade e Tecnologia, *Guia para a expressão de incerteza de medição - GUM2008*, Rio de Janeiro, 2012.
- [46] F. P. Incropera, D. P. Dewitt, T. L. Bergman and A. Lavine, *Fundamentals of Heat and Mass Transfer*, Willey, 2011.
- [47] G. J. Van Wylem, R. E. Sonntag and C. Borgnakke, *Fundamentals of Thermodynamics*, Willey, 2003.
- [48] L. Michalski, K. Eckersdorf, J. Kucharski and J. McGhee, *Temperature Measurement*, John Willey & Sons, Ltd., 2002.
- [49] A. Sciacchitano, F. Scarano and B. Wieneke, "PIV uncertainty quantification by image matching," *Measurement Science and Technology*, vol. 24, pp. 1-20, 2013.

- [50] R. J. Adrian, "Dynamic ranges of velocity and spatial resolution of particle image velocimetry," *Measurement Science and Technology*, vol. 8, pp. 1393-1398, 1997.
- [51] J. D. Luff, T. Drouillard, A. M. Rompage, M. A. Linne and J. R. Herzberg, "Experimental uncertainties associated with particle image velocimetry (PIV) based on vorticity algorithms," *Experiments in Fluids*, vol. 26, no. 1-2, pp. 36-54, 1999.
- [52] Z. Xue, J. J. Charonko and P. P. Vlachos, "Particle image velocimetry correlation signal-to-noise ratio metrics and measurement uncertainty quantification," *Measurement Science and Technology*, vol. 25, no. 11, 2014.
- [53] Z. Xue, J. J. Charonko and P. P. Vlachos, "Particle image pattern mutual information and uncertainty estimation for particle image velocimetry," *Measurement Science and Technology*, vol. 26, no. 7, 2015.
- [54] E. Baum, B. Peterson, B. Böhm and A. Dreizler, "On the validation of LES applied to internal combustion engine flows. Part 1: Comprehensive experimental database," *Flow, Turbulence and Combustion*, vol. 92, no. 1-2, pp. 269-297, 2014.
- [55] F. Zentgraf, E. Baum, B. Böhm, A. Dreizler and B. Peterson, "On the turbulent flow in piston engines: Coupling of statistical theory quantities and instantaneous turbulence," *Physics of Fluids*, vol. 28, no. 4, 2016.
- [56] M. H. Hayes, *Statistical digital signal processing and modeling*, New York: John Wiley & Sons, 2009.
- [57] D. Summer, S. Wong, S. Price and M. Paidoussis, "Fluid behaviour of side-by-side circular cylinders in steady cross-flow," *Journal of Fluids and Structures*, vol. 13, no. 3, pp. 309-338, 1999.
- [58] B. Galmiche, N. Mazellier, F. Halter and F. Foucher, "Turbulence characterization of a high-pressure high-temperature fan-stirred combustion

- vessel using LDV, PIV and TR-PIV measurements," *Experiments in fluids*, vol. 55, no. 1, 2014.
- [59] W. Hwang and J. K. Eaton, "Creating homogeneous and isotropic turbulence without a mean flow," *Experiments in Fluids*, vol. 36, no. 3, pp. 444-454, 2004.
- [60] S. Ravi, S. Perltier, J. Scott and E. Petersen, "Analysis of the impact of impeller geometry on the turbulent statistics inside a fan-stirred, cylindrical flame speed vessel using PIV," *Experiments in fluids*, vol. 54, no. 1, 2013.
- [61] S. B. Pope, *Turbulent Flows*, IOP Publishing, 2001.
- [62] M. P. Wernet, "Temporally resolved PIV for space-time correlations in both cold and hot jet flows," *Measurement Science and Technology*, vol. 15, no. 5, 2007.
- [63] Y. Nakamura, "Vortex shedding from bluff bodies and a universal Strouhal number," *Journal of Fluids and Structures*, vol. 10, no. 2, pp. 159-171, 1996.
- [64] S. Moon, Y. Matsumoto, K. Nishida and J. Gao, "Gas entrainment characteristics of diesel spray injected by a group-hole nozzle," *Fuel*, vol. 89, no. 11, pp. 3287-3299, 2010.
- [65] T. Li, K. Nishida and H. Hiroyasu, "Droplet size distribution and evaporation characteristics of fuel spray by a swirl type atomizer," *Fuel*, vol. 90, no. 7, pp. 2367-2376, 2011.
- [66] Robert Bosch Gmbh, "Gasoline direct injection - key technology for greater efficiency and dynamics," Stuttgart, 2013.
- [67] P. Muhuri and D. Hazra, "Density and Viscosity for Propylene Carbonate + 1, 2 -Dimethoxyethane at 298.15, 308.15, and 318.15 K," *Journal of Chemical and Engineering Data*, vol. 39, pp. 375-377, 1994.

- [68] B. S. Brown, S. N. Rogak and S. Munshi, "Multiple injection strategy in a direct-injection natural gas engine with entrained diesel," *SAE Int. J. Fuels Lubr.*, vol. 2, pp. 953-965, 2009.
- [69] J. Beeckmann, O. Röhl and N. Peters, "Numerical and experimental investigation of laminar burning velocities of iso-octane, ethanol and n-butanol," *SAE Technical Paper 2009-01-2784*, 2009.